Street, Michael William (1997) *Quantum well intermixing for the control of second order non-linear effects in GaAs/AIGaAs asymmetric quantum well waveguides.*

PhD thesis

Quantum Well Intermixing for the Control of Second Order Non-linear Effects in GaAs/AlGaAs Asymmetric Quantum Well Waveguides

by

Michael William Street

Submitted for the degree of

Doctor of Philosophy

to the

Faculty of Engineering

University of Glasgow

March 1997

Acknowledgements

From my earliest days as an undergraduate student, it has been my ambition to do a PhD. I could not, however, have written this thesis without the encouragement and advice of family, friends and colleagues along the way.

In particular, I would like to thank my parents whose love and support is limitless. Everything I am, and everything I have achieved, I owe to you Mum and Dad. I would like to thank my brother Steve, who, unwittingly, was probably the person who inspired me to follow my dreams in the first place. I would also like to thank my girlfriend Alison who, in addition to being lovely, has been very understanding over the past few months. I am also grateful to all my friends outside the department who, despite being scattered all over the British Isles, have had to tolerate my moaning in recent months.

The last three years of my education have undoubtedly been some of the most enjoyable. The friendship of my colleagues both inside and outside normal working hours has been the key to my happiness within the department, and for that I am very grateful.

On a more professional level, I would like to thank John Marsh for his support, his boundless enthusiasm, and the new job. I would like to thank Stewart Aitchison who is "Mr. Semiconductor Non-linear Optics", and whose guidance throughout has been invaluable. I would like to acknowledge Dave Hutchings with whom I have had many useful conversations without which I would understand a lot less about non-linear optics than I do today. I must also acknowledge my co-worker Neil Whitbread, from whom I learnt a great deal over the two year period of his research contract. Throughout this work I have tried to highlight his contributions as much as possible. I am very grateful for all the assistance and advice given to me by Gordon Kennedy from the Department of Physics and Astronomy at the University of St. Andrews. Gordon went beyond the call of duty to provide us with a pulsed source of coherent radiation at 1.55 μm on several occasions. Craig Hamilton too, deserves a "big hand" for all his help with the colour centre laser within the department, and must be acknowledged for his advice relating to H-plasma processing for the suppression of impurity-free vacancy disordering. I would like to thank Dan Ortega for several useful conversations - his English pronunciation may not be the best, but his understanding of the concepts of second order non-linear optics is flawless. I must also acknowledge Brigitta Vögele and John Roberts who persevered with the growth of multiple asymmetric quantum well structures in the face of multiple difficulties. In addition, I would like to thank the Research Assistants of the Optoelectronics Group who have all assisted me with my research at one time or another.

I am heavily indebted to all of the technician staff members within the department. Without their advice, assistance and co-operation, there would have been no experiments. In particular, I am extremely grateful to Jim Gray, who can only be described as a star of the highest order. The cleanroom staff, the dry-etch team, Doogie Irons and the workshop crew, Jimmy Young and Ian McNicholl have all been unfeasibly helpful throughout.

Finally, I would like to thank Derek Nesset and friends at BT Labs in Martlesham Heath where I learnt a great deal about laser diodes and non-linear fibre optics in a short space of time.

Mike Street,

8th March, 1997.

Contents

Glossary of Mathematical Symbols

c	Velocity of light in a vacuum
$c(z)$	Depth-dependent probability current $\frac{1}{m^*(z)}\frac{du(z)}{dz}$
D	Group III interdiffusion coefficient
$\mathbf{d}(-\omega_\sigma;\omega_1,\omega_2)$	Contracted second-order susceptibility tensor for the sum frequency generation process $\omega_1,\omega_2 \rightarrow \omega_\sigma$
$d_{eff}(-\omega_\sigma;\omega_1,\omega_2)$	Effective scalar contracted second-order susceptibility coefficient for the sum frequency generation process $\omega_1,\omega_2 \rightarrow \omega_\sigma$
d_{eff}	Effective scalar contracted second-order susceptibility coefficient for SHG in non-linear starting material
d_{eff}'	Effective scalar contracted second-order susceptibility coefficient for SHG in disordered non-linear material
d_{QPM}	Effective scalar d coefficient of equivalent homogeneous non-linear medium resulting as a consequence of quasi-phase-matching
E	Eigenenergy of relevant particle (electron, light- or heavy-hole) in QW potential (Chapter 4)
$\mathbf{E}(t)$	Time-dependent electric field vector
$E(t)$	Scalar time-dependent electric field
$\mathbf{E}(\omega)$	Fourier transform of $\mathbf{E}(t)$
$\mathbf{E}_\omega(z)$	Amplitude of monchromatic electric field component at frequency ω
$\hat{\mathbf{E}}(\omega,z)$	Complex travelling-wave amplitude of $\mathbf{E}(\omega)$
$\hat{\mathbf{E}}_\omega(z)$	Complex travelling-wave amplitude of monchromatic electric field component at frequency ω
$\hat{E}_\omega(z)$	Scalar complex travelling-wave amplitude of monchromatic electric field component at frequency ω
E_X	Exciton binding energy in QW
E_C	Carbon acceptor binding energy
E_{e1hh1}	Energy of first QW electron level to first QW heavy-hole level transition

E'_{e1hh1}	Energy of first QW electron level to first QW heavy-hole level transition after intermixing
E_{e1hh1X}	e1hh1 exciton peak energy
E_{e1C}	Energy of e1->C transition
E'_{e1C}	Energy of e1->C transition after intermixing
$F^{(2)}$	Overlap integral factor for SHG in waveguide (uniform transverse d_{eff} profile)
$F^{(2)'}$	Overlap integral factor for SHG in waveguide (uniform transverse d_{eff} profile) after intermixing
$FOM^{(2)}$	Figure of merit for second-order non-linear materials $\frac{d_{eff}^2}{n_{\omega}^2 n_{2\omega}}$
$f_{e,lh}, f_{e,hh}$	Relative interband oscillator strengths for electron to light-hole and electron to heavy-hole transitions respectively
$f(z)$	$\frac{2M^*}{\hbar^2}[V-E]$ (Chapter 4)
$g(z)$	$\frac{2}{\hbar^2}[v(z)-E]$ (Chapter 4)
h	Planck's constant
$\hbar$	$\frac{h}{2\pi}$
$I_{\omega}(z)$	Fundamental field intensity
$I_{2\omega}(z)$	Second harmonic field intensity
K	Magnitude of wavevector associated with periodic modulation in the refractive index or d coefficient
$\mathbf{k}(\omega)$	Wavevector at frequency ω
$k(\omega)$	Magnitude of wavevector at frequency ω
L	Length of non-linear medium
L_c	Coherence length
L_d	Diffusion length (Chapter 6), domain length (Appendix B)
M	Constant effective mass of relevant particle (electron, light- or heavy-hole) within a given piecewise constant segment (Chapter 4)
M^*_{BL}	Effective mass of relevant particle (electron, light- or heavy-hole) in left-hand QW barrier

M^*_{BR}	Effective mass of relevant particle (electron, light- or heavy-hole) in right-hand QW barrier
m	Order of the quasi-phase-matching scheme
$m^*(z)$	Depth-dependent effective mass of relevant particle (electron light- or heavy-hole)
$m^*_L(z)$	Depth-dependent effective mass of relevant particle at position just to left of position z
$m^*_R(z)$	Depth-dependent effective mass of relevant particle at position just to right of position z
$n(\omega)$	Refractive index of medium at frequency ω
n_{eff}	Effective waveguide mode index
n_{TE}	Bulk equivalent refractive index of MQW layer for TE-polarised light
n_{TM}	Bulk equivalent refractive index of MQW layer for TM-polarised light
$\mathbf{P}^{NL}(t)$	Non-linear part of the time-dependent polarisation vector
$\mathbf{P}^{NL}(\omega)$	Fourier transform of $\mathbf{P}^{NL}(t)$
$\mathbf{P}^{(2)}_{\omega}(z)$	Amplitude of monchromatic second-order polarisation field component at frequency ω
$P_{\omega}(z)$	Fundamental power as a function of position through non-linear medium
$P_{2\omega}(z)$	Second harmonic power as a function of position through non-linear medium
q	Electronic charge
R	Reflectance
T	Fabry-Perot cavity transmission (Chapter 7)
t	Time
t(z)	Envelope function gradient of relevant particle (electron, light- or heavy-hole) in arbitrary units
u(z)	Envelope function of relevant particle (electron, light- or heavy-hole) in arbitrary units

$u_L(z)$	Envelope function of relevant particle in arbitrary units just to left of position z
$u_R(z)$	Envelope function of relevant particle in arbitrary units just to right of position z
$u'(z)$	Envelope function gradient of relevant particle (electron, light- or heavy-hole) in arbitrary units
$u_L'(z)$	Envelope function gradient of relevant particle in arbitrary units just to left of position z
$u_R'(z)$	Envelope function gradient of relevant particle in arbitrary units just to right of position z
$v(z)$	Conduction or valence band potential profile
V	Constant conduction or valence band potential within a given piecewise constant segment (Chapter 4), visibility of Fabry-Perot oscillations (Chapters 7 and 8)
V_{BL}	Conduction or valence band potential in left-hand QW barrier
V_{BR}	Conduction or valence band potential in right-hand QW barrier
W	QW width
X,Y,Z	Mapped crystal co-ordinates after rotation by 45° around z (= Z) axis
x,y,z	Crystal co-ordinates
$x(z,t)$	Al fraction as a function of depth z and time t

α	Decay constant of envelope function of relevant particle (electron, light- or heavy-hole) in left-hand barrier (Chapter 4), absorption coefficient (Chapter 5), waveguide loss coefficient (Chapters 7 and 8)
β	Decay constant of envelope function of relevant particle (electron, light- or heavy-hole) in right-hand barrier
$\chi^{(2)}(-\omega_\sigma;\omega_1,\omega_2)$	Second-order non-linear susceptibility tensor for the sum frequency generation process $\omega_1,\omega_2 \rightarrow \omega_\sigma$

$\chi^{(2)}_{eff}(-\omega_\sigma;\omega_1,\omega_2)$	Effective scalar second-order susceptibility for the sum frequency generation process $\omega_1,\omega_2 \rightarrow \omega_\sigma$
$\chi^{(2)}_{ijk}$	Second-order non-linear susceptibility tensor element for the SHG process $\omega,\omega \rightarrow 2\omega$
$\chi^{(2)'}_{ijk}$	Second-order non-linear susceptibility tensor element for the SHG process $\omega,\omega \rightarrow 2\omega$ after intermixing
Δk	Wavevector mismatch parameter for SHG
Δk_{QPM}	Effective wavevector mismatch parameter resulting as a consequence of quasi-phase-matching
Δz	Depth increment used during evaluation of envelope functions using shooting method algorithm
$\Delta\Phi^{NL}(z)$	Non-linear phase change
ε_0	Permittivity of free space
$\phi(z)$	Normalised envelope function of relevant particle (electron, light- or heavy-hole)
η	Conversion efficiency parameter for waveguide SHG
Γ	$\sqrt{\frac{8\pi^2}{\varepsilon_0 c\lambda^2}\cdot\frac{d_{eff}^2}{n_\omega^2 n_{2\omega}}\cdot I_\omega(0)}$
γ	$\lvert\gamma\rvert \leq 1$ where $1-\gamma$ is the modulation depth in d_{eff}
Λ	Period of modulation in refractive index or d coefficient used for quasi-phase-matching
λ	Wavelength
μ_0	Permeability of free space
ω	Angular frequency
$\xi_\omega(x,y)$	Normalised transverse fundamental field profile in waveguide
$\xi_{2\omega}(x,y)$	Normalised transverse second harmonic field profile in waveguide
$\Psi_{j\omega}$	$\frac{\omega d_{eff}}{n_\omega c}\cdot\frac{1}{\Delta k}\cdot\sqrt{\frac{n_{j\omega}}{n_{2\omega}}}\cdot\hat{E}_{j\omega}$
ζ	Δkz

Abstract

This work is concerned with the control of second order non-linear effects in GaAs/AlGaAs multiple asymmetric quantum well waveguides using a novel quasi-phase-matching technique with a view to performing ultrafast all-optical signal processing via the cascaded second order effect at 1.55 μm. Asymmetric quantum wells (AQW) have several different tensor components associated with them in addition to the bulk GaAs/AlGaAs non-linearity. All of these non-linearities are potentially modified by QW-intermixing, and it is the study of these effects which constitutes the main subject matter of this thesis.

QW-intermixing was accomplished for several different multiple AQW structures using impurity-free vacancy disordering (IFVD). Unphase-matched second harmonic generation (SHG) experiments were subsequently performed with waveguides fabricated from as-grown and intermixed AQW material. No conclusive evidence was found for the existence of any AQW tensor components. This is consistent with recent calculations which predict, that for the *particular* AQW structures studied, the AQW non-linearities are negligible. Unphase-matched SHG was, however, observed which was attributable to the large bulk GaAs/AlGaAs d_{14} coefficient. Furthermore, d_{14} was reduced by 17% on intermixing. Since the quasi-phase-matching conversion efficiency is proportional to both the square of the magnitude of the non-linearity and the square of the modulation depth, a small but significant reduction in the large d_{14} coefficient such as this, could lead to useful conversion efficiencies.

Selective-area IFVD was achieved using hydrogen plasma processing to inhibit intermixing. Only partial suppression of the IFVD process was, however, achieved. The spatial resolution of the selective-area process was measured for two different MQW structures under different annealing conditions, and was found to be better than 2.2 μm. The resolution of the IFVD process is therefore sufficiently good for the control of second order non-linear interactions in GaAs/AlGaAs MQW waveguides.

Periodically-intermixed waveguides were fabricated for quasi-phase-matching. These waveguides had measured losses ranging between 3.7 dB/cm and 18 dB/cm depending on the intermixing period. Phase-matching was not, however, observed in these devices. This may have been a consequence of one of several factors including, non-ideal laser tuning characteristics, the use of inaccurate intermixing periods, and a negligible modulation depth in d_{14}. Further work is therefore necessary to establish why phase-matching was not achieved, and to improve the selective-area intermixing process. If these difficulties can be overcome and, in addition, an AQW structure can be designed with associated significant non-linearities, then SHG conversion efficiencies of several hundred %/Wcm^2 may be possible.

1

Introduction

The original motivation for this work was the achievement of ultrafast all-optical switching using the cascaded second order effect in AlGaAs at 1.55 μm. However, the phase-matching technology used for this work can also be applied for wavelength conversion and for optical parametric oscillation. These applications are therefore discussed below in addition to the subject of all-optical switching.

1.1 All-optical Switching

With the world-wide explosion in information technology over the last decade, there has been an increasing demand for ultra-high bit rate telecommunication systems. With the advent of the laser diode, and the development of optical fibres with a large bandwidth capacity (a few tens of THz) and low propagation losses, mutligigahertz data transmission has been achieved over long distances. However, the "bandwidth-bottleneck" which occurs as a consequence of "slow" opto-electronic conversion at the receiver, limits the bit rate of optical time division multiplexing (OTDM) systems. The demonstration of ultrafast all-optical switching at 1.55 μm for demultiplexing (DEMUX) at ultrahigh bit rates (> 100 Gb/s) has therefore been a universal goal.

All-optical switching (AOS) has been achieved using many different effects in a wide variety of materials and device geometries. One of the most successful approaches in recent years is based upon the SLALOM (semiconductor laser amplifier in a loop mirror) device illustrated in Fig. 1.1 [1]. As may be seen from Fig. 1.1, a SLALOM essentially consists of a fibre loop mirror incorporating a semiconductor laser amplifier (SLA) which is offset from the centre position of the loop. If, for this device, the SLA is offset in time from the loop centre by T/2 seconds, then the clockwise (cw) circulating data pulse will arrive at the SLA at a time T seconds before the arrival of the counter-clockwise (ccw) circulating pulse.

When no high intensity control pulses are coupled into the loop, the cw and ccw pulses interfere at the input/output coupler and are reflected back to the data input arm of the device. If, however, in the period of duration T seconds between the arrival of the cw and ccw pulses at the SLA, a high intensity control pulse arrives at the SLA, the gain is saturated very rapidly. Furthermore, since the gain recovers on a much slower time scale, the cw and ccw pulses experience different gain and phase changes within the SLA. When the difference between the phase changes experienced by the cw and ccw pulses is equal to π, the interference at the input/output coupler switches the data pulse to the data output arm of the device.

The application of the SLALOM as a fast all-optical demultiplexer has been demonstrated by several groups [2,3,4]. Very high data rates of up to 160 Gb/s have been demultiplexed down to rates of 10 Gb/s which can be processed electronically. Furthermore, the control pulse power levels required for the DEMUX operation, are compatible with existing semiconductor laser diode technology. The DEMUX of higher data rates is, however, limited by the gain recovery time of the SLA.

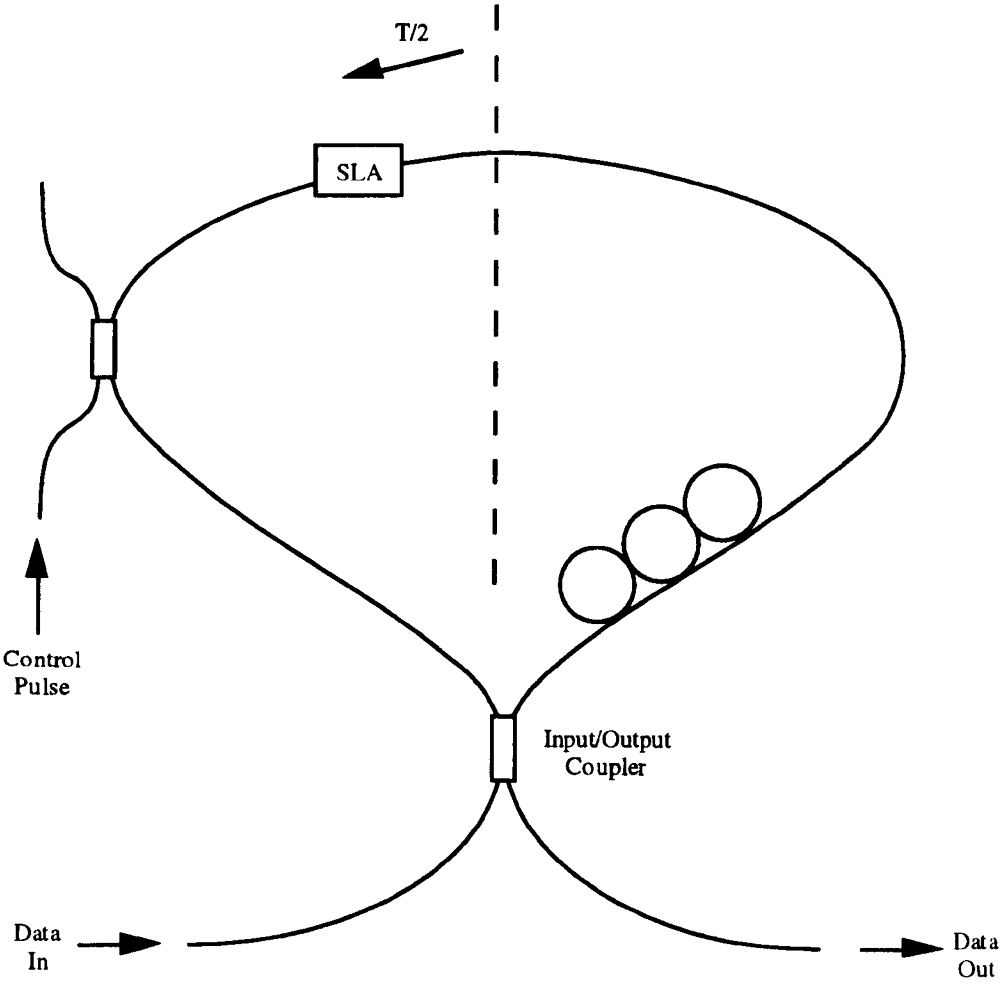

Fig. 1.1 SLALOM all-optical time-division demultiplexer

An alternative approach to all-optical switching utilises ultrafast non-linear effects in passive waveguide structures. For example, ultrafast all-optical switching was demonstrated in a series of experiments with integrated AlGaAs devices in a variety of different geometries using the intensity-dependent refractive index n_2 at photon energies just below the half-band-gap [5,6,7]. Ultrafast operation of these devices was, however, achieved at the expense of high switching powers so that typical peak powers of ~100 W were required for switching.

All-optical switching using the cascaded second order effect was originally proposed by Assanto *et al.* [8]. This effect relies on sum or difference frequency conversion followed by the opposite process in which the original frequencies are regenerated with an accompanying non-linear phase shift. The GaAs/AlGaAs material system has a large second-order non-linear figure of merit which is approximately an order of magnitude greater than that of $LiNbO_3$. Ironside *et al.* [9] therefore proposed an AlGaAs Mach-Zehnder interferometer (MZI) based on the cascaded second order effect with predicted switching powers of ~1 W. Hutchings *et al.* [10] later proposed a dual-wavelength AlGaAs MZI device with estimated switching powers of ~10 W. In the AlGaAs material system, however, no really efficient phase-matching technique has been demonstrated to date, so that cascaded second-order all-optical switching has only been performed in $LiNbO_3$ devices [11,12]. In the two experiments of references [11] and [12], birefringent type I phase-matching was achieved between the $TM_{\omega 00}$ and $TE_{2\omega 00}$ modes in Ti-diffused $LiNbO_3$ channel waveguides using temperature tuning, where the propagation direction was along the X axis of a Y-cut crystal. In the first experiment, Baek *et al.* [11] demonstrated all-optical switching in a hybrid MZI with a 7:1 contrast ratio as a result of the cascaded second order non-linearity. In the second experiment [12], all-optical switching was demonstrated in an integrated non-linear directional coupler. In this case, switching between the cross and bar branches of the coupler was achieved with a ratio of 1:5 and a throughput of 80%. For both of these experiments, however, switching was accomplished via the relatively small d_{31} non-linearity, and the effective waveguide core areas were not optimised. Peak powers of ~1000 W were therefore required for switching.

In conclusion, it should suffice to state that, if an efficient quasi-phase-matching technique can be developed for GaAs/AlGaAs, with its large second-order non-linear figure of merit, ultrafast all-optical switching using the cascaded second-order effect may be feasible at powers of ~10 W.

1.2 Quasi-phase-matching for Wavelength Conversion and Optical Parametric Oscillation

Wavelength conversion is important in its own right for the generation of coherent blue light for high-density optical data storage, and for wavelength division multiplexing (WDM) communication systems. To date, blue light generation has been achieved in both periodically-poled $LiNbO_3$ (PPLN) with conversion efficiencies of several hundred %/Wcm^2 [13,14,15], and in ion-exchanged KTP with conversion efficiencies exceeding 50 %/Wcm^2 [16]. The GaAs/AlGaAs material system is, however, absorbing in the visible and cannot be used for blue-light generation. Second harmonic generation (SHG) has, however, been demonstrated in GaAs/AlGaAs in the near infra-red where conversion efficiencies of 167 %/Wcm^2 were achieved using periodic domain inversion by wafer bonding and re-growth [17]. New possibilities therefore exist for the simultaneous conversion of tens of different wavelengths [18]. Such a technology clearly has very beneficial implications for WDM networks.

Optical parametric oscillators (OPO) have also been realised using quasi-phase-matching in both bulk PPLN [19], and in PPLN waveguides [20]. Such devices are widely tuneable sources of coherent radiation from near to mid infra-red wavelengths. OPO's fabricated from bulk PPLN pumped with 1.064 μm pulsed Nd:YAG lasers, for example, have been operated over the wavelength range 1.4 - 4 μm, with tuning by temperature or quasi-phase-matching period [21]. In addition, a cw doubly resonant PPLN OPO near 1.96 μm pumped directly with a commercial cw laser diode at 978 nm, has also been demonstrated [20]. To date, optical parametric amplification has not been achieved in GaAs/AlGaAs essentially because no efficient phase-matching technique exists for this material system.

1.3 Thesis Outline

This work is concerned with the development of a novel quasi-phase-matching technique for the control of second order non-linear effects in the GaAs/AlGaAs material system. After a review of second order non-linear effects in Chapter 2, a novel domain-disordering technique is described in Chapter 3. This technique involves the suppression of the non-linear coefficients associated with multiple asymmetric quantum well (AQW) waveguides. The algorithm used throughout this work for the numerical solution of Schrödinger's equation in an arbitrary potential profile, is outlined in Chapter 4. This algorithm is subsequently used in Chapter 5 for the design and characterisation of AQW structures. Chapter 6 is concerned with the QW-intermixing technique used to suppress both the bulk GaAs/AlGaAs d_{14} coefficient, and the AQW second-order susceptibility tensor components. The experiments with AQW waveguides which are described in Chapter 7, demonstrate that the unphase-matched second harmonic signal generated through the bulk d_{14} coefficient is significantly reduced on QW-intermixing. In Chapter 8, experiments with periodically-intermixed AQW waveguides for quasi-phase-matched SHG are described. Finally, conclusions are drawn, and some further experiments are proposed in a separate section.

---

[1] M. Eiselt, W. Pieper, and H. G. Weber, "SLALOM: Semiconductor Laser Amplifier in a Loop Mirror", J. Lightwave Technol. **13**, 2099 (1995)

[2] A. D. Ellis and D. M. Spirit, "Compact 40 Gbit/s Optical Demultiplexer Using a GaInAsP Optical Amplifier", Electron. Lett. **29**, 2115 (1993)

[3] I. Glesk, J. P. Sokoloff, and P. R. Prucnal, "Demonstration of All-optical Demultiplexing of TDM Data at 250 Gbit/s", Electron. Lett. **30**, 339 (1994)

[4] K. Suzuki, K. Iwatsuki, S. Nishi, and M. Saruwatari, "160 Gbit/s Single Polarisation Subpicosecond Transform Limited Pulse Signal Demultiplexing Using Ultrafast Optical Loop Mirror Including MQW Travelling Wave Semiconductor Laser Amplifier", Electron. Lett. **30**, 660 (1994)

[5] J. S. Aitchison, A. H. Kean, C. N. Ironside, A. Villeneuve, and G. I. Stegeman, "Ultrafast All-optical Switching in $Al_{0.18}Ga_{0.82}As$ Directional Coupler in 1.55 µm Spectral Region", Electron. Lett. **27**, 1709 (1991)

[6] K. Al-hemyari, J. S. Aitchison, C. N. Ironside, G. T. Kennedy, R. S. Grant, and W. Sibbett, "Ultrafast All-optical Switching in GaAlAs Integrated Interferometer in 1.55 µm Spectral Region", Electron. Lett. **28**, 1090 (1992)

[7] J. S. Aitchison, A. Villeneuve, and G. I. Stegeman, "All-optical Switching in a Nonlinear GaAlAs X Junction", Opt. Lett. **18**, 1153 (1993)

[8] G. Assanto, G. I. Stegeman, M. Sheik-Bahae, and E. Van Stryland, "All-optical Switching Devices Based on Large Nonlinear Phase Shifts from Second Harmonic Generation", Appl. Phys. Lett. **62**, 1323 (1993)

[9] C. N. Ironside, J. S. Aitchison, and J. M. Arnold, "An All-optical Switch Employing the Cascaded Second-order Nonlinear Effect", J. Quantum. Electron **29**, 2650 (1993)

[10] D. C. Hutchings, J. S. Aitchison, and C. N. Ironside, "All-optical Switching Based on Nondegenerate Phase Shifts from a Cascaded Second-order Nonlinearity", Opt. Lett. **18**, 793 (1993)

[11] Y. Baek, R. Scheik, and G. I. Stegeman, "All-optical Switching in a Hybrid Mach-Zehnder Interferometer as a Result of Cascaded Second-order Nonlinearity", Opt. Lett. **20**, 2168 (1995)

[12] R. Scheik, Y. Baek, G. Krijnen, G. I. Stegeman, I Baumann, and W. Sohler, "All-optical Switching in Lithium Niobate Directional Couplers with Cascaded Nonlinearity", Opt. Lett. **21**, 940 (1996)

[13] M. Yamada, N. Nada, M. Saitoh, and K. Watanabe, "First-order Quasi-phase-matched $LiNbO_3$ Waveguide Periodically Poled by Applying an External Field for Efficient Blue Second-harmonic Generation", Appl. Phys. Lett. **62**, 435 (1993)

[14] C. Q. Xu, H. Okayama, K. Shinozaki, K. Watanabe, and M. Kawahara, "Wavelength Conversions ~ 1.5 μm by Difference Frequency Generation in Periodically Domain-inverted $LiNbO_3$ Channel Waveguides", Appl. Phys. Lett. **63**, 1170 (1993)

[15] K. Kintaka, M. Fujimura, T. Suhara, and H. Nishihara, "High-efficiency $LiNbO_3$ Waveguide Second-Harmonic Generation Devices with Ferroelectric-Domain-Inverted Gratings Fabricated by Applying Voltage", J. Lightwave Technol. **14**, 462 (1996)

[16] C. J. van der Poel, J. D. Bierlein, J. B. Brown, and S. Colak, "Efficient Type I Blue Second-harmonic Generation in Periodically Segmented $KTiOPO_4$ Waveguides", Appl. Phys. Lett. **57**, 2074 (1990)

[17] S. J. B. Yoo, C. Caneau, R. Bhat, M. A. Koza, A. Rajhel, and N. Antoniades, "Wavelength Conversion by Difference Frequency Generation in AlGaAs Waveguides with Periodic Domain Inversion Achieved by Wafer Bonding", Appl. Phys. Lett. **68**, 2609 (1996)

[18] S. J. B. Yoo, "Wavelength Conversion Technologies for WDM Network Applications", J. Lightwave Technol. **14**, 955 (1996)

[19] L. E. Myers, G. D. Miller, R. C. Eckardt, M. M. Fejer, R. L. Byer, and W. R. Bosenburg, "Quasi-phase-matched 1.064-μm-pumped Optical Parametric Oscillator in Bulk Periodically Poled $LiNbO_3$", Opt. Lett. **20**, 52 (1995)

[20] M. L. Bortz, M. A. Arbore, and M. M. Fejer, "Quasi-phase-matched Optical Parametric Amplification and Oscillation in Periodically Poled $LiNbO_3$ Waveguides", Opt. Lett. **20**, 49 (1995)

[21] L. E. Myers, R. C. Eckardt, M. M. Fejer, R. L. Byer, W. R. Bosenburg, and J. W. Pierce, "Quasi-phase-matched Optical Parametric Oscillators in Bulk Periodically Poled $LiNbO_3$", J. Opt. Soc. Am. B **12**, 2102 (1995)

2

Second Order Non-linear Effects and All-optical Switching

There are several different optical phenomena associated with a second order non-linear medium: second harmonic generation, sum and difference frequency mixing, parametric amplification and oscillation, optical rectification, and the linear electro-optic effect. Throughout this work, we are only concerned with second harmonic generation (which is the degenerate case of sum frequency mixing) and the opposite down-conversion process from the second harmonic frequency to the fundamental frequency (which is a special case of difference frequency mixing) and the application of these effects to all-optical switching.

In this chapter we introduce the coupled wave equations which govern the evolution of the second harmonic and fundamental fields, when a high intensity beam is incident on a second order non-linear medium. The solutions of the equations are discussed at some length with particular emphasis placed on the GaAs/AlGaAs material system and in other common materials for near/mid-IR applications. In addition to second harmonic generation (SHG), the cascaded second order process and its application for all-optical switching is described. The concept of quasi-phase-matching (QPM) is also introduced for the control of the power exchange between fundamental and second harmonic fields. Finally, the advantages of guided wave interactions in a second order non-linear medium are outlined and compared with SHG conversion efficiencies reported in the literature for GaAs/AlGaAs, $LiNbO_3$ and KTP waveguide devices.

2.1 The Coupled Wave Equations for Uniform Plane Waves in a Second Order Non-linear Medium

2.1.1 The Vector Coupled Wave Equations

In a non-linear medium which is also non-magnetic and non-conducting, the time-independent vector wave equation, is given by:

$$\nabla^2\mathbf{E}(\omega) = -\frac{n^2(\omega)\cdot\omega^2}{c^2}\mathbf{E}(\omega) - \mu_0\omega^2\mathbf{P}^{NL}(\omega) \tag{2.1}$$

where it has been assumed that there are no free charges present. In expression (2.1), $\mathbf{E}(\omega)$ is the Fourier transform of the electric field vector $\mathbf{E}(t)$, $\mathbf{P}^{NL}(\omega)$ is the Fourier transform of the non-linear part of the polarisation vector $\mathbf{P}^{NL}(t)$, $n(\omega)$ is the refractive index of the medium at the frequency ω, c is the velocity of light in vacuum, and μ_0 is the permeability of free space. If we now assume that $\mathbf{E}(\omega)$ is a uniform travelling plane waveform which propagates in the +z direction, we may write:

$$\mathbf{E}(\omega) = \mathbf{E}(\omega,z) = \hat{\mathbf{E}}(\omega,z)\exp[ik(\omega)z] \tag{2.2}$$

where $\hat{\mathbf{E}}(\omega,z)$ is a complex envelope function which contains information about both the amplitude and phase of the wave which is travelling in the +z direction, and $k(\omega) = n(\omega)\cdot\omega/c$ is the wavevector from the solution of the wave equation (2.1) without the non-linear polarisation term. Substituting expression (2.2) for $\mathbf{E}(\omega)$ into (2.1) we may deduce:

$$\left[\frac{\partial^2\hat{\mathbf{E}}(\omega,z)}{\partial z^2} + 2ik(\omega)\frac{\partial\hat{\mathbf{E}}(\omega,z)}{\partial z}\right]\exp[ik(\omega)z] = -\mu_0\omega^2\mathbf{P}^{NL}(\omega,z) \tag{2.3}$$

In the slowly varying envelope approximation [1]:

$$\left|\frac{\partial^2\hat{\mathbf{E}}(\omega,z)}{\partial z^2}\right| << \left|2ik(\omega)\frac{\partial\hat{\mathbf{E}}(\omega,z)}{\partial z}\right| \tag{2.4}$$

and (2.3) becomes

$$\frac{\partial\hat{\mathbf{E}}(\omega,z)}{\partial z} = \frac{i\omega}{2n(\omega)c\varepsilon_0}\mathbf{P}^{NL}(\omega,z)\exp[-ik(\omega)z] \tag{2.5}$$

Expression (2.5) therefore governs the evolution of the complex envelopes of *all* the fields present in the non-linear medium.

At this stage it is perhaps simpler to restrict our attention to the case of a second order non-linear medium with only 2 monochromatic uniform plane waves at frequencies ω_1 and ω_2 travelling in the +z direction so that the total electric field in the medium may be expressed as:

$$\begin{aligned}\mathbf{E}(\omega,z) = \tfrac{1}{2}\Big[&\mathbf{E}_{\omega_1}(z)\delta(\omega-\omega_1)+\mathbf{E}_{-\omega_1}(z)\delta(\omega+\omega_1)\\ &+\mathbf{E}_{\omega_2}(z)\delta(\omega-\omega_2)+\mathbf{E}_{-\omega_2}(z)\delta(\omega+\omega_2)\Big]\end{aligned} \tag{2.6}$$

Moreover, the most general case of sum frequency generation will be treated first $(\omega_1,\omega_2 \rightarrow \omega_1+\omega_2=\omega_\sigma$ say, where $\omega_1 \neq \omega_2)$ before considering the special cases of SHG $(\omega,\omega \rightarrow 2\omega)$ and second harmonic down-conversion or SHD $(2\omega,-\omega \rightarrow \omega)$.

For the sum frequency generation process $(\omega_1,\omega_2 \rightarrow \omega_\sigma)$ we have from (2.5):

$$\frac{\partial \hat{\mathbf{E}}_{\omega_\sigma}(z)}{\partial z} = \frac{i\omega_\sigma}{2n_{\omega_\sigma}c\varepsilon_0}\mathbf{P}^{(2)}_{\omega_\sigma}(z)\exp\left(-ik_{\omega_\sigma}z\right) \tag{2.7}$$

where the sum frequency component of the second order non-linear polarisation vector $\mathbf{P}^{(2)}_{\omega_\sigma}(z)$ is given by [1]:

$$\mathbf{P}^{(2)}_{\omega_\sigma}(z) = \varepsilon_0\chi^{(2)}(-\omega_\sigma;\omega_1,\omega_2)\big|\mathbf{E}_{\omega_1}(z)\mathbf{E}_{\omega_2}(z) \tag{2.8a}$$

i.e.

$$\left[P^{(2)}_{\omega_\sigma}(z)\right]_\mu = \varepsilon_0\sum_{\alpha\beta}\chi^{(2)}_{\mu\alpha\beta}(-\omega_\sigma;\omega_1,\omega_2)\left[E_{\omega_1}(z)\right]_\alpha\left[E_{\omega_2}(z)\right]_\beta \tag{2.8b}$$

In (2.8a) $\chi^{(2)}(-\omega_\sigma;\omega_1,\omega_2)$ is the second order non-linear susceptibility tensor which characterises the sum frequency generation response of the medium. In (2.8b) $\left[P^{(2)}_{\omega_\sigma}(z)\right]_\mu$ is the Cartesian component (μ = x, y or z) of the polarisation vector $\mathbf{P}^{(2)}_{\omega_\sigma}(z)$ which is being evaluated, while $\sum\limits_{\alpha\beta}$ signifies that the terms on the right hand side of (2.8b) need to be summed over all permutations of αβ where the subscripts α and β also denote Cartesian components x, y or z. Now from (2.2), for $\omega_j \geq 0$ we have:

$$\mathbf{E}_{\omega_j}(z) = \hat{\mathbf{E}}_{\omega_j}(z)\exp\left(ik_{\omega_j}z\right) \tag{2.9a}$$

$$\mathbf{E}_{-\omega_j}(z) = \hat{\mathbf{E}}^*_{\omega_j}(z)\exp\left(-ik_{\omega_j}z\right) \tag{2.9b}$$

where (2.9b) follows since for $\mathbf{E}(t,z)$ real we must have $\mathbf{E}_{-\omega_j}(z) = \mathbf{E}^*_{\omega_j}(z)$. Hence, from (2.7), (2.8) and (2.9) we may deduce that

$$\frac{\partial\hat{\mathbf{E}}_{\omega_\sigma}(z)}{\partial z} = \frac{i\omega_\sigma}{2n_{\omega_\sigma}c}\cdot\chi^{(2)}\left(-\omega_\sigma;\omega_1,\omega_2\right)\Big|\hat{\mathbf{E}}_{\omega_1}(z)\hat{\mathbf{E}}_{\omega_2}(z)\exp\left[i\left(k_{\omega_1}+k_{\omega 2}-k_{\omega_\sigma}\right)z\right] \tag{2.10}$$

Equation (2.10) describes the evolution of the sum frequency field envelope $\hat{\mathbf{E}}_{\omega_\sigma}(z)$ as a function of the distance propagated through the second order non-linear medium. We now consider 2 special cases of sum frequency generation: the frequency-degenerate process of SHG $(\omega,\omega \rightarrow 2\omega)$ and the reverse non-degenerate process of SHD $(2\omega,-\omega \rightarrow \omega)$ which also occurs.

(i) Second Harmonic Generation $(\omega,\omega \rightarrow 2\omega)$

Although SHG is the degenerate case of sum frequency generation i.e. $(\omega_1 = \omega, \omega_2 = \omega \rightarrow \omega_1 + \omega_2 = 2\omega)$ the second harmonic envelope evolution equation is *not* simply derived from the sum frequency generation equation of (2.10) by writing $\omega_1 = \omega_2 = \omega$. Instead, due to the degeneracy of the frequencies ω_1 and ω_2, (2.8) becomes:

$$\mathbf{P}^{(2)}_{2\omega}(z) = \tfrac{1}{2}\varepsilon_0\chi^{(2)}(-2\omega;\omega,\omega)\Big|\mathbf{E}_\omega(z)\mathbf{E}_\omega(z) \tag{2.11}$$

Consequently, the equation governing the propagation of the second harmonic field envelope is given by:

$$\frac{\partial \hat{\mathbf{E}}_{2\omega}(z)}{\partial z} = \frac{i\omega}{2n_{2\omega}c} \cdot \chi^{(2)}(-2\omega;\omega,\omega) \Big| \hat{\mathbf{E}}_{\omega}(z)\hat{\mathbf{E}}_{\omega}(z)\exp(i\Delta kz) \qquad (2.12)$$

where $n_{2\omega}$ is the refractive index of the medium at the second harmonic frequency, and $\Delta k = 2k_{\omega} - k_{2\omega}$ is the wavevector mismatch parameter.

(ii) Second Harmonic Down-conversion $(2\omega, -\omega \rightarrow \omega)$

Any second harmonic field generated in the second order non-linear medium can subsequently undergo further frequency mixing with the original fundamental field leading to second harmonic down-conversion. Unlike SHG however, the down-conversion process $(2\omega, -\omega \rightarrow \omega)$ is a non-degenerate frequency conversion process. The equation describing the evolution of the down-converted fundamental field is therefore derived by simply substituting $\omega_1 = 2\omega$, $\omega_2 = -\omega$ and $\omega_\sigma = \omega$ into equation (2.10) to give:

$$\frac{\partial \hat{\mathbf{E}}_{\omega}(z)}{\partial z} = \frac{i\omega}{2n_{\omega}c} \cdot \chi^{(2)}(-\omega;2\omega,-\omega) \Big| \hat{\mathbf{E}}_{2\omega}(z)\hat{\mathbf{E}}^{*}_{\omega}(z)\exp(-i\Delta kz) \qquad (2.13)$$

where n_{ω} is the refractive index of the medium at the fundamental frequency and, as for the SHG case, $\Delta k = 2k_{\omega} - k_{2\omega}$.

Expressions (2.12) and (2.13) are the vector coupled wave equations which govern the exchange of power between the fundamental and second harmonic fields during propagation through the second order non-linear medium. A detailed discussion of the different solutions to these equations will however be deferred until later in this chapter.

2.1.2 Symmetry Properties of the Susceptibility Tensors $\chi^{(2)}(-2\omega;\omega,\omega)$ and $\chi^{(2)}(-\omega;2\omega,-\omega)$

Although in general the number of $\chi^{(2)}(-\omega_\sigma;\omega_1,\omega_2)$ tensor elements required to define the sum frequency generation response of a second order non-linear medium is 27, various symmetry properties exist which can be invoked under different conditions to reduce the number of independent tensor elements. Initially, these symmetry properties will be introduced for the most general case of sum frequency generation before examining the consequences of the properties for the special cases of SHG and SHD.

(i) Intrinsic Permutation Symmetry

Intrinsic permutation symmetry is a universal tensor property which gives:

$$\chi^{(2)}_{\mu\alpha\beta}(-\omega_\sigma;\omega_1,\omega_2)=\chi^{(2)}_{\mu\beta\alpha}(-\omega_\sigma;\omega_2,\omega_1) \tag{2.14}$$

i.e. we can permute pairs (α,ω_1) and (β,ω_2).

(ii) Overall Permutation Symmetry (Zero Absorption)

Provided no absorption occurs at any of the frequencies present (either applied or generated) in the second order non-linear medium, overall permutation symmetry applies [1]:

$$\begin{aligned}&\chi^{(2)}_{\mu\alpha\beta}(-\omega_\sigma;\omega_1,\omega_2)=\chi^{(2)}_{\mu\beta\alpha}(-\omega_\sigma;\omega_2,\omega_1)\\&=\chi^{(2)}_{\alpha\mu\beta}(\omega_1;-\omega_\sigma,\omega_2)=\chi^{(2)}_{\alpha\beta\mu}(\omega_1;\omega_2,-\omega_\sigma)\\&=\chi^{(2)}_{\beta\alpha\mu}(\omega_2;\omega_1,-\omega_\sigma)=\chi^{(2)}_{\beta\mu\alpha}(\omega_2;-\omega_\sigma,\omega_1)\end{aligned} \tag{2.15}$$

i.e. we can permute pairs $(\mu,-\omega_\sigma)$, (α,ω_1) and (β,ω_2).

(iii) Kleinman Symmetry and the Contracted Susceptibility Tensor

In the low frequency limit when all the frequencies in the medium (either applied or generated) are far below the resonant frequencies of the medium (i.e. the dispersion of the medium is negligible over the range of frequencies present), all the frequencies become indistinguishable so that we may freely permute them:

$$\begin{aligned}&\chi^{(2)}_{\mu\alpha\beta}(-\omega_\sigma;\omega_1,\omega_2)=\chi^{(2)}_{\mu\alpha\beta}(-\omega_\sigma;\omega_2,\omega_1)\\ &=\chi^{(2)}_{\mu\alpha\beta}(\omega_1;-\omega_\sigma,\omega_2)=\chi^{(2)}_{\mu\alpha\beta}(\omega_1;\omega_2,-\omega_\sigma)\\ &=\chi^{(2)}_{\mu\alpha\beta}(\omega_2;-\omega_\sigma,\omega_1)=\chi^{(2)}_{\mu\alpha\beta}(\omega_2;\omega_1,-\omega_\sigma)\end{aligned} \tag{2.16}$$

This is known as Kleinman symmetry and when it applies we may use intrinsic permutation symmetry to deduce that for the sum frequency generation process:

$$\chi^{(2)}_{\mu\alpha\beta}(-\omega_\sigma;\omega_1,\omega_2)=\chi^{(2)}_{\mu\beta\alpha}(-\omega_\sigma;\omega_1,\omega_2) \tag{2.17}$$

(2.8) then becomes:

$$\mathbf{P}^{(2)}_{\omega_\sigma}(z)=2\varepsilon_0\mathbf{d}(-\omega_\sigma;\omega_1,\omega_2)|\mathbf{E}_{\omega_1}(z)\mathbf{E}_{\omega_2}(z) \tag{2.18a}$$

i.e.

$$\left(\mathrm{P}^{(2)}_{\omega_\sigma}\right)_\mu=2\varepsilon_0\sum_{\alpha\beta}\mathrm{d}_{\mu m}(-\omega_\sigma;\omega_1,\omega_2)\left(\mathrm{E}_{\omega_1}\right)_\alpha\left(\mathrm{E}_{\omega_2}\right)_\beta \tag{2.18b}$$

or, more explicitly still:

$$\begin{bmatrix}\left(\mathrm{P}^{(2)}_{\omega_\sigma}\right)_x\\ \left(\mathrm{P}^{(2)}_{\omega_\sigma}\right)_y\\ \left(\mathrm{P}^{(2)}_{\omega_\sigma}\right)_z\end{bmatrix}=2\varepsilon_0\begin{bmatrix}\mathrm{d}_{11}&\mathrm{d}_{12}&\mathrm{d}_{13}&\mathrm{d}_{14}&\mathrm{d}_{15}&\mathrm{d}_{16}\\ \mathrm{d}_{21}&\mathrm{d}_{22}&\mathrm{d}_{23}&\mathrm{d}_{24}&\mathrm{d}_{25}&\mathrm{d}_{26}\\ \mathrm{d}_{31}&\mathrm{d}_{32}&\mathrm{d}_{33}&\mathrm{d}_{34}&\mathrm{d}_{35}&\mathrm{d}_{36}\end{bmatrix}\begin{bmatrix}\left(\mathrm{E}_{\omega_1}\right)_x\left(\mathrm{E}_{\omega_2}\right)_x\\ \left(\mathrm{E}_{\omega_1}\right)_y\left(\mathrm{E}_{\omega_2}\right)_y\\ \left(\mathrm{E}_{\omega_1}\right)_z\left(\mathrm{E}_{\omega_2}\right)_z\\ \left(\mathrm{E}_{\omega_1}\right)_y\left(\mathrm{E}_{\omega_2}\right)_z+\left(\mathrm{E}_{\omega_1}\right)_z\left(\mathrm{E}_{\omega_2}\right)_y\\ \left(\mathrm{E}_{\omega_1}\right)_x\left(\mathrm{E}_{\omega_2}\right)_z+\left(\mathrm{E}_{\omega_1}\right)_z\left(\mathrm{E}_{\omega_2}\right)_x\\ \left(\mathrm{E}_{\omega_1}\right)_x\left(\mathrm{E}_{\omega_2}\right)_y+\left(\mathrm{E}_{\omega_1}\right)_y\left(\mathrm{E}_{\omega_2}\right)_x\end{bmatrix} \tag{2.18c}$$

where $\mathbf{d}(-\omega_\sigma;\omega_1,\omega_2)=\chi^{(2)}(-\omega_\sigma;\omega_1,\omega_2)/2$ is the contracted susceptibility tensor for the sum frequency generation process. In (2.18) $\left(P^{(2)}_{\omega_\sigma}\right)_\mu$ is the Cartesian component (μ = x, y or z) of the polarisation vector $\mathbf{P}^{(2)}_{\omega_\sigma}$ which is being evaluated, while the individual **d** tensor coefficients, $d_{\mu m}$, are defined according to the integer subscripts μ and m. The first subscript μ = 1, 2 or 3 depending on which Cartesian component of the polarisation vector $\mathbf{P}^{(2)}_{\omega_\sigma}$ x, y or z is being evaluated respectively. The second subscript m indicates the Cartesian components α and β of the electric fields $\mathbf{E}_{\omega_1}$ and $\mathbf{E}_{\omega_2}$ respectively according to the correspondences set out below:

m	1	2	3	4	5	6
$\alpha\beta$	xx	yy	zz	yz zy	xz zx	xy yx

(2.19)

In (2.18b) and (2.18c), the z dependence of the polarisation vector components and the electric field components have been omitted for clarity. In addition, the frequency arguments of the coefficients $d_{\mu m}$ are omitted to emphasise, that in the low frequency limit, the dispersion of the **d** tensor is negligible. From (2.18) it may therefore be seen that the number of independent tensor elements required to define the sum frequency generation response of the medium is reduced from 27 to 18 in the low frequency limit.

From the above arguments it may be seen that the contracted tensor notation should only strictly be used in the low frequency limit. However, d coefficients are often still used in the literature for non-degenerate frequency conversion when not operating in the low frequency limit. The significance of the d coefficients in these circumstances is then simply that $d_{\mu m}=\chi^{(2)}_{\mu\alpha\beta}/2$.

The implications of these various susceptibility tensor properties for the SHG and SHD tensors $\chi^{(2)}(-2\omega;\omega,\omega)$ and $\chi^{(2)}(-\omega;2\omega,-\omega)$ will now be examined.

(a) SHG Tensor $\chi^{(2)}(-2\omega;\omega,\omega)$

SHG is a frequency degenerate conversion process so that as a consequence of intrinsic permutation symmetry *alone* we have:

$$\chi^{(2)}_{\mu\alpha\beta}(-2\omega;\omega,\omega) = \chi^{(2)}_{\mu\beta\alpha}(-2\omega;\omega,\omega) \qquad (2.20)$$

and we may write (2.11) as

$$\mathbf{P}^{(2)}_{2\omega}(z) = \varepsilon_0 \mathbf{d}(-2\omega;\omega,\omega) | \mathbf{E}_\omega(z)\mathbf{E}_\omega(z) \qquad (2.21a)$$

i.e.

$$\left(P^{(2)}_{2\omega}\right)_\mu = \varepsilon_0 \sum_{\alpha\beta} d_{\mu m}(-2\omega;\omega,\omega)(E_\omega)_\alpha (E_\omega)_\beta \qquad (2.21b)$$

or, more explicitly still:

$$\begin{bmatrix} \left(P^{(2)}_{2\omega}\right)_x \\ \left(P^{(2)}_{2\omega}\right)_y \\ \left(P^{(2)}_{2\omega}\right)_z \end{bmatrix} = \varepsilon_0 \begin{bmatrix} d_{11} & d_{12} & d_{13} & d_{14} & d_{15} & d_{16} \\ d_{21} & d_{22} & d_{23} & d_{24} & d_{25} & d_{26} \\ d_{31} & d_{32} & d_{33} & d_{34} & d_{35} & d_{36} \end{bmatrix} \begin{bmatrix} (E_\omega)_x^2 \\ (E_\omega)_y^2 \\ (E_\omega)_z^2 \\ 2(E_\omega)_y(E_\omega)_z \\ 2(E_\omega)_x(E_\omega)_z \\ 2(E_\omega)_x(E_\omega)_y \end{bmatrix} \qquad (2.21c)$$

where $\mathbf{d}(-2\omega;\omega,\omega) = \chi^{(2)}(-2\omega;\omega,\omega)/2$ and the notation for the **d** tensor element subscripts is defined by (2.19) as before.

(b) SHD Tensor $\chi^{(2)}(-\omega;2\omega,-\omega)$

Since, for the second harmonic down-conversion process, the frequencies $\omega_1 = 2\omega$ and $\omega_2 = -\omega$ are non-degenerate, we cannot use contracted susceptibility tensor notation unless Kleinman symmetry applies. When Kleinman symmetry does apply however, we may simply substitute $\omega_1 = 2\omega$ and $\omega_2 = -\omega$ into (2.18c) to give:

$$\begin{bmatrix} \left(P_{\omega}^{(2)}\right)_x \\ \left(P_{\omega}^{(2)}\right)_y \\ \left(P_{\omega}^{(2)}\right)_z \end{bmatrix} = 2\varepsilon_0 \begin{bmatrix} d_{11} & d_{12} & d_{13} & d_{14} & d_{15} & d_{16} \\ d_{21} & d_{22} & d_{23} & d_{24} & d_{25} & d_{26} \\ d_{31} & d_{32} & d_{33} & d_{34} & d_{35} & d_{36} \end{bmatrix} \begin{bmatrix} (E_{2\omega})_x(E_{-\omega})_x \\ (E_{2\omega})_y(E_{-\omega})_y \\ (E_{2\omega})_z(E_{-\omega})_z \\ (E_{2\omega})_y(E_{-\omega})_z + (E_{2\omega})_z(E_{-\omega})_y \\ (E_{2\omega})_x(E_{-\omega})_z + (E_{2\omega})_z(E_{-\omega})_x \\ (E_{2\omega})_x(E_{-\omega})_y + (E_{2\omega})_y(E_{-\omega})_x \end{bmatrix} \tag{2.22}$$

Here, $\mathbf{d}(-\omega;2\omega,-\omega) = \chi^{(2)}(-\omega;2\omega,-\omega)/2$ and the notation for the $\mathbf{d}$ tensor element subscripts is defined by (2.19) as before.

(iv) Crystal Symmetry

A final reduction in the number of independent $\chi^{(2)}(-2\omega;\omega,\omega)$ tensor elements may arise according to the particular crystal class to which the second order non-linear material belongs. GaAs, LiNbO$_3$ and KTP, for example, are common second order non-linear crystals for near and mid-IR applications with cubic class $\bar{4}3m$, trigonal class 3m, and orthorhombic class mm2 structures respectively. The contracted susceptibility tensor for SHG in each of these crystal classes is listed below. (The supplementary relations appearing on the right apply when Kleinman symmetry holds) [1]:

Cubic Class $\bar{4}3m$ (GaAs)

$$\mathbf{d} = \begin{bmatrix} 0 & 0 & 0 & d_{14} & 0 & 0 \\ 0 & 0 & 0 & 0 & d_{14} & 0 \\ 0 & 0 & 0 & 0 & 0 & d_{14} \end{bmatrix} \tag{2.23a}$$

Trigonal Class 3m (LiNbO$_3$)

$$\mathbf{d} = \begin{bmatrix} 0 & 0 & 0 & 0 & d_{15} & \bar{d}_{22} \\ \bar{d}_{22} & d_{22} & 0 & d_{15} & 0 & 0 \\ d_{31} & d_{31} & d_{33} & 0 & 0 & 0 \end{bmatrix} \quad \{d_{15} = d_{31} \tag{2.23b}$$

Orthorhombic Class mm2 (KTP)

$$\mathbf{d}=\begin{bmatrix}0 & 0 & 0 & 0 & d_{15} & 0\\ 0 & 0 & 0 & d_{24} & 0 & 0\\ d_{31} & d_{32} & d_{33} & 0 & 0 & 0\end{bmatrix}\quad\begin{cases}d_{15}=d_{31}\\ d_{24}=d_{32}\end{cases}\tag{2.23c}$$

2.1.3 The Reality Condition and the Relation Between Up-conversion and Down-conversion Tensor Elements in the Zero Absorption Regime

Kleinman symmetry does *not* apply for the common second order non-linear materials GaAs/AlGaAs, LiNbO$_3$ and KTP at near/mid-IR wavelengths. However, when operating at photon energies such that no absorption occurs at any of the frequencies present in the medium (either applied or generated), the up-conversion tensor element $\chi^{(2)}(-2\omega;\omega,\omega)$ can be related to the down-conversion tensor element $\chi^{(2)}(-\omega;2\omega,-\omega)$. To establish this relationship we may begin with the reality condition for the non-degenerate sum frequency tensor $\chi^{(2)}(-\omega_\sigma;\omega_1,\omega_2)$ where $\omega_\sigma=\omega_1+\omega_2$ [1]:

$$\left[\chi^{(2)}(-\omega_\sigma;\omega_1,\omega_2)\right]^*=\chi^{(2)}(\omega_\sigma;-\omega_1,-\omega_2)\tag{2.24a}$$

i.e.

$$\left[\chi^{(2)}_{\mu\alpha\beta}(-\omega_\sigma;\omega_1,\omega_2)\right]^*=\chi^{(2)}_{\mu\alpha\beta}(\omega_\sigma;-\omega_1,-\omega_2)\tag{2.24b}$$

This intrinsic tensor property arises because the electric field $\mathbf{E}(t)$ and the polarisation $\mathbf{P}^{(2)}(t)$ are both real.

When none of the field frequencies in the medium approach any of the material resonance frequencies (i.e. there is no absorption at ω_σ, ω_1 or ω_2), $\chi^{(2)}(-\omega_\sigma;\omega_1,\omega_2)$ is itself real, and (2.24a) becomes:

$$\chi^{(2)}(-\omega_\sigma;\omega_1,\omega_2)=\chi^{(2)}(\omega_\sigma;-\omega_1,-\omega_2)\tag{2.25a}$$

i.e.

$$\chi^{(2)}_{\mu\alpha\beta}(-\omega_\sigma;\omega_1,\omega_2)=\chi^{(2)}_{\mu\alpha\beta}(\omega_\sigma;-\omega_1,-\omega_2)\tag{2.25b}$$

Furthermore, for the case of zero absorption, overall permutation symmetry applies and from sub-section 2.1.2 we have:

$$\chi^{(2)}_{\mu\alpha\beta}(\omega_\sigma;-\omega_1,-\omega_2)=\chi^{(2)}_{\alpha\mu\beta}(-\omega_1;\omega_\sigma,-\omega_2)=\chi^{(2)}_{\alpha\beta\mu}(-\omega_1;-\omega_2,\omega_\sigma) \tag{2.26}$$

Hence, combining (2.25b) and (2.26) we obtain:

$$\chi^{(2)}_{\mu\alpha\beta}(-\omega_\sigma;\omega_1,\omega_2)=\chi^{(2)}_{\alpha\mu\beta}(-\omega_1;\omega_\sigma,-\omega_2)=\chi^{(2)}_{\alpha\beta\mu}(-\omega_1;-\omega_2,\omega_\sigma) \tag{2.27}$$

For the specific case of second harmonic down-conversion for which $\omega_\sigma=\omega$, $\omega_1=2\omega$, and $\omega_2=-\omega$, (2.27) implies that:

$$\chi^{(2)}_{\mu\alpha\beta}(-\omega;2\omega,-\omega)=\chi^{(2)}_{\alpha\mu\beta}(-2\omega;\omega,\omega)=\chi^{(2)}_{\alpha\beta\mu}(-2\omega;\omega,\omega) \tag{2.28}$$

Equation (2.28) is very significant because it relates the second harmonic down conversion tensor element $\chi^{(2)}_{\mu\alpha\beta}(-\omega;2\omega,-\omega)$, to the up-conversion tensor elements $\chi^{(2)}_{\alpha\mu\beta}(-2\omega;\omega,\omega)$ and $\chi^{(2)}_{\alpha\beta\mu}(-2\omega;\omega,\omega)$ in the regime of zero absorption. Using (2.28) in the vector coupled wave equation of (2.13) will then yield an equation in terms of up-conversion tensor elements alone.

2.1.4 The Scalar Coupled Wave Equations in the Zero Absorption Regime

Defining $\mathbf{e}_\sigma$, $\mathbf{e}_1$ and $\mathbf{e}_2$ to be unit vectors in the direction of the polarisation vector $\mathbf{P}^{(2)}_{\omega_\sigma}$ and the electric field vectors $\mathbf{E}_{\omega_1}$ and $\mathbf{E}_{\omega_2}$ respectively, (2.8a) may be re-written as:

$$\mathrm{P}^{(2)}_{\omega_\sigma}\mathbf{e}_\sigma=\varepsilon_0\chi^{(2)}(-\omega_\sigma;\omega_1,\omega_2)\,|\,(\mathrm{E}_{\omega_1}\mathbf{e}_1)(\mathrm{E}_{\omega_2}\mathbf{e}_2) \tag{2.29}$$

Taking the scalar product of both sides with $\mathbf{e}_\sigma$ we have

$$P^{(2)}_{\omega_\sigma} = \varepsilon_0 \left[\chi^{(2)}(-\omega_\sigma;\omega_1,\omega_2) \middle| \mathbf{e}_1 \mathbf{e}_2 \right] \cdot \mathbf{e}_\sigma E_{\omega_1} E_{\omega_2} \tag{2.30a}$$

i.e.

$$P^{(2)}_{\omega_\sigma} = \varepsilon_0 \chi^{(2)}_{\mathrm{eff}}(-\omega_\sigma;\omega_1,\omega_2) E_{\omega_1} E_{\omega_2} \tag{2.30b}$$

where

$$\chi^{(2)}_{\mathrm{eff}}(-\omega_\sigma;\omega_1,\omega_2) = \sum_{\mu\alpha\beta} \chi^{(2)}_{\mu\alpha\beta}(-\omega_\sigma;\omega_1,\omega_2)(e_\sigma)_\mu (e_1)_\alpha (e_2)_\beta \tag{2.30c}$$

Here, $\chi^{(2)}_{\mathrm{eff}}(-\omega_\sigma;\omega_1,\omega_2)$ is an effective scalar non-linear susceptibility for the sum frequency generation process which accounts for the particular orientations of the polarisation vector $\mathbf{P}^{(2)}_{\omega_\sigma}$ and the electric field vectors $\mathbf{E}_{\omega_1}$ and $\mathbf{E}_{\omega_2}$.

In terms of effective scalar susceptibilities, the vector wave equations of (2.12) and (2.13) then become:

$$\frac{\partial \hat{E}_{2\omega}(z)}{\partial z} = \frac{i\omega}{n_{2\omega} c} \frac{\chi^{(2)}_{\mathrm{eff}}(-2\omega;\omega,\omega)}{2} \left[\hat{E}_\omega(z) \right]^2 \exp(i\Delta k z) \tag{2.31a}$$

and

$$\frac{\partial \hat{E}_{\omega}(z)}{\partial z} = \frac{i\omega}{n_{\omega} c} \frac{\chi^{(2)}_{\mathrm{eff}}(-\omega;2\omega,-\omega)}{2} \hat{E}_{2\omega}(z) \hat{E}^*_\omega(z) \exp(-i\Delta k z) \tag{2.31b}$$

where

$$\chi^{(2)}_{\mathrm{eff}}(-2\omega;\omega,\omega) = \sum_{\mu\alpha\beta} \chi^{(2)}_{\mu\alpha\beta}(-2\omega;\omega,\omega)(e_{2\omega})_\mu (e_\omega)_\alpha (e_\omega)_\beta \tag{2.31c}$$

and

$$\chi^{(2)}_{\mathrm{eff}}(-\omega;2\omega,-\omega) = \sum_{\mu\alpha\beta} \chi^{(2)}_{\mu\alpha\beta}(-\omega;2\omega,-\omega)(e_\omega)_\mu (e_{2\omega})_\alpha (e_{-\omega})_\beta \tag{2.31d}$$

It should be noted that for the scalar wave equations of (2.31) the field polarisations are implicitly understood. For a [100]-grown GaAs/AlGaAs crystal cleaved along a (110) plane, for example, it is relatively straightforward to show that, for $\hat{E}_\omega$ polarised in the plane of the crystal, $\hat{E}_{2\omega}$ is vertically-polarised, and in the regime of zero absorption we have:

$$\frac{\chi^{(2)}_{\rm eff}(-2\omega;\omega,\omega)}{2} = \frac{\chi^{(2)}_{\rm eff}(-\omega;2\omega,-\omega)}{2} = d_{\rm eff} = d_{14} \tag{2.32}$$

In deriving (2.32), use was made of the crystal symmetry relation of (2.23a) and the relation between the up-conversion and down-conversion tensor elements of (2.28).

Similarly, for z-cut $LiNbO_3$ and KTP, with a vertically-polarised fundamental field, the second harmonic field is also vertically-polarised, and in the regime of zero absorption:

$$\frac{\chi^{(2)}_{\rm eff}(-2\omega;\omega,\omega)}{2} = \frac{\chi^{(2)}_{\rm eff}(-\omega;2\omega,-\omega)}{2} = d_{\rm eff} = d_{33} \tag{2.33}$$

Hence, for these particular crystals and field polarisations in the zero absorption regime, the equations of (2.31) may be written in the generic scalar wave equation form:

$$\frac{\partial \hat{E}_{2\omega}(z)}{\partial z} = \frac{i\omega}{n_{2\omega}c} d_{\rm eff}\left[\hat{E}_\omega(z)\right]^2 \exp(i\Delta kz) \tag{2.34a}$$

$$\frac{\partial \hat{E}_{\omega}(z)}{\partial z} = \frac{i\omega}{n_{\omega}c} d_{\rm eff}\hat{E}_{2\omega}(z)\hat{E}^*_\omega(z)\exp(-i\Delta kz) \tag{2.34b}$$

The solutions of equations (2.34) may be broadly classified according to the value of Δk: the more general case for $\Delta k \neq 0$ will be treated in Section 2.3 while the special case of phase-matched SHG for which $\Delta k = 0$ will be discussed in Section 2.4. Before solving the equations however, the relevant material constants for GaAs/AlGaAs, $LiNbO_3$ and KTP will be introduced in Section 2.2.

2.2 GaAs/AlGaAs and Other Common Second Order Non-linear Materials for Near and Mid-IR Applications

Second order non-linear optical effects constitute the main subject matter of this work. In this section the relevant properties of the GaAs/AlGaAs material system shall therefore be discussed. These will be compared with the corresponding properties of $LiNbO_3$ and KTP which are common materials for near and mid-IR applications. The properties of these three materials are summarised in Table 2.1 where all dispersive quantities are quoted for wavelengths at, or as close as possible, to the 1.55 μm communications wavelength of interest for our application.

Of all the data in Table 2.1 the relative magnitudes of the d coefficients for the different materials are perhaps of most significance. The measured d_{14} coefficient of GaAs at 10.6 μm is approximately 6 times greater than the largest d coefficient d_{33} of $LiNbO_3$ at 1.3 μm, and 18 times greater than the largest d coefficient d_{33} of KTP at 1.064 μm. Now, the d coefficient in any material can, in turn, be translated into a figure of merit for second order non-linear materials $FOM^{(2)}$ given by:

$$FOM^{(2)} = \frac{d_{eff}^2}{n_\omega^2 n_{2\omega}} \tag{2.35}$$

The $FOM^{(2)}$ defined in this way then reflects the degree of optical non-linearity of the medium: the larger the $FOM^{(2)}$, the shorter the interaction length and the lower the optical intensities that are required in the medium to produce the same second order non-linear effect. Figures of merit for GaAs, $LiNbO_3$ and KTP as defined by (2.35) are 943, 102 and 19 pm^2/V^2 respectively, indicating that GaAs is approximately an order of magnitude "more non-linear" than $LiNbO_3$, and some 50 times "more non-linear" than KTP.

Comparing the degree of non-linearity of these materials in this fashion is, however, somewhat academic, since, in practice, the magnitude of all second order non-linear effects is dependent on the efficiency of the particular phase-matching technique employed for the control of the wavevector mismatch parameter Δk. The GaAs/AlGaAs material system, for example, is non-birefringent so that conventional birefringent phase-matching for efficient SHG is not possible. $LiNbO_3$ and KTP are, in contrast, uniaxially and biaxially birefringent respectively. Nevertheless, control of Δk for interactions involving the largest d coefficient d_{33} in $LiNbO_3$ and KTP cannot be achieved by birefringent techniques, because, to access d_{33}, requires that the interacting electric fields are co-linearly polarised. In order to overcome these difficulties, an alternative phase-matching technique known as quasi-phase-matching may be employed. Any true comparison of the second order non-linearities of the different materials must then account for the efficiency of the specific quasi-phase-matching scheme adopted. A discussion of the topic of quasi-phase-matching is however deferred until Section 2.5. Quasi-phase-matched guided wave interactions are also discussed in Section 2.6.

Property	**GaAs/AlGaAs**	**$LiNbO_3$**	**KTP**
Crystal Class	$\bar{4}3m$	3m	mm2
Transmission Window	$0.870 < \lambda < 16\ \mu m$	$0.4 < \lambda < 5.0\ \mu m$	$0.35 < \lambda < 4.5\ \mu m$
Birefringence	Non-birefringent	Uniaxially Birefringent	Biaxially Birefringent
n_ω @ 1.55 μm	3.26899[a]	2.13813[b]	1.81593[c]
$n_{2\omega}$ @ 0.775 μm	3.54553[a]	2.17947[b]	1.84610[c]
Intrinsic Δk (/m) at 1.55 μm $\lvert\Delta k\rvert = \frac{4\pi}{\lambda}\lvert n_\omega - n_{2\omega}\rvert$	2.242×10^6	0.335×10^6	0.244×10^6
d Coefficients (pm/V)	d_{14} 189 @ 10.6 μm[d]	d_{31}[e] 5.77 @ 2.12 μm 5.95 @ 1.06 μm d_{33}[e] 29.1 @ 2.12 μm 31.8 @ 1.318 μm 33.4 @ 1.15 μm 34.4 @ 1.06 μm	$d_{15}=d_{31}$[f] +1.4 @ 1.064 μm $d_{24}=d_{32}$[f] +2.65 @ 1.064 μm d_{33}[f] +10.7 @ 1.064 μm
d_{eff} (pm/V)	189[g]	31.8[h]	+10.7[i]
$FOM^{(2)}$ (pm^2/V^2)	943	102	19

Table 2.1 Summary of the relevant properties of GaAs/AlGaAs, $LiNbO_3$ and KTP for second order non-linear interactions

[a] Refractive indices for $Al_{0.2}Ga_{0.8}As$ calculated using the modified Afromowitz model. Ref. S.I. Hansen, PhD Thesis, University of Glasgow, (1993)

[b] n_e for z-cut congruently melting $LiNbO_3$. Ref. D. F. Nelson and R. M. Mikulyak, J. Appl. Phys. **45**, 3688 (1974)

[c] n_z for z-cut hydrothermally-grown KTP. Ref. J. D. Bierlein and H. Vanherzeele, J. Opt. Soc. Am. B **6**, 622 (1989)

[d] Measured d_{14} for GaAs at 10.6 μm. Ref. J. J. Wynne and N. Bloembergen, Phys. Rev. 188, 1211 (1969)

[e] M. M. Choy and R. L. Byer, Phys. Rev. B **14**, 1693 (1976)

[f] B. Boulanger, J. P. Fève, G. Marnier, B. Ménaert, and X. Cabirol, J. Opt. Soc. Am. B **11**, 750 (1994)

[g] $d_{eff} = d_{14}$ for a [110]-polarised fundamental field. Second harmonic is then generated in the [100] direction

[h] $d_{eff} = d_{33}$ may be accessed by pumping with a [100]-polarised fundamental beam

[i] $d_{eff} = d_{33}$ may be accessed by pumping with a [100]-polarised fundamental beam

2.3 Second Order Non-linear Effects for a Non-zero Wavevector Mismatch Parameter ($\Delta k \neq 0$)

For a non-zero wavevector mismatch parameter, Δk, the solutions of the coupled wave equations of (2.34) describe several well-known second order non-linear phenomena including unphase-matched SHG and the cascaded $\chi^{(2)}:\chi^{(2)}$ process. In addition, the coupled wave equations may be solved as a function of the wavevector mismatch parameter in the vicinity of $\Delta k=0$ to determine the form of the SHG tuning curve. In this section unphase-matched SHG, the cascaded $\chi^{(2)}:\chi^{(2)}$ interaction and SHG tuning curves will be discussed primarily for GaAs/AlGaAs although reference will also be made to $LiNbO_3$ and KTP when appropriate. Although all of what follows appears in the literature [2,3,4,5,6], a review which indicates the inter-relationships between the different solutions of the coupled wave equations for a non-zero wavevector mismatch parameter, will prove very useful.

The exact numerical solutions of the coupled wave equations appearing in the literature are often presented for scaled versions of the coupled wave equations. Although the exact solutions of these scaled equations are more general than the exact solutions of the original unscaled equations, they often have no direct physical meaning. The exact solutions of the unscaled equations will therefore be discussed in this section before briefly introducing the scaled equations and their solutions to demonstrate the feasibility of all-optical switching via the cascaded $\chi^{(2)}:\chi^{(2)}$ effect. It will be assumed throughout that Δk is continuously variable and that all refractive indices and d_{eff} coefficients are constant and independent of Δk. Although no physical mechanism exists for the control of Δk in this manner for either bulk GaAs/AlGaAs, or when attempting to employ the maximum d_{33} coefficients for $LiNbO_3$ and KTP, it is instructive to proceed with this analysis before introducing the concept of quasi-phase-matching for the control of Δk in Section 2.5.

2.3.1 Derivation of the Second Order Non-linear Fundamental Field Evolution Equation

We begin by re-stating the equations of (2.34):

$$\frac{\partial \hat{E}_{2\omega}(z)}{\partial z} = \frac{i\omega}{n_{2\omega}c} d_{eff}\left[\hat{E}_{\omega}(z)\right]^2 \exp(i\Delta kz) \tag{2.34a}$$

$$\frac{\partial \hat{E}_{\omega}(z)}{\partial z} = \frac{i\omega}{n_{\omega}c} d_{eff}\hat{E}_{2\omega}(z)\hat{E}^*_{\omega}(z)\exp(-i\Delta kz) \tag{2.34b}$$

Then, differentiating (2.34b) with respect to z and substituting from (2.34a) gives:

$$\frac{\partial^2 \hat{E}_{\omega}(z)}{\partial z^2} + i\Delta k\frac{\partial \hat{E}_{\omega}(z)}{\partial z} + \frac{\omega^2 d_{eff}^2}{c^2 n_{\omega}^2 n_{2\omega}}\left[n_{\omega}\left|\hat{E}_{\omega}(z)\right|^2 - n_{2\omega}\left|\hat{E}_{2\omega}(z)\right|^2\right]\hat{E}_{\omega}(z) = 0 \tag{2.36}$$

In the absence of absorption of any of the fields, we have energy conservation and the Manley-Rowe relation applies [1]:

$$\frac{1}{2\omega}\frac{\partial I_{2\omega}(z)}{\partial z} = -\frac{1}{2\omega}\frac{\partial I_{\omega}(z)}{\partial z} \tag{2.37}$$

where $I_{\omega}(z)$ and $I_{2\omega}(z)$ are the fundamental and second harmonic field intensities respectively defined by:

$$I_{j\omega}(z) = \tfrac{1}{2}\varepsilon_0 c n_{j\omega} \cdot \left|\hat{E}_{j\omega}(z)\right|^2 \qquad (j = 1,2) \tag{2.38}$$

For zero input second harmonic intensity (i.e. $I_{2\omega}(0) = 0$), we may then deduce that:

$$I_{2\omega}(z) = I_{\omega}(0) - I_{\omega}(z) \tag{2.39a}$$

i.e.

$$n_{2\omega}\left|\hat{E}_{2\omega}(z)\right|^2 = n_{\omega}\left(\left|\hat{E}_{\omega}(0)\right|^2 - \left|\hat{E}_{\omega}(z)\right|^2\right) \tag{2.39b}$$

Relation (2.39b) then allows us to express (2.36) in terms of the fundamental field envelope $\hat{E}_{\omega}(z)$ only:

$$\frac{\partial^2 \hat{E}_{\omega}(z)}{\partial z^2} + i\Delta k \frac{\partial \hat{E}_{\omega}(z)}{\partial z} + \Gamma^2 \left[2\left|\frac{\hat{E}_{\omega}(z)}{\hat{E}_{\omega}(0)}\right|^2 - 1 \right] \hat{E}_{\omega}(z) = 0 \tag{2.40a}$$

where we have introduced the intensity-dependent quantity Γ with dimensions of /m defined by:

$$\Gamma^2 = \frac{8\pi^2}{\varepsilon_0 c \lambda^2} \cdot \frac{d_{\mathrm{eff}}^2}{n_{\omega}^2 n_{2\omega}} \cdot I_{\omega}(0) \tag{2.40b}$$

From (2.40b) it should be noted that Γ^2 is proportional to the usual figure of merit $\mathrm{FOM}^{(2)}$ for second order non-linear materials.

Although the second order non-linear fundamental field evolution equation of (2.40) may be solved exactly using numerical methods, considerable insight may be gained by first discussing the various approximate solutions which are valid in the limit of low fundamental pump depletion.

2.3.2 Approximate Solutions of the Second Order Non-linear Fundamental Field Evolution Equation for Negligible Pump Depletion

For negligible pump depletion we may assume $\left|\hat{E}_\omega(z)\right| \approx \left|\hat{E}_\omega(0)\right|$ and (2.40) becomes:

$$\frac{\partial^2 \hat{E}_\omega(z)}{\partial z^2} + i\Delta k \frac{\partial \hat{E}_\omega(z)}{\partial z} + \Gamma^2 \hat{E}_\omega(z) = 0 \tag{2.41}$$

Equation (2.41) is a homogeneous linear differential equation and is therefore trivial to solve yielding:

$$\hat{E}_\omega(z) = \hat{E}_\omega(0) \exp\left\{ \frac{i\Delta k}{2} \left[-1 + \sqrt{1 + \left(\frac{2\Gamma}{\Delta k} \right)^2} \right] z \right\} \tag{2.42}$$

Further levels of approximation may now be made depending on the magnitude of $(2\Gamma/\Delta k)^2$:

(i) $\left|(2\Gamma/\Delta k)^2\right| < 1$

$$\hat{E}_\omega(z) \approx \hat{E}_\omega(0) \exp\left\{ \frac{i\Delta k}{2} \left[\frac{1}{2} \left(\frac{2\Gamma}{\Delta k} \right)^2 - \frac{1}{8} \left(\frac{2\Gamma}{\Delta k} \right)^4 + \cdots \right] z \right\} \tag{2.43}$$

(ii) $\left|(2\Gamma/\Delta k)^2\right| << 1$

$$\hat{E}_\omega(z) \approx \hat{E}_\omega(0) \exp\left(\frac{i\Gamma^2 z}{\Delta k} \right) \tag{2.44}$$

(iii) $\left|(2\Gamma/\Delta k)^2\right| \to 0$

$$\hat{E}_\omega(z) \approx \hat{E}_\omega(0) \tag{2.45}$$

To appreciate when the approximations of (2.44) and (2.45) are valid, we may calculate the errors associated with them as functions of $\left|(2\Gamma/\Delta k)^2\right|$. Listed in Table 2.2 are the percentage errors associated with (2.44) and (2.45) for values of $\left|(2\Gamma/\Delta k)^2\right|$ of 0.1 and 0.01. From the respective errors it may be seen that the approximation of (2.44) may be considered valid for $\left|(2\Gamma/\Delta k)^2\right| < 0.1$, while the approximation of (2.45) may be considered valid for $\left|(2\Gamma/\Delta k)^2\right| < 0.01$.

$\left\|(2\Gamma/\Delta k)^2\right\|$	Exact Expression $\sqrt{1+(2\Gamma/\Delta k)^2}$	Approximation of (2.44): $1+\frac{1}{2}(2\Gamma/\Delta k)^2$	Approximation of (2.45): 1
0.1	1.04881	1.05 (Error ≈ 0.113 %)	1 (Error ≈ 4.654 %)
0.01	1.00499	1.005 (Error ≈ 9.95×10^{-4} %)	1 (Error ≈ 0.497 %)

Table 2.2 Errors associated with the approximations of equations (2.44) and (2.45)

The significance of the fundamental field envelope solutions of (2.44) and (2.45) will now be discussed in turn.

(ii) The Fundamental Field Envelope Solution for Negligible Pump Depletion when $\left|(2\Gamma/\Delta k)^2\right| << 1$ and the Effective Intensity-dependent Refractive Index

From inspection of (2.44) we see that for $\left|(2\Gamma/\Delta k)^2\right| << 1$, $\hat{E}_\omega(z)$ is of the form:

$$\hat{E}_\omega(z) \approx \hat{E}_\omega(0)\exp\left[i\Delta\Phi^{NL}(z)\right] \tag{2.46a}$$

where

$$\Delta\Phi^{NL}(z) = \frac{\Gamma^2 z}{\Delta k} \tag{2.46b}$$

i.e. for $\left|(2\Gamma/\Delta k)^2\right| << 1$, as the fundamental field propagates through the second order non-linear medium, it experiences an intensity-dependent non-linear phase change $\Delta\Phi^{NL}(z)$ given by (2.46b) which is proportional to the figure of merit for second order non-linear media $FOM^{(2)}$ as defined by (2.35). In other words, we can think of the second order non-linear medium as an *effective* third order non-linear medium possessing an effective intensity-dependent refractive index $(n_2)_{eff}$ defined by:

$$\Delta\Phi^{NL}(z) = \frac{2\pi}{\lambda}(n_2)_{eff} I_\omega(0) z \tag{2.47}$$

It should be emphasised, however, that the refractive index of the second order non-linear medium does not change with intensity and $(n_2)_{eff}$ is inferred from the non-linear phase change. Substituting for $\Delta\Phi^{NL}(z)$ from (2.46b) into (2.47) and re-arranging terms we eventually obtain:

$$(n_2)_{eff} = \frac{4\pi}{\varepsilon_0 c\lambda} \cdot \frac{d_{eff}^2}{n_\omega^2 n_{2\omega}} \cdot \frac{1}{\Delta k} \tag{2.48a}$$

i.e.

$$(n_2)_{eff} = \frac{4\pi}{\varepsilon_0 c\lambda} \cdot FOM^{(2)} \cdot \frac{1}{\Delta k} \tag{2.48b}$$

From the data of Table 2.1, we therefore expect the ratio of the $(n_2)_{eff}$ values of GaAs:LiNbO$_3$:KTP to be 943:102:19 for any given wavevector mismatch parameter Δk.

It should be obvious from (2.48) that for Δk small enough and Γ correspondingly small enough to guarantee $\left|(2\Gamma/\Delta k)^2\right| << 1$, $(n_2)_{eff}$ can be as large as we like, and certainly many times the corresponding third order intensity-dependent index n_2 of the medium. However, because $\Delta\Phi^{NL}(z)$ is proportional to $\Gamma^2/\Delta k$, for Δk small, although $(n_2)_{eff}$ may be relatively large, the corresponding $\Delta\Phi^{NL}(z)$ must necessarily be small for the condition $\left|(2\Gamma/\Delta k)^2\right| << 1$ to be satisfied. In practice however, the non-linear phase change $\Delta\Phi^{NL}(z)$

is the important quantity which we would ideally like to be as large as possible. Any meaningful comparison of an *effective* third order non-linearity arising through a second order non-linear interaction and an *actual* third order non-linearity in the same medium must therefore be conducted in terms of $\Delta\Phi^{NL}(z)$. Such a comparison must, however, be postponed until the exact solutions to the scalar wave equations (which are valid for large $\Delta\Phi^{NL}(z)$) have been discussed in Section 2.3.3.

(iii) The Fundamental Field Envelope Solution for Negligible Pump Depletion when $\left|(2\Gamma/\Delta k)^2\right| \rightarrow 0$ and Unphase-matched SHG

Comparing (2.45) and (2.46a) for $\left|(2\Gamma/\Delta k)^2\right| \rightarrow 0$, it may be seen that $\hat{E}_\omega(z) \approx \hat{E}_\omega(0)$ and $\Delta\Phi^{NL}(z) \approx 0$. Under these conditions, the original coupled wave equations of (2.34) may be simplified quite considerably:

$$\frac{\partial \hat{E}_{2\omega}(z)}{\partial z} = \frac{i\omega}{n_{2\omega}c} d_{\text{eff}} \left[\hat{E}_\omega(0)\right]^2 \exp(i\Delta kz) \tag{2.49a}$$

$$\frac{\partial \hat{E}_\omega(z)}{\partial z} = 0 \tag{2.49b}$$

By simple integration of (2.49a) we then obtain for $\Delta k \neq 0$:

$$\hat{E}_{2\omega}(z) = \frac{2i\omega}{n_{2\omega}c} \frac{d_{\text{eff}}\left[\hat{E}_\omega(0)\right]^2}{\Delta k} \sin\left(\frac{\Delta kz}{2}\right) \exp\left(\frac{-i\Delta kz}{2}\right) \tag{2.50}$$

from which we may deduce:

$$\frac{I_{2\omega}(z)}{I_\omega(0)} = 4\frac{\Gamma^2}{(\Delta k)^2} \sin^2\left(\frac{\Delta kz}{2}\right) \tag{2.51}$$

where

$$\Delta k = 2k_{\omega} - k_{2\omega} = \frac{4\pi}{\lambda}(n_{\omega} - n_{2\omega}) \tag{2.52}$$

as before. Equation (2.51) therefore describes the evolution of the second harmonic field intensity in the limit as $\left|(2\Gamma/\Delta k)^2\right| \rightarrow 0$ (or equivalently in the limit as $\Delta\Phi^{NL}(z) \rightarrow 0$). From inspection of (2.51) it may be seen that $I_{2\omega}(z)/I_{\omega}(0)$ is proportional to Γ^2 and therefore also proportional to the figure of merit $FOM^{(2)}$. When Δk arises as a consequence of intrinsic dispersion within the non-linear medium, (2.51) describes unphase-matched SHG. Using the data from Table 2.1, we may calculate that in $Al_{0.2}Ga_{0.8}As$ for a fundamental wavelength of 1.55 μm and a fundamental input intensity of 1×10^{12} W/m², $\left|(2\Gamma/\Delta k)^2\right| \approx 9.302 \times 10^{-6}$ due to intrinsic dispersion. The normalised second harmonic intensity $I_{2\omega}(z)/I_{\omega}(0)$ as derived from (2.51) and the corresponding normalised fundamental intensity $I_{\omega}(z)/I_{\omega}(0)$ derived from the Manley-Rowe relation of (2.39a) are then plotted for $Al_{0.2}Ga_{0.8}As$ under these conditions in Fig. 2.1 as functions of the distance propagated. In Fig. 2.1, z is expressed in terms of a characteristic length of the medium known as the coherence length L_c which is defined by $L_c = \pi/|\Delta k|$ and is approximately equal to $1.401\mu m$ for $Al_{0.2}Ga_{0.8}As$ at 1.55 μm. In Fig. 2.1, it may also be seen that the oscillations in the conversion efficiency $I_{2\omega}(z)/I_{\omega}(0)$ have an amplitude of less than $1x10^{-5}$ and that $I_{\omega}(z)/I_{\omega}(0)$ correspondingly deviates from unity by less than 0.001% as expected when operating in the regime of low pump depletion for $\left|(2\Gamma/\Delta k)^2\right| \rightarrow 0$.

To appreciate the physical significance of Fig. 2.1 and the definition of coherence length given above, we may consider the non-linear medium for a non-zero phase mismatch parameter $\Delta k \neq 0$ such that $\left|(2\Gamma/\Delta k)^2\right| \rightarrow 0$. Then, a continuous wave fundamental field travelling in the +z direction with a phase velocity c/n_{ω} will interact with the non-linear medium to produce a second harmonic field which subsequently propagates with a phase velocity $c/n_{2\omega}$. This means that the second harmonic field generated at any point along the direction of propagation will, in general, be out of phase with the second harmonic field existing at the same point which was generated at an earlier point along the direction of propagation. Due to the difference in phase velocities, the second harmonic field will eventually become 180° out of phase with the second harmonic polarisation being excited by the fundamental field after a distance equal to the coherence length. If propagation continues, the second harmonic field intensity $I_{2\omega}(z)$ oscillates with a period $2L_c$ due to the continuous drift in phase between the second harmonic field and the second harmonic polarisation (see Fig. 2.1). As a consequence of the Manley-Rowe relation of (2.39a), the fundamental field intensity $I_{\omega}(z)$ correspondingly oscillates: the second harmonic field intensity grows at the expense of the fundamental field intensity and vice versa so that there is a periodic exchange of power between the two fields.

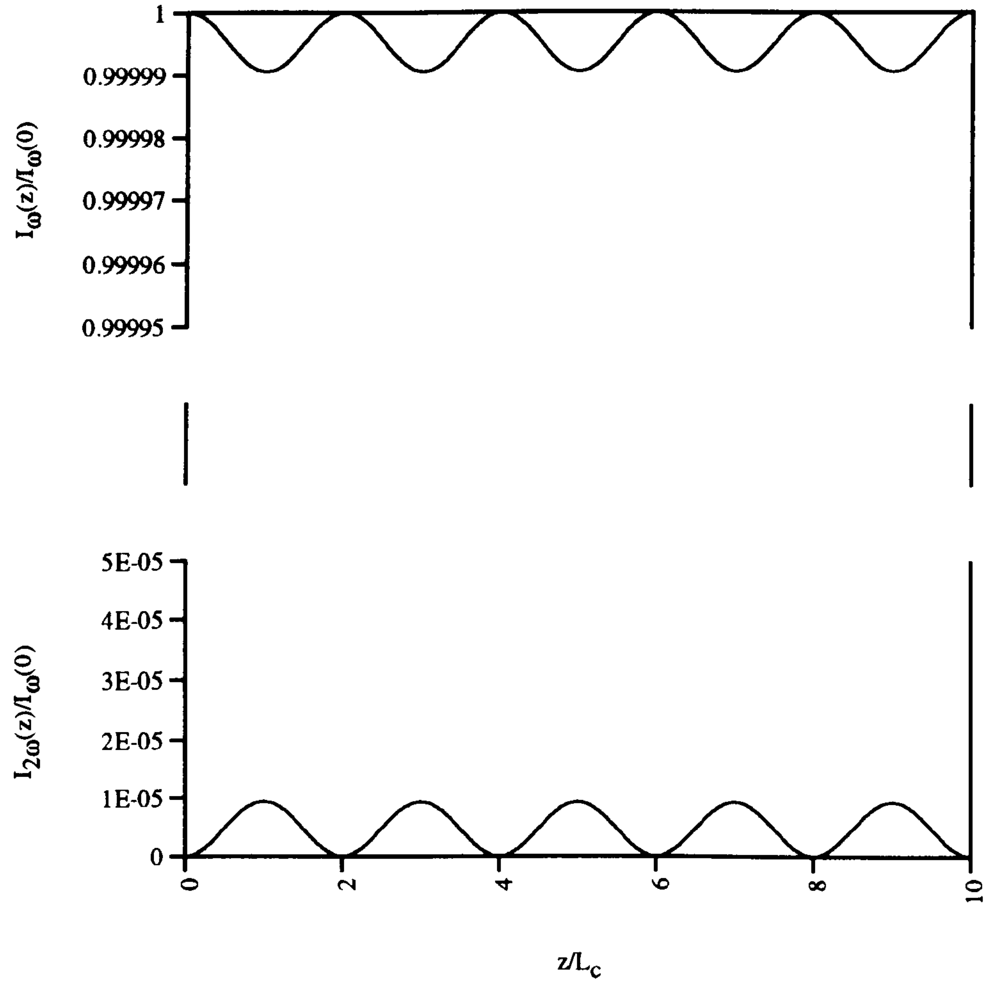

Fig. 2.1 Unphase-matched SHG in $Al_{0.2}Ga_{0.8}As$ for a fundamental wavelength of 1.55 μm and an input intensity of 1×10^{12} W/m^2

When still operating in the regime of negligible pump depletion with $\left|(2\Gamma/\Delta k)^2\right| \rightarrow 0$, (2.44) may be re-arranged to express $I_{2\omega}(L)/I_\omega(0)$ as a function of the wavevector mismatch parameter Δk:

$$\frac{I_{2\omega}(L)}{I_\omega(0)} = \Gamma^2 L^2 \operatorname{sinc}^2\left(\frac{\Delta k L}{2}\right) \tag{2.53}$$

where L has been deliberately written in place of z to emphasise that we are now considering propagation through a second order non-linear medium of fixed length L. From (2.53) it may be seen that $I_{2\omega}(L)/I_\omega(0)$ is still proportional to Γ^2 and therefore to the usual figure of merit $FOM^{(2)}$. The tuning curve resulting from (2.53) appears in Fig. 2.2 where the parameters used are for $Al_{0.2}Ga_{0.8}As$ at 1.55 μm (see Table 2.1) and, in addition, L = 4 mm and $I_\omega(0) = 1\times10^6$ W/m². From Fig. 2.2 it may be seen that the peak in the conversion efficiency $I_{2\omega}(L)/I_\omega(0)$ is less than 2×10^{-4} which is consistent with the assumption of low fundamental pump depletion. When $\Delta k \rightarrow 0$ however, the assumption that $\left|(2\Gamma/\Delta k)^2\right| \approx 0$ breaks down so that for small $|\Delta k|$, the tuning curve of Fig. 2.2 may be inaccurate. In fact, for $\left|(2\Gamma/\Delta k)^2\right| = 0.01$, $|\Delta k| = 88$ / m. Hence, Fig. 2.2 is not strictly valid for $|\Delta k| < 88$ / m.

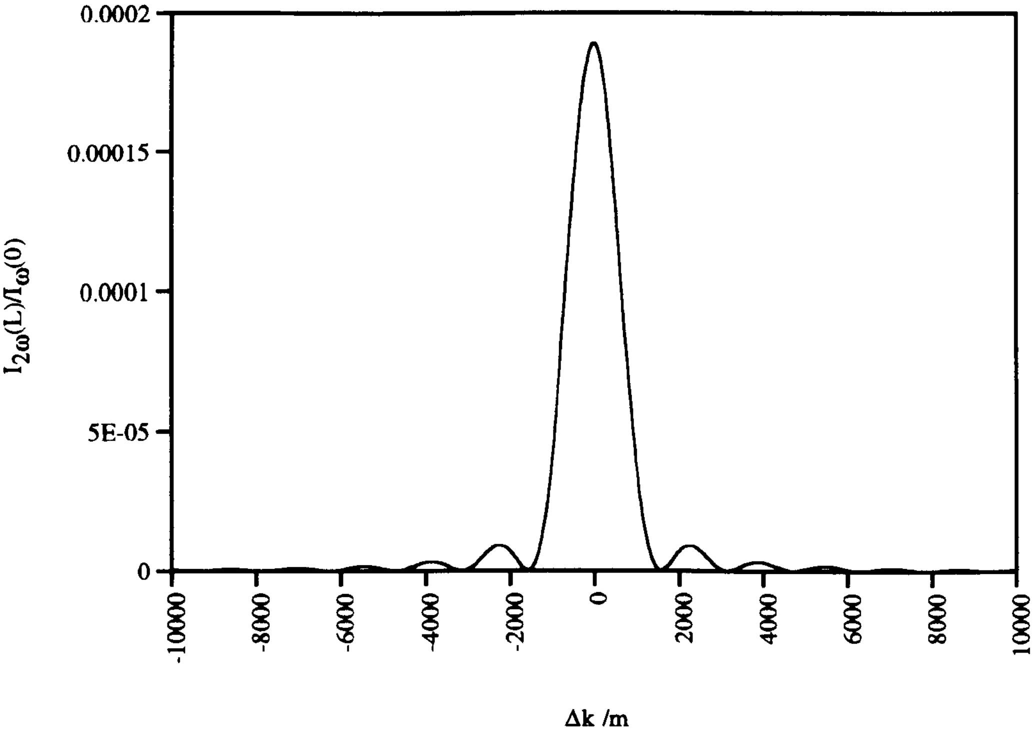

Fig. 2.2 Tuning curve for second harmonic generation in the limit of negligible fundamental pump depletion when $\left|(2\Gamma/\Delta k)^2\right| \approx 0$ and correspondingly $\Delta\Phi^{NL}(z) \approx 0$

2.3.3 Exact Solutions of the Scalar Coupled Wave Equations for Δk≠0

For significant fundamental pump depletion and correspondingly large non-linear phase shifts of the fundamental field envelope, equations (2.34) must be solved exactly. Although the equations may be solved analytically in terms of Jacobi elliptic functions [5], they are solved here using the fourth order Runge-Kutta algorithm for numerical integration. As mentioned earlier, scaling the coupled wave equations for extra generality often results in the solutions being difficult to interpret in meaningful physical terms, and so the unscaled equations of (2.34) will be solved with realistic data for $Al_{0.2}Ga_{0.8}As$ at 1.55 μm taken from Table 2.1. In Fig. 2.3 the normalised fundamental field intensity $I_\omega(z)/I_\omega(0)$ is plotted along with the corresponding fundamental field non-linear phase shift $\Delta\Phi^{NL}(z)$ as functions of the distance z propagated through the $Al_{0.2}Ga_{0.8}As$ medium for several different values of the wavevector mismatch parameter Δk. A wavelength of 1.55 μm and an input intensity of $I_\omega(0) = 1 \times 10^{12}$ W/m^2 have also been assumed in each case. Exact solutions of the normalised fundamental intensity $I_\omega(L)/I_\omega(0)$ and the non-linear phase shift $\Delta\Phi^{NL}(L)$ are also plotted in Fig. 2.4 as functions of the input fundamental field intensity $I_\omega(0)$ in $Al_{0.2}Ga_{0.8}As$ at 1.55 μm for several different Δk. For the case of Fig. 2.4, the crystal length L is assumed to be 4 mm and the fundamental throughput is written as $I_\omega(L)/I_\omega(0)$ to emphasise this fact.

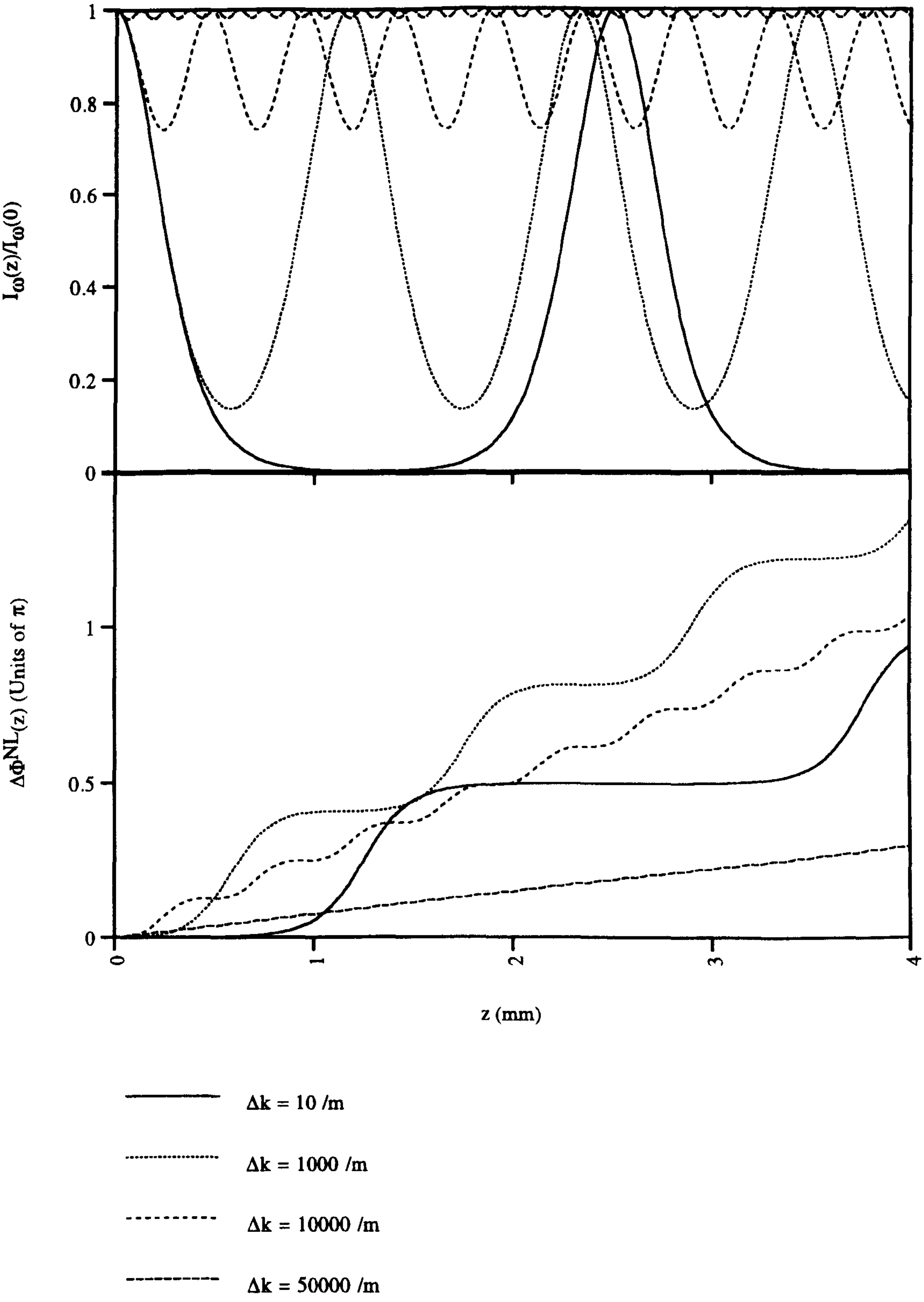

Fig. 2.3 Normalised fundamental field intensity $I_\omega(z)/I_\omega(0)$ and the corresponding non-linear phase shift $\Delta\Phi^{NL}(z)$ as functions of distance z propagated through $Al_{0.2}Ga_{0.8}As$ at 1.55 μm for several different values of the wavevector mismatch parameter Δk when $I_\omega(0) = 1 \times 10^{12}$ W/m^2.

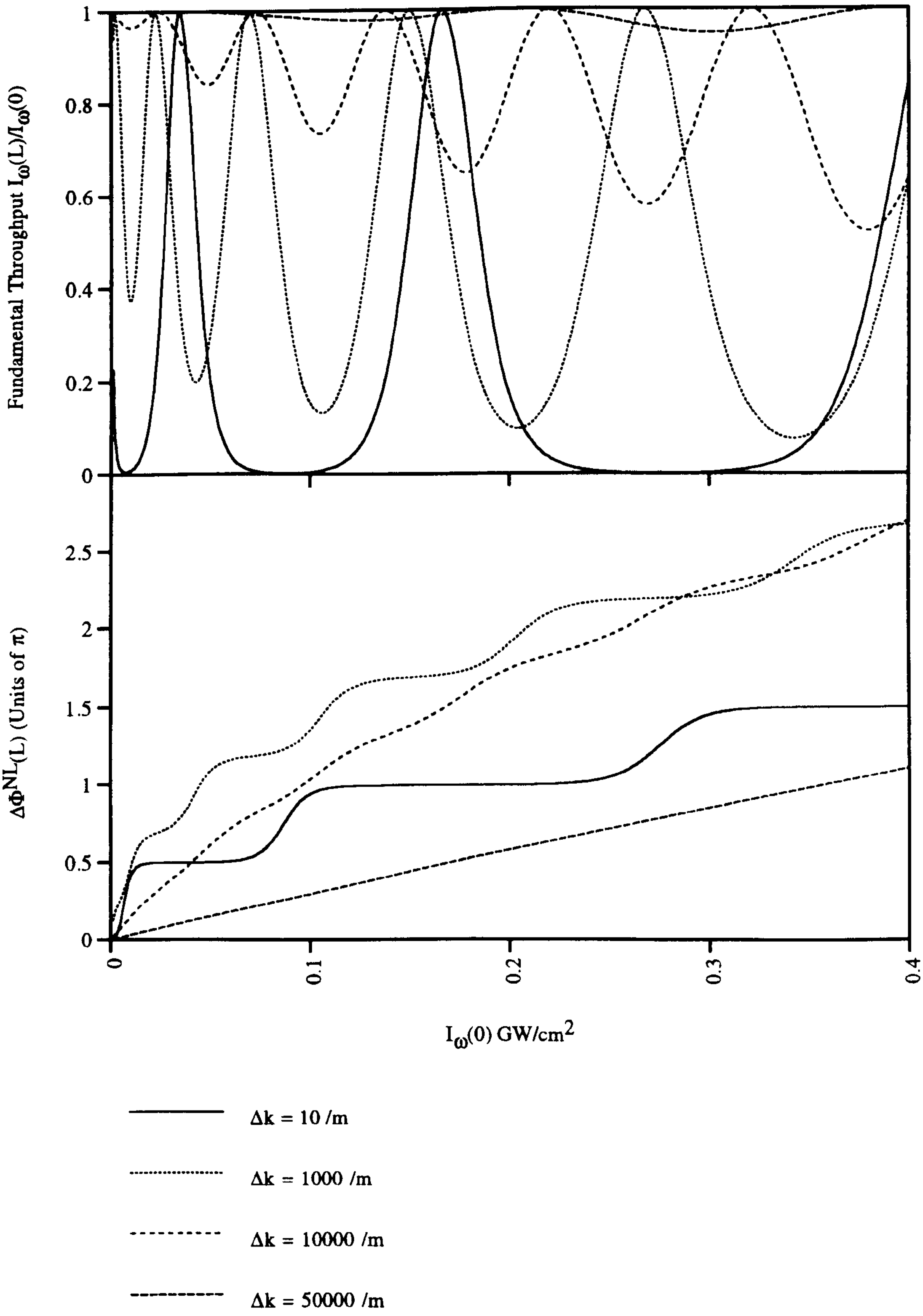

Fig. 2.4 Fundamental throughput $I_\omega(L)/I_\omega(0)$ and the corresponding non-linear phase shift $\Delta\Phi^{NL}(L)$ as functions of the input fundamental intensity $I_\omega(0)$ in $Al_{0.2}Ga_{0.8}As$ at 1.55 μm for several different values of the wavevector mismatch parameter Δk when L = 4 mm.

The curves of Figs. 2.3 and 2.4 display several interesting features:

(i) For a given Δk, the amplitude of the normalised fundamental field intensity oscillates with both z and the input field intensity $I_\omega(0)$ - the smaller the Δk, the deeper the modulation of the field intensity. Also, for an appropriate choice of crystal length L or input intensity $I_\omega(0)$, unity transmission of the fundamental field is obtained.

(ii) The non-linear phase $\Delta\Phi^{NL}$ grows in a stepwise fashion with both z and $I_\omega(0)$ for small Δk. For larger Δk, the phase "plateau's" become shorter and the phase "steps" become smaller until the non-linear phase becomes approximately linear in both z and $I_\omega(0)$ in accordance with (2.46b).

The origin of the term "cascaded second order interaction" should be obvious from Figs. 2.3 and 2.4: up-conversion to the second harmonic frequency is followed by down-conversion back to the fundamental frequency with the net result that the fundamental field experiences a non-linear phase shift.

Exact tuning curve solutions may also be calculated for fixed L and $I_\omega(0)$. The tuning curves of Figs. 2.5, 2.6 and 2.7 for example, correspond to input fundamental field intensities of 1×10^8 W/m^2, 1×10^{10} W/m^2, and 1×10^{12} W/m^2 respectively for an interaction length of 4 mm in $Al_{0.2}Ga_{0.8}As$.

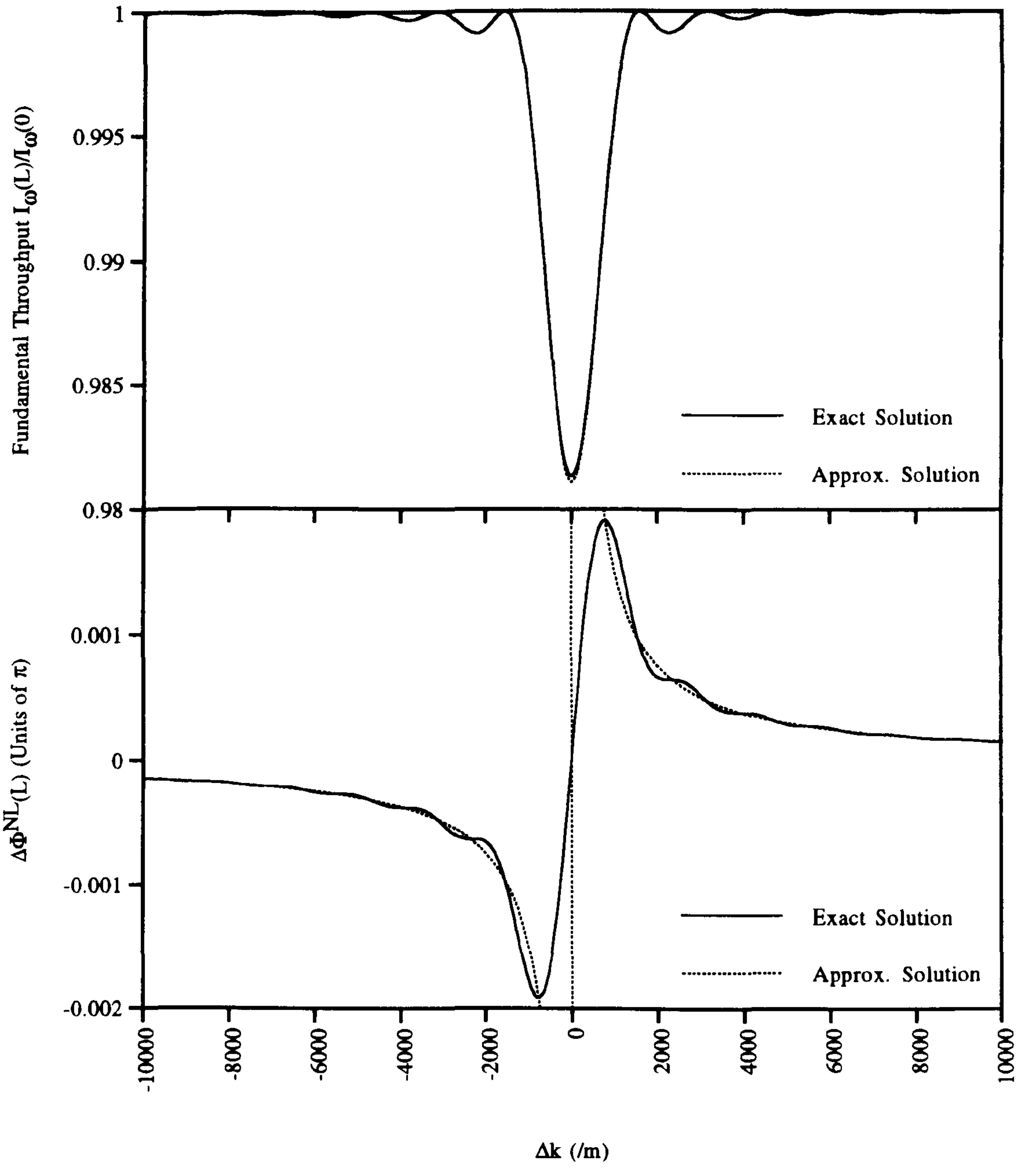

Fig. 2.5 Tuning curves for $Al_{0.2}Ga_{0.8}As$ at 1.55 μm: fundamental throughput $I_\omega(L)/I_\omega(0)$ and the corresponding non-linear phase shift $\Delta\Phi^{NL}(L)$ as functions of the wavevector mismatch parameter Δk for an interaction length $L = 4$ mm and an input fundamental field intensity $I_\omega(0) = 1\times10^8$ W/m^2.

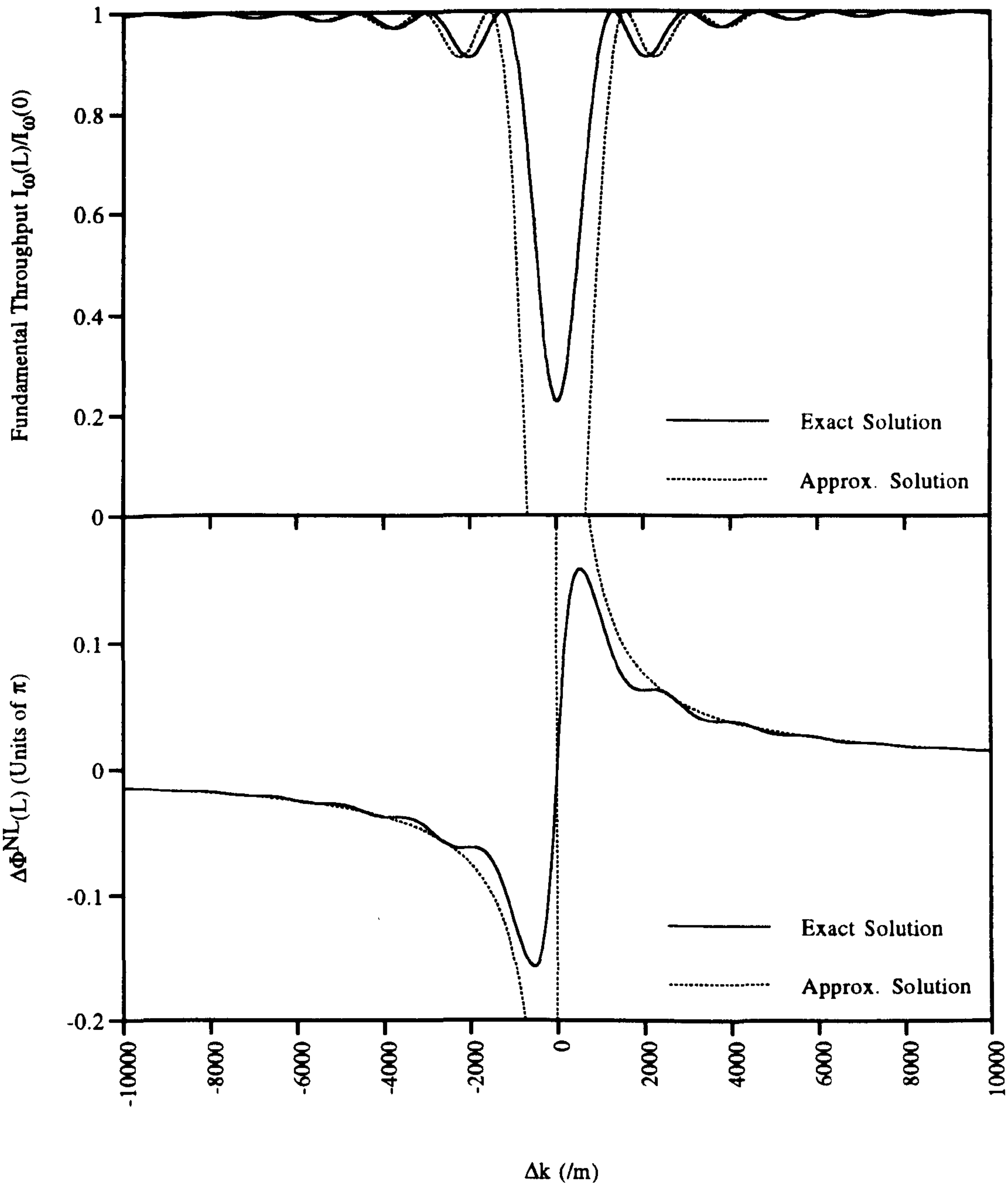

Fig. 2.6 Tuning curves for $Al_{0.2}Ga_{0.8}As$ at 1.55 μm: fundamental throughput $I_\omega(L)/I_\omega(0)$ and the corresponding non-linear phase shift $\Delta\Phi^{NL}(L)$ as functions of the wavevector mismatch parameter Δk for an interaction length L = 4 mm and an input fundamental field intensity $I_\omega(0) = 1\times10^{10}$ W/m^2.

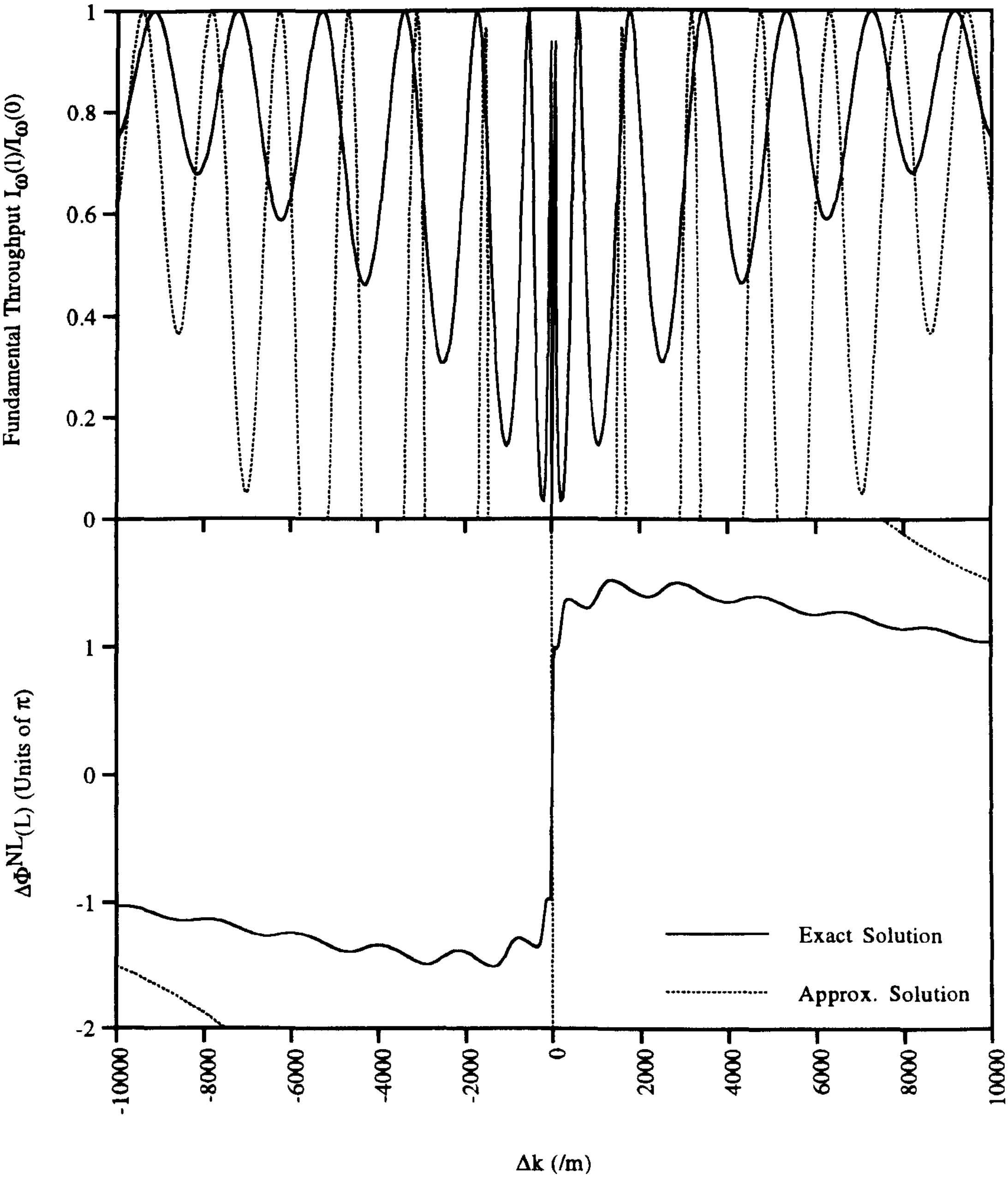

Fig. 2.7 Tuning curves for $Al_{0.2}Ga_{0.8}As$ at 1.55 μm: fundamental throughput $I_\omega(L)/I_\omega(0)$ and the corresponding non-linear phase shift $\Delta\Phi^{NL}(L)$ as functions of the wavevector mismatch parameter Δk for an interaction length $L = 4$ mm and an input fundamental field intensity $I_\omega(0) = 1\times10^{12}$ W/m^2.

From examination of these curves it may be seen that:

(i) $\Delta\Phi^{NL}(L)$ and Δk have the same sign

(ii) For a given $I_\omega(0)$, as $|\Delta k|$ increases from zero, $|\Delta\Phi^{NL}(L)|$ increases initially, reaches a maximum, and then tails off towards zero as $|\Delta k| \to \infty$.

(iii) For large $I_\omega(0)$, we have high conversion efficiencies and large non-linear phase shifts

(iv) For lower $I_\omega(0)$ and larger $|\Delta k|$, the exact tuning curve solutions for $I_\omega(L)/I_\omega(0)$ and $\Delta\Phi^{NL}(L)$ approach the approximate low pump depletion solutions defined by (2.53) and (2.46b) respectively (The approximate solutions for $I_\omega(L)/I_\omega(0)$ and $\Delta\Phi^{NL}(L)$ in Fig. 2.7 when $I_\omega(0) = 1\times10^{12}$ W/m^2 however, hardly resemble the exact solutions at all, simply because they are not strictly valid for the range of Δk over which the graphs are plotted.)

It should also be noted that, although we chose $I_\omega(0)$ was chosen as the parameter when plotting the tuning curves of Figs. 2.5 to 2.7, the length L could equally have been chosen as the parameter with qualitatively similar results.

Finally, we return to a comparison of the non-linear phase shifts occurring as a result of the cascaded $\chi^{(2)}:\chi^{(2)}$ interaction with those occurring through a third order non-linearity. From Figs. 2.5 to 2.7 it may be seen that the maximum non-linear phase shift does not, in general, occur for a wavevector mismatch parameter Δk corresponding to unity fundamental transmission $I_\omega(L)/I_\omega(0) = 1$. Although operating at such a Δk would result in a maximum non-linear phase shift, we would also observe an effective loss in the fundamental field due to up-conversion to the second harmonic field. A more suitable operating point is therefore the smallest non-zero Δk for which the normalised transmission $I_\omega(L)/I_\omega(0)$ first returns to unity. In Fig. 2.8 this operating wavevector mismatch parameter Δk is plotted along with the associated non-linear phase shift as functions of the input fundamental intensity for a 4 mm long $Al_{0.2}Ga_{0.8}As$ medium at 1.55 µm. A series of all-optical switching experiments performed at or around 1.55 µm with AlGaAs waveguide devices suggest that n_2 for $Al_{0.18}Ga_{0.82}As$ is approximately equal to 1×10^{-17} m^2/W [7,8,9,10,11]. The non-linear phase change occurring as a consequence of such an n_2 is therefore plotted on the same set of axes as the $\chi^{(2)}:\chi^{(2)}$ non-linear phase change in Fig. 2.8. Clearly, the size of the non-linear phase change attainable with the cascaded second order process in $Al_{0.2}Ga_{0.8}As$ at 1.55 μm is over an order of magnitude greater than the third order non-linear phase change in the same material for the interaction length and the range of input fundamental intensity chosen. Any large non-linear phase changes generated through the $\chi^{(2)}:\chi^{(2)}$ process are, however, critically wavelength-dependent and this can pose considerable constraints when designing a realistic all-optical switch device.

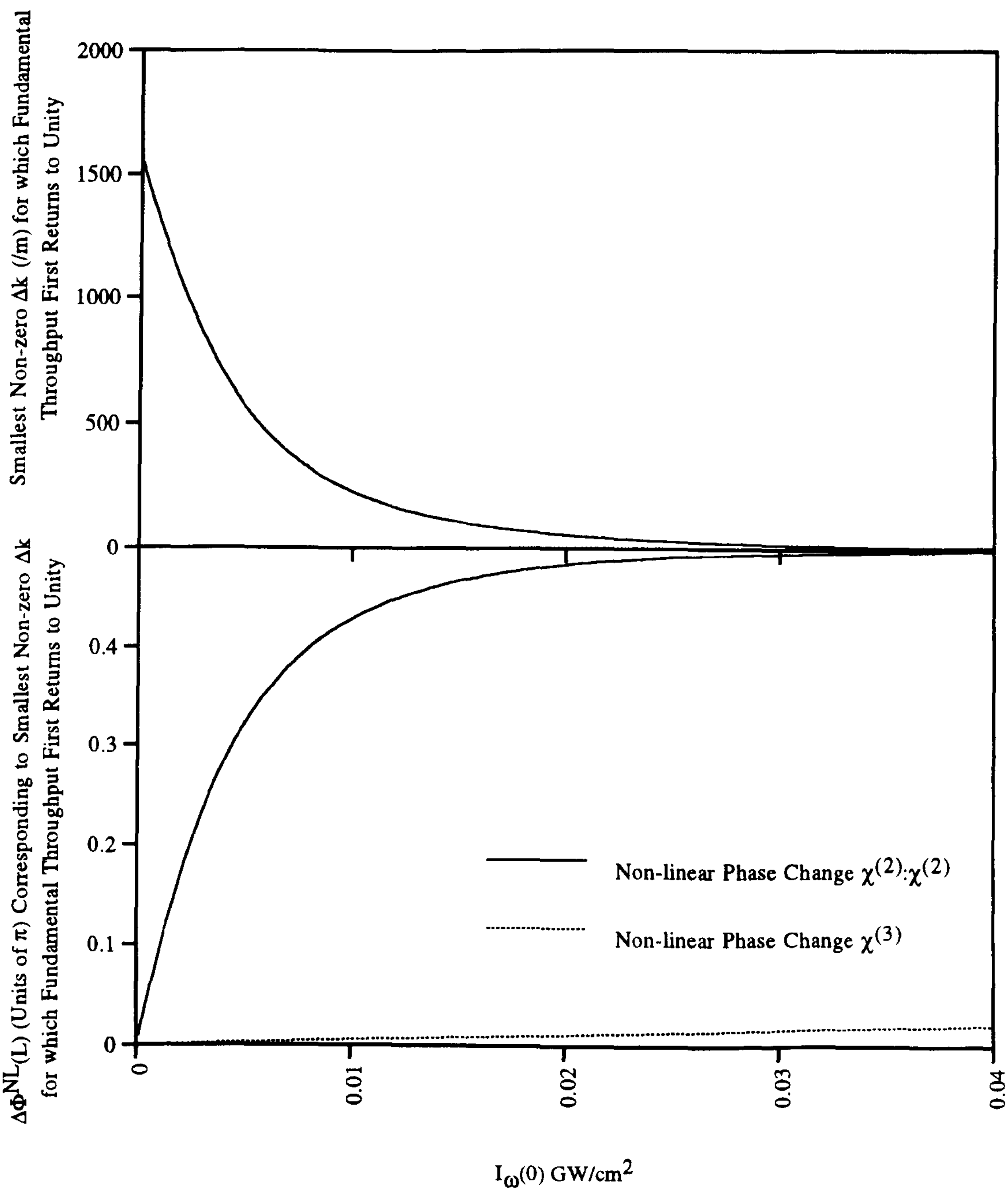

Fig. 2.8 A comparison of the non-linear phase changes attainable through the cascaded second order effect and the third order Kerr effect in a 4 mm long $Al_{0.2}Ga_{0.8}As$ medium at 1.55 μm.

2.3.4 The Cascaded Second Order Process for All-optical Switching

All-optical switching in a non-linear Mach-Zehnder interferometer with a push-pull configuration [5] requires equal but opposite non-linear phase shifts of $+\pi/2$ and $-\pi/2$ in the different arms. These non-linear phase shifts may be achieved for a sufficiently high input fundamental intensity to the arms of the device provided that we arrange for equal but opposite wavevector mismatch parameters $+\Delta k$ and $-\Delta k$ in the two arms respectively. To calculate the input fundamental power required to induce these non-linear phase changes via the cascaded $\chi^{(2)}:\chi^{(2)}$ effect, we now introduce a complete scaling of the coupled wave equations following Hutchings *et al.* [6]. Under this scaling the coupled wave equations of (2.34) become:

$$\frac{d\Psi_{2\omega}}{d\zeta} = i\Psi_{\omega}^{2}\exp(i\zeta) \tag{2.54a}$$

$$\frac{d\Psi_{\omega}}{d\zeta} = i\Psi_{2\omega}\Psi_{\omega}^{*}\exp(-i\zeta) \tag{2.54b}$$

where the dimensionless scaled parameters $\Psi_{j\omega}$ (j=1,2) and ζ are defined by:

$$\Psi_{j\omega} = \frac{\omega d_{eff}}{n_{\omega}c}\cdot\frac{1}{\Delta k}\cdot\sqrt{\frac{n_{j\omega}}{n_{2\omega}}}\cdot\hat{E}_{j\omega} \quad (j=1,2) \tag{2.55a}$$

$$\zeta = \Delta k z \tag{2.55b}$$

Plotted in Fig. 2.9 are the exact numerical solutions of (2.54) as a function of the scaled input fundamental intensity $|\Psi_{\omega}(\zeta=0)|^2$. These graphs were generated using the fourth-order Runge-Kutta algorithm. From Fig. 2.9, it may be seen that when $\zeta=+2\pi$, the fundamental throughput returns to unity with an associated non-linear phase shift of $+\pi/2$ for a scaled input fundamental intensity of $|\Psi_{\omega}(\zeta=0)|^2 \approx 0.64$. (When $\zeta=-2\pi$, the fundamental throughput returns to unity with an associated non-linear phase shift of $-\pi/2$ for the same scaled input fundamental intensity.) For a 4 mm long sample of $Al_{0.2}Ga_{0.8}As$ at 1.55 μm, this scaled input fundamental intensity of $|\Psi_{\omega}(\zeta=0)|^2 \approx 0.64$ translates into an absolute input fundamental intensity $I_{\omega}(0)$ of 13.4×10^{-3} GW/cm^2. If we further assume an effective cross-sectional area of 10 μm^2 for the optical beam profile, $I_{\omega}(0)=13.4\times10^{-3}$

GW/cm^2 translates into a switching power of 1.34 W. Switching in bulk LiNbO$_3$ and KTP would, in contrast, require input fundamental powers of 12.4 W and 66.7 W respectively. It should be re-iterated however, that these switching powers are not very realistic since no perfect phase-matching mechanism exists in practice for GaAs/AlGaAs or for the largest d_{33} coefficients in LiNbO$_3$ and KTP. A realistic GaAs/AlGaAs all-optical switch device is, however, described in Chapter 3, and it's projected performance is compared with the performance of existing all-optical switch devices fabricated from LiNbO$_3$ and KTP.

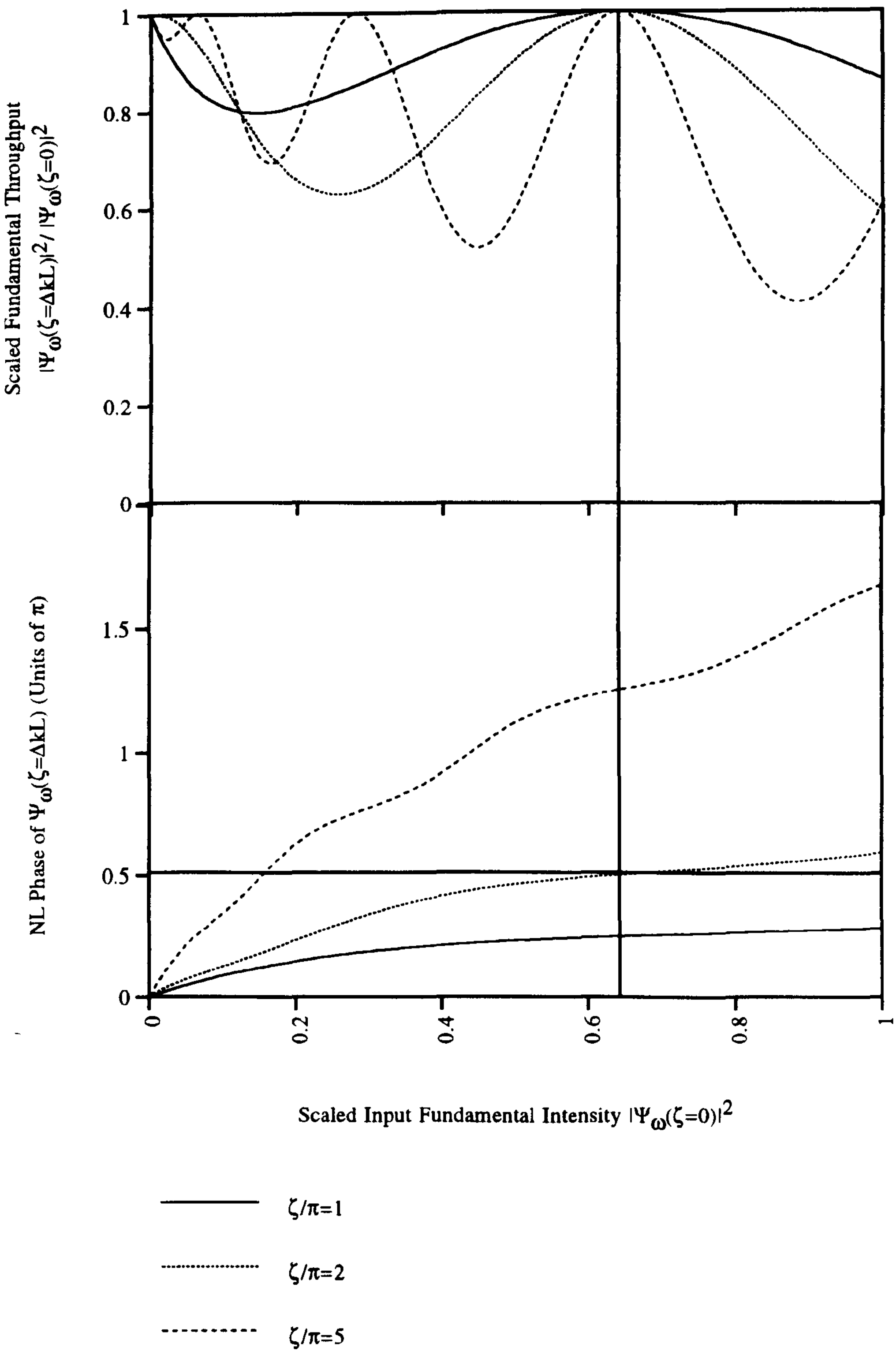

Fig. 2.9 Exact solutions of the scaled coupled wave equations of (2.54) for several different values of the scaled parameter ζ, and the generation of a $+\pi/2$ non-linear phase change for unity fundamental throughput.

2.4 Phase-matched SHG ($\Delta k=0$)

When $\Delta k = 0$ (and correspondingly $L_c \rightarrow \infty$), the second harmonic polarisation and the second harmonic field are in phase everywhere, and a unidirectional power flow occurs from the fundamental wave to the second harmonic wave. Initially, for small Γ and z, fundamental pump depletion can be neglected so that for $\Delta k = 0$ (2.53) gives:

$$\frac{I_{2\omega}(z)}{I_\omega(0)} = \Gamma^2 z^2 \tag{2.56}$$

where it has been assumed that the input second harmonic field intensity $I_{2\omega}(0) = 0$ and Γ is defined by (2.40b) as before. Hence, the second harmonic field intensity initially grows parabolically with distance z and is proportional to $\mathrm{FOM}^{(2)}$.

For higher input field intensities or for longer z, significant depletion of the pump occurs and the second harmonic field intensity starts to saturate. In this regime, (2.56) is no longer valid and an exact solution of the coupled wave equations of (2.34) is required. The exact solutions when $\Delta k = 0$ were originally derived by Armstrong *et al.* [12] and are given by:

$$\frac{I_{2\omega}(z)}{I_\omega(0)} = \tanh^2(\Gamma z) \tag{2.57a}$$

$$\frac{I_\omega(z)}{I_\omega(0)} = \mathrm{sech}^2(\Gamma z) \tag{2.57b}$$

Fig. 2.10 is a plot of the normalised intensities $I_{2\omega}(z)/I_\omega(0)$ and $I_\omega(z)/I_\omega(0)$ as defined by (2.57) for the case of $Al_{0.2}Ga_{0.8}As$ at 1.55 μm where an input fundamental field intensity of $I_\omega(0) = 1 \times 10^{12}$ W/m^2 has been assumed. Plotted on the same set of axes is the initial parabolic dependence of $I_{2\omega}(z)/I_\omega(0)$ as derived from (2.56) which serves as an approximation to the exact solution of (2.57a) for small z. From Fig. 2.10 it may be seen that the second harmonic field grows monotonically with distance propagated at the expense of the fundamental field, and that 100% conversion efficiency is theoretically achievable for the case of uniform plane waves. In practice however, a laser beam has finite transverse dimensions and the maximum conversion efficiency is limited by diffraction of the fundamental beam.

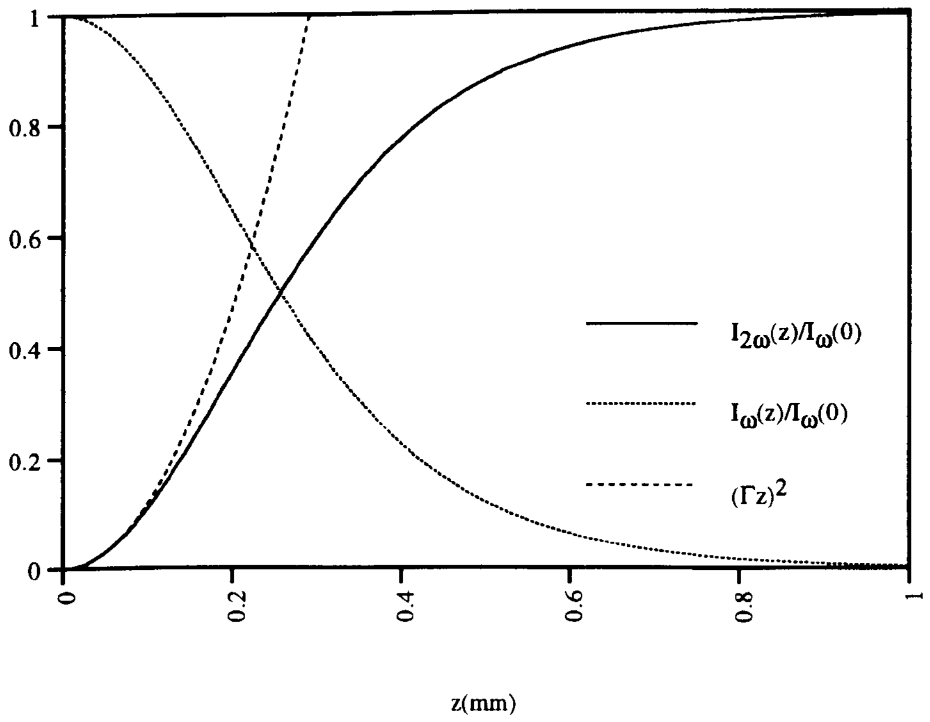

Fig. 2.10 Phase-matched SHG in $Al_{0.2}Ga_{0.8}As$ at 1.55 μm for an input fundamental field intensity $I_{\omega}(0)=1\times10^{12}$ W/m^2.

2.5 Quasi-phase-matching for Control of the Wavevector Mismatch Parameter Δk

Quasi-phase-matching (QPM) is a technique, originally conceived by Armstrong and Bloembergen [12], which may be used for the control of the wavevector mismatch parameter Δk in both non-birefringent media, and in media such as $LiNbO_3$ and KTP in which we wish to produce second order non-linear effects via the largest d_{33} coefficient which requires that the interacting electric fields are all co-linearly polarised. All quasi-phase-matching schemes involve the periodic modulation of the refractive index difference $(n_{2\omega} - n_{\omega})$ and/or periodic modulation of the d_{eff} coefficient itself. In either case, the wavevector mismatch parameter Δk_{QPM} which results is given by:

$$\Delta k_{QPM} = k_{2\omega} - 2k_{\omega} - mK \quad (m = 1, 3, 5, \ldots) \qquad (2.58a)$$

where

$$K = \frac{2\pi}{\Lambda} \tag{2.58b}$$

In (2.58), m is an odd integer, and Λ is the modulation period of the refractive index difference and/or the d_{eff} coefficient. Periodic modulation of the refractive index difference for QPM is, however, inherently inefficient due to scattering losses associated with the index changes. This work is therefore concerned with modulation of the d_{eff} coefficient for control of the wavevector mismatch parameter. Any simultaneous modulation of the refractive index is then detrimental to the quasi-phase-matching efficiency.

For the special case of quasi-phase-matched SHG, $\Delta k_{QPM} = 0$ and from (2.58) we may deduce that:

$$\Lambda = 2mL_c \tag{2.59}$$

where the coherence length $L_c = \pi/|\Delta k|$ as usual. The integer m determines the order of the QPM scheme: the higher the order, the longer the quasi-phase-matching period given by (2.59) and the less efficient the conversion process becomes. The conversion efficiency also depends on the depth of modulation in the non-linearity: for a modulation of the non-linear coefficient between d_{eff} and d_{eff}' for example, it can be shown that, in the low pump depletion regime (see Appendix B):

$$\frac{I_{2\omega}(M \cdot 2mL_c)}{I_\omega(0)} = \frac{8\pi^2}{\varepsilon_0 c \lambda^2} \frac{\left|d_{eff} - d_{eff}'\right|^2}{n_\omega^2 n_{2\omega}} \cdot I_\omega(0) \cdot \frac{4M^2 L_c^2}{\pi^2} \tag{2.60}$$

where M is an integer greater or equal to zero. Writing $d_{eff}' = \gamma d_{eff}$ where $|\gamma| < 1$ we then obtain:

$$\frac{I_{2\omega}(M \cdot 2mL_c)}{I_\omega(0)} = \frac{8\pi^2}{\varepsilon_0 c \lambda^2} \frac{{d_{eff}}^2 |1-\gamma|^2}{n_\omega^2 n_{2\omega}} \cdot I_\omega(0) \cdot \frac{4M^2 L_c^2}{\pi^2} \tag{2.61}$$

Then, for $z = M \cdot 2mL_c$, (2.61) becomes:

$$\frac{I_{2\omega}(z = M \cdot 2mL_c)}{I_\omega(0)} = \Gamma^2 |1-\gamma|^2 \cdot \frac{z^2}{m^2\pi^2} \tag{2.62}$$

where Γ is given by (2.40b) as before. From (2.62) it may be seen that $I_{2\omega}(z)/I_\omega(0)$ is proportional to both the figure of merit for second order non-linear materials, $FOM^{(2)}$, *and* the square of the modulation depth $|1-\gamma|^2$. For convenience, a further parameter d_{QPM} may be defined as the d_{eff} coefficient of an equivalent homogeneous second order non-linear medium in which perfect phase matching results in the same rate of parabolic growth of the second harmonic conversion efficiency:

$$d_{QPM} = \frac{d_{eff}|1-\gamma|}{m\pi} \tag{2.63}$$

The conversion efficiency $I_{2\omega}(z)/I_\omega(0)$ is plotted in Fig. 2.11 as a function of distance for several different QPM schemes in $Al_{0.2}Ga_{0.8}As$ at 1.55 μm for an input fundamental intensity of 1×10^{12} W/m^2. The various curves of Fig. 2.11 were generated using the fourth-order Runge-Kutta algorithm for the numerical solution of the coupled wave equations of (2.34) subject to different modulation schemes for the d_{eff} coefficient. Of particular interest here, and perhaps the most commonly encountered in practice, are the domain disordering (DD) and domain reversal (DR) schemes, which require that d_{eff} is periodically suppressed (i.e. $d_{eff}' = 0$ and $\gamma = 0$), and periodically negated (i.e. $d_{eff}' = -d_{eff}$ and $\gamma = -1$) respectively. Plotted in Fig. 2.11, are the second harmonic conversion efficiency curves for first order domain reversal (DR1), first order domain disordering (DD1) and third order domain disordering (DD3). In addition, the conversion efficiency curves are plotted for the case of unphase-matched SHG for which Δk is large and determined by the intrinsic dispersion of the $Al_{0.2}Ga_{0.8}As$ medium (see Fig. 2.1, Section 2.3), and for the case of perfectly phase-matched SHG for which $\Delta k = 0$ (see Fig. 2.10, Section 2.4).

Considering the case of DR1 first (i.e. $\gamma = -1$, $m = 1$), we see that the evolution of the second harmonic field is the same as that for unphase-matched SHG over the first coherence length L_c so that the second harmonic field and the non-linear polarisation are approaching antiphase as z approaches L_c. Reversing the d_{eff} coefficient at $z = L_c$ then flips the phase of the non-linear polarisation so that the phase difference between the second harmonic field and the non-linear polarisation decreases again and power continues to flow from the fundamental excitation field to the second harmonic field. By reversing d_{eff} over alternate coherence lengths, a unidirectional power flow is achieved from the fundamental field to the second harmonic field and quasi-parabolic growth of the second harmonic conversion efficiency $I_{2\omega}(z)/I_{\omega}(0)$ results. Also plotted in Fig. 2.11, is the relation of (2.62) for the case of DR1 ($\gamma = -1$, $m = 1$):

$$\frac{I_{2\omega}(z = M \cdot 2L_c)}{I_{\omega}(0)} = \frac{4\Gamma^2 z^2}{\pi^2} \tag{2.64}$$

The second harmonic field evolution over the first coherence length for the DD1 scheme ($\gamma = 0$, $m = 1$) also resembles that of unphase-matched SHG. To prevent power flow back from the second harmonic field to the fundamental field during the second coherence length in this case, the d_{eff} coefficient of the medium is suppressed. To achieve a stepwise quasi-parabolic growth of the second harmonic conversion efficiency then requires that d_{eff} is suppressed over alternate coherence lengths. From (2.62) it may be seen that for DD1:

$$\frac{I_{2\omega}(z = M \cdot 2L_c)}{I_{\omega}(0)} = \frac{\Gamma^2 z^2}{\pi^2} \tag{2.65}$$

For a third order QPM scheme, the domain length $L_d = \Lambda/2$, is equal to $3L_c$. From Fig. 2.11 it may be seen that for DD3 ($\gamma = 0$, $m = 3$), the second harmonic field evolution follows the unphase-matched second harmonic field evolution over the first domain ($0 < z < 3L_c$). If d_{eff} is subsequently suppressed over alternate domains, a stepwise quasi-parabolic growth in the second harmonic conversion efficiency is obtained. From consideration of (2.62) with $\gamma = 0$ and $m = 3$, it may be shown that:

$$\frac{I_{2\omega}(z = M \cdot 6L_c)}{I_{\omega}(0)} = \frac{\Gamma^2 z^2}{9\pi^2} \tag{2.66}$$

Although the different quasi-phase-matching schemes have been discussed for the special case of SHG, they also generalise to second order processes for which $\Delta k_{QPM} \neq 0$. For example, a quasi-phase-matched $\chi^{(2)}:\chi^{(2)}$ interaction in a medium in which d_{eff} is modulated with a period Λ, is equivalent to a $\chi^{(2)}:\chi^{(2)}$ interaction in a homogeneous medium with a wavevector mismatch parameter $\Delta k = \Delta k_{QPM}$ and a constant coefficient d_{QPM}.

The exact nature of the quasi-phase-matching technique used in practice differs from material to material. In $LiNbO_3$ for example, domain reversal may be accomplished through periodic indiffusion of Ti [13] or periodic poling with an electric field [14], while in KTP, domain inversion is believed to occur as a result of ion-exchange achieved using Rb/Tl/Ba nitrate molten salt baths [15]. In the GaAs/AlGaAs system, domain inversion and domain disordering schemes have been implemented but with limited success. Gordon *et al.* [16] for example, demonstrated quasi-phase-mismatched SHG using domain reversal at 10.6 µm in diffusion-bonded stacks of up to 9 layers of (110) and -(110) GaAs substrates. Also, Janz *et al.* [17] demonstrated enhancements of between 30 and 40 in the SHG from heterostructures composed of seven quasi-phase-matching periods in a reflection geometry. For efficient quasi-phase-matching however, a coherent interaction is required which involves hundreds or perhaps even thousands of domains with little or no scattering losses. It is for this reason that QPM is used to control second order non-linear interactions along waveguide devices as discussed in the next section.

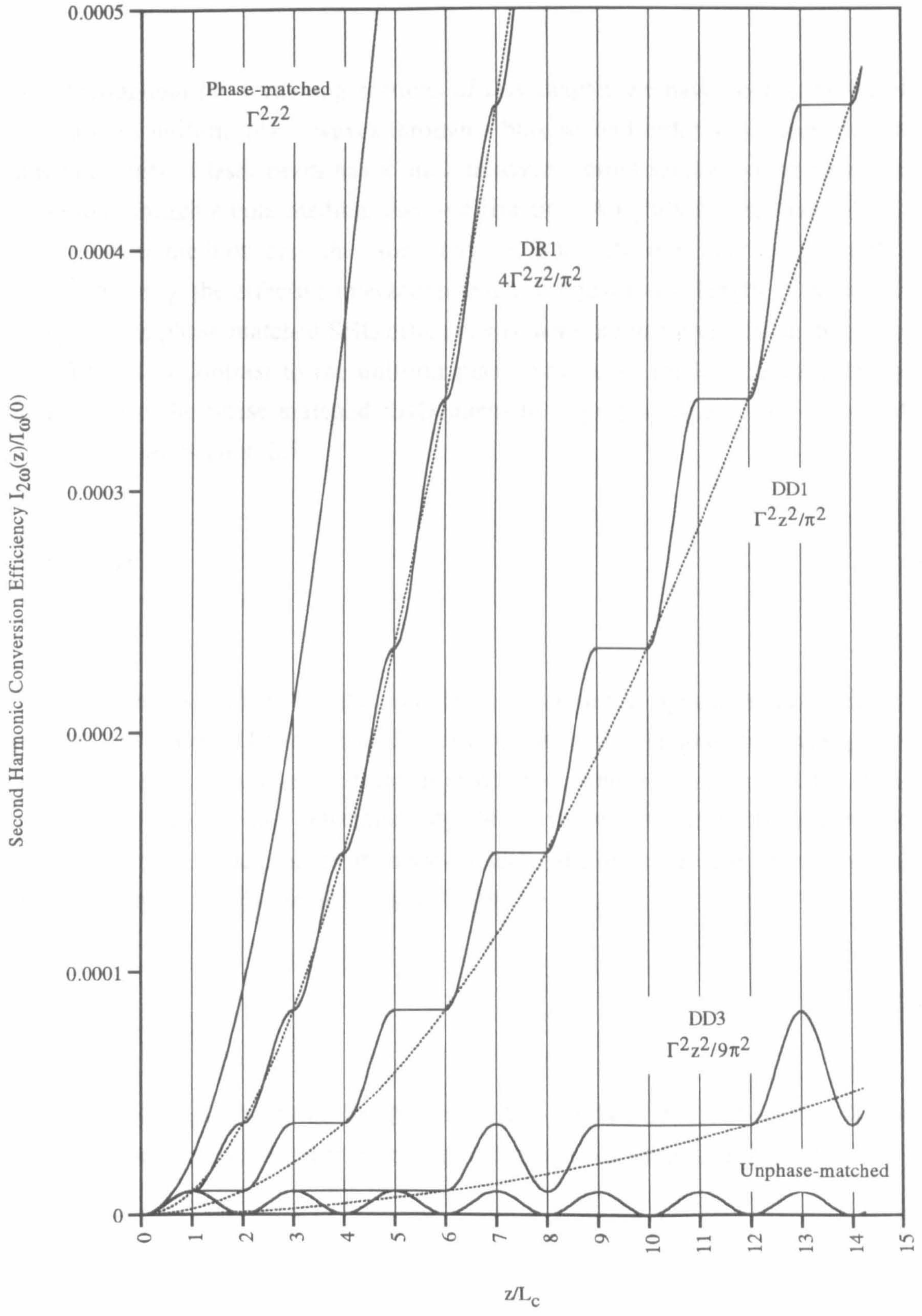

Fig. 2.11 Quasi-phase-matching of SHG in $Al_{0.2}Ga_{0.8}As$ at 1.55 μm for an input fundamental field intensity of 1×10^{12} W/m^2

2.6 Guided Wave Second Order Non-linear Effects

Throughout the foregoing sections of this chapter we have been considering the propagation of uniform plane waves through a bulk second order non-linear medium. In practice however, a laser beam has a finite transverse cross-section which varies during propagation through a bulk medium due to diffraction. A tightly focused laser beam in a bulk non-linear medium can, therefore, have a short effective interaction length. For optimum focusing, the effective interaction length is equal to the length of the non-linear medium and the phase-matched SHG efficiency is therefore just proportional to the crystal length. This is in contrast to the uniform plane wave case for low fundamental pump depletion when the phase-matched SHG intensity is proportional to the square of the crystal length (see Section 2.4):

$$\frac{I_{2\omega}(z)}{I_{\omega}(0)} = \Gamma^2 z^2 \tag{2.56}$$

Waveguides are ideal for the production of non-linear optical effects because they allow high intensities to be maintained over long interaction lengths. In a waveguide, the field intensities are no longer uniform in space, but rather the fundamental and second harmonic field profiles are determined by the waveguide mode profiles at ω and 2ω respectively. These mode profiles are invariant along the direction of propagation so that a modified version of (2.56) should be used [18,19]:

$$P_{2\omega} = \eta P_{\omega}^2 L^2 \tag{2.67}$$

where P_{ω} and $P_{2\omega}$ represent the power at the fundamental and second harmonic frequencies respectively, and η is the conversion efficiency parameter defined by:

$$\eta = \frac{8\pi^2}{\varepsilon_0 c \lambda^2 n_{\omega\mathrm{eff}}^2 n_{2\omega\mathrm{eff}}} \cdot \left| \int_{-\infty}^{\infty} \int_{-\infty}^{\infty} d_{\mathrm{eff}}(x,y) \xi_{\omega}^2(x,y) \xi_{2\omega}(x,y) dxdy \right|^2 \tag{2.68}$$

In (2.68), x and y are the transverse waveguide co-ordinates defined in Fig. 2.12 and $\xi_\omega(x,y)$ and $\xi_{2\omega}(x,y)$ are the transverse fundamental and second harmonic field profiles respectively normalised to unity:

$$\int_{-\infty}^{\infty}\int_{-\infty}^{\infty}\xi_\omega^2(x,y)dxdy = \int_{-\infty}^{\infty}\int_{-\infty}^{\infty}\xi_{2\omega}^2(x,y)dxdy = 1 \tag{2.69}$$

$d_{eff}(x,y)$ also represents the transverse spatial distribution of the non-linearity. The overlap integral term of (2.68) therefore reflects the fact that any second harmonic generated by the fundamental mode in a region where the second harmonic is poorly confined or the non-linearity is small, will not contribute significantly to the total second harmonic power at the output of the waveguide. Furthermore, if $d_{eff}(x,y)$ is such that:

$$d_{eff}(x,y) = \begin{cases} d_{eff} \text{ , } x{:}x_1 < x < x_2 \text{ , } y{:}y_1 < y < y_2 \\ 0 \text{ , otherwise} \end{cases} \tag{2.70}$$

then

$$\eta = \frac{8\pi^2}{\varepsilon_0 c\lambda^2}\frac{d_{eff}^2}{n_{\omega eff}^2 n_{2\omega eff}} \times F^{(2)} \tag{2.71a}$$

where

$$F^{(2)} = \left|\int_{x_1}^{x_2} dx \int_{y_1}^{y_2} dy \xi_\omega^2(x,y)\xi_{2\omega}(x,y)\right|^2 \tag{2.71b}$$

The factor $1/F^{(2)}$ has units of area and can therefore be thought of as an effective area A_{eff} for the non-linear interaction:

$$\frac{1}{F^{(2)}} = A_{eff} \tag{2.72}$$

Therefore, the larger $F^{(2)}$, the smaller A_{eff}, the higher the effective intensity, and the larger the conversion efficiency parameter η.

For quasi-phase-matched interactions, the non-linear coefficient $d_{QPM}(x,y)$ should be substituted for $d_{eff}(x,y)$, and the expression for the conversion efficiency parameter becomes:

$$\eta = \frac{8\pi^2}{\varepsilon_0 c \lambda^2 n_{\omega eff}^2 n_{2\omega eff}} \cdot \left| \int_{-\infty}^{\infty} \int_{-\infty}^{\infty} d_{QPM}(x,y) \xi_{\omega}^2(x,y) \xi_{2\omega}(x,y) dxdy \right|^2 \tag{2.73}$$

The conversion efficiency parameter η as defined by (2.68) or (2.73) is then normally expressed in units of %/Wcm^2 and acts as a figure of merit for the SHG process which is dependent on *both* the non-linear material *and* the particular phase-matching scheme adopted.

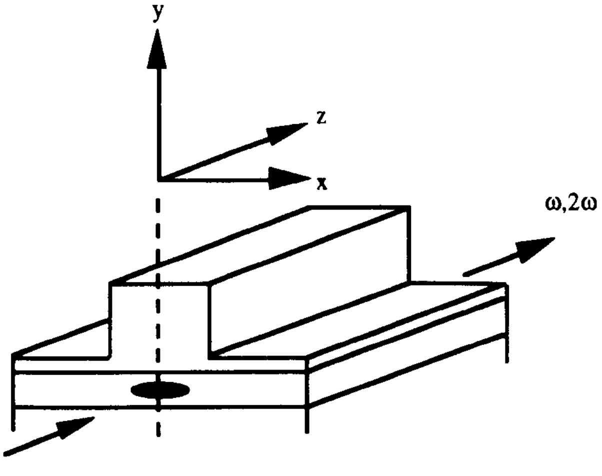

Fig. 2.12 Co-ordinate definitions for the evaluation of the overlap integral terms of (2.68) and (2.73)

The other obvious difference between guided wave non-linear interactions and the uniform plane wave interactions described in previous sections, is that the wavevector mismatch parameter is now determined by the mode effective indices rather than the bulk refractive indices. The intrinsic birefringence and modal dispersion of waveguides can then open up new phase-matching possibilities. For example, in GaAs waveguides with a large index step which support several higher order modes, the lowest-order fundamental frequency mode can be matched to a higher even-order mode at the second harmonic frequency [20]. The problem with such a scheme is, however, that the mode overlap integral of (2.68) can be quite small, and the resulting SHG efficiency correspondingly low. Quasi-phase-matching in a guided-wave geometry can, however, overcome these problems and has been the subject of much research activity in recent years. SHG conversion efficiency parameters of up to 600 %/Wcm^2 have been achieved by first order quasi-phase-matching in periodically poled LiNbO$_3$ waveguides at 852 nm [14], while efficiency parameters exceeding 100 %/Wcm^2 have been reported in ion-exchanged KTP waveguides at 851 nm [15]. At the time of writing the largest reported SHG conversion efficiency parameter in the GaAs/AlGaAs system is 167 %/Wcm^2 at 1542 nm, where quasi-phase-matching was achieved by periodic domain inversion using wafer-bonding and re-growth [21]. This conversion efficiency was, however, much lower than the theoretically predicted efficiency due to large waveguide scattering losses caused by corrugations in the guiding layer.

Suppression of the second order susceptibility in GaAs/AlGaAs for domain disordering has also been successfully demonstrated by ion-beam induced amorphization [22]. Waveguides fabricated from the amorphous material after annealing however, exhibited losses as high as 30 dB/cm, and domain disordering by periodic suppression of the non-linear susceptibility was not attempted. In Chapter 3 a novel domain disordering technique is therefore described for the control of the wavevector mismatch parameter Δk_{QPM} in GaAs/AlGaAs asymmetric quantum well waveguides with a view to achieving all-optical switching for a fundamental wavelength of 1.55 μm.

---

[1] P. N. Butcher and D. Cotter, "The Elements of Non-linear Optics", Cambridge University Press, Cambridge, 1991

[2] R. DeSalvo, D. J. Hagan, M. Sheik-Bahae, G. I. Stegeman, E. W. Van Stryland, and H. Vanherzeele, "Self-focusing and Self-defocusing by Cascaded Second-order Effects in KTP", Opt. Lett. **17**, 28 (1992)

[3] G. I. Stegeman, M. Sheik-Bahe, E. W. Van Stryland, and G. Assanto, "Large Nonlinear Phase Shifts in Second-order Nonlinear-optical Processes", Opt. Lett. **18**, 13 (1993)

[4] G. Assanto, G. I. Stegeman, M. Sheik-Bahae, and E. W. Van Stryland, "All-optical Switching Devices Based on Large Nonlinear Phase Shifts from Second Harmonic Generation", Appl. Phys. Lett. **62**, 1323 (1993)

[5] C. N. Ironside, J. S. Aitchison, and J. M. Arnold, "An All-optical Switch Employing the Cascaded Second-order Nonlinear Effect", J. Quantum. Electron. **29**, 2650 (1993)

[6] D. C. Hutchings, J. S. Aitchison, and C. N. Ironside, "All-optical Switching Based on Nondegenerate Phase Shifts from a Cascaded Second-order Nonlinearity", Opt. Lett. **18**, 793 (1993)

[7] J. S. Aitchison, A. H. Kean, C. N. Ironside, A. Villeneuve, and G. I. Stegeman, "Ultrafast All-optical Switching in $Al_{0.18}Ga_{0.82}As$ Directional Coupler in 1.55 μm Spectral Region", Electron. Lett. **27**, 1709 (1991)

[8] K. Al-hemyari, J. S. Aitchison, C. N. Ironside, G. T. Kennedy, R. S. Grant, and W. Sibbett, "Ultrafast All-optical Switching in GaAlAs Integrated Interferometer in 1.55 μm Spectral Region", Electron. Lett. **28**, 1090 (1992)

[9] A. Villeneuve, C. C. Yang, P. G. Wigley, G. I. Stegeman, J. S. Aitchison, and C. N. Ironside, "Ultrafast All-optical Switching in Semiconductor Nonlinear Directional Couplers at Half the Band Gap", Appl. Phys. Lett. **61**, 147 (1992)

[10] J. S. Aitchison, A. Villeneuve, and G. I. Stegeman, "All-optical Switching in a Nonlinear GaAlAs X Junction", Opt. Lett. **18**, 1153 (1993)

[11] K. Al-hemyari, A. Villeneuve, J. U. Kang, J. S. Aitchison, C. N. Ironside, and G. I. Stegeman, "Ultrafast All-optical Switching in GaAlAs Directional Couplers at 1.55 μm without Multiphoton Absorption", Appl. Phys. Lett. **63**, 3562 (1993)

[12] J. A. Armstrong, N. Bloembergen, J. Ducuing, and P. S. Pershan, "Interactions between Light Waves in a Nonlinear Dielectric", Phys. Rev. **127**, 1918 (1962)

[13] C. Q. Xu, H. Okayama, K. Shinozaki, K. Watanabe, and M. Kawahara, "Wavelength Conversions ~ 1.5 μm by Difference Frequency Generation in Periodically Domain-inverted $LiNbO_3$ Channel Waveguides", Appl. Phys. Lett. **63**, 1170 (1993)

[14] M.Yamada, N. Nada, M. Saitoh, and K. Watanabe, "First-order Quasi-phase-matched $LiNbO_3$ Waveguide Periodically Poled by Applying an External Field for Efficient Blue Second-harmonic Generation", Appl. Phys. Lett. **62**, 435 (1993)

[15] C. J. van der Poel, J. D. Bierlein, J. B. Brown, and S. Colak, "Efficient Type I Blue Second-harmonic Generation in Periodically Segmented $KTiOPO_4$ Waveguides", Appl. Phys. Lett. **57**, 2074 (1990)

[16] L. Gordon, G. L. Woods, R. C. Eckardt, R. R. Route, R. S. Feigelson, M. M. Fejer, and R. L. Byer, "Diffusion-bonded Stacked GaAs for Quasi-phase-matched Second-harmonic Generation of a Carbon Dioxide Laser", Electron. Lett. **29**, 1942 (1993)

[17] S. Janz, C. Fernando, H. Dai, F. Chatenoud, M. Dion, and R. Normandin, "Quasi-phase-matched Second-harmonic Generation in Reflection from $Al_xGa_{1-x}As$ Heterostructures", Opt. Lett. **18**, 589 (1993)

[18] M. L. Bortz, L. A. Eyres, and M. M. Fejer, "Depth Profiling of the d_{33} Nonlinear Coefficient in Annealed Proton Exchanged $LiNbO_3$ Waveguides", Appl. Phys. Lett. **62**, 2012 (1993)

[19] M. L. Bortz, S. J. Field, M. M. Fejer, D. W. Nam, R. G. Waarts, and D. F. Welch, "Noncritical Quasi-phase-matched Second Harmonic Generation in an Annealed Proton-exchanged $LiNbO_3$ Waveguide", Transactions on Quantum Electron. **30**, 2953 (1994)

[20] J. P. van der Ziel, M. Ilegems, P. W. Foy, and R. M. Mikulyak, "Phase-matched Second Harmonic Generation in a Periodic GaAs Waveguide", Appl. Phys. Lett. **29**, 775 (1976)

[21] S. J. B. Yoo, C. Caneau, R. Bhat, M. A. Koza, A. Rajhel, and N Antoniades, "Wavelength Conversion by Difference Frequency Generation in AlGaAs Waveguides with Periodic Domain Inversion Achieved by Wafer Bonding", Appl. Phys. Lett. **68**, 2609 (1996)

[22] S. Janz, M. Buchanan, F. Chatenoud, J. P. McCaffrey, R. Normandin, U. G. Akano, and I. V. Mitchell, "Modification of the Second-order Optical Susceptibility in $Al_xGa_{1-x}As$ by Ion-beam Induced Amorphization", Appl. Phys. Lett. **65**, 216 (1994)

3

Second Order Non-linear Effects in GaAs/AlGaAs Asymmetric Quantum Well Waveguides and All-optical Switching

As mentioned at the end of the previous chapter, no efficient phase-matching technique exists for III-V semiconductors. In the present work, we investigate a novel approach to solving this problem. In particular, attention is focused on the study of second order non-linear effects in GaAs/AlGaAs asymmetric quantum well (AQW) structures. Such materials are of interest primarily because the AQWs have second order non-linear susceptibility tensor components associated with them which may be potentially suppressed by QW-intermixing. Thus, it should be possible to apply quantum well intermixing techniques to periodically modulate the AQW non-linearities for quasi-phase-matching.

3.1 GaAs/AlGaAs AQW Second Order Non-linearities

The AQW waveguide structures used in this work all incorporated either asymmetric stepped QWs (ASQWs) or asymmetric coupled QWs (ACQWs) in the guiding layers. For example, the B563 ASQW and B578 ACQW structures are depicted in Figs. 3.1 and 3.2 respectively. From Fig. 3.1, it can be seen that the ASQW structure is composed of two well layers of different Al fractions (and different thicknesses in general) sandwiched between two higher Al fraction barrier layers. This gives rise to a "step-like" potential profile in the conduction and valence bands. From Fig. 3.2, it can be seen that the ACQW consists of two well layers of different thicknesses but of the same composition separated by a thin barrier layer.

GaAs/AlGaAs AQW structures have associated with them both bulk GaAs/AlGaAs tensor components:

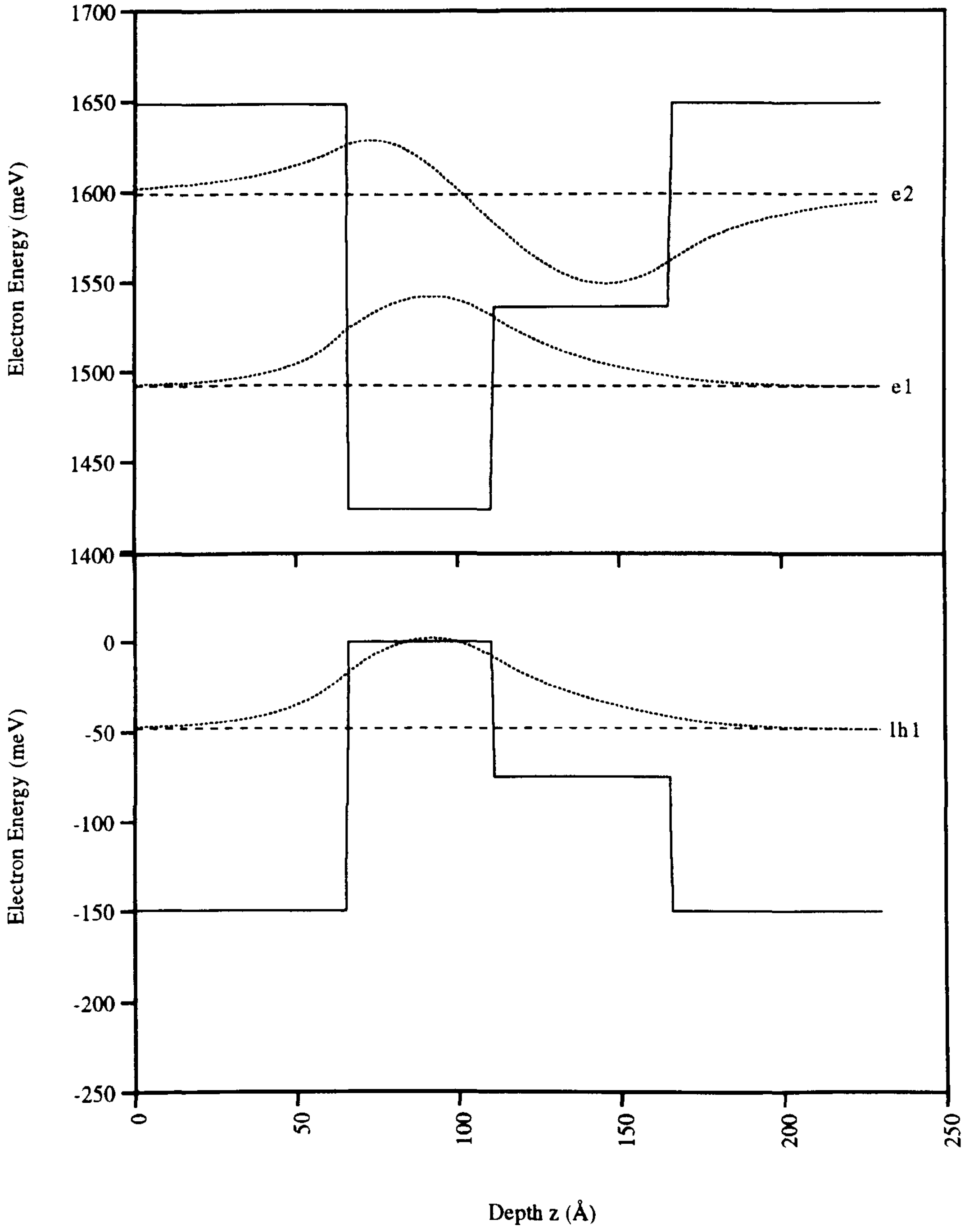

Fig. 3.1 B563 ASQW potential profile, and selected electron and hole envelope functions

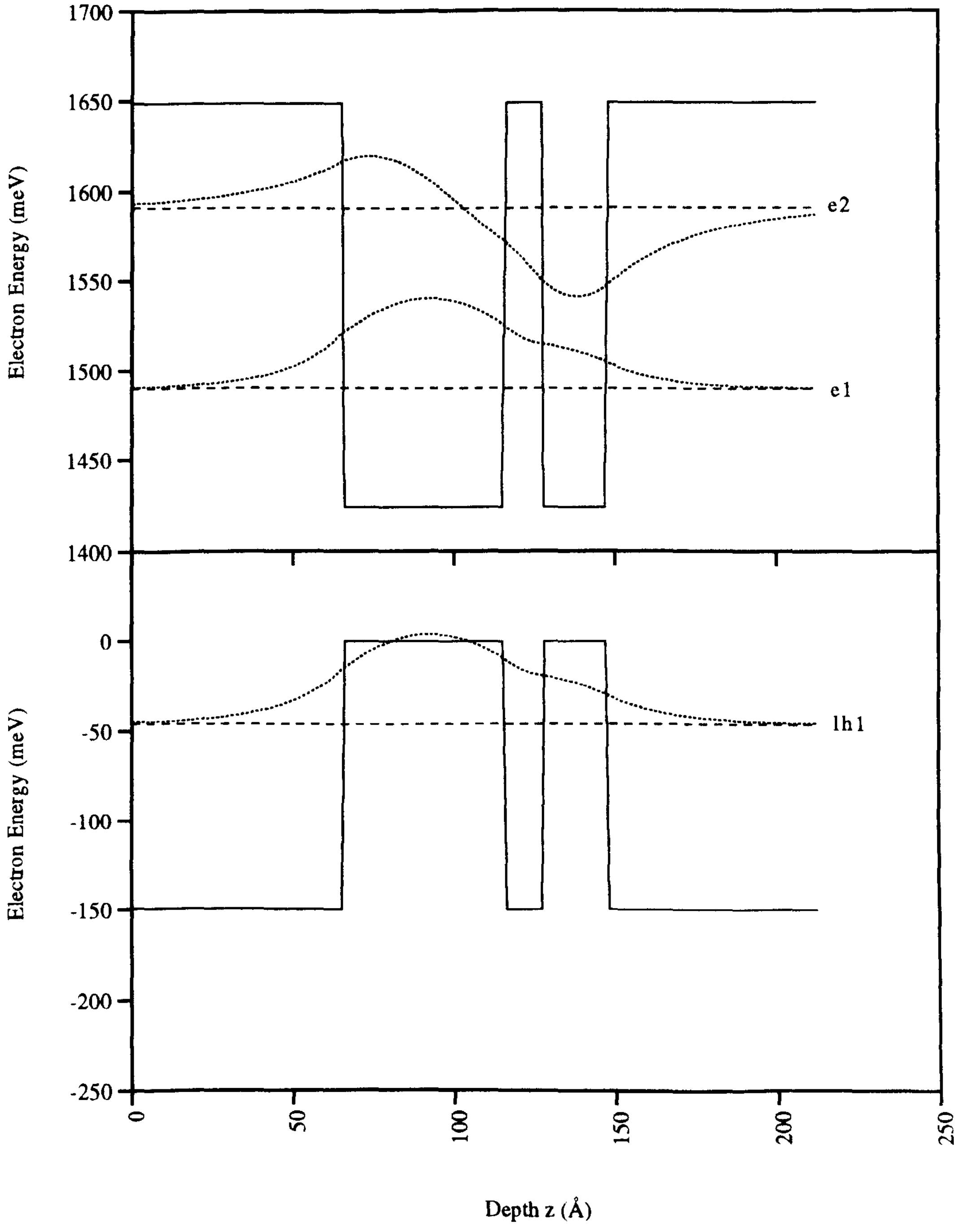

Fig. 3.2 B578 ACQW potential profile, and selected electron and hole envelope functions

$$\chi^{(2)}_{xyz} = \chi^{(2)}_{yxz} = \chi^{(2)}_{zxy} \tag{3.1}$$

and additional tensor components which exist only by virtue of the well asymmetry:

$$\chi^{(2)}_{xzx} = \chi^{(2)}_{yzy} \tag{3.2a}$$

$$\chi^{(2)}_{zxx} = \chi^{(2)}_{zyy} \tag{3.2b}$$

and

$$\chi^{(2)}_{zzz} \tag{3.2c}$$

where the z direction is the direction of growth. The tensor components of (3.2) will be referred to as the AQW tensor components to distinguish them from the bulk GaAs/AlGaAs components of (3.1). The contracted susceptibility tensor for SHG in an AQW waveguide structure is then given by:

$$\mathbf{d} = \begin{bmatrix} 0 & 0 & 0 & d_{14} & d_{15} & 0 \\ 0 & 0 & 0 & d_{15} & d_{14} & 0 \\ d_{31} & d_{31} & d_{33} & 0 & 0 & d_{14} \end{bmatrix} \tag{3.3}$$

The magnitudes of the AQW tensor components has been the subject of much debate in the recent literature. The first calculations were performed by Khurgin [1], who predicted $\left|\chi^{(2)}_{xzx}\right| \approx 3.6$ pm/V for a detuning of 50 meV below the half-band-gap energy of an ACQW structure with GaAs in the well layers and $Al_{0.4}Ga_{0.6}As$ in the barriers. Khurgin later went on to calculate $\left|\chi^{(2)}_{xzx}\right|$ as a function of the various ACQW layer thicknesses, and estimated a maximum $\left|\chi^{(2)}_{xzx}\right|$ value of approximately 12 pm/V at a detuning of 75 meV [2]. This structure had well layer thicknesses of 37.5 Å and 13.5 Å separated by a 7 Å barrier layer. In the same paper, Khurgin also estimated that $\left|\chi^{(2)}_{zxx}\right|$ was much smaller than $\left|\chi^{(2)}_{xzx}\right|$, and that $\left|\chi^{(2)}_{zzz}\right|$ was effectively zero. Harshman and Wang [3] have also reported a calculated value of $\left|\chi^{(2)}_{xzx}\right| \approx 30$

pm/V for a detuning of 50 meV in a deep narrow ASQW structure. This structure had 15Å-thick GaAs and 25Å-thick $Al_{0.3}Ga_{0.7}As$ well layers sandwiched between $Al_{0.85}Ga_{0.15}As$ barriers.

The first measurements of $\left|\chi^{(2)}_{xzx}\right|$ and $\left|\chi^{(2)}_{zxx}\right|$ were performed by Janz *et al.* [4] for an ACQW structure, and Qu *et al.* [5] for an ASQW structure. Janz *et al.* [4] inferred values of $\left|\chi^{(2)}_{xzx}\right| \approx 15$ pm/V and $\left|\chi^{(2)}_{zxx}\right| \approx 13$ pm/V from a complicated set of measurements on an ACQW structure with GaAs well layers and $Al_{0.5}Ga_{0.5}As$ barrier layers. The well layers were 38.5 Å and 13 Å thick, and were separated by 8.8 Å barriers. These results were however obtained at a wavelength corresponding to a photon energy some 130 meV *above* the half-band-gap energy, so that a direct comparison with the predicted results of Khurgin [2] for a very similar structure below half the band-gap is not very meaningful. In fact, Janz *et al.* [4] believed that it was precisely *because* they were operating above the half-bang-gap energy, that they measured comparable $\left|\chi^{(2)}_{zxx}\right|$ and $\left|\chi^{(2)}_{xzx}\right|$ values, rather than values of $\left|\chi^{(2)}_{zxx}\right| << \left|\chi^{(2)}_{xzx}\right|$ as predicted by Khurgin [2]. In a very similar experiment, Qu *et al.* [5] estimated $\left|\chi^{(2)}_{xzx}\right| \approx 13$ pm/V and $\left|\chi^{(2)}_{zxx}\right| \approx 11$ pm/V for ASQW's with 50Å-thick GaAs and 50Å-thick $Al_{0.3}Ga_{0.7}As$ well layers sandwiched between $Al_{0.8}Ga_{0.2}As$ barriers. Again, the comparable $\left|\chi^{(2)}_{xzx}\right|$ and $\left|\chi^{(2)}_{zxx}\right|$ values were attributed to operation at an energy above the 2ω resonance energy.

More recent calculations by Atanasov *et al.* [6] which account for exciton effects and continuum states in a *multiple* ACQW structure, suggest that $\left|\chi^{(2)}_{xzx}\right| \sim 1000$ pm/V for a detuning of 10 - 20 meV below the half-band-gap energy, while a $\left|\chi^{(2)}_{zzz}\right|$ value of ≈ 5 pm/V is predicted for a detuning of 30 - 40 meV. The *multiple* ACQW structure in this case consisted of 22 Å and 28 Å GaAs well layers separated by 22 Å and 38 Å $Al_{0.5}Ga_{0.5}As$ barrier layers. Using a band-structure model which incorporated valence band mixing effects, Kelaidis *et al.* [7] estimated $\left|\chi^{(2)}_{xzx}\right| \sim 200$ pm/V and $\left|\chi^{(2)}_{zzz}\right| \sim 50 - 100$ pm/V. These tensor component values were calculated for a detuning of approximately 50 meV for several different ASQW geometries.

Many papers have also been published on the subject of second order non-linearities in symmetrically-grown biased QW structures. Most notably, Fiore *et al.* [8] considered the influence of continuum states for both 3 nm and 10 nm wide GaAs QWs sandwiched between $Al_{0.4}Ga_{0.6}As$ barriers at energies close to the half-band-gap. They predict that the continuum states above the well contribute to the $\chi^{(2)}_{xzx}$ component under bias and that the QWs do not lead to an enhancement of this non-linearity by more than a few pm/V for detunings of 50 meV. In their conclusions, Fiore *et al.* also argue that the AQW tensor component $\chi^{(2)}_{zzz}$ should be virtually non-existent. Fiore *et al.* later went on to measure the $\left|\chi^{(2)}_{xzx}\right|$ and $\left|\chi^{(2)}_{zxx}\right|$ components in a biased GaAs/$Al_{0.4}Ga_{0.6}As$ MQW structure at a wavelength of 1.66 μm (corresponding to a detuning of 73 meV from the half the band-gap) [9]. Using a control sample which was identical to the MQW sample in every respect except that the MQW layer was replaced with a thick GaAs layer, Fiore *et al.* were able to extract the AQW tensor components $\left|\chi^{(2)}_{xzx}\right| \approx 25$ pm/V and $\left|\chi^{(2)}_{zxx}\right| \approx 0$ pm/V. These measured tensor component values are consistent with Khurgin's original prediction that $\left|\chi^{(2)}_{xzx}\right| >> \left|\chi^{(2)}_{zxx}\right|$ for energies below the 2ω resonance [1].

The most recent predictions of ***multiple*** AQW tensor components below half the band-gap are due to Hutchings and Arnold [10]. They use pseudospin equations for a 3-level system and a bandstructure model with 2 conduction and 5 valence sub-bands, to estimate $\left|\chi^{(2)}_{xzx}\right|$, $\left|\chi^{(2)}_{zxx}\right|$ and $\left|\chi^{(2)}_{zzz}\right|$, as a function of the detuning for the B690 multiple ACQW and B635 multiple ASQW structures which appear in Appendix A. At an operating wavelength of 1.55 μm, which represents detunings of ≈ 70 meV and 90 meV for the B690 and B635 structures respectively, Hutchings and Arnold calculate the multiple AQW tensor components of Table 3.1:

	B690 (ACQW)	B635 (ASQW)
Detuning at 1.55 μm (meV)	70	90
$\left\|\chi^{(2)}_{xzx}\right\|$ (pm/V)	0.01	0.40
$\left\|\chi^{(2)}_{zxx}\right\|$ (pm/V)	0.20	1.0
$\left\|\chi^{(2)}_{zzz}\right\|$ (pm/V)	0.08	0.25

Table 3.1 Approximate multiple AQW tensor component magnitudes at 1.55 μm predicted for the B690 ACQW and B635 ASQW structures by Hutchings and Arnold [10]

Clearly, all of the multiple AQW tensor component magnitudes of Table 3.1 are considerably smaller than those estimated previously in the literature for ***single*** AQWs with different structures but for similar detunings. Furthermore, for a detuning of 1 meV, Hutchings and Arnold estimate the tensor component magnitudes for the B690 and B635 structures listed in Table 3.2. It should be emphasised however, that the B690 and B635 structures were not optimised to maximise the AQW non-linearities, but, were rather designed with several practical constraints in mind (see Chapter 5). A refinement of the AQW structures may therefore yield non-linearities approaching the non-resonant component of bulk GaAs.

It is, in fact, possible to estimate the *relative* magnitude of the $\left|\chi^{(2)}_{zzz}\right|$ component in different AQW structures, within the effective mass approximation. Simple arguments based on the equations in [10] predict that, for a constant detuning, $\left|\chi^{(2)}_{zzz}\right|$ is proportional to the product of 3 momentum matrix elements:

$$\left|\chi^{(2)}_{zzz}\right| \propto \langle \phi_{lh1}(z) | \phi_{e1}(z) \rangle \langle \phi_{e1}(z) | -i\hbar\, d/dz | \phi_{e2}(z) \rangle \langle \phi_{e2}(z) | \phi_{lh1}(z) \rangle \tag{3.4}$$

Here, $\phi_{lh1}(z)$, $\phi_{e1}(z)$, and $\phi_{e2}(z)$, are the first bound light hole, the first bound electron, and the second bound electron envelope functions respectively, which are expressed as functions of the depth z. Within the effective mass approximation, these may be estimated from the solution of the 1D Schrödinger equation in the AQW potential profile of interest (see Chapter 4). The momentum matrix element product of (3.4) then reflects the asymmetry of the envelope functions which, in turn, is caused by the asymmetry of the QW potential. This may be seen from inspection of Figs. 3.1 and 3.2 once again, in which the lh1, e1 and e2 envelope functions are shown for the B563 ASQW and B578 ACQW profiles respectively. From these figures we notice that the envelope functions are indeed asymmetric in that $\langle \phi_{e2}(z) | \phi_{lh1}(z) \rangle \neq 0$. This is in contrast to the case of a symmetric QW, for which $\langle \phi_{e2}(z) | \phi_{lh1}(z) \rangle = 0$ and $\left|\chi^{(2)}_{zzz}\right|$ is correspondingly zero. To demonstrate that the effective mass approximation relation of (3.4) is consistent with the $\left|\chi^{(2)}_{zzz}\right|$ results quoted in Table 3.2, we have calculated $\left|\chi^{(2)}_{zzz}\right|$ asymmetry factors for the B690 and B635 structures. The ratio of the B690 to the B635 asymmetry factors was found to be 0.57, which agrees very well with the ratio of 0.55 calculated using the absolute $\left|\chi^{(2)}_{zzz}\right|$ values listed in Table 3.2.

	B690 (ACQW)	B635 (ASQW)
$\left\|\chi^{(2)}_{xzx}\right\|$ (pm/V)	3.5	0.6
$\left\|\chi^{(2)}_{zxx}\right\|$ (pm/V)	1.0	1.0
$\left\|\chi^{(2)}_{zzz}\right\|$ (pm/V)	0.30	0.55

Table 3.2 Approximate maximum tensor component magnitudes for a 1 meV detuning for the B690 ACQW and B635 ASQW structures as calculated by Hutchings and Arnold [10]

3.2 Full Model for Second Order Non-linear Effects in GaAs/AlGaAs Multiple Asymmetric Quantum Well Waveguides

A full model of the second order non-linear effects in GaAs/AlGaAs AQW waveguides must include interactions between all frequencies (either applied or generated) and all the non-zero tensor components (both bulk and AQW) listed in Section 3.1. Rather than combining all the non-zero tensor components into one effective scalar tensor coefficient which is polarisation-dependent, it is more illuminating to retain the explicit dependence of the polarisation vectors on the separate bulk and AQW tensor coefficients. Assuming that the fundamental and second harmonic field vectors have a negligible component in the direction of propagation (i.e. the weakly guiding approximation), 4 scalar wave equations are then derived which describe the evolution of the fundamental and second harmonic fields in terms of the TE and TM-polarised field components only. This set of scalar coupled wave equations will be referred to as the "full model" for second order non-linear interactions in AQW waveguides.

3.2.1 GaAs/AlGaAs Multiple AQW Ridge Waveguides

For the purposes of introducing the scalar coupled wave equations and the various second order non-linear phenomena which they describe, z-propagating fields were assumed in Chapter 2. In addition, when discussing guided-wave non-linear interactions, the transverse co-ordinate definitions of Fig. 2.12 were adopted. All second order susceptibility tensor components are, however, referenced with respect to the crystallographic axes. When developing the full coupled wave equations for guided-wave interactions, the direction of propagation and the transverse co-ordinate directions are therefore determined by the orientation of the waveguide device with respect to the crystallographic axes. GaAs/AlGaAs layers are normally grown in the [100] direction and cleave along (110) planes, so that the orientation of a GaAs/AlGaAs waveguide device relative to the crystallographic axes may be defined as shown in Fig. 3.3. From this figure it may be seen that TE-polarised light has electric field components in both the x and y crystallographic directions, while TM-polarised light has only one electric field component in the z crystallographic direction.

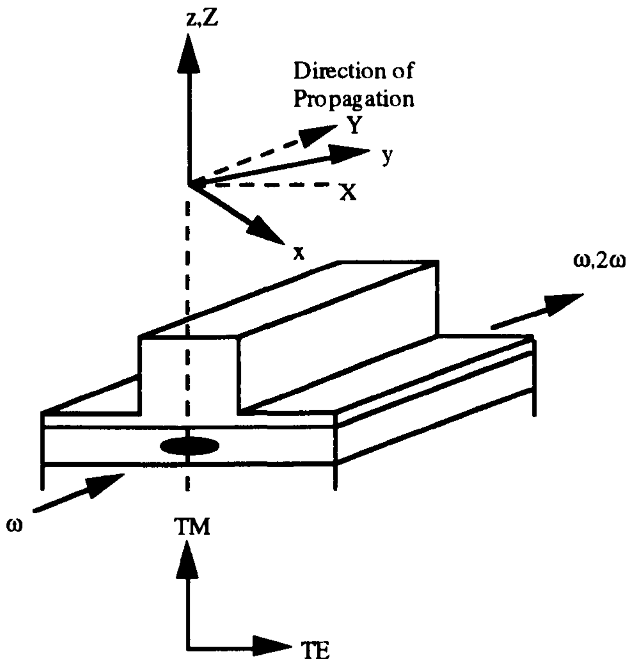

Fig. 3.3 The orientation of a GaAs/AlGaAs waveguide device with respect to the crystallographic axes

3.2.2 The Effective Mode Indices of a Multiple AQW Ridge Waveguide

To calculate the effective mode indices for an MQW ridge waveguide as required for the development of a tensor model, the bulk equivalent refractive index for the MQW guiding layer must first be determined. At photon energies well below the exciton resonance energy, the polarisation-dependent bulk equivalent refractive indices for the MQW guiding layer are given by [11]:

$$n_{TE}^2 = \frac{\sum_i n_i^2 t_i}{\sum_i t_i} \tag{3.5a}$$

$$n_{TM}^2 = \frac{\sum_i t_i}{\sum_i \left(t_i / n_i^2\right)} \tag{3.5b}$$

Here n_i and t_i are the individual quantum well layer refractive indices and thicknesses respectively, and the summations are performed over all layers within one period of the MQW. Having determined a bulk equivalent refractive index for the MQW layer, the effective indices for the MQW waveguide structure can be calculated using the effective index method, or other more sophisticated finite difference methods for the solution of the vector electromagnetic wave equation.

3.2.3 The Coupled Wave Equations for Second Order Non-linear Interactions in GaAs/AlGaAs AQW Waveguides

In this section, the coupled wave equations which govern the evolution of the fields in GaAs/AlGaAs AQW waveguides are introduced. The equations are derived from plane wave considerations and use waveguide mode effective indices. Zero absorption and zero scattering losses are also assumed at both the fundamental and second harmonic frequencies. It should be acknowledged that the model presented here was derived in its original form by N. D. Whitbread.

The four scalar coupled wave equations which describe the evolution of the TE and TM-polarised fundamental and second harmonic fields are given by (see Appendix C):

$$\frac{\partial\left(\hat{E}_{2\omega}\right)_{TE}}{\partial Y}=\frac{i\omega}{\left(n_{2\omega}\right)_{TE}c}\times$$

$$\left[\chi^{(2)}_{xzx}(-2\omega;\omega,\omega)+\chi^{(2)}_{xyz}(-2\omega;\omega,\omega)\right]\left(\hat{E}_{\omega}\right)_{TM}\left(\hat{E}_{\omega}\right)_{TE}\exp\left[i\left(\left(k_{\omega}\right)_{TM}+\left(k_{\omega}\right)_{TE}-\left(k_{2\omega}\right)_{TE}\right)Y\right]$$

(3.6a)

$$\frac{\partial\left(\hat{E}_{2\omega}\right)_{TM}}{\partial Y}=\frac{i\omega}{2\left(n_{2\omega}\right)_{TM}c}\times$$

$$\left\{\left[\chi^{(2)}_{zxx}(-2\omega;\omega,\omega)+\chi^{(2)}_{xyz}(-2\omega;\omega,\omega)\right]\left(\hat{E}_{\omega}\right)^{2}_{TE}\exp\left[i\left(2\left(k_{\omega}\right)_{TE}-\left(k_{2\omega}\right)_{TM}\right)Y\right]\right.$$

$$\left.+\chi^{(2)}_{zzz}(-2\omega;\omega,\omega)\left(\hat{E}_{\omega}\right)^{2}_{TM}\exp\left[i\left(2\left(k_{\omega}\right)_{TM}-\left(k_{2\omega}\right)_{TM}\right)Y\right]\right\}$$

(3.6b)

$$\frac{\partial\left(\hat{E}_{\omega}\right)_{TE}}{\partial Y}=\frac{i\omega}{2\left(n_{\omega}\right)_{TE}c}\times$$

$$\left\{\left[\chi^{(2)}_{zxx}(-2\omega;\omega,\omega)+\chi^{(2)}_{xyz}(-2\omega;\omega,\omega)\right]\left(\hat{E}_{2\omega}\right)_{TM}\left(\hat{E}_{\omega}\right)^{*}_{TE}\exp\left[i\left(\left(k_{2\omega}\right)_{TM}-2\left(k_{\omega}\right)_{TE}\right)Y\right]+\right.$$

$$\left.\left[\chi^{(2)}_{xzx}(-2\omega;\omega,\omega)+\chi^{(2)}_{xyz}(-2\omega;\omega,\omega)\right]\left(\hat{E}_{2\omega}\right)_{TE}\left(\hat{E}_{\omega}\right)^{*}_{TM}\exp\left[i\left(\left(k_{2\omega}\right)_{TE}-\left(k_{\omega}\right)_{TM}-\left(k_{\omega}\right)_{TE}\right)Y\right]\right\}$$

(3.6c)

$$\frac{\partial\left(\hat{E}_{\omega}\right)_{TM}}{\partial Y}=\frac{i\omega}{2\left(n_{\omega}\right)_{TM}c}\times$$

$$\left\{\left[\chi^{(2)}_{xzx}(-2\omega;\omega,\omega)+\chi^{(2)}_{xyz}(-2\omega;\omega,\omega)\right]\left(\hat{E}_{2\omega}\right)_{TE}\left(\hat{E}_{\omega}\right)^{*}_{TE}\exp\left[i\left(\left(k_{2\omega}\right)_{TE}-\left(k_{\omega}\right)_{TE}-\left(k_{\omega}\right)_{TM}\right)Y\right]\right.$$

$$\left.+\chi^{(2)}_{zzz}(-2\omega;\omega,\omega)\left(\hat{E}_{2\omega}\right)_{TM}\left(\hat{E}_{\omega}\right)^{*}_{TM}\exp\left[i\left(\left(k_{2\omega}\right)_{TM}-2\left(k_{\omega}\right)_{TM}\right)Y\right]\right\}$$

(3.6d)

In these equations, Y represents the direction of propagation as indicated in Fig. 3.3. $\left(\hat{E}_{\omega}\right)_{TE}$ and $\left(\hat{E}_{\omega}\right)_{TM}$ are the TE and TM-polarised fundamental field component amplitudes, and $\left(\hat{E}_{2\omega}\right)_{TE}$ and $\left(\hat{E}_{2\omega}\right)_{TM}$ are the second harmonic field component amplitudes. $\left(n_{\omega}\right)_{TE}$ and $\left(n_{\omega}\right)_{TM}$ are the effective TE and TM mode indices at the fundamental frequency and $\left(n_{2\omega}\right)_{TE}$ and $\left(n_{2\omega}\right)_{TM}$ are the effective mode indices at the second harmonic frequency. The different propagation constants are also defined by:

$$\left(k_{\omega}\right)_{TE} = \left(n_{\omega}\right)_{TE} \cdot \frac{2\pi}{\lambda_{\omega}} \tag{3.7a}$$

$$\left(k_{\omega}\right)_{TM} = \left(n_{\omega}\right)_{TM} \cdot \frac{2\pi}{\lambda_{\omega}} \tag{3.7b}$$

$$\left(k_{2\omega}\right)_{TE} = \left(n_{2\omega}\right)_{TE} \cdot \frac{2\pi}{\lambda_{2\omega}} \tag{3.7c}$$

$$\left(k_{2\omega}\right)_{TM} = \left(n_{2\omega}\right)_{TM} \cdot \frac{2\pi}{\lambda_{2\omega}} \tag{3.7d}$$

From inspection of the 4 scalar wave equations of (3.6) we may conclude that:

(i) For an input fundamental field with TE and TM components, a second harmonic field is generated with both TE and TM components

(ii) For a TE-polarised input fundamental field, only TM-polarised second harmonic is generated through the $\left(\chi^{(2)}_{zxx} + \chi^{(2)}_{xyz}\right)$ term of (3.6b). This TM-polarised second harmonic may subsequently mix with the original TE-polarised field through the $\left(\chi^{(2)}_{zxx} + \chi^{(2)}_{xyz}\right)$ term of (3.6c) to produce a TE-polarised fundamental component. Therefore, when pumping with a TE-polarised fundamental field, only TM-polarised second harmonic is generated as a consequence of both the AQW tensor component $\chi^{(2)}_{zxx}$ and the bulk GaAs/AlGaAs tensor component $\chi^{(2)}_{xyz}$.

(iii) For a TM-polarised input fundamental field, only TM-polarised second harmonic is generated, through the $\chi^{(2)}_{zzz}$ term of (3.6b). Subsequently, the TM-polarised second harmonic field may undergo down-conversion through the $\chi^{(2)}_{zzz}$ term of (3.6d) with the production of a TM-polarised fundamental field. Therefore, when pumping with a TM-polarised fundamental field, only TM-polarised second harmonic is generated as a consequence of the AQW tensor component $\chi^{(2)}_{zzz}$ alone.

3.2.4 Evaluation of the Overlap Factors for Second Order Non-linear Effects in GaAs/AlGaAs AQW Ridge Waveguides

The scalar wave equations of the previous section were derived from uniform plane wave considerations and use effective mode indices. In any realistic device, however, it is important to account for any spatial mismatch between the interacting field profiles and the waveguide non-linearities. This requires the use of overlap factors which were introduced in Section 2.6.

When studying second order effects in GaAs/AlGaAs AQW waveguides there are two main polarisation configurations of interest : TM-polarised SHG with a TE-polarised fundamental beam ($TE_{\omega}:TM_{2\omega}$), and TM-polarised SHG with a TM-polarised fundamental beam ($TM_{\omega}:TM_{2\omega}$). Recalling the full model of the previous section, it may be seen that, for the $TE_{\omega}:TM_{2\omega}$ case, the contributing non-linearities are the bulk GaAs/AlGaAs $\chi^{(2)}_{xyz}$ non-linearity and the AQW $\chi^{(2)}_{zxx}$ non-linearity. However, for the structures considered here $\chi^{(2)}_{xyz} >> \chi^{(2)}_{zxx}$ (see Section 3.1), and $\chi^{(2)}_{zxx}$ can be neglected. The conversion efficiency parameter for the $TE_{\omega}:TM_{2\omega}$ case is then given by:

$$\eta = \frac{8\pi^2}{\varepsilon_0 c \lambda^2} \frac{d_{14}^2}{n_{\omega}^2 n_{2\omega}} \times F^{(2)}_{xyz} \tag{3.8a}$$

where

$$F^{(2)}_{xyz} = \left| \int_{-\infty}^{\infty} dX \int_{-\infty}^{\infty} dZ \cdot \xi_{\omega X}^2(X,Z)\xi_{2\omega Z}(X,Z) \right|^2 \tag{3.8b}$$

and the co-ordinates used in expression (3.8b) are defined in Fig. 3.3.

In the TM_{ω}:$TM_{2\omega}$ configuration, the AQW non-linearity $\chi_{zzz}^{(2)}$ is the only contributing non-linearity, and the conversion efficiency parameter is given by:

$$\eta = \frac{8\pi^2}{\varepsilon_0 c\lambda^2} \frac{d_{33}^2}{n_{\omega}^2 n_{2\omega}} \times F_{zzz}^{(2)} \tag{3.9a}$$

where

$$F_{zzz}^{(2)} = \left| \int_{-\infty}^{\infty} dX \int_{MAQW} dZ \cdot \xi_{\omega Z}^2(X,Z)\xi_{2\omega Z}(X,Z) \right|^2 \tag{3.9b}$$

In (3.9b) the integration over Z is only performed over the multiple AQW guiding layer of the waveguide where $\chi_{zzz}^{(2)}$ is non-zero.

Now, it may be recalled from Section 2.6. that the effective area for the non-linear interaction is given by $A_{eff} = 1/F^{(2)}$. It is therefore relatively straightforward to convert the field solutions of the scalar wave equations of (3.6) for the TE_{ω}:$TM_{2\omega}$ and TM_{ω}:$TM_{2\omega}$ configurations into powers for a realistic device using the expressions of (3.8) and (3.9) respectively.

3.3 QW Intermixing for the Suppression of the GaAs/AlGaAs AQW Second Order Non-linearities

Quasi-phase-matching by domain disordering requires that the second order non-linearities of interest are periodically suppressed. The underlying reason for the use of the AQWs is therefore simply that the tensor elements associated with the QW asymmetry $\chi_{xzx}^{(2)}$, $\chi_{zxx}^{(2)}$, and $\chi_{zzz}^{(2)}$ are potentially suppressed by QW intermixing. In addition, the "bulk" tensor elements $\chi_{xyz}^{(2)} \approx \chi_{yxz}^{(2)} \approx \chi_{zxy}^{(2)}$ arising as a consequence of the non-centro-symmetric crystal structure of the GaAs/AlGaAs material in the MQW layers are also potentially reduced by QW intermixing.

At sufficiently high temperatures (see Chapter 6), Ga and Al atoms interdiffuse within the multiple AQW layer, causing the heterointerfaces to become graded so that a smeared or "intermixed" AQW potential profile results. In the limit, when intermixing is complete, the AQW potential profile is completely destroyed and a bulk alloy remains.

Therefore, as intermixing proceeds, the degree of asymmetry of the QW gradually reduces, causing a reduction in the asymmetry of the electron and hole envelope functions which, in turn, gives rise to a reduction in the magnitudes of the AQW non-linearities. To illustrate these arguments, the partially intermixed conduction band and valence band potential profiles are plotted, along with the corresponding e1, e2 and lh1 envelope functions for the B563 and B578 AQW structures in Figs. 3.4 and 3.5 respectively. These compare with the B563 and B578 starting material structures of Figs. 3.1 and 3.2. From these figures it may be seen that the potential profiles do indeed become more symmetric on intermixing. Correspondingly, with respect to the position of the band-gap minimum for the intermixed structures, we see that the e1 and lh1 envelope functions resemble even functions of depth, while the e2 envelope functions resemble odd functions of depth. This means that $\langle \phi_{e2}(z) | \phi_{lh1}(z) \rangle$ is reduced and from (3.2) we would expect $\chi^{(2)}_{zzz}$ to be reduced. Also, because the other AQW tensor components $\chi^{(2)}_{xzx}$ and $\chi^{(2)}_{zxx}$ only exist by virtue of the wavefunction asymmetry, we would expect them to be similarly reduced on intermixing. Furthermore, the AQW non-linear tensor elements $\chi^{(2)}_{xzx}$, $\chi^{(2)}_{zxx}$, and $\chi^{(2)}_{zzz}$ are resonant at the half-bandgap. Therefore, when operating at a sub-half-bandgap photon energy $\hbar\omega$, the bandgap widening which occurs on intermixing means that the detuning of $\hbar\omega$ below the half-bandgap will increase. This effect will tend to further reduce the AQW non-linearities on intermixing.

It should also be emphasised that, like the AQW non-linearities, the "bulk" tensor elements $\chi^{(2)}_{xyz} \approx \chi^{(2)}_{yxz} \approx \chi^{(2)}_{zxy}$ are resonant at the half-bandgap. When operating at sub-half-bandgap energies, these large tensor elements are therefore also potentially reduced on intermixing due to bandgap widening.

In conclusion, we assert that, if the AQW's of Figs. 3.1 and 3.2 are intermixed to completion, $\chi^{(2)}_{zzz}$ and the other AQW non-linearities will be suppressed. In addition, the large "bulk" non-linearities $\chi^{(2)}_{xyz} \approx \chi^{(2)}_{yxz} \approx \chi^{(2)}_{zxy}$ associated with the GaAs/AlGaAs crystal structure are also potentially reduced on intermixing. By periodically intermixing a multiple AQW waveguide along its length, it is therefore possible, in theory, to achieve quasi-phase-matching for the control of guided-wave second order non-linear effects.

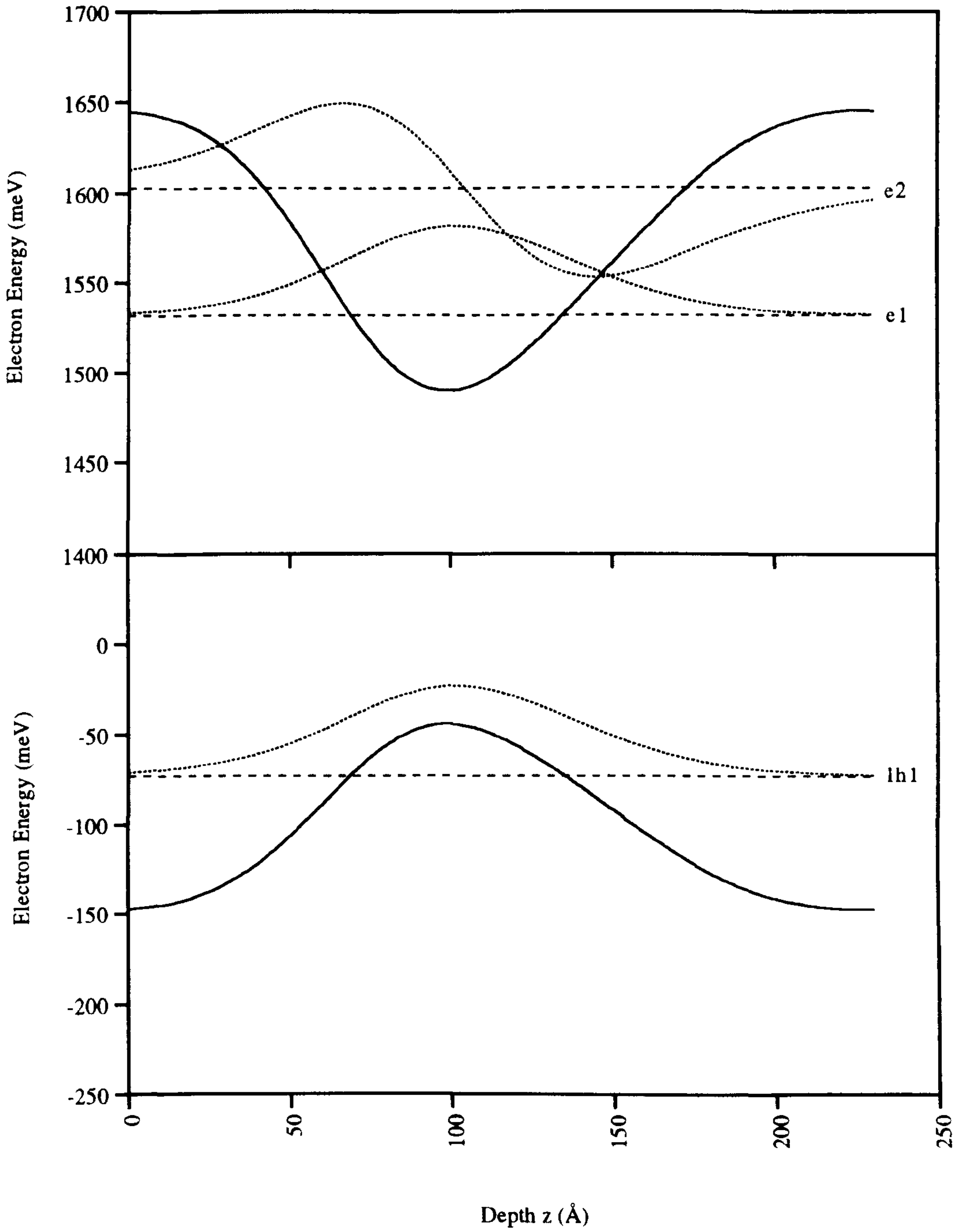

Fig. 3.4 Partially intermixed B563 ASQW potential profile, and selected electron and hole envelope functions

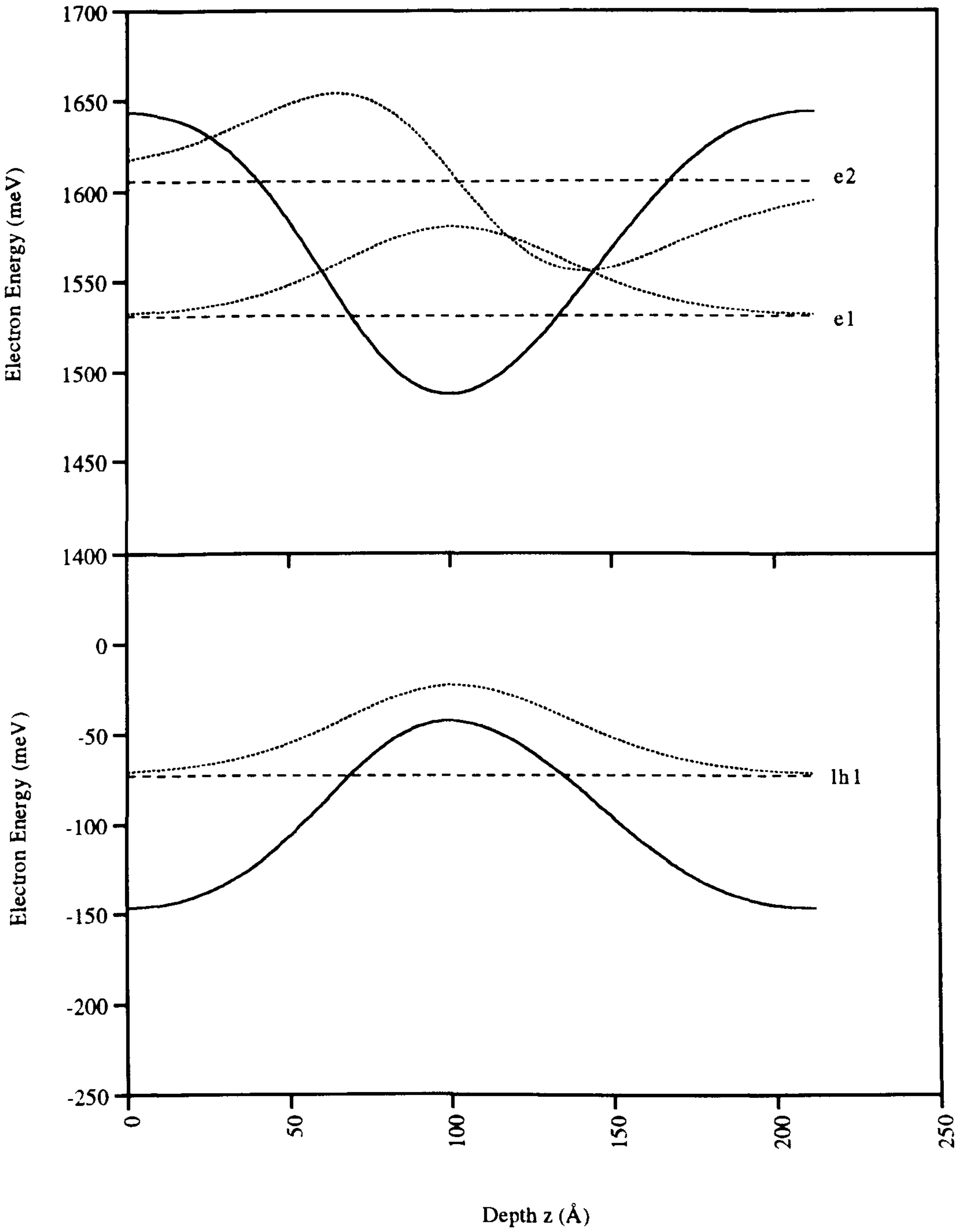

Fig. 3.5 Partially intermixed B578 ACQW potential profile, and selected electron and hole envelope functions

3.4 A GaAs/AlGaAs Multiple AQW Integrated Non-linear Mach-Zehnder All-optical Switch

The original motivation for this project was all-optical switching via the cascaded second order effect in GaAs/AlGaAs multiple AQW waveguide devices. The ultimate objective was, therefore, to realise an integrated non-linear Mach-Zehnder all-optical switch device such as that depicted in Fig. 3.6 for operation at 1.55 μm. Such a device was originally conceived by Assanto *et al.* [12], while Ironside *et al.* [13] later used analytical methods and realistic GaAs/AlGaAs material data to predict the device performance.

For this work, it was proposed that the waveguide arms of the device would be fabricated from regions in which the MQW layer was periodically intermixed to achieve a wavevector mismatch for the production of non-linear phase shifts via the $\chi^{(2)}:\chi^{(2)}$ effect. Such a device may then be described as an intensity-dependent switch: with no high intensity pump present at the input of the device, there are no non-linear phase changes induced in either arm of the device (Φ=0) so that constructive interference occurs at the device output, and the signal beam I_{signal} is transmitted (Fig. 3.6a). In the OFF state however, as depicted in Fig. 3.6b, a high intensity pump beam generates equal but opposite phase shifts of $\pi / 2$ in the arms of the device. This causes destructive interference and extinction of the signal at the output of the device.

The intermixing periods required in the waveguide arms of the device and the corresponding power levels required for switching may be estimated from the results of Section 2.3.4. These calculations will be performed for ridge waveguides fabricated from the B690 ACQW material (see Appendix A) with ribs of width 3 μm and an etch depth of 0.9 μm. In addition, a $TM_{\omega}:TM_{2\omega}$ polarisation configuration will be assumed.

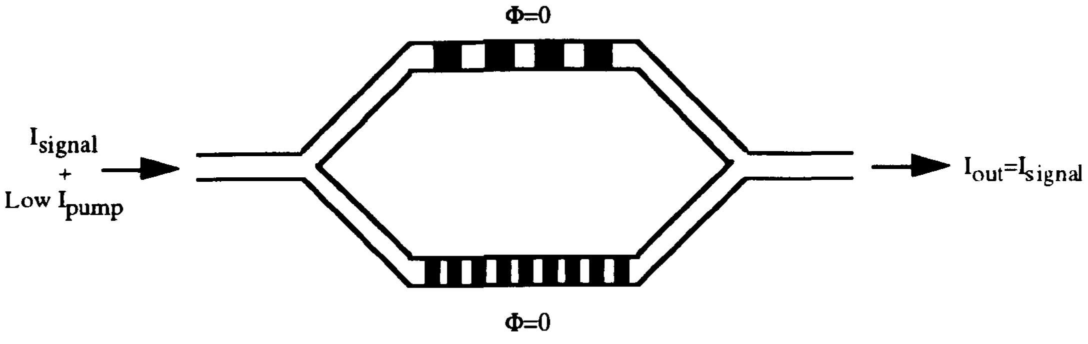

(a) ON state

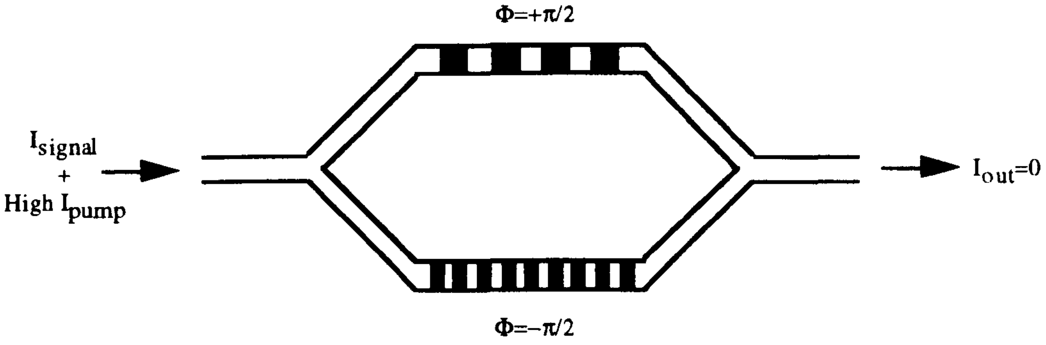

(b) OFF state

Fig. 3.6 A GaAs/AlGaAs multiple AQW integrated non-linear Mach-Zehnder all-optical switch with periodically intermixed waveguide arms for the generation of non-linear phase shifts at high intensities via the cascaded second order effect (a) ON state (b) OFF state

Now, $\pm\pi/2$ phase shifts require $\Delta k_{QPM}L = \pm 2\pi$, which, in turn, requires:

$$\left[\frac{2}{\lambda}\left(n_{2\omega\text{eff}} - n_{\omega\text{eff}}\right) - \frac{1}{\Lambda}\right]L = \pm 1 \tag{3.10}$$

where the relations of (2.58) for first order quasi-phase-matching have been used. L is the device length and Λ is the quasi-phase-matching period in either arm of the device. At 1.55 μm, the $TM_{\omega00}$ mode effective index $n_{\omega\text{eff}}$=3.173982, and, at the second harmonic frequency, the $TM_{2\omega00}$ mode effective index $n_{2\omega\text{eff}}$=3.425296. From (3.10) we then have, for a 1cm-long device, Λ_1 = 3.082841 μm and Λ_2 = 3.084743 μm. Now, $\pm\pi/2$ phase shifts require a scaled fundamental input intensity of $\left|\Psi_\omega(\zeta = 0)\right|^2$=0.64 (see Section 2.3.4), which translates into an absolute input fundamental intensity $I_\omega(z = 0)$ given by:

$$I_\omega(z=0)=\frac{0.64\varepsilon_0 c\lambda^2\cdot n_{\omega\mathrm{eff}}^2\cdot n_{2\omega\mathrm{eff}}}{2d_{\mathrm{QPM}}^2L^2} \tag{3.11}$$

However, expression (3.11), neglects any spatial mismatch between the field mode profiles and the AQW non-linearity. Introducing the overlap factor $F_{zzz}^{(2)}$, as defined by (3.9b) to account for this mismatch, then gives:

$$P_\omega(z=0)=\frac{0.64\varepsilon_0 c\lambda^2\cdot n_{\omega\mathrm{eff}}^2\cdot n_{2\omega\mathrm{eff}}}{2d_{\mathrm{QPM}}^2L^2\cdot F_{zzz}^{(2)}} \tag{3.12}$$

where $P_\omega(z=0)$ is the input fundamental power. For the B690 rib waveguides at 1.55 μm $F_{zzz}^{(2)}$ is approximately 1.456×10^{11} /m² (see Appendix A). For ideal first-order domain disordering, $d_{\mathrm{QPM}} = d_{33}/\pi$, so that for the B690 AQW structure with a predicted $\left|\chi_{zzz}^{(2)}\right|\approx 0.1$ pm/V at 1.55 μm, $d_{\mathrm{QPM}}\approx 0.0159$ pm/V. Then, from (3.12), $P_\omega(z=0)\approx$ 19.1 MW i.e. the switching power requirement in one waveguide arm is 19.1 MW. Therefore, 38.2 MW is required at the input of the device to achieve switching! Clearly, such predicted switching powers are impractical, and the ACQW structure should be optimised for a larger $\left|\chi_{zzz}^{(2)}\right|$.

Another possibility is to operate in a TE_ω:$\mathrm{TM}_{2\omega}$ polarisation configuration and find some way of modulating the large bulk GaAs/AlGaAs $\chi_{xyz}^{(2)}$ non-linearity. In fact, in Chapter 7, it will be shown that QW-intermixing also gives rise to a significant modulation of the large bulk $\chi_{xyz}^{(2)}$ component. Further, it may be recalled that the total non-linearity associated with a multiple AQW waveguide structure in the TE_ω:$\mathrm{TM}_{2\omega}$ configuration is $\chi_{xyz}^{(2)}+\chi_{zxx}^{(2)}$. Hence, if, for an optimised AQW structure, $\chi_{zxx}^{(2)}$ is comparable to $\chi_{xyz}^{(2)}$, the total non-linearity $\chi_{xyz}^{(2)}+\chi_{zxx}^{(2)}$ will be comparable to $2\chi_{xyz}^{(2)}$, and QW-intermixing should result in a significant reduction of this large *total* non-linearity. The first-order quasi-phase-matching efficiency attainable in this way might be comparable to that of first-order ideal domain disordering in bulk GaAs/AlGaAs for which $d_{\mathrm{QPM}} = 60.5$ pm/V.

However, even for $d_{\mathrm{QPM}} = 60.5$ pm/V, the push-pull device geometry of Fig. 3.6 is impractical because the non-linearity modulation periods Λ_1 and Λ_2 required in the different waveguide arms of the device for the TM_ω:$\mathrm{TM}_{2\omega}$ configuration at 1.55 μm, are such that $\Lambda_1-\Lambda_2\approx 2$ nm. Controlling the modulation period with such accuracy is beyond the capabilities of existing e-beam writer technology.

A much more realistic all-optical switch device was proposed by Hutchings *et al.* [14] and is illustrated in Fig. 3.7. This device has only one non-linear waveguide arm in which a phase shift of π must be induced to achieve switching. Hutchings *et al.* [13] further suggested that, for telecommunications applications, an all-optical switch of this type should operate with non-degenerate frequencies ω_1 and ω_2, where ω_1 represents a low-intensity signal beam, and ω_2 is a high-intensity pump or control beam as indicated in Fig. 3.7. Such a device would then operate via the non-degenerate cascaded second order effect which involves the periodic exchange of power between the input fields at ω_1 and ω_2, and the sum frequency field at $\omega_1+\omega_2$, with an accompanying non-linear phase shift in the signal at ω_1. A π phase shift in the non-linear arm of this device when operating in a TE_ω:$TM_{2\omega}$ configuration requires a pump power $P_2(z=0)$ given by [13]:

$$P_2(z=0)=\frac{0.38\varepsilon_0 c\lambda_1^2\cdot n_{1eff}\cdot n_{2eff}\cdot n_{3eff}}{2d_{QPM}^2 L^2\cdot F_{xyz}^{(2)}} \tag{3.13}$$

In (3.13), the subscripts indicate the frequency to which the relevant quantity corresponds. For the same B690 waveguide rib geometry, and choosing $\lambda_1 = 1.55$ μm, the $TE_{\omega 00}$ mode effective index $n_{1eff} = 3.176010$ and $F_{xyz}^{(2)} \approx 1.632\times10^{11}$ /m^2. Furthermore, choosing $n_{2eff} \approx n_{1eff}$ and n_{3eff} to be equal to the $TM_{2\omega 00}$ mode effective index (i.e. $n_{3eff} = 3.425296$), we have for L = 1 cm and $d_{QPM} = 60.5$ pm/V, $P_2(z=0) \approx 700$ mW. Such peak switching power levels are obviously much more realistic. More importantly, these peak power levels are compatible with existing Q-switched laser diode technology.

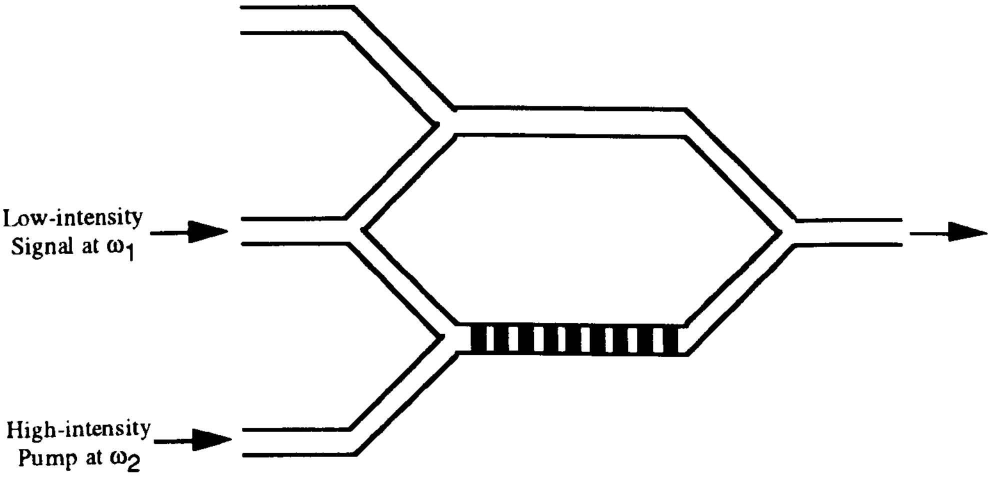

Fig. 3.7 A Mach-Zehnder dual-wavelength all-optical switch as proposed by Hutchings *et al.* [13].

---

[1] J. Khurgin, "Second-order Susceptibility of Asymmetric Coupled Quantum Well Structures ", Appl. Phys. Lett. **51**, 2100 (1987)

[2] J. Khurgin, "Second-order Nonlinear Effects in Asymmetric Quantum-well Structures", Phys. Rev. B **38**, 4056 (1988)

[3] P. J. Harshman and S. Wang, "Asymmetric AlGaAs Quantum Wells for Second-harmonic Generation and Quasi-phase-matching of Visible Light in Surface Emitting Waveguides", Appl. Phys. Lett. **60**, 1277 (1992)

[4] S. Janz, F. Chatenoud, and R. Normandin, "Quasi-phase-matched Second-harmonic Generation from Asymmetric Coupled Quantum Wells", Opt. Lett. **19**, 622 (1994)

[5] X. H. Qu, H. Ruda, S. Janz, and A. J. Springthorpe, "Enhancement of Second Harmonic Generation at 1.06 μm Using a Quasi-phase-matched AlGaAs/GaAs Asymmetric Quantum Well Structure", Appl. Phys. Lett. **65**, 3176 (1994)

[6] R. Atanasov, F. Bassani, and V. M. Agranovich, "Second-order Nonlinear Optical Susceptibility of Asymmetric Quantum Wells", Phys. Rev. B **50**, 7809 (1994)

[7] C. Kelaidis, D. C. Hutchings, and J. M. Arnold, "Asymmetric Two-Step GaAlAs Quantum Well for Cascaded Second-Order Process", J. Quantum Electron. **30**, 2998 (1994)

[8] A. Fiore, E. Rosencher, B. Vinter, D. Weill, and V. Berger, "Second-order Optical Susceptibility of Biased Quantum Wells in the Interband Regime", Phys. Rev. B **51**, 13192 (1995)

[9] A. Fiore, E. Rosencher, V. Berger, and J. Nagle, "Electric Field Induced Interband Second Harmonic Generation in GaAs/AlGaAs Quantum Wells", Appl. Phys. Lett. **67**, 3765 (1995)

[10] D. C. Hutchings and J. M. Arnold, "Determination of Second-order Nonlinear Coefficients in Semiconductors Using Pseudospin Equations for Three-level Systems", Phys. Rev. B (to be published)

[11] R. A. Sammut and I. M. Skinner, "Effective Index Models for MQW Waveguides", Opt. Comms. **76**, 213 (1990)

[12] G. Assanto, G. I. Stegeman, M. Sheik-Bahae, and E. Van Stryland, "All-optical Switching Devices Based on Large Nonlinear Phase Shifts from Second Harmonic Generation", Appl. Phys. Lett. **62** 1323 (1993)

[13] C. N. Ironside, J. S. Aitchison, and J. M. Arnold, "An All-Optical Switch Employing the Cascaded Second-Order Nonlinear Effect", J. Quantum Electron. **29**, 2650 (1993)

[14] D. C. Hutchings, J. S. Aitchison, and C. N. Ironside, "All-optical Switching Based on Nondegenerate Phase Shifts from a Cascaded Second-order Nonlinearity", Opt. Lett. **18**, 793 (1993)

4

The Numerical Solution of the 1D Schrödinger Equation for an Arbitrary GaAs/AlGaAs Quantum Well Structure

The operation of the integrated GaAs/AlGaAs multiple AQW all-optical switch devices described in Section 3.4 relies upon the modification of the QW asymmetry (and therefore of the envelope function asymmetry) by quantum well intermixing. During the design and characterisation of such a device, it is important to be able to predict how the AQW eigenenergies and envelope functions change as intermixing proceeds. In this chapter we will therefore be concerned with the numerical solution of the 1D time-independent Schrödinger equation in an arbitrary GaAs/AlGaAs QW structure before moving on to discuss the solution for the special case of a GaAs/AlGaAs AQW structure. Modelling of the intermixing process itself and the solution of Schrödinger's equation in a partially intermixed GaAs/AlGaAs multiple AQW potential profile, is, however, postponed until Chapter 6. It should also be emphasised at this stage that we will be working within the effective mass approximation throughout, so that the 1D Schrödinger equation may be solved for the electron and hole envelope functions.

Although sophisticated finite element techniques exist for the numerical solution of Schrödinger's equation in an arbitrary potential profile within an arbitrary semiconductor material system [1], we shall only discuss a few simple methods here which are applicable for an arbitrary GaAs/AlGaAs quantum well structure: transfer matrix methods, finite difference methods and shooting methods. Transfer matrix methods [2,3] are based upon two key properties of the Schrödinger equation: in a constant or linear potential profile the envelope functions may be expressed as the sum of exponential or Airy functions respectively. By approximating an arbitrary smoothly-varying profile with piecewise constant or piecewise linear functions (see Fig 4.1) and applying the appropriate boundary conditions, a dispersion relation may then be deduced which involves exponential or Airy functions respectively. Solving this dispersion relation yields the eigenenergies of the arbitrary well system. Obviously, the accuracy of these numerical techniques improves as the number of piecewise segments is increased (and the piecewise segment size is correspondingly decreased), so that the approximate piecewise potential profiles approach the actual continuous profile. To determine the envelope functions from the eigenvalues, it is necessary to calculate all the arbitrary constants of the system (2 for each piecewise constant or piecewise linear section) before "patching" together the envelope function solutions in all the different sections. Clearly, this method becomes cumbersome and inefficient for rapidly varying potential profiles which can require up to several hundred piecewise segments to guarantee that the approximate piecewise QW profile resembles the true QW profile to a high enough degree of accuracy.

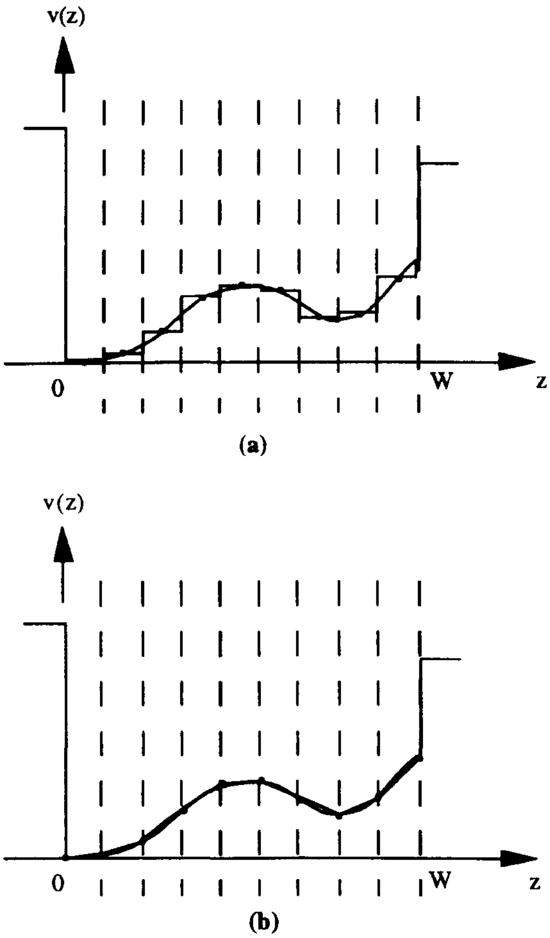

Fig. 4.1 Arbitrary QW potential profile **(a)** piecewise constant approximation (potential and effective mass values within each strip are defined by the corresponding values at the strip mid-points) **(b)** piecewise linear approximation (the potential and the effective mass within each strip are linear functions of depth)

Finite difference methods for an arbitrary GaAs/AlGaAs potential profile, in contrast, involve an initial estimate of the envelope function that is to be determined. This trial envelope function is successively amended using a finite difference formula which approximates the 1D Schrödinger equation until the trial envelope function converges to an actual envelope function solution. The corresponding eigenenergy is then straightforwardly obtained by substitution of the envelope function solution into the finite difference version of the 1D Schrödinger equation. From the foregoing description however, it is obvious that an efficient finite difference solution depends on a good initial trial envelope function which will result in convergence to the actual desired envelope function. Alternatively, shooting methods have no convergence control problems and may be employed to calculate all the eigenenergies and the envelope functions directly in increasing order i.e. from the fundamental order up to the highest bound order. Davé for example, outlines a shooting method which involves the repeated numerical integration of Schrödinger's equation across an arbitrary piecewise linear potential profile until the boundary conditions are satisfied at the 2 well/barrier interfaces [4]. There are however, several problems with Davé's original algorithm which shall be highlighted in the following sections, where the algorithms used in this work for the solution of the 1D Schrödinger equation in an arbitrary GaAs/AlGaAs QW potential profile are described.

4.1 The 1D Schrödinger Equation in an Arbitrary GaAs/AlGaAs QW Potential Profile

Any numerical technique for the solution of Schrödinger's equation in an arbitrary potential profile, involves the evaluation of the envelope functions at discrete positions $z = i \times \Delta z$ $(i = 0, 1, 2, \ldots N)$ as indicated in Fig. 4.2 which represents an arbitrary conduction band potential profile v as a function of the depth z.

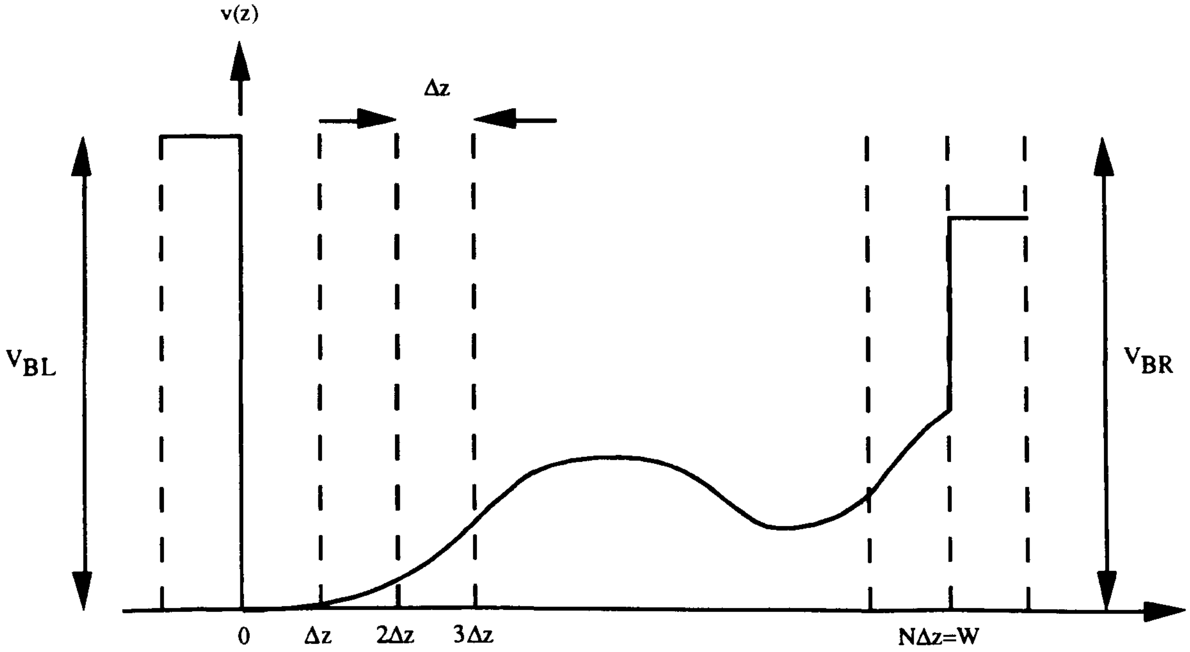

Fig. 4.2 Arbitrary QW potential profile (dashed lines indicate positions where envelope function is evaluated)

Within the effective mass approximation, the eigenenergies E and the envelope functions u(z) of the bound electrons in such an arbitrary well profile are given by the solution of the 1D Schrödinger equation:

$$\frac{-\hbar^2}{2}\frac{d}{dz}\left(\frac{1}{m^*(z)}\frac{du(z)}{dz}\right)+v(z)u(z)=Eu(z) \tag{4.1}$$

where $m^*(z)$ is the depth-dependent effective mass of electrons in the well profile and is assumed to be independent of energy. (Bound light hole and heavy hole energies and the corresponding envelope functions are similarly determined from the solution of (4.1) using a valence band potential profile $v(z)$ and the appropriate light or heavy hole effective mass $m^*(z)$.) It should be noted that equation (4.1) implicitly assumes that the well known boundary conditions for probability current conservation at any GaAs/AlGaAs heterointerface are satisfied:

$$u_L(z_i)=u_R(z_i) \tag{4.2a}$$

$$\frac{1}{m_L^*(z_i)}u_L'(z_i)=\frac{1}{m_R^*(z_i)}u_R'(z_i) \tag{4.2b}$$

where $u'(z)=du(z)/dz$. L subscripts indicate that the relevant quantities refer to the region to the left of the interface at position $z_i=i\times\Delta z$, while the R subscripts indicate that the quantities refer to the region to the right hand side of the interface. In other words, the envelope function $u(z)$ and the probability current $u'(z)/m^*(z)$ are continuous quantities.

Alternatively, we can approximate our arbitrary continuous potential profile with a piecewise constant potential profile (see Fig. 4.1a). $v(z)$ and $m^*(z)$ are then constant *within a given piecewise segment* so that $u(z)$ and $u'(z)$ are correspondingly continuous *within a given piecewise segment* and (4.1) becomes:

$$\frac{-\hbar^2}{2M^*}\frac{d^2u(z)}{dz^2}+Vu(z)=Eu(z) \tag{4.3}$$

where we have written $m^*(z)=M^*$ and $v(z)=V$ to emphasise that these quantities are constant. At the heterointerfaces between segments however, the boundary conditions of (4.2) apply and $u'(z)$ is discontinuous as illustrated in Fig. 4.3. Equation (4.3) is identical to the equation used by Davé who then proceeded to (incorrectly) assume piecewise linear functions $m^*(z)$ and $v(z)$. Under these circumstances (4.3) is not Hermitian and we must employ (4.1) instead. Although approximating a continuous potential profile with a piecewise constant function introduces errors, we will continue to develop a piecewise constant model in addition to a continuous potential model. This is because, for the piecewise constant model, the way in which we define the potential and the effective mass within each strip to be equal to the corresponding values at the strip mid-points while evaluating the envelope function at the strip interfaces, can have important consequences for the solution of Schrödinger's equation in AQWs as discussed later in Section 4.4.

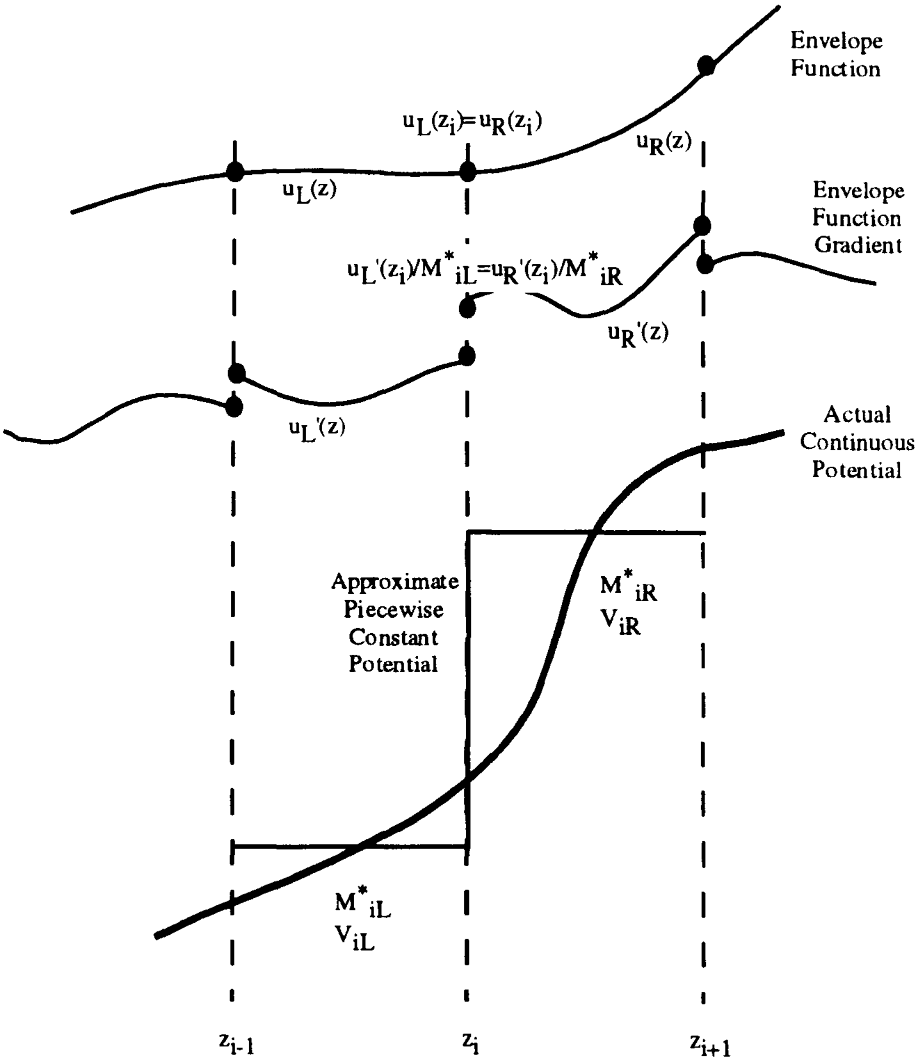

Fig. 4.3 The boundary conditions of (4.2) at the heterointerface between segments in the piecewise constant approximation. M^*_{iL} and V_{iL} are the effective mass and the potential within the strip to the left of the interface at z_i while M^*_{iR} and V_{iR} are the corresponding quantities in the strip on the right hand side of the interface. The black dots represent discrete values of $u(z)$ and $u'(z)$ at the heterointerfaces

For both the continuous potential model and the piecewise constant potential model, constant potential barriers of height V_{BL} to the left of the arbitrary well and V_{BR} to the right of the well are assumed along with effective masses M^*_{BL} and M^*_{BR} respectively, as shown in Fig. 4.2. Exponentially-decaying envelope function solutions $u_{BL}(z)$ and $u_{BR}(z)$ may then be assumed in the left and right semi-infinite barrier layers respectively, and the complete envelope function $u(z)$ may be expressed in 3 parts:

$$u(z) = \begin{cases} u_{BL}(z) = Ae^{\alpha z} & z \le 0 \\ u_W(z) & 0 \le z \le W \\ u_{BR}(z) = Be^{-\beta z} & z \ge W \end{cases} \tag{4.4a}$$

where

$$\alpha = \sqrt{\frac{2M^*_{BL}(V_{BL} - E)}{\hbar^2}} \tag{4.4b}$$

and

$$\beta = \sqrt{\frac{2M^*_{BR}(V_{BR} - E)}{\hbar^2}} \tag{4.4c}$$

and $u_W(z)$ is that portion of the envelope function in the well region $0 \le z \le W$ which we wish to evaluate at discrete intervals through integration of Schrödinger's equation using corresponding discrete values of $v(z)$ and $m^*(z)$. We now consider the shooting method algorithms for the solution of Schrödinger's equation in an arbitrary continuous potential and an arbitrary piecewise constant potential in turn.

4.2 The Shooting Method Algorithm in a Continuous GaAs/AlGaAs Potential Profile

Defining the probability current by:

$$c(z) = \frac{1}{m^*(z)} \frac{du(z)}{dz} \tag{4.5}$$

we may write

$$\frac{du(z)}{dz} = m^*(z)c(z) \tag{4.6a}$$

and from (4.1)

$$\frac{dc(z)}{dz} = g(z)u(z) \tag{4.6b}$$

where

$$g(z) = \frac{2}{\hbar^2}[v(z) - E] \tag{4.6c}$$

i.e. we have decomposed the second order differential equation of (4.1) into the 2 first order coupled differential equations of (4.6). The definition of $c(z)$ in (4.5) is also significant because the boundary condition of (4.2b) which is implicitly assumed in (4.1) means that $c(z)$ defined in this way will be continuous. From knowledge of $u(z)$ and $c(z)$ at some position z therefore, the fourth-order Runge-Kutta numerical integration algorithm may be used to evaluate $u(z+\Delta z)$ and $c(z+\Delta z)$ from (4.6) where Δz is the depth increment.

The shooting method algorithm for the continuous potential profile case may therefore be summarised in five basic steps:

(i) A trial eigenenergy is chosen in the vicinity of the actual eigenenergy of interest

(ii) An arbitrary value is chosen for the constant A of (4.4), and the corresponding envelope function value $u_W(0)$ and the current $c_W(0)$ at the left hand barrier are calculated from consideration of the boundary conditions of (4.2):

$$u_W(0) = A \qquad (4.7a)$$

$$c_W(0) = \frac{\alpha A}{M^*_{BL}} \qquad (4.7b)$$

(iii) Schrödinger's equation is integrated across the well using the fourth-order Runge-Kutta algorithm as outlined above until we arrive at the right hand barrier.

(iv) In general, the boundary conditions of (4.2) are not satisfied at the right hand barrier and a new trial eigenenergy must be chosen in such a way as to reduce the "mismatch" of these boundary conditions.

(v) When the boundary condition mismatch at the right hand barrier is small enough, the trial eigenvalue is approximately equal to the actual eigenvalue and we may consider the corresponding trial envelope function to be equal to the actual envelope function.

The question now naturally arises as to which definition of the right hand barrier boundary condition mismatch should be used. From consideration of (4.4) and the boundary condition of (4.2a) at the right hand barrier we get:

$$u_W(W) = u_{BR}(W) \qquad (4.8)$$

Furthermore, applying the boundary condition of (4.2b) at the right hand barrier and using (4.8) gives:

$$c_W(W) = -\frac{\beta}{M^*_{BR}} u_W(W) \qquad (4.9)$$

Which, upon re-arrangement yields:

$$\beta = -M^*_{BR} \frac{c_W(W)}{u_W(W)} \tag{4.10}$$

where $u_W(W)$ and $c_W(W)$ are obtained by numerical integration of equations (4.6) across the well. We therefore have two independent expressions for β: (4.4c) and (4.10) which must be equal before all the boundary conditions are satisfied and a bound solution is found. It is the difference between these two β values (call it $\Delta\beta$ say) which Davé advocates for the definition of the boundary condition mismatch which must be reduced to zero for a solution by choosing successively better trial eigenenergy values E. However, defining the mismatch in this way can have serious consequences for the search algorithm used to "home-in" on the correct eigenvalue solution because, for certain trial eigenenergies E, $u_W(W)$ will be zero, and a singularity will occur in the mismatch function $\Delta\beta(E)$. It is possible, however, to define a superior boundary condition mismatch as a function of E by dividing the boundary conditions of (4.2) as applied to the right hand barrier:

$$\frac{c_W(W)}{u_W(W)} = \frac{c_{BR}(W)}{u_{BR}(W)} \tag{4.11}$$

Upon re-arrangement this becomes:

$$c_W(W) - u_W(W)\frac{c_{BR}(W)}{u_{BR}(W)} = 0 \tag{4.12}$$

Now, from consideration of (4.4) in the right hand barrier we may deduce:

$$\frac{c_{BR}(W)}{u_{BR}(W)} = -\frac{\beta}{M^*_{BR}} \tag{4.13}$$

and substituting this expression into (4.12) gives:

$$c_W(W) + \frac{\beta}{M_{BR}^*} u_W(W) = 0 \tag{4.14}$$

From (4.14) we may therefore define a new mismatch function:

$$\text{Mismatch}(E) = c_W(W) + \frac{\beta}{M_{BR}^*} u_W(W) \tag{4.15}$$

where β is defined by (4.4c). Hence, by choosing estimates for E which continually reduce $\text{Mismatch}(E)$ defined in this way, we will eventually obtain $\text{Mismatch}(E) = 0$ and equation (4.14) will be satisfied. From the definition of $\text{Mismatch}(E)$ of (4.15), it may also be seen that neither of the quantities $u_W(W)$ or $c_W(W)$ which are obtained by integrating across the well appear in a denominator term. $\text{Mismatch}(E)$ is therefore a continuous function and as such, represents a suitable goal function for any search algorithm. However, (4.14) was derived by matching the *ratio* of the boundary conditions of (4.2) at the right hand barrier. Therefore, on reducing Mismatch(E) to zero, it is still necessary to match $u_W(W) = u_{BR}(W)$ to ensure that both boundary conditions of (4.2) are simultaneously satisfied at the right hand barrier. This is easily achieved by defining:

$$B = u_W(W)e^{\beta W} \tag{4.16}$$

which can be seen from consideration of (4.4) once again. Hence, having reduced $\text{Mismatch}(E)$ as defined by (4.15) to zero so that E is equal to the actual eigenenergy of interest, the envelope function is completely determined: with reference to (4.4a), $u_{BL}(z)$ is determined from our arbitrarily assumed value of A and from α as calculated from (4.4b), $u_W(W)$ is the envelope function obtained by integrating Schrödinger's equation across the well when E is equal to the eigenenergy and $\text{Mismatch}(E) = 0$, and $u_{BR}(z)$ is completely determined from B and β as calculated from (4.16) and (4.4c) respectively.

Finally, in order to determine all the bound eigenenergies and the corresponding envelope functions within a given well profile (for the particle of interest), we need to say something about the search algorithm employed. To find all the bound solutions, a trial eigenenergy E is normally chosen which is equal to the minimum potential in the well and E is incremented in small steps until an interval (E_1, E_2) containing a solution is identified (i.e. $\text{Mismatch}(E_1) \cdot \text{Mismatch}(E_2) < 0$). A bisection search routine may then be executed to "home-in" on the solution by choosing successively better E values which reduce the goal function Mismatch(E) to zero. On locating the solution, E may be incremented further in search of a second bound level. Having found a second bound level the search may be continued for a third bound level and so on. Clearly however, if E is incremented until it exceeds the lower of the 2 barrier potentials V_{BL} or V_{BR} without identifying a third solution interval, we must conclude that a third bound level does not exist and that there are only 2 bound levels.

4.3 The Shooting Method Algorithm in a GaAs/AlGaAs Approximate Piecewise Constant Potential Profile

Proceeding in a similar fashion to the continuous potential profile case of the previous section we may define:

$$\frac{du(z)}{dz} = t(z) \tag{4.17a}$$

and from (4.3) we get:

$$\frac{dt(z)}{dz} = f(z)u(z) \tag{4.17b}$$

where

$$f(z) = \frac{2M^*}{\hbar^2}[V - E] \tag{4.17c}$$

and M^* and V are the (constant) effective mass and potential respectively. The original second order differential equation of (4.3) has therefore been decomposed into the 2 coupled first order differential equations of (4.17a) and (4.17b). However, equations (4.17) only apply within a given piecewise element, and t(z) is not continuous at a heterointerface between elements. Having integrated equations (4.17) across an element in discrete steps Δz using the fourth-order Runge-Kutta method therefore, it is necessary to exit from the Runge-Kutta routine and explicitly enforce the boundary condition of (4.2b) at the heterointerface as will be clear from inspection of Fig. 4.3. Integration may then be continued across the next element until the next heterointerface is reached and the boundary condition of (4.2b) must be applied once again

Having implemented such an integration scheme, the shooting method algorithm for the piecewise constant potential case is very similar to that outlined in Section 4.2 for the continuous potential profile case. However, for the piecewise constant algorithm, the boundary conditions at the left-hand barrier must be re-defined:

$$u_W(0) = A \tag{4.18a}$$

and

$$t_W(0) = \frac{M^*_{R0}}{M^*_{BL}} \alpha A \tag{4.18b}$$

Also, the right-hand barrier boundary condition mismatch function is a slightly modified version of (4.15):

$$\text{Mismatch}(E) = \frac{t_W(W)}{M^*_{LN}} + \frac{\beta}{M^*_{BR}} u_W(W) \tag{4.19}$$

And finally, for continuity of the envelope function at the right-hand barrier, B is just defined as before by (4.16):

$$B = u_W(W) e^{\beta W} \tag{4.16}$$

4.4 The Solution of Schrödinger's Equation in a GaAs/AlGaAs Asymmetric QW

For GaAs/AlGaAs asymmetric QWs such as those depicted in Figs. 3.1 and 3.2, discontinuities exist in the Al fraction (and therefore in the potential and the effective mass) at the heterointerfaces within the well: for an ASQW there is only one such interface, while for an ACQW there are two. Now, within the continuous potential profile model of Section 4.2, such discontinuities cannot be represented in an unambiguous way, as shall be explained for the case of an ASQW with the aid of Fig. 4.4. It may be seen that an ASQW with a lower Al fraction layer of width W_1 is represented by a series of discrete Al fraction values at the strip interface positions. For the continuous potential model these strip interface positions are also the positions where we evaluate the envelope function values. At the discontinuity position $z=W_1$ however, it may be seen that the Al fraction can either be defined as AlW_1 or AlW_2. For the former definition of the Al fraction (Fig. 4.4a) the shooting algorithm "sees" a lower Al fraction layer of width $>W_1$, while for the latter definition (Fig. 4.4b) the algorithm "sees" a lower Al fraction layer of width $<W_1$. Intuitively the true eigenvalues of an ASQW with an abrupt interface and a lower Al fraction layer of width exactly equal to W_1 will lie between the eigenvalues corresponding to the Al fraction profiles of Figs. 4.4a and 4.4b. In the limit, therefore, as the number of strips increases to infinity and the strip width Δz reduces towards zero, we would expect this ambiguity in the definition of the Al fraction at the discontinuity to disappear. To deduce just how many strips N are required to reduce the error associated with the well profiles of Fig. 4.4 to a tolerable level however, we must look to the piecewise constant model which is exact for the step-like potential profile of an ASQW, and for which there is no ambiguity in the definition of W_1. Using conduction band potential and electron effective mass data from Adachi's review paper [5], the first bound electron energies for the ASQW structure of material B563 (see Appendix A) corresponding to the Al fraction definitions depicted in Figs. 4.4a and 4.4b were found to be 68.043 meV and 68.726 meV above the conduction band edge of GaAs respectively. These energies were calculated by evaluating the envelope functions every 0.5Å (i.e. Δz = 0.5 Å and the number of strips N=200) and compare with an exact first bound electron energy of 68.156 meV above the conduction band edge of GaAs as determined using the piecewise constant model for the same Δz = 0.5Å. We therefore see that the error associated with the ambiguity in the definition of the Al fraction for the continuous potential model is less than 1 meV for the B563 structure when Δz = 0.5Å. Furthermore, none of the B563 interband transition wavelengths for either of the two cases of Fig 4.4 differ from the exact transition wavelengths calculated from the piecewise constant model by more than 1 nm and many of the transition wavelengths differ by less than 0.1 nm when Δz = 0.5Å. We therefore conclude that the errors associated with the Al fraction definition ambiguity for the B563 ASQW structure using the continuous model are insignificant for $\Delta z \leq$ 0.5Å.

In general however, especially for deep narrow well regions, the errors associated with the definition of the Al fraction for the continuous potential model may be appreciable, so that the piecewise constant model is used to solve Schrödinger's equation in the GaAs/AlGaAs ASQW and ACQW starting material profiles in all subsequent chapters.

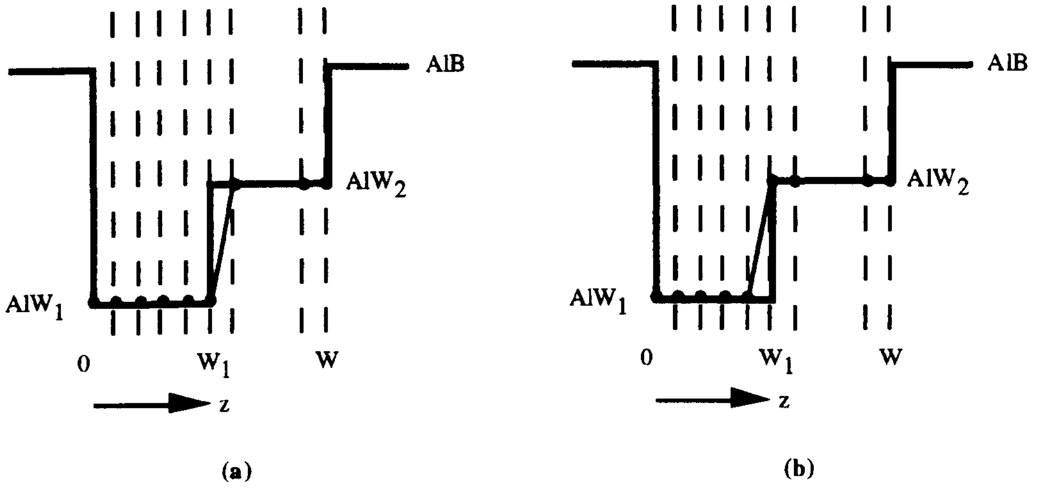

Fig. 4.4 Discrete representation of an asymmetric stepped QW Al fraction profile (a) Al fraction at $z=W_1$ defined equal to AlW$_1$ (b) Al fraction at $z=W_1$ defined equal to AlW$_2$.

On a final note, it should be stressed that for any continuous potential profile and, in particular, for a partially intermixed potential profile, the piecewise constant model is only approximate, and we would expect the continuous model to be more accurate than the piecewise constant model. However, the discrete Al fraction profiles derived from intermixing the starting material Al fraction profiles of Fig. 4.4 will be slightly different leading to ambiguity in the eigenenergies and envelope functions of intermixed QW structures. The piecewise constant model is therefore used throughout for the consistent and unambiguous solution of Schrödinger's equation in all GaAs/AlGaAs starting material *and* intermixed AQW potential profiles appearing in subsequent chapters. The accuracy of the piecewise constant model results are then improved by simply increasing the number of piecewise segments which is used to describe the Al fraction profile of interest.

4.5 The Calculation of Interband Transition Wavelengths and Oscillator Strengths for QW Structures

Having calculated the bound electron and hole levels and the corresponding envelope functions in a QW potential, the interband transition wavelengths λ, are given by:

$$\lambda = \frac{hc}{q\left[e_i + h_j + E_g(\text{GaAs})\right]} \tag{4.17}$$

In expression (4.17), h is Planck's constant, c is the speed of light in a vacuum, q is the electronic charge, e_i is the energy of the i th bound electron level above the conduction band edge of GaAs in eV, h_j is the energy of the j th bound hole energy below the valence band edge of GaAs in eV, and $E_g(\mathrm{GaAs})$ is the band-gap of GaAs in eV.

The *relative* interband oscillator strengths $f_{e,lh}$ and $f_{e,hh}$ for electron to light hole, and electron to heavy hole interband transitions respectively, can be expressed in arbitrary units by (4.18) [6]:

$$f_{e,lh} = \begin{cases} \frac{2}{3}\left|\langle \phi_e(z) | \phi_{lh}(z) \rangle\right|^2 & \text{Polarisation} \perp \text{to layers} \\ \frac{1}{6}\left|\langle \phi_e(z) | \phi_{lh}(z) \rangle\right|^2 & \text{Polarisation} \parallel \text{to layers} \end{cases} \tag{4.18a}$$

$$f_{e,hh} = \begin{cases} 0 & \text{Polarisation} \perp \text{to layers} \\ \frac{1}{2}\left|\langle \phi_e(z) | \phi_{hh}(z) \rangle\right|^2 & \text{Polarisation} \parallel \text{to layers} \end{cases} \tag{4.18b}$$

In the expressions of (4.18), $\phi_e(z)$ and $\phi_h(z)$ are the normalised electron and hole envelope functions given by:

$$\phi_{e,h}(z) = \frac{u_{e,h}(z)}{\left[\int_{-\infty}^{\infty} u_{e,h}^2(z)dz\right]^{1/2}} \tag{4.19}$$

where $u_{e,h}(z)$ are the electron and hole envelope functions calculated using the Schrödinger solver routine described in the previous sections of this chapter.

The interband transition wavelengths and oscillator strengths quoted for the different AQW structures appearing in all subsequent chapters were calculated using (4.17) and (4.18) respectively. Effective mass and bandgap data from Adachi's review paper [5] were used throughout.

---

[1] K. Nakamura, A. Shimizu, M. Koshiba, and K. Hayata, "Finite-Element Analysis of Quantum Wells of Arbitrary Semiconductors with Arbitrary Potential Profiles", J. Quantum Electron. **25**, 889 (1989)

[2] W. W. Lui and M. Fukuma, "Exact Solution of the Schrödinger Equation Across an Arbitrary One-dimensional Piecewise-linear Potential Barrier", J. Appl. Phys. **60**, 1555 (1986)

[3] Y. Ando and T. Itoh, "Calculation of Transmission Tunneling Current Across Arbitrary Potential Barriers", J. Appl. Phys. **61**, 1497 (1987)

[4] D. P. Davé, "Numerical Technique to Calculate Eigenenergies and Eigenstates of Quantum-wells with Arbitrary Potential Profile", Electron. Lett. **27**, 1735 (1991)

[5] S. Adachi, "GaAs, AlAs and $Al_xGa_{1-x}As$: Material Parameters for Use in Research and Device Applications", J. Appl. Phys. **58**, R1 (1985)

[6] C. Kelaidis, D. C. Hutchings, and J. M. Arnold, "Asymmetric Two-Step GaAlAs Quantum Well for Cascaded Second-Order Processes", Transactions on Quantum Electron. **30**, 2998, (1994)

5

The Design and Characterisation of GaAs/AlGaAs Multiple AQW Waveguide Structures

Considerable effort was invested in the design and characterisation of the various multiple AQW waveguide structures grown for this work, primarily because no SHG attributable to any of the AQW tensor components was observed in waveguides fabricated from the multiple ASQW QT613 material (see Chapter 7). To determine the reason for the absence of the AQW non-linearities in this structure, it was necessary to examine the linear optical properties. In the wake of the characterisation of the QT613 material, it was apparent that the growth of such multiple AQW structures was relatively demanding and subsequent multiple AQW designs were therefore amended to be tolerant to growth inaccuracies. All structures grown subsequent to the QT613 material were also characterised using X-ray diffraction, photoluminescence spectroscopy, and absorption spectroscopy, prior to fabrication of waveguide devices for the study of second order non-linear optical effects.

Detailed nominal structures of all the AQW materials investigated in this work are listed in Appendix A. Also listed are the corresponding interband transition wavelengths and normalised oscillator strengths at both 77 K and room temperature. These were calculated from the numerical solution of Schrödinger's equation in the effective mass approximation using energy-independent electron and hole effective mass data from Adachi's review paper [1] (see Chapter 4).

5.1 The Design of GaAs/AlGaAs Multiple AQW Structures

5.1.1 General GaAs/AlGaAs Multiple AQW Design Criteria

Any practical GaAs/AlGaAs AQW design should take into account growth inaccuracies in the Al fractions and thicknesses of the various QW layers. Current GaAs/AlGaAs MBE and MOCVD growth technology is sufficiently advanced to allow control of the Al fraction in a particular layer to within ±10% of the nominal value, while individual layer thicknesses can often be controlled to within one or two monolayers. It is with these tolerances in mind that the general design criteria for GaAs/AlGaAs multiple AQWs will be discussed.

For an all-optical switch device such as that described in Section 3.4 which operates via the cascaded second order effect, the most obvious design criterion is that the lowest interband transition energy of the AQW must be significantly greater than twice the photon energy of the fundamental field to avoid both linear absorption of the second harmonic field and two-photon absorption of the fundamental field. More precisely, this requires that the photon energy hc/λ ,corresponding to the fundamental wavelength of operation λ, must be significantly below half the first bound electron to first bound heavy hole transition energy $e1 - hh1$ minus the corresponding fundamental excitonic binding energy E_{ex}:

$$\frac{hc}{\lambda} < \tfrac{1}{2}\left[(e1 - hh1) - E_{ex}\right] \qquad (5.1)$$

$e1$ and $hh1$ were therefore obtained for the different GaAs/AlGaAs AQW structures by solving Schrödinger's equation in the appropriate well profile as described in Chapter 4, while the fundamental excitonic binding energy in a GaAs/AlGaAs QW is of the order of 10 meV [2].

Furthermore, from consideration of Section 3.1, it may be recalled that the second order optical non-linearities associated with an AQW structure exist by virtue of the asymmetric envelope functions associated with a first bound hole level and the lowest two bound electron levels. In other words, the Al fraction profile of the QW design must be asymmetric, and must support two bound electron levels in the presence of Al fraction and layer thickness inaccuracies which may occur during growth. Furthermore, in the effective mass approximation, the $\chi^{(2)}_{zzz}$ tensor component is proportional to the momentum matrix element product $\langle\phi_{lh1}(z)|\phi_{e1}(z)\rangle\langle\phi_{e1}(z)|-i\hbar\, d/dz|\phi_{e2}(z)\rangle\langle\phi_{e2}(z)|\phi_{lh1}(z)\rangle$ which should ideally be maximised during the design of an optimum AQW structure (see Section 3.1). (In practice however, this matrix element product was not maximised due to the other AQW design constraints discussed both in this section and the next section.) For the particular case of an ASQW, this momentum matrix element product is only really significant (and hence the ASQW optical non-linearities are only really significant), when the first bound electron level resides below the step in the conduction band potential and the second bound electron level resides above it. ASQW structures were therefore designed within these guidelines. To check that a given design satisfied all of the above conditions, Schrödinger's equation was solved using the algorithm described in Chapter 4.

A further design constraint on the multiple AQW structures is that the QW barrier layers must be sufficiently thick to ensure negligible coupling between neighbouring QWs. For the multiple AQW structures used in this work, this requirement was somewhat arbitrarily interpreted to mean that the second bound electron envelope function associated with a given AQW should decay to 1% of its value at the well/barrier interface after a distance equal to the barrier layer thickness. Again, to check that this condition was fulfilled for a particular multiple AQW design, Schrödinger's equation was solved using the numerical method discussed in the previous chapter.

Finally, all the epitaxial layers were nominally undoped to prevent the formation of any built-in fields that could lead to shifting of the bound energy levels and the accompanying distortion of the envelope functions through the quantum confined Stark effect [3].

5.1.2 Design Criteria for Specific Multiple AQW Structures

All of the AQW structures used throughout this work were designed in accordance with the general principles set out above with the exception of the QT613 ASQW structure which was *not* designed to be tolerant to growth inaccuracies. Instead, the QT613 structure was designed for operation at 1.55 μm in accordance with the calculations of Kelaidis *et al* [4]. These suggest that the ASQW tensor component $\chi^{(2)}_{zzz}$ is relatively insensitive to small changes in layer compositions or thicknesses, provided the first and second bound electron levels lie below and above the conduction band potential step respectively. Furthermore, the QT613 ASQW structure, with three different Al fraction layers per period of the MQW, was subject to an additional relatively severe constraint: the availability of only two Al cells during growth meant that, while the two well layer Al fractions AlW_1 and AlW_2 could be chosen independently, the barrier layer Al fraction AlB was then completely determined according to the relation:

$$\mathrm{AlB} = \left[\frac{\mathrm{AlW}_1}{(1-\mathrm{AlW}_1)} + \frac{\mathrm{AlW}_2}{(1-\mathrm{AlW}_2)}\right] \Bigg/ \left[1 + \frac{\mathrm{AlW}_1}{(1-\mathrm{AlW}_1)} + \frac{\mathrm{AlW}_2}{(1-\mathrm{AlW}_2)}\right] \tag{5.2}$$

Physically this constraint arises because the Al flux from a given cell cannot be altered during growth of the MQW. This means that, with two Al cells, only three flow rates are possible corresponding to one or other of the Al cell shutters open, or both of the Al cell shutters open. For the QT613 structure $\mathrm{AlW}_1 = 0.15$ and $\mathrm{AlW}_2 = 0.37$ and from (5.2) we therefore obtain $\mathrm{AlB} \approx 0.44$.

B563 and B578 were diagnostic multiple ASQW and multiple ACQW waveguide structures respectively. These structures were both designed with GaAs layers in the wells to allow characterisation by photoluminescence excitation spectroscopy (PLE) using a tuneable Ti:sapphire laser in the wavelength range 700 - 850 nm i.e. the AQW structures were designed to guarantee that all first and second bound electron level to first and second bound hole level interband transitions lay within the wavelength range 700 - 850 nm. This may be seen from inspection of the calculated room temperature interband transition wavelengths for the B563 and B578 nominal material structures which are listed in Appendix A. Furthermore, since characterisation of an actual QW structure involves the experimental determination of the QW parameters (layer thicknesses and compositions), choosing GaAs as the lowest Al fraction QW layer for the B563 and B578 structures meant that there was no uncertainty associated with the composition of this layer, and that one of the QW variables was effectively eliminated. Also, choosing GaAs as the lowest Al fraction for the B563 ASQW structure had the added advantage that the Al fractions in the higher Al fraction QW layer and the barrier layer could be chosen independently during growth when using only two Al cells.

Like the B563 ASQW structure, the B635 ASQW structure was designed with GaAs in the lower Al fraction QW layer. Unlike the B563 structure however, the B635 structure was designed for operation at 1.55 μm. This required a thin (six monolayers) deeper well region and high Al fractions of 0.4 and 0.6 in the shallower well region and in the barrier layer respectively.

Finally, the B690 nominal material structure (which is the same for the B672 and QT849A nominal material structures), is an ACQW structure designed for operation at 1.55 μm with 20% AlGaAs in the well layers and 44% AlGaAs in the barrier layers.

In way of summary, all of the specific design criteria for the different material structures discussed in this sub-section are listed in Table 5.1 along with the corresponding momentum matrix element products $\langle\phi_{\mathrm{lh1}}(z)|\phi_{\mathrm{e1}}(z)\rangle\langle\phi_{\mathrm{e1}}(z)|-i\hbar\, d/dz|\phi_{\mathrm{e2}}(z)\rangle\langle\phi_{\mathrm{e2}}(z)|\phi_{\mathrm{lh1}}(z)\rangle$ which reflect the magnitudes of the second order susceptibility tensor components $\chi^{(2)}_{zzz}$, as described in Section 3.1. These specific criteria were satisfied in addition to the general design criteria of the previous section as will be apparent from the experimental characterisation results of Section 5.3.

Material	**Wavelength of Operation**	**Specific Design Criteria**	**Momentum Matrix Element Product (a.u.)**
QT613 (ASQW)	1.55 μm	**i.** Structure *not* designed to be tolerant to growth inaccuracies **ii.** During growth with two Al cells, the barrier layer Al fraction is determined by the Al fractions in the two QW layers	5.807×10^6
B563 (ASQW)	QW structure designed to allow PLE in wavelength range 700 - 850 nm	GaAs in the deeper QW layer meant that Al fractions in shallower QW layer and barrier layers could be chosen independently	4.421×10^6
B578 (ACQW)	QW structure designed to allow PLE in wavelength range 700 - 850 nm	GaAs in the QW layers	3.773×10^6
B635 (ASQW)	1.55 μm	GaAs in the deeper QW layer meant that Al fractions in shallower QW layer and barrier layers could be chosen independently	1.048×10^7
B690, B672 and QT849A (ACQW)	1.55 μm	Different Al fractions in well and barrier layers chosen independently	5.929×10^6

Table 5.1 Specific design criteria for the different AQW structures which were satisfied in addition to the general AQW design criteria of Section 5.1.1 and the resulting momentum matrix element products which reflect the relative magnitude of $\chi^{(2)}_{zzz}$

5.2 The Design of Multiple AQW Waveguide Structures

The multiple AQW waveguide epitaxial structures used throughout this work consisted of, a lower cladding or isolation layer grown on top of the substrate, followed by, the multiple AQW guiding layer, an upper cladding layer, and a thin GaAs protective cap layer. Having finalised the AQW designs, the polarisation-dependent bulk equivalent refractive indices for the multiple AQW guiding layer were estimated using (3.5). The thickness of the multiple AQW layer was then considered to be variable during the waveguide structure design according to the number of AQW periods selected. The thicknesses of the GaAs protective cap layer and the upper cladding layer were predetermined due to constraints imposed by the IFVD process used for QW intermixing and, for the purposes of designing the waveguide structure, were assumed to be 0.1 μm and 0.8 μm respectively (see Chapter 6). The waveguide structures for confinement of the optical fields were subsequently designed according to several criteria which were the same for all of the materials used during this work. These design criteria will therefore be illustrated by considering the B690 multiple ACQW waveguide material structure throughout this section.

Firstly, and most importantly, the slab waveguide structures were designed to offer sufficient confinement in the vertical direction so as to minimise leakage into the GaAs substrate without supporting any higher order modes at the fundamental wavelength of operation. The B690 multiple ACQW slab waveguide structure, for example, was designed to be single-moded at 1.55 μm and to have an evanescent field strength at the GaAs substrate/lower cladding interface which was approximately 0.1% of the peak field strength in the guiding layer. This may be seen from Figs. 5.1a and 5.1b which are plots of the normalised horizontal and vertical electric field components for TE and TM-polarised input fields respectively in the B690 waveguide structure. The mode profiles of Fig. 5.1 were generated using a multilayer slab-solver routine and refractive index data based on the modified Afromowitz model [5]. For the TE case, the normalised horizontal electric field component was 0.0011 at the substrate/lower cladding interface, while for the TM case the normalised vertical field component at the same interface was 0.0012.

The effective indices of all the supported TE and TM modes of the various multiple AQW slab waveguide structures were calculated using refractive index data generated by the modified Afromowitz model and are listed in Appendix A. It will be seen that, in contradiction to the criteria discussed above, the B563 and B578 waveguide structures are multi-moded at a wavelength of 1.7 μm. By comparing the first order mode effective indices at 1.7 μm with the refractive indices in the cladding layers of these structures (also appearing in Appendix A), it may be seen that these first order modes are, however, only very weakly guided at 1.7 μm. Furthermore, because of their AQW design, these materials were absorbing at wavelengths shorter than approximately 1.66 μm so that their waveguides were designed for single-moded operation between 1.7 and 1.8 μm, using data generated from the refractive index model proposed by Adachi [1]. From the data of Appendix A, however, it would appear that, when using refractive index data generated by the modified Afromowitz model (which we believe to be more accurate), these waveguides are multi-moded (although only just) at 1.7 μm. Obviously at operating wavelengths longer than 1.7 μm, the waveguides will tend to become single-moded once again.

Since we are interested in second order non-linear optical effects in the multiple AQW guiding layer, we must naturally also consider the confinement of any second harmonic field that may be generated in the waveguide structure. For maximum conversion efficiency in a 2D ridge waveguide, the overlap integral factor between the normalised fundamental and second harmonic mode profiles in the non-linear multiple AQW guiding layer should be maximised as discussed in Section 2.6. An optimum ridge waveguide design may therefore be determined by adjusting the various slab waveguide layer thicknesses and compositions until the overlap factor is maximised. Rather than implementing such a rigorous waveguide design algorithm, a quasi-optimum approach was adopted instead: the various slab waveguide layer thicknesses and compositions were adjusted until symmetrical confinement of the optical fields was achieved i.e. the peaks in the lowest order fundamental frequency and second harmonic frequency modes were more or less coincident in the middle of the multiple AQW guiding layer. This may be seen from inspection of Figs. 5.1 and 5.2, which are plots of the lowest order fundamental frequency and second harmonic frequency modes for the B690 material at 1.55 μm and 775 nm respectively. The overlap factor, and therefore the power exchange process between the two guided fields in the multiple AQW layer, should therefore be approximately optimised.

From a comparison of the B690 first order second harmonic frequency (775 nm) mode profiles of Figs. 5.3 with the B690 lowest order fundamental frequency (1.55 μm) mode profiles of Figs. 5.1, it may also be seen that the overlap factor between the lowest order fundamental frequency mode and the first order second harmonic frequency mode is minimised (i.e. the coupling between the modes via the non-linear interaction with the multiple AQW layer is minimised). This is because, due to the confinement symmetry, the lowest order fundamental frequency mode is essentially an even function of depth within the non-linear multiple AQW guiding layer, while the first order second harmonic frequency mode is essentially an odd function of depth.

Finally, it may be recalled from Section 5.1.1 that, to avoid any built-in field effects, all of the epitaxial structures studied throughout this project were nominally undoped. It should then also be pointed out, that by using such passive structures, free carrier absorption is avoided and waveguide losses should be correspondingly reduced.

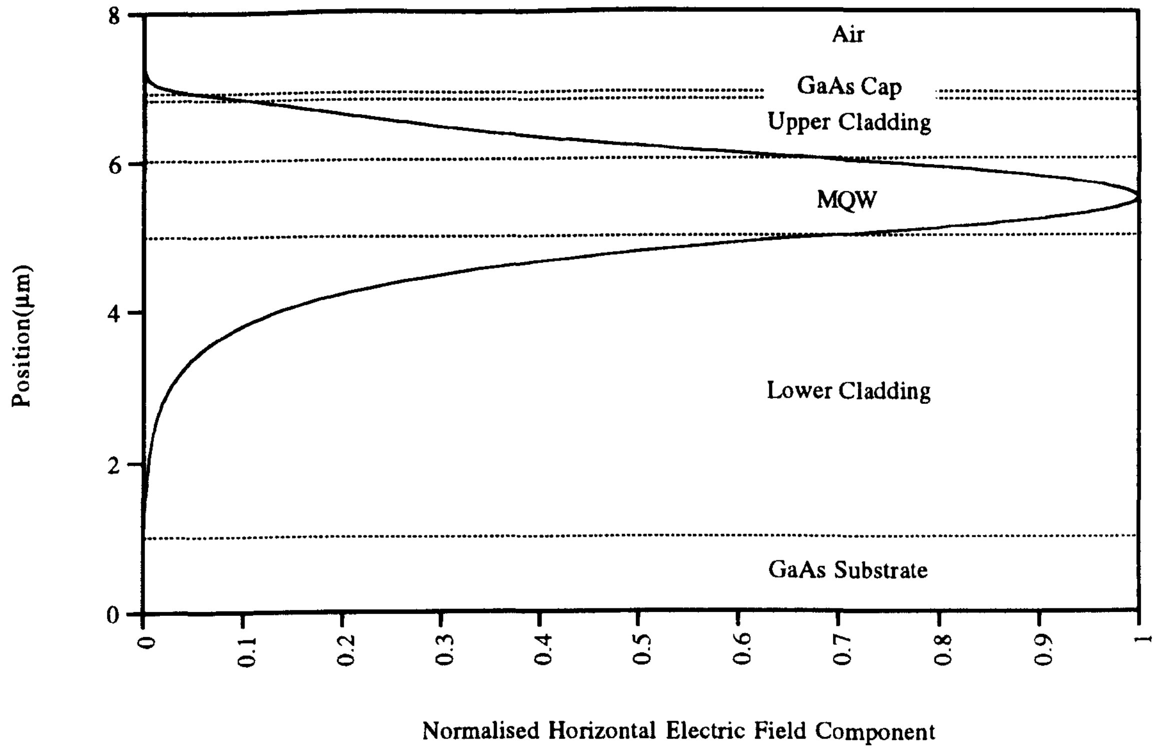

(a)

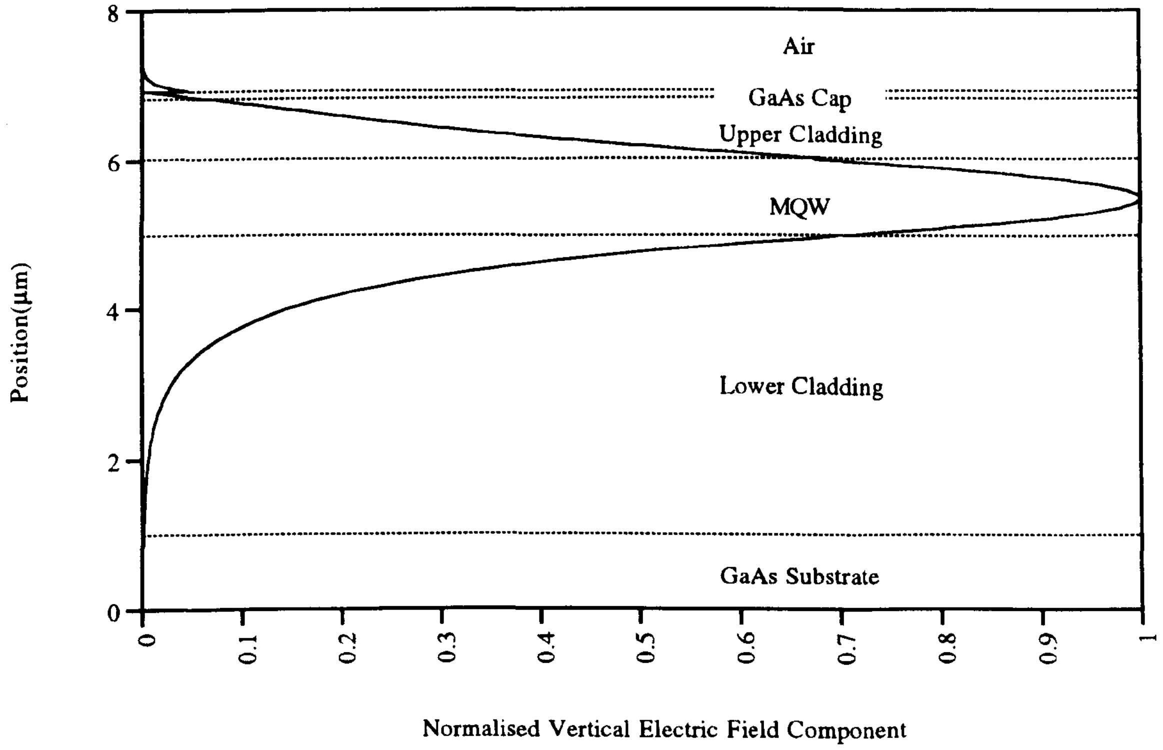

(b)

Fig. 5.1 Normalised lowest order mode profiles at 1.55 μm for a B690 multiple ACQW slab waveguide (**a**) TE-polarised input field (**b**) TM-polarised input field

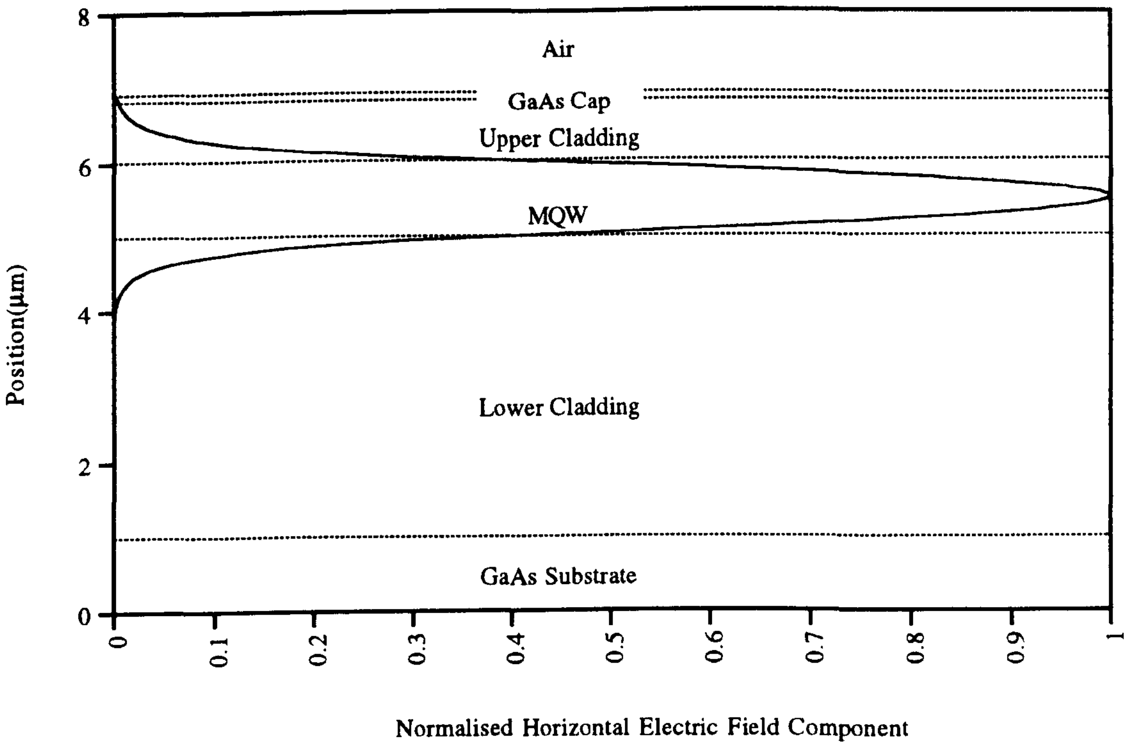

(a)

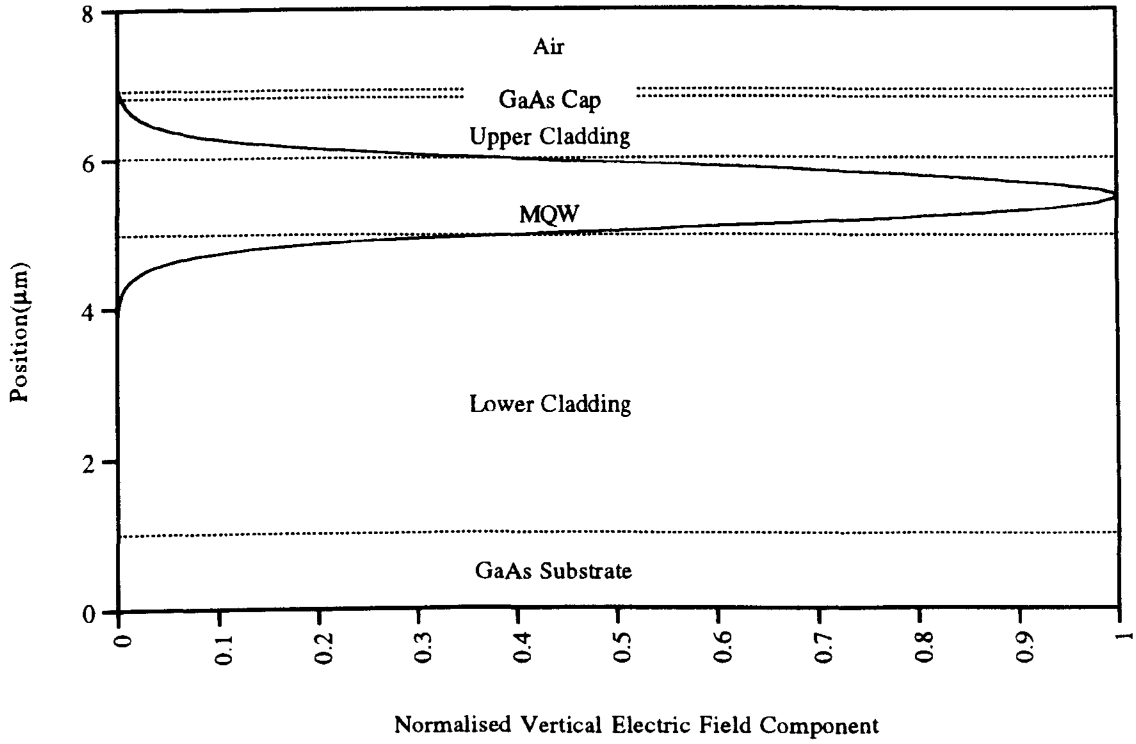

(b)

Fig. 5.2 Normalised lowest order mode profiles at 775 nm for a B690 multiple ACQW slab waveguide (a) TE-polarised input field (b) TM-polarised input field

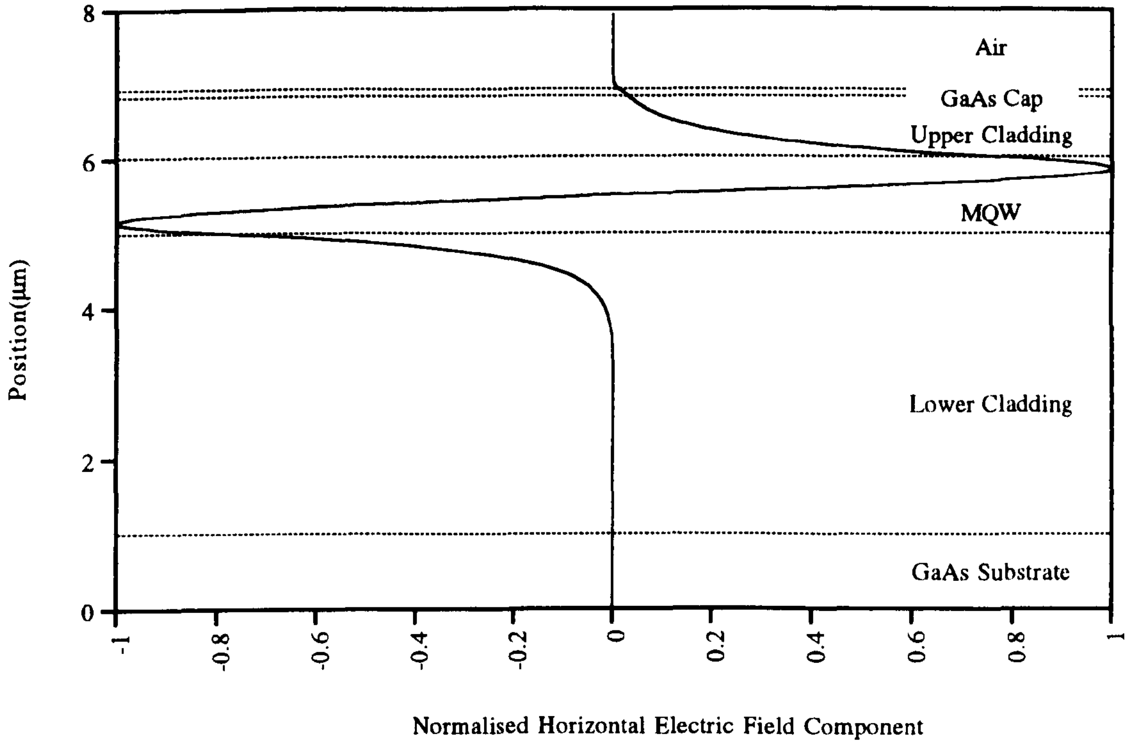

(a)

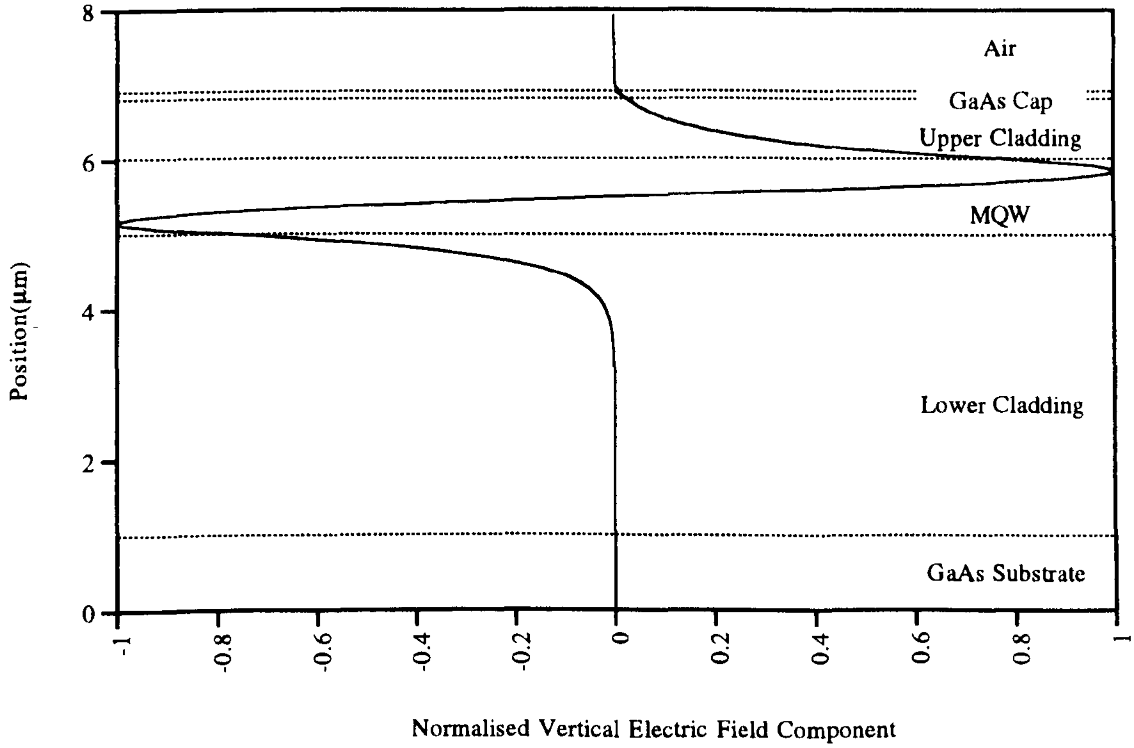

(b)

Fig. 5.3 Normalised first order mode profiles at 775 nm for a B690 multiple ACQW slab waveguide (a) TE-polarised input field (b) TM-polarised input field

5.3 The Characterisation of GaAs/AlGaAs Multiple AQW Waveguide Structures

It should be noted that the characterisation measurement results described next are not presented in chronological order. Rather, they are presented in an order which was chosen in hindsight to allow the most logical development of the arguments which lead to the conclusions summarised in Section 5.3.6.

5.3.1 X-ray Diffraction

X-ray diffraction measurements were performed by the growers themselves on most of the GaAs/AlGaAs multiple AQW waveguide structures analysed during this work. The growers were also largely responsible for the interpretation of the X-ray diffraction rocking curves. The deduction of the *average* Al fraction in the MQW layer and the period of the MQW layer from typical rocking curve features will therefore be described in very simple terms.

X-ray rocking curves are essentially plots of the X-ray radiation diffracted from the surface of a wafer epitaxial structure as a function of the angle of incidence of the X-rays which is varied by tilting or "rocking" the sample. Several large peaks are typically observed for a GaAs/AlGaAs epitaxial structure at different rocking angles from which the Al fractions of the different wafer layers may be derived. For the particular case of a GaAs/AlGaAs MQW waveguide structure, rocking curve peaks may often be resolved which correspond to the Al fractions in the upper and lower cladding layers, the GaAs substrate, and the *average* Al fraction in the MQW guiding layer itself. Furthermore, from the angular separation of any observable secondary or "satellite" peaks (which occur periodically as a function of the rocking angle due to the periodic nature of the MQW) the MQW period itself may be unambiguously determined.

Double crystal X-ray diffractometry results for all of the epitaxial structures examined are summarised in Table 5.2. Clearly, the measured MQW periods for the QT613 and B672 structures agree with the nominal periods to within ±10%. There is also good agreement between the measured layer compositions and the nominal layer compositions in every case except two: the layer compositions were not measured for the B690 structure as the X-ray diffractometer was not operational in the period immediately following its growth, while, for the B672 structure, the Al fractions in the cladding layers, and the average Al fraction in the MQW guiding layer, are well in excess of the corresponding nominal values.

Material	**MQW Period(Å)**	**Layer Al Fractions**		
		Lower Cladding	**MQW**	**Upper Cladding**
QT613 (MOCVD)	335 (300)	0.490 (0.49)	0.390 (0.39)	0.490 (0.49)
B563 (MBE)	- (230)	0.420 (0.42)	0.213 (0.21)	0.330 (0.32)
B578 (MBE)	- (212)	0.460 (0.44)	0.213 (0.20)	0.351 (0.34)
B635 (MBE)	- (187)	≈0.545* (0.56)	≈0.47* (0.47)	≈0.545* (0.55)
B672 (MBE)	199 (210)	0.65 (0.47)	0.502 (0.35)	0.65 (0.47)
B690 (MBE)	- (210)	- (0.47)	- (0.35)	- (0.47)
QT849A (MOCVD)	- (210)	0.48 (0.47)	0.353 (0.35)	0.48 (0.47)

Table 5.2 X-ray diffraction results for different multiple AQW epitaxial waveguide structures (nominal quantities are enclosed in brackets)

*Individual layer peaks could not be clearly resolved so that the Al fractions quoted are only approximate

5.3.2 Room Temperature Absorption

Although an absorption spectrum contains information about *all* the interband transitions between the bound energy levels in a QW structure, the absorption measurement (when performed in a transmission geometry) requires the removal of the GaAs substrate, and is therefore both relatively time-consuming and destructive. In practice substrate removal was accomplished by first mounting the sample epitaxial side down on a clean glass microscope slide using index matching glue. The sample was then lapped to a thickness of approximately 100 µm prior to selective wet etching with a 19:1 hydrogen peroxide:ammonia solution which etched the GaAs substrate approximately 100 times faster than the underlying epitaxial cladding layers. The wet etching was performed in several stages. After each stage, the sample was examined under a microscope while illuminating it with a white light source from below. Once the substrate layer had effectively been removed, "red" light was observed to be transmitted through the sample, and no further etching was performed.

Prior to undertaking the absorption measurement itself, a quarter wavelength AR coating of Al_2O_3 was sputtered onto the exposed surface of the sample to help suppress Fabry-Perot oscillations which were observed to be superimposed on top of the multiple AQW transmission spectra of interest and which occurred due to multiple reflection effects within the thinned samples. Fig. 5.4 is a schematic diagram of the experimental set-up for the absorption measurement which was performed in a transmission geometry:

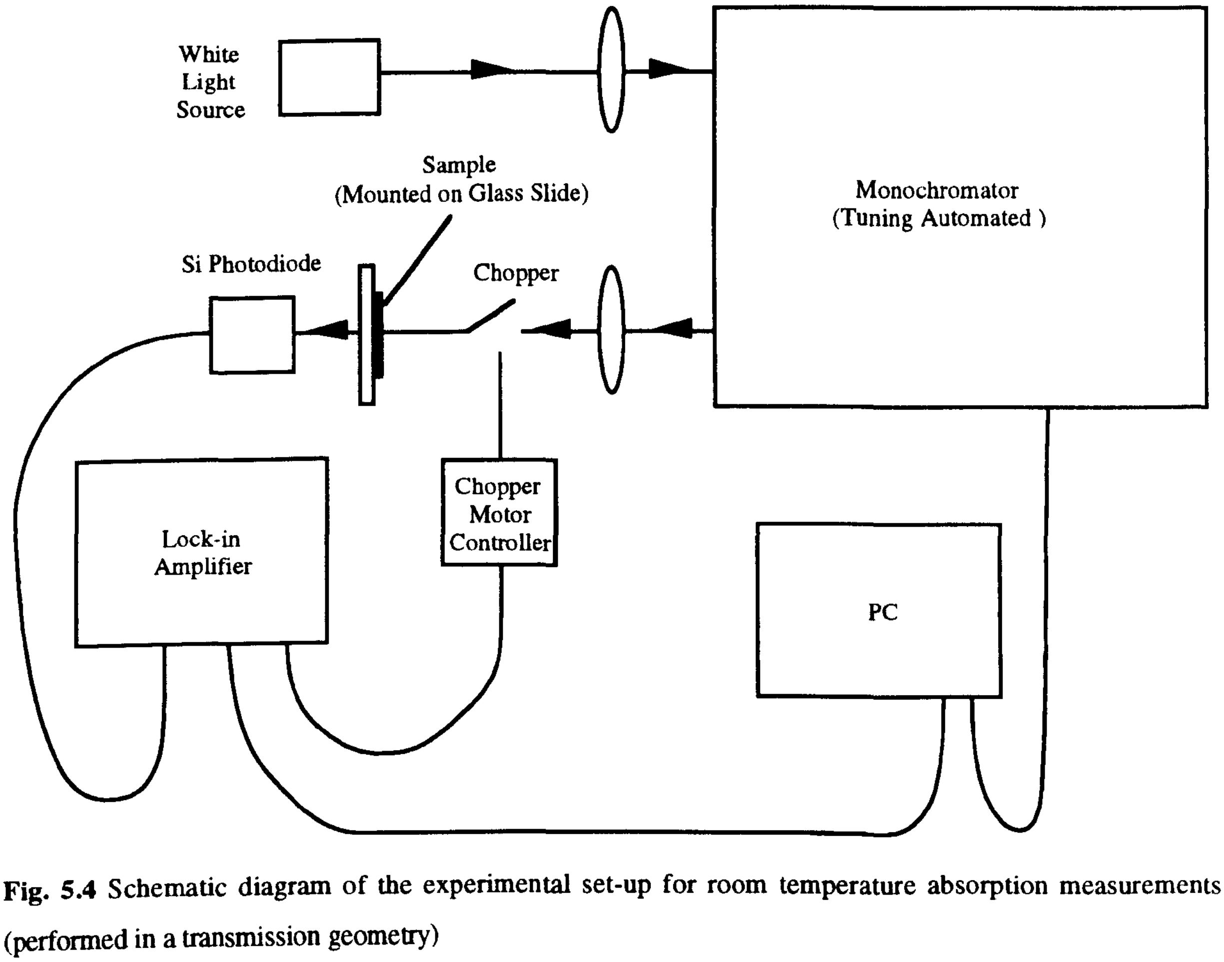

Fig. 5.4 Schematic diagram of the experimental set-up for room temperature absorption measurements (performed in a transmission geometry)

White light was focused onto the entrance slit of the monochromator. The tuning of the monochromator was automated using a stepper motor interfaced to a PC, and light at the selected wavelength from the exit slit of the monochromator was focused onto a Si photodiode through a chopper wheel and the thinned sample itself. Lock-in detection was used to monitor the intensity transmitted by the sample as a function of wavelength. The lock-in amplifier was also interfaced to the PC and the transmission spectrum $I_t(\lambda)$ was recorded over the interband transition wavelength range of interest. Subsequently, the spectrum of the white light source $I_i(\lambda)$ was recorded over the same wavelength range using an identical set-up, but with the sample removed. The normalised transmission spectrum $I_t(\lambda)/I_i(\lambda)$ was then obtained by dividing the two recorded spectra. Since absorption spectra generally appear more often in the literature and therefore tend to be more familiar than transmission spectra, it is a simple matter to show that, when neglecting multiple reflection effects within the sample and ignoring the presence of the glass slide, the absorption coefficient α is given by:

$$\alpha = \frac{1}{d}\left\{2\ln(1-R) - \ln\left[I_t(\lambda)/I_i(\lambda)\right]\right\} \tag{5.3}$$

In (5.3), d is the thickness of the thinned sample and R is the reflectance at the sample/air interface. Plotting $-\ln\left[I_t(\lambda)/I_i(\lambda)\right]$ as a function of the wavelength λ should therefore result in a spectrum which is essentially an absorption spectrum expressed in arbitrary units. The absorption spectra derived in this way for 6 out of 7 of the different multiple AQW structures grown for this work appear in Figs. 5.5 to 5.10. The free electron to free hole interband transition wavelengths indicated in the figures, and the corresponding normalised oscillator strengths listed in the tables (which reflect the expected size of the edges in the step-like absorption continuum and the size of the corresponding exciton absorption peaks themselves in the effective mass approximation), were calculated for the nominal structures at 300 K as described in Section 4.5.

Also marked in Figs. 5.5 to 5.10, are the room temperature peak photoluminescence wavelengths, which will be discussed at some length in Section 5.3.5. It should be emphasised that the interband transition wavelengths indicated were calculated for free electron to free hole transitions and have *not* therefore been corrected to account for exciton binding energies. From the experimental data presented by Koteles and Chi [1] and the modelling results of Greene and Bajaj [6] for the fundamental heavy hole exciton binding energy as a function of the well width for GaAs symmetric QW's with AlGaAs barriers, we estimate the fundamental heavy hole exciton binding energies in *all* of the AQW structures to be approximately 8 - 10 meV. These binding energies translate into wavelength differences of approximately 3.2 - 4.0 nm for the AlGaAs AQW structures, QT613, B672, B690 and QT849A (i.e. the AQW structures with no GaAs layers in the wells), which have their fundamental exciton heavy hole exciton peaks around 700 nm. For the GaAs AQW structures B563 and B578, however, with their fundamental heavy hole exciton peaks around 800 nm, these binding energies correspond to a wavelength difference in the range 4.1 - 5.2 nm. We would therefore expect fundamental heavy hole exciton peaks to occur in the absorption spectra of the AlGaAs AQW structures (QT613, B672, B690 and QT849A) at wavelengths approximately 3 - 4 nm longer than the e1hh1 predicted transition wavelengths indicated, while, for the GaAs AQW structures (B563 and B578), we would expect the fundamental heavy hole exciton peaks to occur at wavelengths approximately 4 - 5 nm longer than the predicted e1hh1 transitions indicated.

Furthermore, it is well known that 3D exciton binding energies are inversely proportional to the quantum number j squared [7]:

$$E_X(3D) \propto 1/j^2 \tag{5.4a}$$

while in the 2D limit they are inversely proportional to $(j-1/2)^2$ [8]:

$$E_X(2D) \propto 1/(j-1/2)^2 \tag{5.4b}$$

Hence, for the e2hh2 excitons, we might expect the fundamental heavy hole AQW exciton binding energies quoted above to be reduced by a factor of between 4 and 2.25. Similarly, for the e3hh3 excitons, the reduction factor is between 9 and 6.25. It may therefore be seen that *higher order* heavy hole AQW exciton binding energies are likely to be no more than 2 meV, which is essentially negligible for the purposes of interpreting the AQW absorption spectra.

With these considerations in mind, some general observations regarding the absorption spectra of Figs. 5.5 to 5.10 will now be made before discussing the interpretation of individual spectra. It is immediately obvious from the observed wavelengths of the most prominent e1hh1 and e1lh1 fundamental exciton peak features relative to the calculated e1hh1 and e1lh1 transition wavelengths for the AlGaAs AQW structures (QT613, B672, B690 and QT849A), that the actual AQW structures would appear to offer more quantum confinement to the e1, hh1 and lh1 levels than the nominal structures. This could be the result of several different growth inaccuracies: the actual QW layer thicknesses may be less than the corresponding nominal layer thicknesses; the actual QWs may be deeper than the nominal QWs; the Al fractions in the QW layers may all be proportionately higher than their nominal values; or, all of the above may be true. However, judging from the X-ray diffraction results of Table 5.2, the measured average MQW Al fractions agree very well with the nominal average MQW Al fractions for all the AlGaAs AQW structures apart from B672 which had a significantly higher average Al fraction in the MQW layer. The additional quantum confinement observed in these structures is therefore attributed to the actual QW layers grown being thinner than the nominal corresponding layers. Although the fundamental exciton peaks for the GaAs AQW structures B563 and B578 of Figs. 5.6 and 5.7

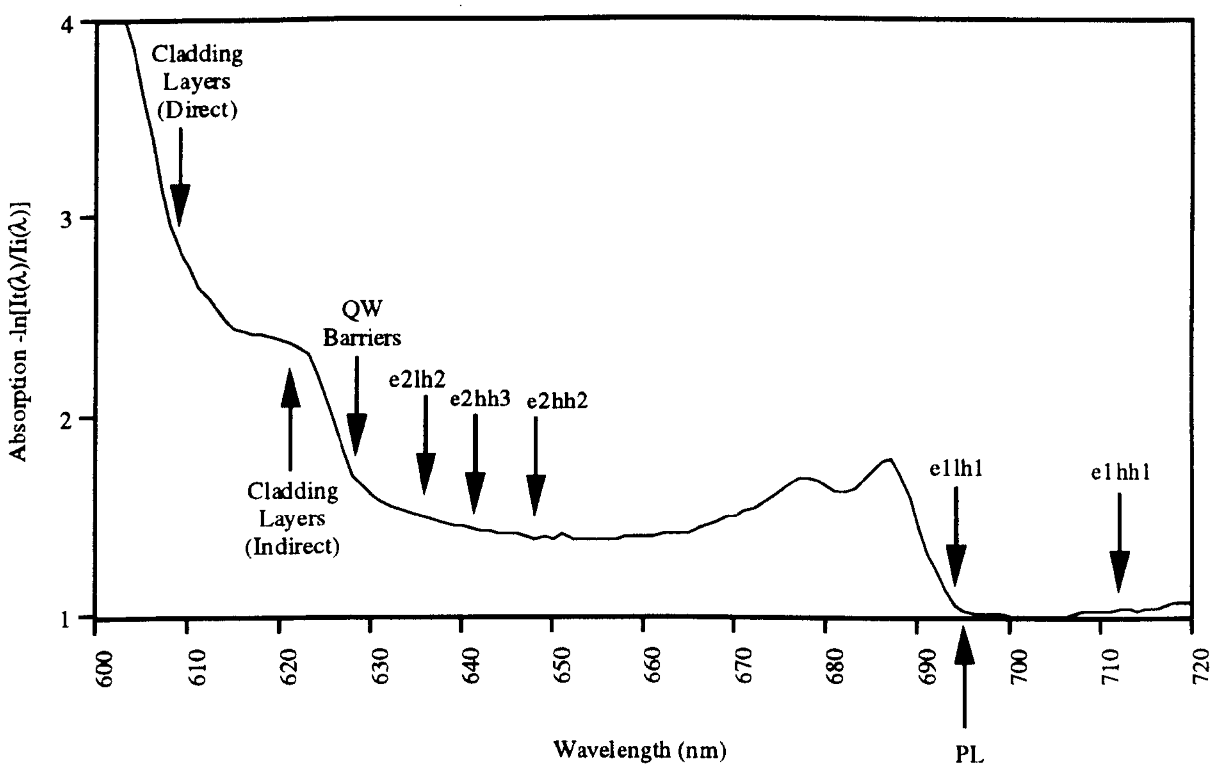

	e1	e2
lh1	0.388	0.001
lh2	0.001	0.379
hh1	1.000	0.028
hh2	0.017	0.207
hh3	0.045	0.725
hh4	0.039	0.116

Fig. 5.5 QT613 room temperature absorption spectrum (transitions indicated calculated for the nominal structure at 300 K) and the corresponding normalised interband transition oscillator strengths at 300 K for the polarisation parallel to the layers

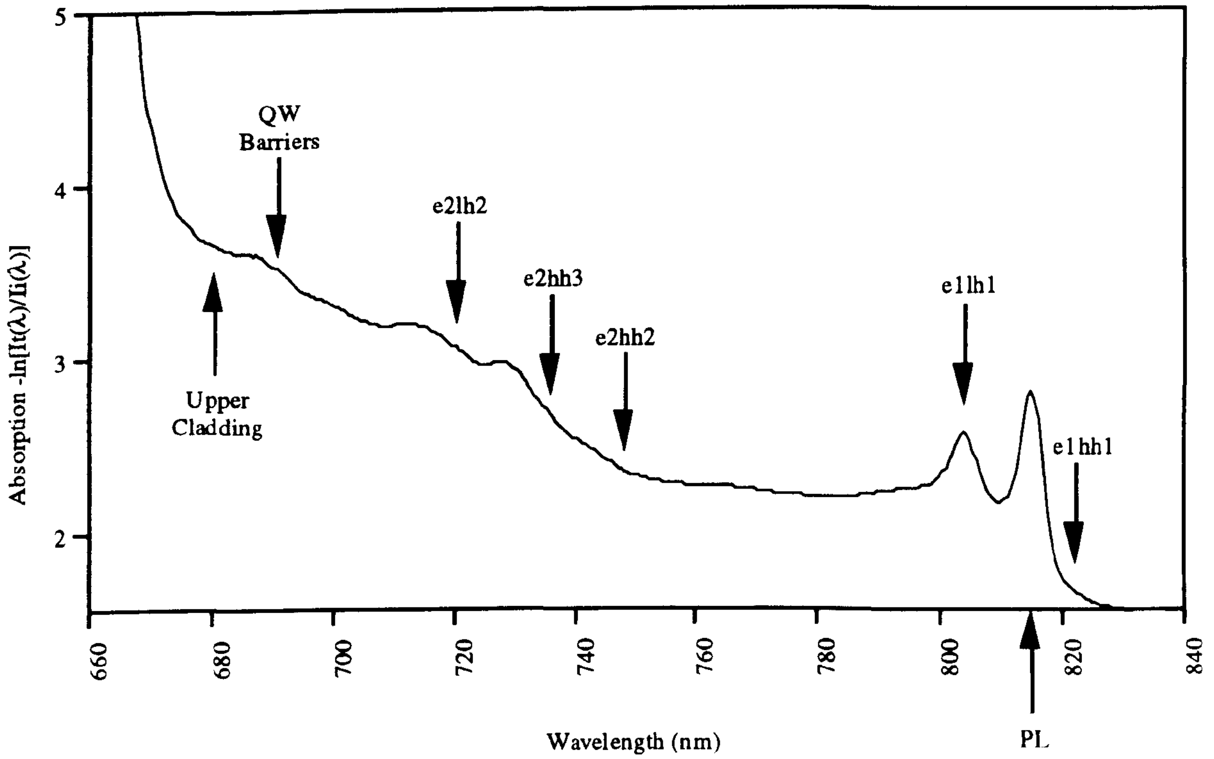

	e1	e2
lh1	0.384	0.001
lh2	0.001	0.381
hh1	1.000	0.058
hh2	0.016	0.305
hh3	0.090	0.597
hh4	0.026	0.082
hh5	0.010	0.000

Fig. 5.6 B563 room temperature absorption spectrum (transitions indicated calculated for the nominal structure at 300 K) and the corresponding normalised interband transition oscillator strengths at 300 K for the polarisation parallel to the layers

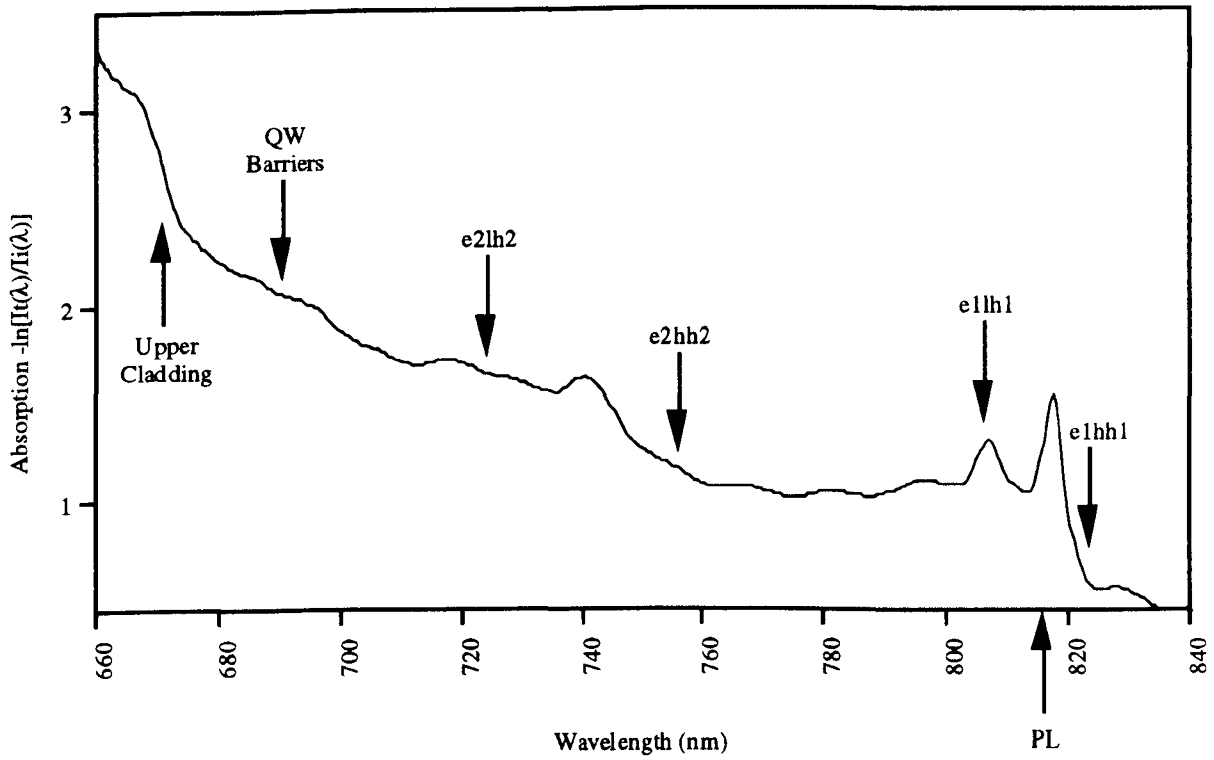

	e1	e2
lh1	0.385	0.000
lh2	0.000	0.381
hh1	1.000	0.068
hh2	0.078	0.882
hh3	0.014	0.003
hh4	0.039	0.018

Fig. 5.7 B578 room temperature absorption spectrum (transitions indicated calculated for the nominal structure at 300 K) and the corresponding normalised interband transition oscillator strengths at 300 K for the polarisation parallel to the layers

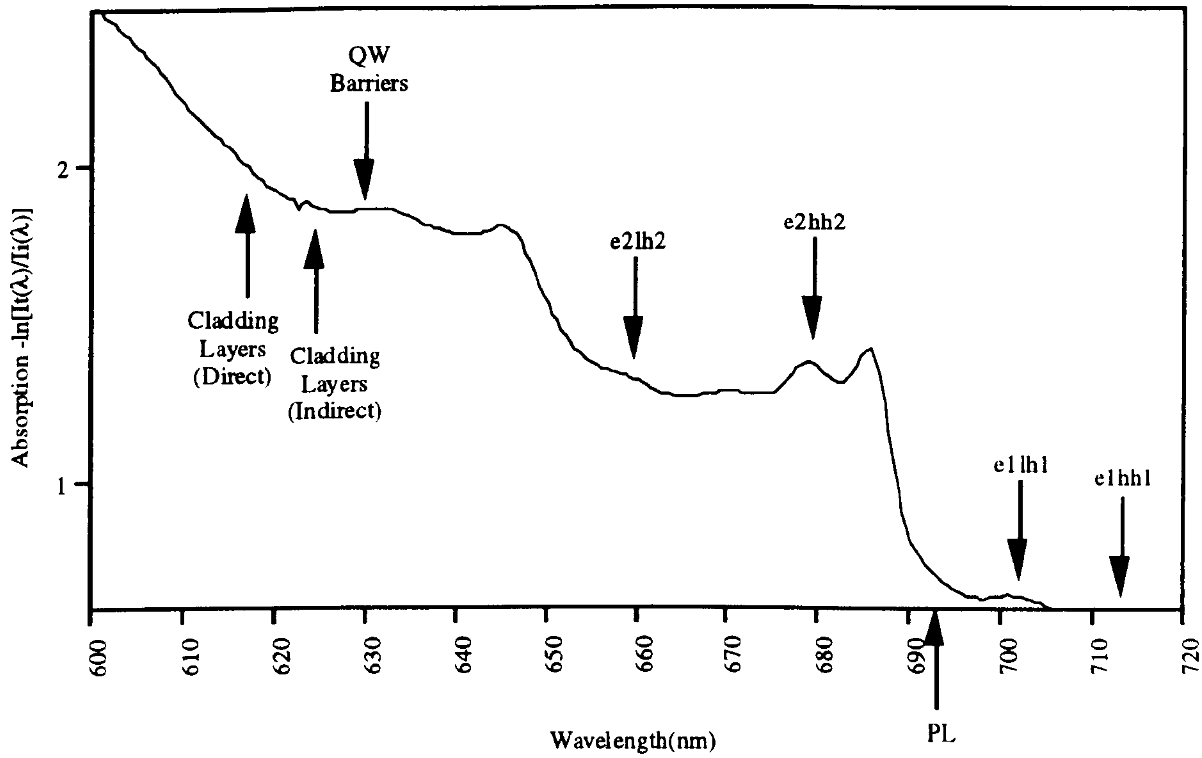

	e1	e2
lh1	0.388	0.001
lh2	0.001	0.383
hh1	1.000	0.092
hh2	0.104	0.899
hh3	0.000	0.025
hh4	0.035	0.025

Fig. 5.8 B672 room temperature absorption spectrum (transitions indicated calculated for the nominal structure at 300 K) and the corresponding normalised interband transition oscillator strengths at 300 K for the polarisation parallel to the layers

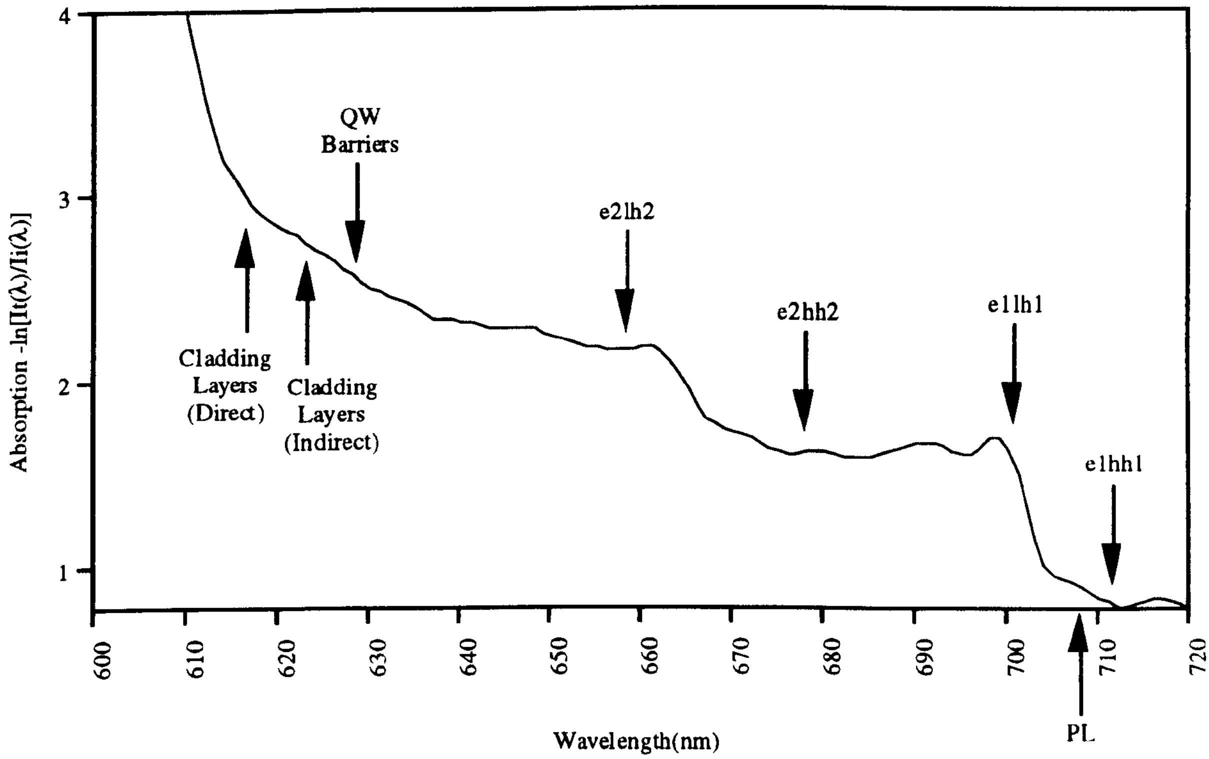

	e1	e2
lh1	0.388	0.001
lh2	0.001	0.383
hh1	1.000	0.092
hh2	0.104	0.899
hh3	0.000	0.025
hh4	0.035	0.025

Fig. 5.9 B690 room temperature absorption spectrum (transitions indicated calculated for the nominal structure at 300 K) and the corresponding normalised interband transition oscillator strengths at 300 K for the polarisation parallel to the layers

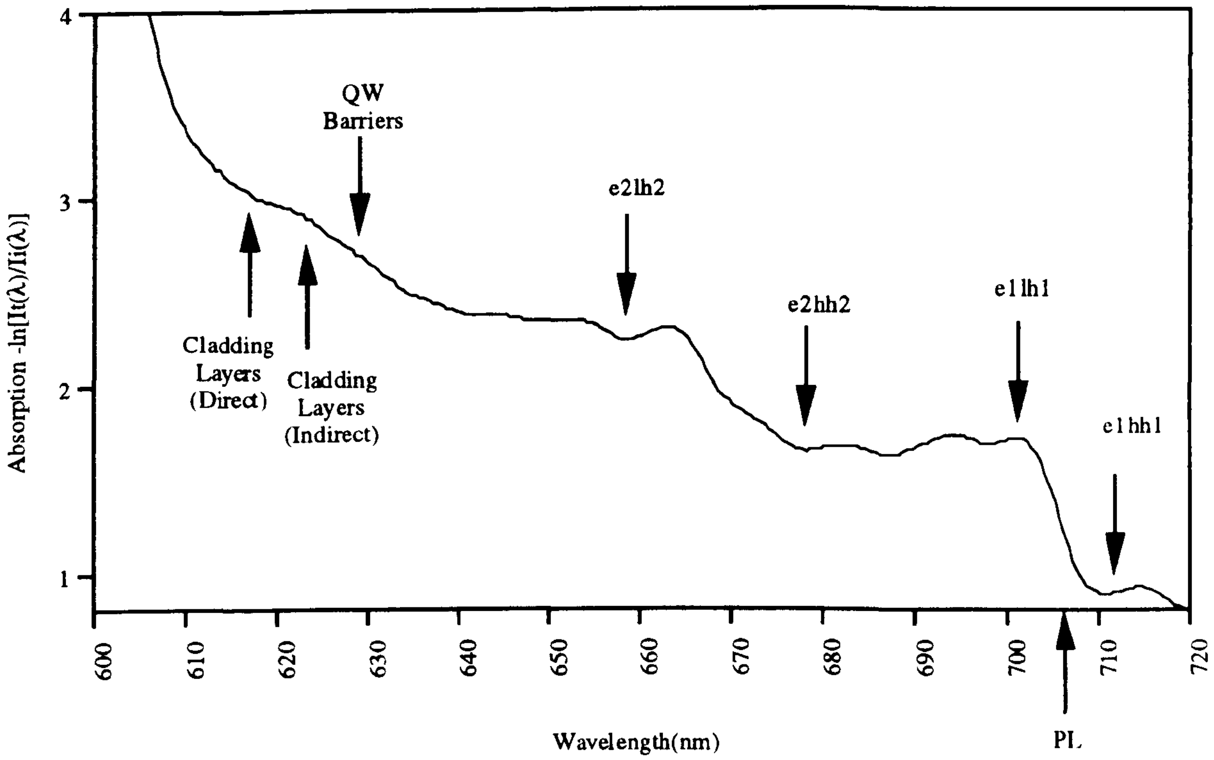

	e1	e2
lh1	0.388	0.001
lh2	0.001	0.383
hh1	1.000	0.092
hh2	0.104	0.899
hh3	0.000	0.025
hh4	0.035	0.025

Fig. 5.10 QT849A room temperature absorption spectrum (transitions indicated calculated for the nominal structure at 300 K) and the corresponding normalised interband transition oscillator strengths at 300 K for the polarisation parallel to the layers

respectively, are better aligned with the calculated e1hh1 and e1lh1 transition wavelengths, once exciton binding energies have been taken into account, it is clear that for these structures too, the observed fundamental exciton peaks occur at wavelengths which are several nm shorter than expected for the nominal structures. The additional quantum confinement observed for all the multiple AQW waveguide structures should not, however, have any particularly detrimental consequences for SHG and the study of other second order non-linear optical processes in these structures, provided that the asymmetry factor of (3.4), and therefore $\chi^{(2)}_{zzz}$ are not reduced significantly as a result.

Despite the extra quantum confinement observed in practice, the transition wavelengths calculated using the Schrödinger solver model of Chapter 4 allow ready identification of the major features in all the absorption spectra except the QT613 ASQW material spectrum. This spectrum does not appear to have any obvious features (neither continuum edges nor exciton peaks) corresponding to the e2hh2, e2lh2 and e2hh3 transitions, which are all relatively significant for the nominal structure (as may be seen from the corresponding normalised oscillator strengths). One could argue, however, that the pronounced edge at 625 nm and the "ledge" between approximately 615 nm and 623 nm could be the result of the superposition of the different absorption features corresponding to these 3 transitions, given that the actual ASQW structure offers more quantum confinement than the nominal structure.

Alternatively, we may consider the possibility that, due to the extra quantum confinement, the second bound electron level has been "squeezed" out of the well, which would result in the extinction of the second order non-linear susceptibility tensor components associated with the AQWs. Since e2 is relatively near the top of the well for the nominal structure in the first instance, this may be a likely explanation. To further support this argument, the calculated first and second bound electron levels e1 and e2 are plotted with respect to the right-hand vertical axis of Fig. 5.11 as functions of the well width W for the QT613 structure. In this figure, it has been assumed that the widths of the two different well layers W_1 and W_2 ($W_1+W_2=W$) are decreased proportionately (i.e. W_1/W_2 is constant). Also indicated on the graph, are the conduction band potentials corresponding to the two different nominal Al compositions in the well layers, and the Al composition in the barrier layers. In addition, the calculated e1hh1 interband transition wavelength is plotted with respect to the left-hand vertical axis as a function of the well width. By further assuming an e1hh1 exciton binding energy of 10 meV which translates into a wavelength difference of approximately 4 nm (i.e. we neglect any variations in the exciton binding energy with well width), the calculated e1hh1 exciton peak wavelength is also plotted as a function of W. It may then be seen that the e1hh1 exciton peak wavelength of 687 nm observed in the absorption spectrum of Fig. 5.5, corresponds to a well width of approximately 60 Å in Fig. 5.11, and that for this well width there is no second bound electron level in the well.

We may find further credence in the hypothesis that e2 does not exist, by referring to the nominal AQW structures in Appendix A. It may then be noticed that the QW barrier layer thickness for the QT613 structure is 200 Å, which compares with QW barrier layer thicknesses of 120 - 130 Å for the other AQW structures. We would therefore expect a more pronounced QW barrier absorption edge for the case of the QT613 material relative to the QW barrier absorption edges for the other AQW materials. By referring to the absorption spectra of Figs. 5.6 to 5.10, it may be confirmed that there are no such distinctive edges corresponding to the QW barriers in these other structures. This is consistent with the supposition that the edge at 625 nm in the QT613 absorption spectrum of Fig. 5.5 corresponds to absorption in the thicker QW barriers for this structure. The absence of an e2 level would then also have the effect of accentuating this absorption edge still further so that we conclude that *no e2 level exists for the QT613 ASQW structure* as a consequence of the actual QW layers grown being too thin, and that the edge at 625 nm in the QT613 absorption spectrum of Fig. 5.5 corresponds to absorption in the QW barriers.

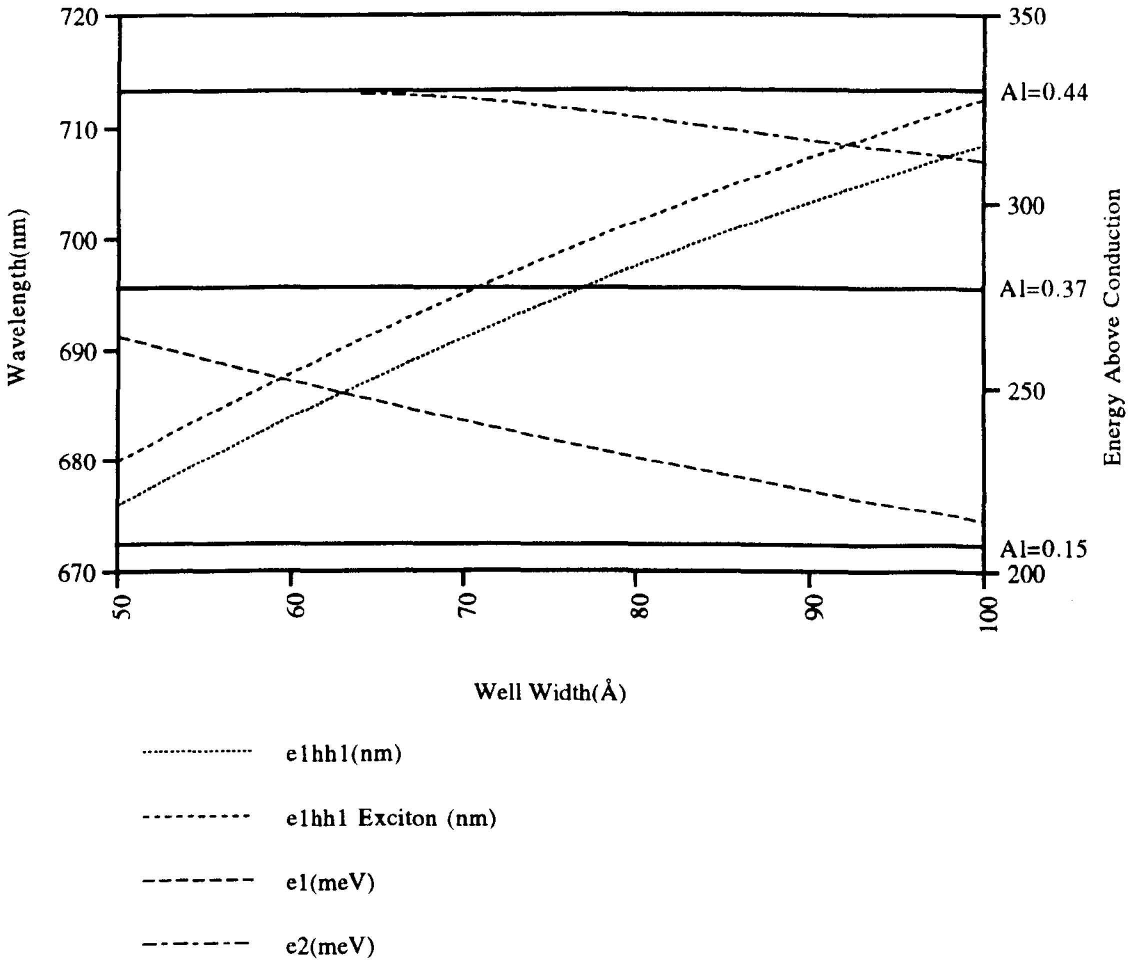

Fig. 5.11 Calculated first and second bound electron energies (right-hand vertical axis) and the corresponding e1hh1, and e1hh1 exciton, interband transition wavelengths (left-hand vertical axis) for the nominal QT613 ASQW structure as a function of the total well width W.

5.3.3 Transmission Electron Microscopy

Transmission electron microscopy (TEM) of some of the multiple AQW waveguide structures was attempted for the unambiguous determination of all the epitaxial layer thicknesses including the individual AQW layer thicknesses. TEM measurements are, however, destructive and require difficult and extremely time consuming sample preparation, so that after disintegration of a few samples, TEM measurements were abandoned. Although complete characterisation of the various multiple AQW waveguide structures was not possible without TEM results, the X-ray diffraction, and absorption measurement results gave a good indication as to how closely the actual structure grown resembled the nominal structure.

5.3.4 Photoluminescence Excitation Spectroscopy (B563 and B578 Multiple AQW Structures Only)

As mentioned in the previous section, complete characterisation of the AQW structures required destructive absorption and TEM measurements. An all-optical switch device such as that described in Section 3.4 relies upon periodic intermixing of the multiple AQW layer along the length of the waveguide device for the periodic suppression of the AQW second order non-linearities. It would therefore be desirable to measure non-destructively in some way the reduction in the degree of QW asymmetry after the intermixing stage. For this reason, photoluminescence excitation spectroscopy (PLE) measurements were attempted on the B563 and B578 multiple AQW structures before and after QW intermixing.

PLE is essentially an absorption measurement technique which involves the resonant excitation of electron-holes pairs. These hot carriers rapidly thermalise and subsequently recombine via the intrinsic photoluminescence (PL) transition (which is predominantly e1hh1 at temperatures of 77 K and higher, as discussed in the next section) with the spontaneous emission of a photon. By monitoring the PL intensity at the e1hh1 wavelength as a function of the excitation wavelength, a PLE spectrum is then obtained. At low enough temperatures even weak "forbidden" interband transitions have been observed in PLE spectra [9] (i.e. transitions such as those which occur in symmetric QWs between bound electron and hole levels with quantum numbers j_e and j_h respectively such that $\Delta j = j_e - j_h = 2p$ where $p = \pm 1$ ± 2, ± 3, ...). (These "forbidden" symmetric QW transitions are also observable using conventional destructive absorption measurement methods at temperatures < 3K [10].)

For the AQW structures B563 and B578, it was therefore hoped that e2hh1 and e2lh1 PLE transition features (which do not occur for symmetric QW's) would be observable and, that furthermore, these features would diminish in size after intermixing due to the reduced QW asymmetry. Observing such transition features in the PLE spectra of the B563 and B578 materials before and after intermixing under different conditions would therefore have given an indication of the magnitude of the second order non-linear susceptibility tensor components associated with the wells, and the efficiency with which the intermixing process suppressed these non-linearities.

Fig. 5.12 is a schematic diagram of the experimental set-up used for the PLE measurements. The excitation was provided by a Ti:sapphire laser with a standard short wavelength mirror set which allowed tuning in the approximate range 700 - 850 nm. Light from the Ti:sapphire laser was coupled into the input fibre of a 3 dB fibre coupler as shown. The sample was fixed onto the end of the coupler output fibre using transparent glue and immersed in liquid nitrogen. A small solid angle of the total PL emitted from the multiple AQW layers was then automatically collected by the fibre in which it propagated backwards via the fibre coupler into the monochromator which was tuned to the e1hh1 intrinsic PL wavelength. Lock-in detection with a cooled Ge photodiode was then used to measure the PL signal intensity as a function of the excitation wavelength. As indicated in Fig. 5.12, the Ti:sapphire power was also monitored to allow normalisation of the detected PL intensity so eliminating the effects of variations in the Ti:sapphire power which occurred during tuning.

At room temperature (i.e. before the sample was immersed in the liquid nitrogen) no meaningful features were observed in the normalised PLE spectrum for the B563 multiple ASQW structure. After immersion of the sample in liquid nitrogen however, the normalised excitation spectrum of Fig. 5.13 was obtained. The arrows on this figure indicate the positions of the interband transition wavelengths calculated for the nominal structure at 77K before correction for the exciton binding energies, and the corresponding normalised oscillator strengths (which reflect the size of the continuum absorption edges and the exciton absorption peaks) are listed in the table below. Although the e1lh1 exciton absorption peak is clearly visible, it is difficult to convince oneself that there are any absorption features corresponding to the other calculated transitions indicated. Certainly there is no real evidence at this temperature of the e2hh1 and e2lh1 transitions which must exist for the AQW tensor components discussed in Section 3.1 to exist. We therefore conclude that PLE at 77 K using the Ti:sapphire laser with the standard short mirror set tells us nothing about the asymmetry of the QWs in the B563 structure. Given the complexity of the PLE measurement, and, due to restrictions on time and equipment, PLE was not attempted at liquid helium temperatures. Furthermore, no PLE measurements were performed on the B578 sample, and, due to the absence of a readily available source tuneable over the 600 - 700 nm range within the department, no PLE measurements were attempted with the AlGaAs AQW structures (QT613, B635, B672, B690 and QT849A).

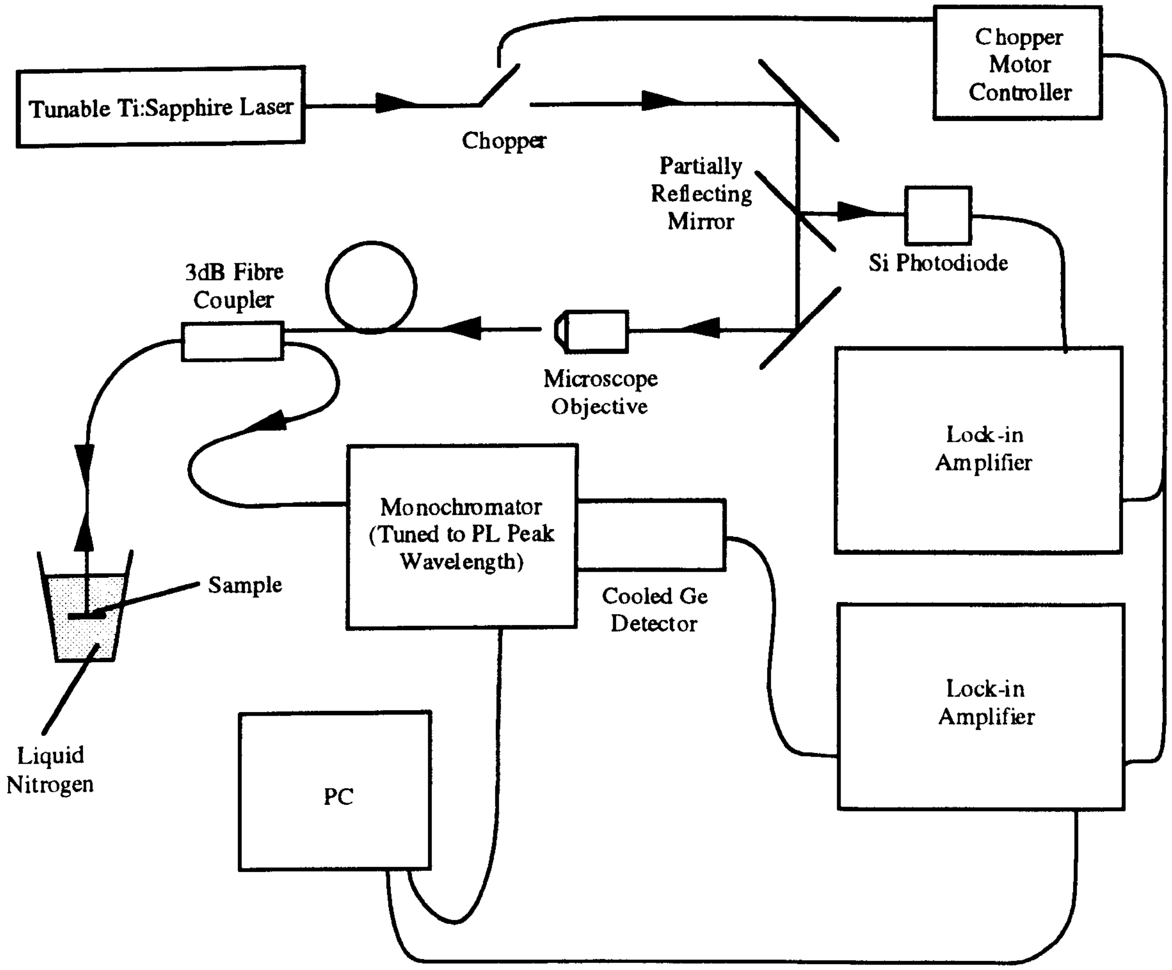

Fig. 5.12 Schematic diagram of the experimental set-up for PLE

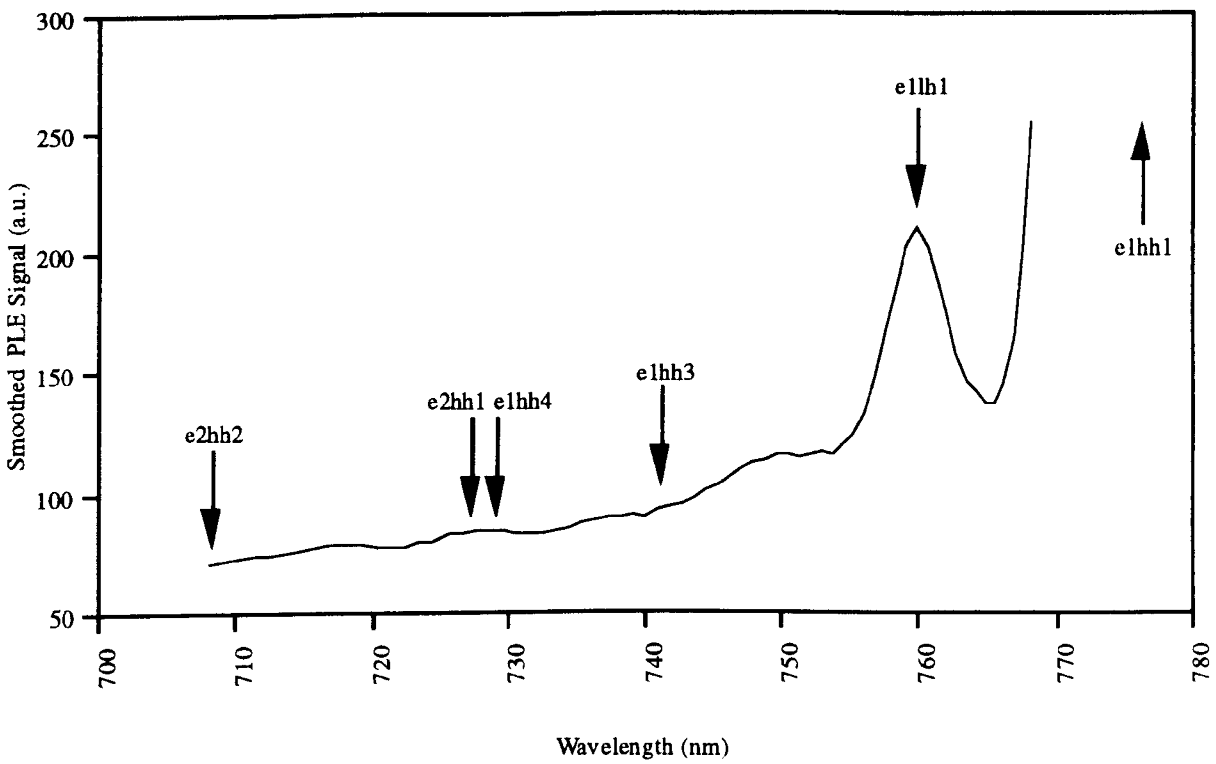

	e1	e2
lh1	0.383	0.001
lh2	0.001	0.380
hh1	1.000	0.057
hh2	0.016	0.300
hh3	0.090	0.605
hh4	0.026	0.081
hh5	0.009	0.000

Fig. 5.13 B563 ASQW PLE spectrum at 77 K (transitions indicated calculated for the nominal structure at 77 K) and the corresponding normalised interband transition oscillator strengths at 77 K for the polarisation parallel to the layers

5.3.5 Photoluminescence

Although the photoluminescence (PL) blueshift that occurs on intermixing a multiple AQW sample tells us nothing directly about the changes in the QW asymmetry, we can infer from it the degree of intermixing achieved after annealing the sample at high temperatures (see Chapter 6). Since the PL measurement is also essentially non-destructive and requires no sample preparation, it was the technique of choice for characterising intermixed multiple AQW structures during this work.

Fig. 5.14 is a schematic diagram of the experimental PL set-up which is a simpler version of the PLE set-up of Section 5.3.4.

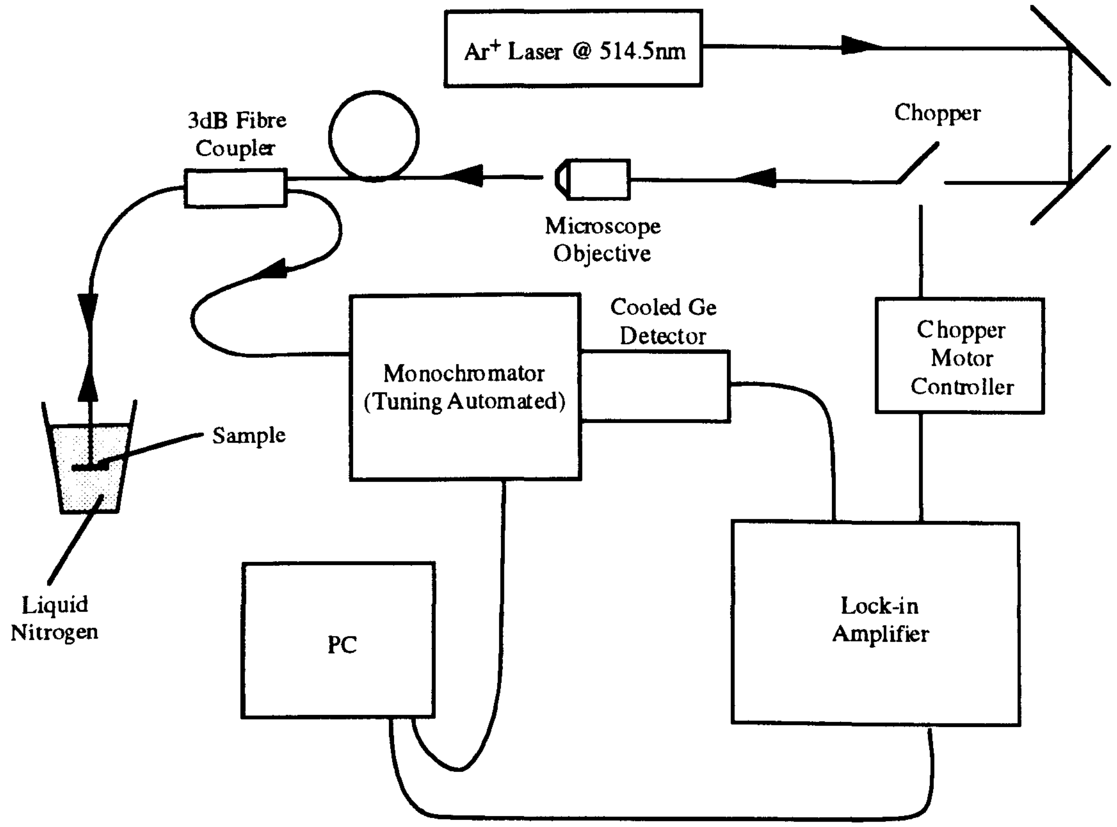

Fig. 5.14 Schematic diagram of the experimental PL set-up

An argon ion laser provided constant wavelength excitation at 514.5 nm. Light from the laser was coupled into one of the fibre inputs of the 3 dB fibre coupler, as for the PLE measurement, and the sample itself was fixed onto the end of the fibre output from the coupler using transparent glue. PL emanating from the multiple AQW layers of the sample was then automatically collected by the same fibre. The other fibre pig-tail from the 3 dB coupler was connected to the monochromator. The PL spectrum of the sample was then obtained by monitoring the PL signal intensity using a Ge photodiode with lock-in detection, while scanning the monochromator wavelength using a stepper motor which was interfaced to the PC. The resulting PL spectra for the various AQW structures appear in Figs. 5.15 - 5.21 (the PL spectra at 77K were obtained by simply immersing the sample in liquid nitrogen). The peak PL wavelengths and PL peak FWHM values are also recorded in Table 5.4 at both 300K and 77K along with the PL peak wavelengths calculated for the corresponding nominal structures which are enclosed in brackets. In addition, both the measured peak PL wavelength differences $\Delta\lambda(\text{meas}) = \lambda_{300K}(\text{meas}) - \lambda_{77K}(\text{meas})$ and the corresponding calculated differences $\Delta\lambda(\text{calc}) = \lambda_{300K}(\text{calc}) - \lambda_{77K}(\text{calc})$ are listed in the table.

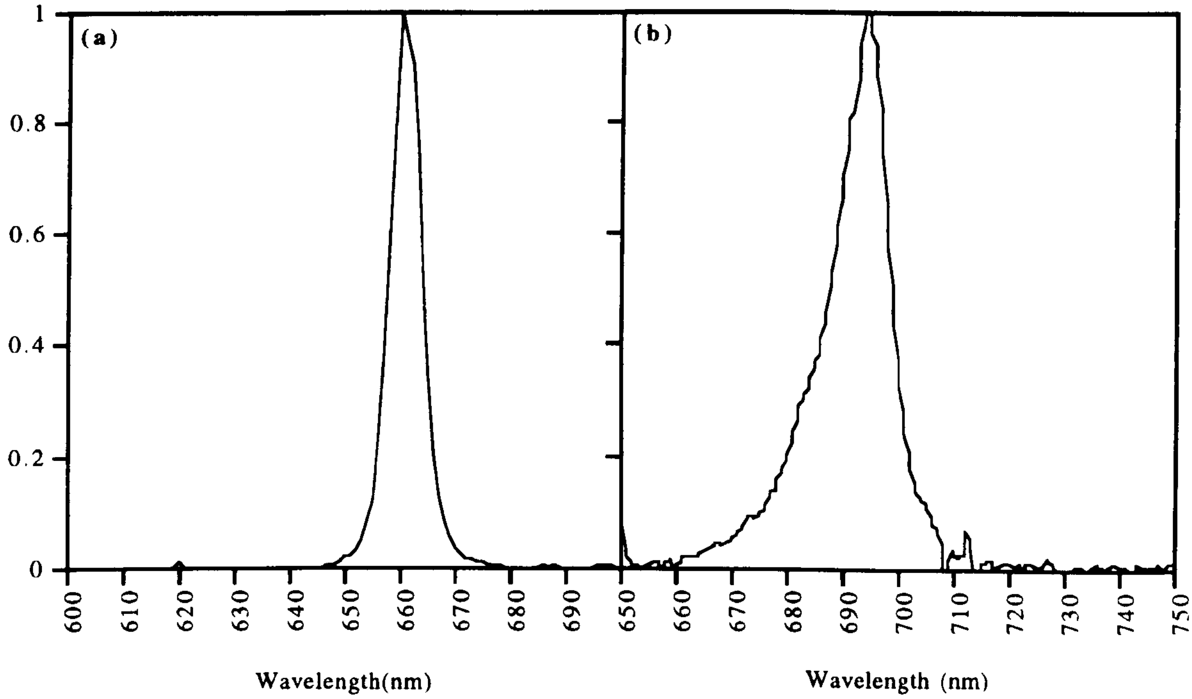

Fig 5.15 QT613 normalised PL spectra at **(a)** 77 K and **(b)** 300 K

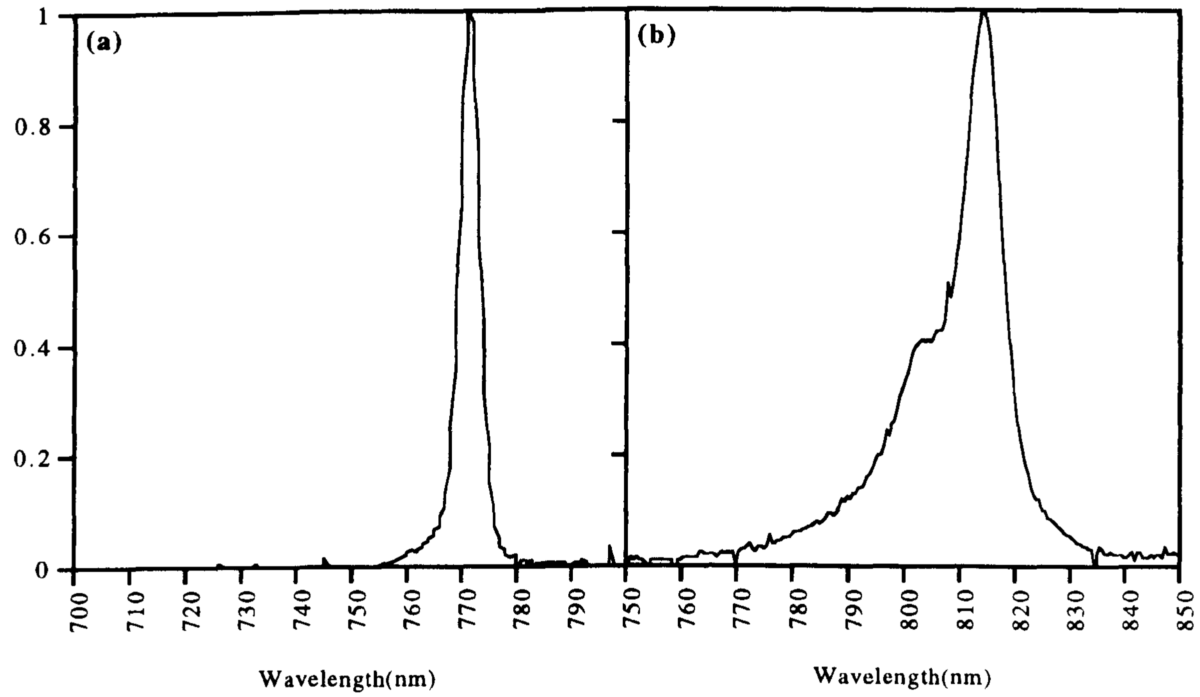

Fig. 5.16 B563 normalised PL spectra at (a) 77 K and (b) 300 K

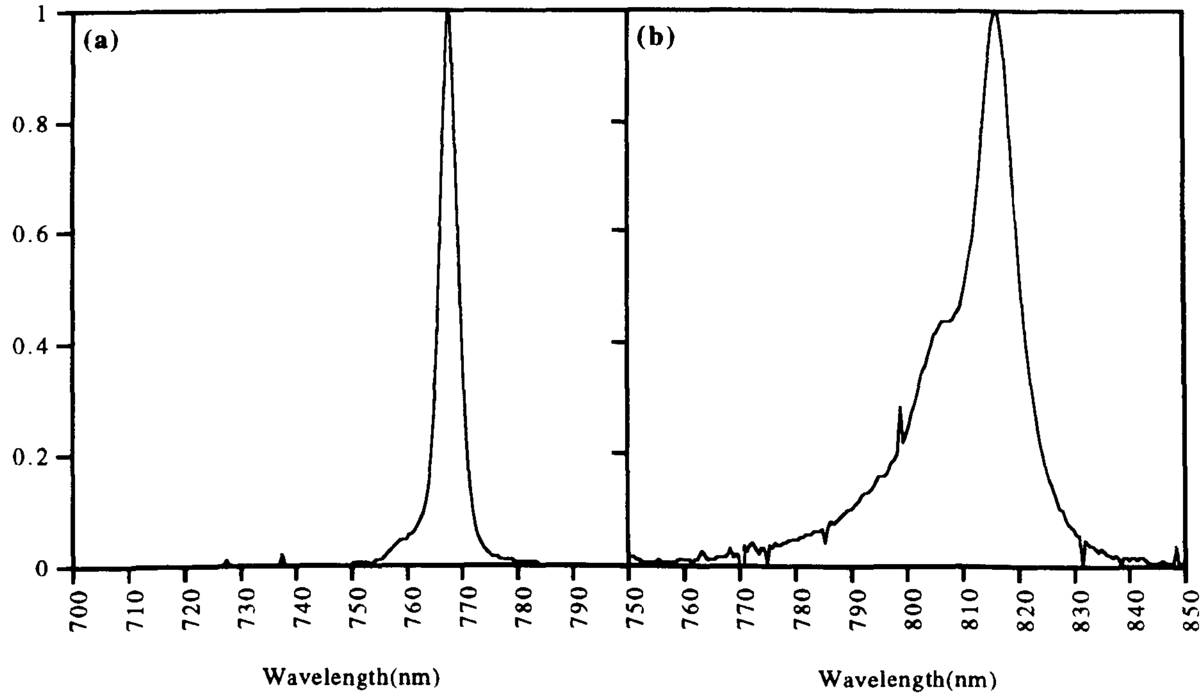

Fig. 5.17 B578 normalised PL spectra at (a) 77 K and (b) 300 K

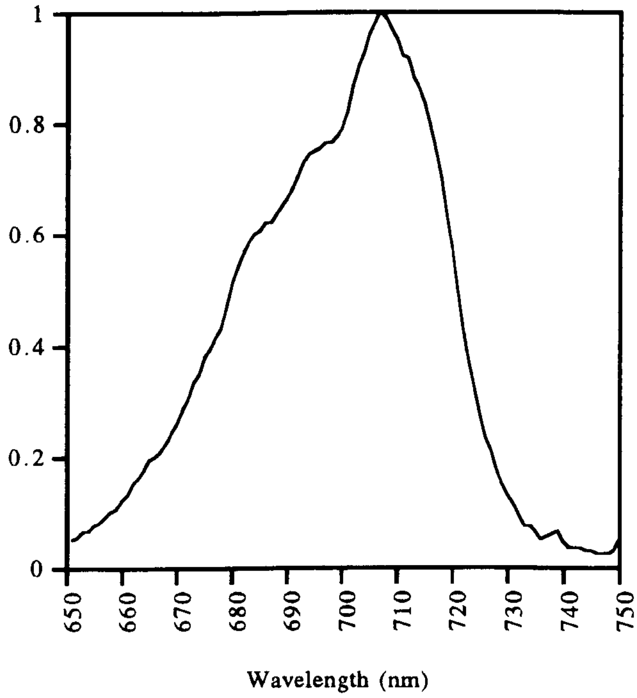

Fig. 5.18 B635 normalised PL spectrum at 77 K

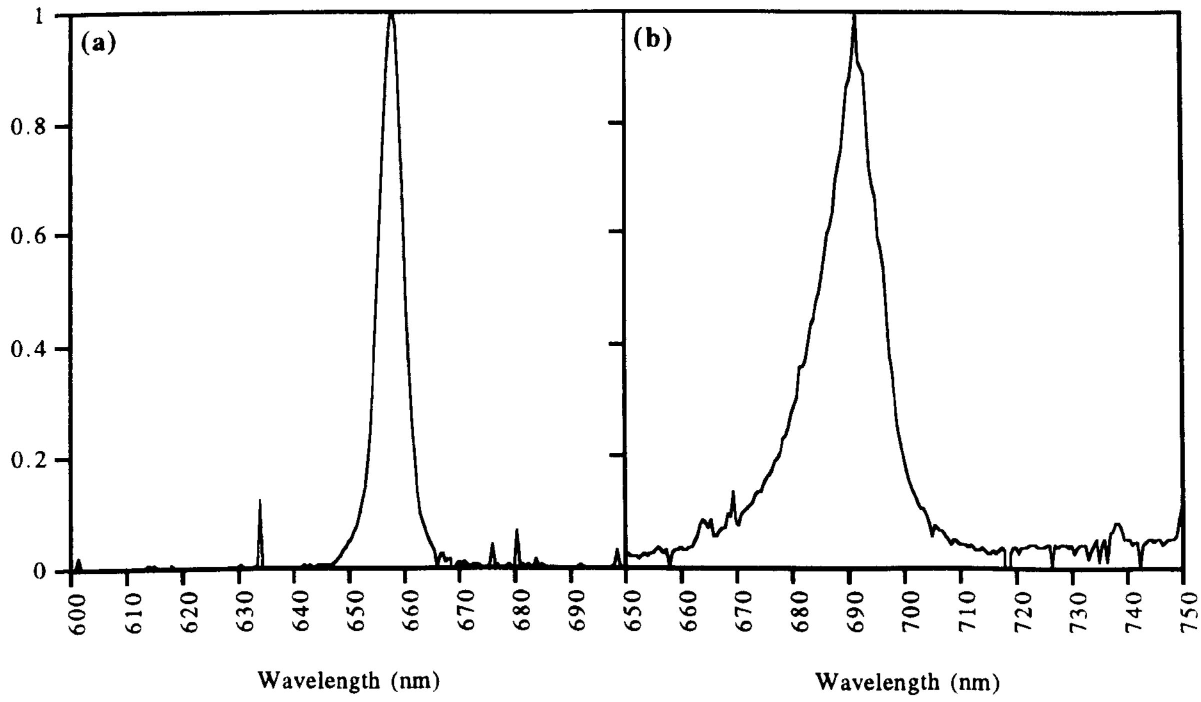

Fig. 5.19 B672 normalised PL spectra at **(a)** 77 K and **(b)** 300 K

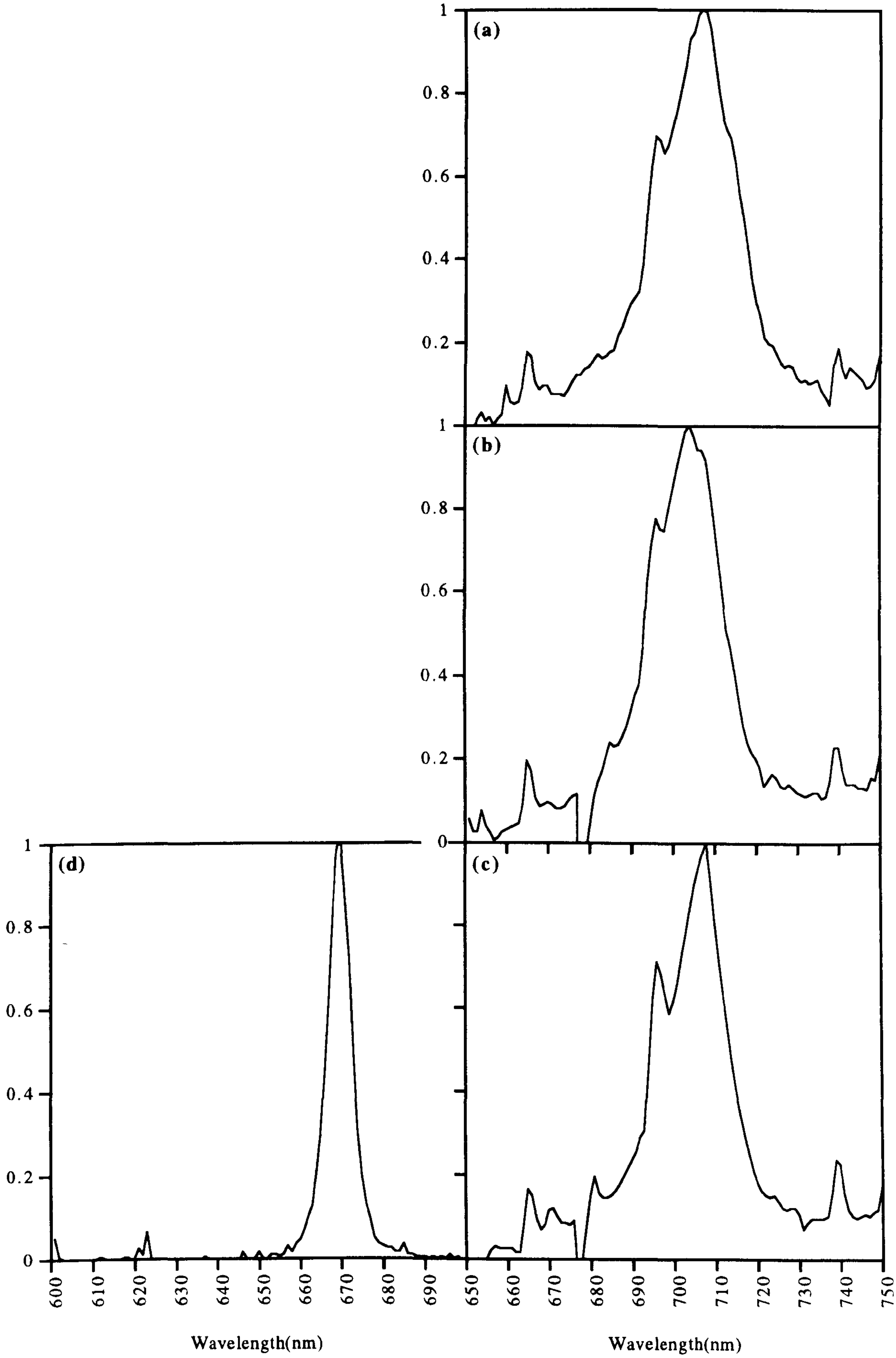

Fig. 5.20 B690 normalised PL spectra at **(a)** wafer centre (300 K) **(b)** 10 mm from wafer centre (300 K) **(c)** 20 mm from wafer centre (300 K) **(d)** 20 mm from wafer centre (77 K)

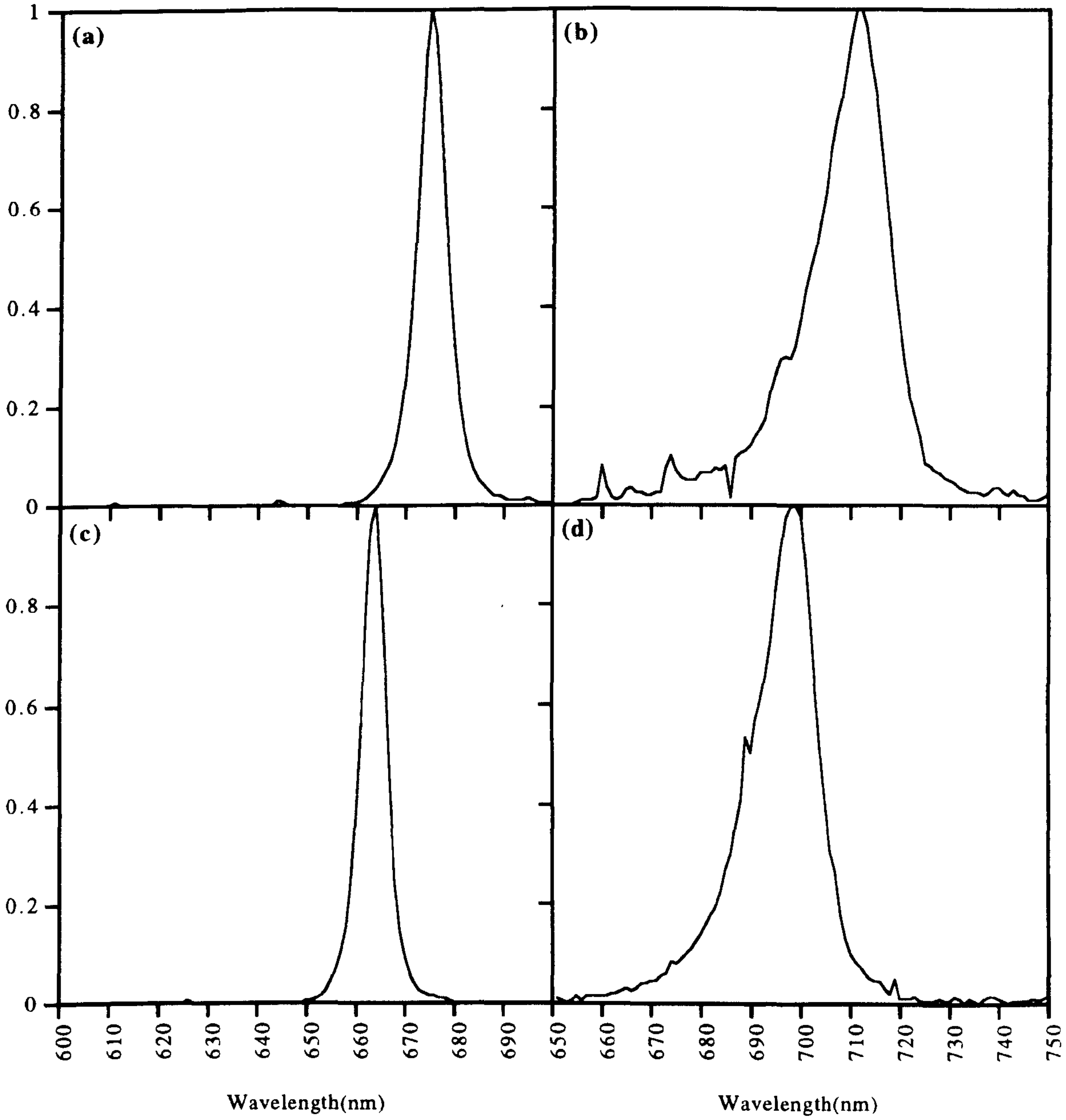

Fig. 5.21 QT849A normalised PL spectra at **(a)** edge of wafer opposite major flat (77 K) **(b)** edge of wafer opposite major flat (300 K) **(c)** edge of wafer adjacent to minor flat (77 K) **(d)** edge of wafer adjacent to minor flat (300 K)

Material	Growth Method	300K PL Peak λ (nm)	300K FWHM (meV)	77K PL Peak λ (nm)	77K FWHM (meV)	$\Delta\lambda = \lambda_{300K}-\lambda_{77K}$ (nm)
QT613 (ASQW)	MOCVD	695 (708.5)	28.2	660 (672.6)	22.8	35 (35.9)
B563 (ASQW)	MBE	814.4 (817.8)	17.6	771.4 (772.4)	9.0	43 (45.4)
B578 (ACQW)	MBE	817 (819.9)	20.4	768 (774.3)	8.4	49 (45.6)
B635 (ASQW)	MBE	- (709.4)	-	707 (673.8)	101.7	-
B672 (ACQW)	MBE	692 (710.2)	31.1	658 (673.9)	15.8	34 (36.3)
B690 (ACQW)	MBE	708 (710.2)	58.1	670 (673.9)	16.6	38 (36.3)
QT849A (ACQW)	MOCVD	698 - 712* (710.2)	35.4	664 - 675* (673.9)	19.3	31 - 42* (36.3)

Table 5.3 Summary of multiple AQW structure PL results at room temperature and 77 K (parameter values enclosed in brackets are calculated values for the nominal structures)

*Variations in the PL peak wavelength were observed across this wafer

The observed PL peak wavelengths have also been marked on the corresponding absorption spectra of Figs. 5.5 - 5.10, and, for the AQW structures with only AlGaAs in the well layers (QT613, B672, B690 and QT849A), the PL peak wavelength is considerably longer than the e1hh1 exciton wavelength. (For the QT849A material, variations in the layer compositions and thicknesses in the region of the wafer from which both the absorption and PL samples originated mean that the PL peak wavelength corresponding to the absorption spectrum of Fig. 5.10 cannot be accurately established. The range of the PL peak wavelengths observed is therefore indicated instead). For the AQW structures with GaAs in the well layers (B563 and B578), in contrast, the PL peak wavelengths are 1 - 2 nm shorter than the observed exciton peak wavelength. This is consistent with the fact that PL in these structures is occurring via the intrinsic e1hh1 interband transition mechanism.

There are several possible reasons why the peak PL wavelengths observed for the AlGaAs AQW structures do not occur within a few nm to the short wavelength side of the corresponding observed e1hh1 exciton peaks in the absorption spectra. Firstly, differences may exist in the MQW layer compositions or thicknesses between the absorption and PL samples. For all of the MBE-grown structures, however, no variations were observed in the PL peak wavelengths (see Fig. 5.20, for example, from which we notice that the room temperature PL peak wavelength is virtually constant across the B690 wafer). Variations were observed in the PL peak wavelength of the MOCVD-grown QT849A structure. These variations are consistent with the flow of reactant gases during MOCVD growth which gives rise to variations in the epitaxial structure, especially at the wafer edges adjacent to and opposite the minor flat. As both the transmission sample corresponding to the absorption spectrum of Fig. 5.10 and the PL sample corresponding to the room temperature PL spectrum of Fig. 5.21d were both taken from the region adjacent to the minor flat, it is difficult to make any conclusions regarding the position of the peak PL wavelength relative to the observed e1hh1 exciton peak for this structure. For the only other MOCVD-grown structure, the QT613 ASQW structure, both the PL and absorption samples were taken from a position near the centre of the wafer where no fluctuations were observed in the PL peak wavelength. We therefore conclude, that the observed differences in the e1hh1 absorption and PL wavelengths at room temperature for the MBE-grown structures and the MOCVD-grown QT613 structure, cannot be attributed to variations in the epitaxial structures occurring during growth.

Another possible explanation for the observed differences in the PL and e1hh1 wavelengths in the AlGaAs AQW structures is that, at the higher excitation intensities required to obtain a clear peak in the PL spectrum at room temperature, band-gap renormalisation [9] and/or sample heating occurred, both of which would cause a red shift in the PL wavelength. To examine this possibility we may refer to the results of Table 5.3 from which we notice that $\Delta\lambda$(meas) is approximately equal to $\Delta\lambda$(calc) for the AlGaAs AQW structures QT613, B672 and B690. We therefore conclude that neither band-gap renormalisation nor heating effects occurred at the higher excitation levels required to obtain a PL spectrum at 300K.

Finally, it may be recalled that the observed peak PL/e1hh1 wavelength differences were only observed for the AlGaAs AQW structures and not for the GaAs AQW structures. This suggests that the discrepancy between the PL and e1hh1 absorption wavelengths may be explained by the relative electron affinities of Ga and Al: Al has a higher electron affinity and is therefore much more reactive than Ga so that the concentrations of impurities incorporated into AlGaAs layers during growth are often orders of magnitude greater than the impurity concentrations in GaAs layers. It is universally acknowledged that C is the main unintentional impurity in nominally undoped MBE- and MOCVD-grown GaAs/AlGaAs layers in which it forms shallow acceptor levels [11,12,13,14]. We may therefore hypothesise that, in contrast to the GaAs AQW structures for which the dominant room temperature PL transition was observed to be the intrinsic e1hh1 transition, the dominant PL recombination mechanism for the AlGaAs AQW structures is the free electron to C shallow acceptor level transition, e1->C. From the modelling results of Masselink *et al.* [15] and the experimental results of Miller *et al.* [16], we estimate that the C acceptor binding energies E_C in the AlGaAs AQW structures relative to the first bound heavy hole sub-band edge are between 30 and 40 meV. To estimate the expected energy separation of the e1->C transition from the e1hh1 bound exciton transition we then simply subtract the exciton binding energy E_X from the C acceptor binding energy i.e. if E_{e1C} denotes the energy of the e1->C transition, and E_{e1hh1X} denotes the energy of the e1hh1 bound exciton absorption feature, then:

$$E_{e1hh1X} - E_{e1C} = E_C - E_X \qquad (5.5)$$

Estimating the e1hh1 exciton binding energies to be between 8 and 10 meV for the AlGaAs AQW structures as before, then yields:

$$20\ \text{meV} < E_C - E_X < 32\ \text{meV} \qquad (5.6a)$$

which, in terms of wavelengths is:

$$7.9\ \text{nm} < \Delta\lambda < 12.6\ \text{nm} \qquad (5.6b)$$

i.e. if e1->C is the dominant PL mechanism for the AlGaAs AQW structures, then we would expect the PL peak wavelength to be between 7.9 and 12.6 nm longer than the e1hh1 exciton peak wavelength. From inspection of the absorption spectra of Figs. 5.5, 5.8 and 5.9, we see that this is indeed approximately the case, and we conclude that the identification of the e1->C transition as the room temperature PL mechanism for the QT613, B672 and B690 structures is consistent with our experimental results.

Further evidence that the observed PL spectral peaks for the AlGaAs AQW structures are, in fact, due to extrinsic PL as a result of the e1->C transition may be found from consideration of the PL spectra obtained for *all* the AQW structures (both AlGaAs and GaAs) of Figs. 5.15 - 5.21 *at both room temperature and 77K*. Examining the PL spectra of the AlGaAs AQW structures QT613, B672, B690 and QT849A first, (which we have hypothesised are the result of an e1->C transition) we notice that, in going from 77 K to 300 K, phonon broadening occurs which is more pronounced at shorter wavelengths resulting in "shoulder-type" features for QT849A and even peak features for B690. The wavelength separation of these features from the PL peak in both cases is consistent with their identification as e1hh1 transitions. Physically this behaviour arises because, after excitation at 514.5 nm, the hot carriers rapidly thermalise so that the electrons relax to e1 while the holes relax to hh1; at 77 K only a very small proportion of the (finite number of) C acceptors will be ionised (since $E_C \approx 30 - 40$ meV while $kT \approx 6.6$ meV) so that e1->C transitions dominate. At 300 K however, more of the C acceptors will be ionised so that spontaneous emission begins to occur as a result of recombination from e1->hh1 in addition to e1->C.

For the GaAs AQW structures B563 and B578 which exhibit intrinsic PL on excitation (since the C concentration is orders of magnitude lower in the GaAs well layers of these structures), an even more pronounced broadening towards shorter wavelengths may be observed in the PL spectra of Figs. 5.16 and 5.17 respectively at 300 K. Now, it is well known that any excitons present in QW structures are rapidly ionised at room temperature due to collisions with LO phonons [17] and that the intrinsic PL recombination transition is the e1hh1 free electron to free hole transition. There is also evidence to suggest that such excitons are still ionised even at 77 K [18] when $kT \approx 6.6$ meV. Now, it may be recalled that, for the B563 and B578 structures, the observed room temperature PL wavelength was indeed approximately equal to the observed e1hh1 absorption wavelengths in Figs. 5.6 and 5.7 respectively. We may therefore attribute the significant shoulders on the shorter wavelength side of the main peaks in the room temperature PL spectra of Figs. 5.16 and 5.17 to the e1lh1 recombination which occurs due to thermal population of the lh1 level at 300 K. Furthermore, to appreciate why the short wavelength shoulders in the room temperature PL spectra are more pronounced in general for the GaAs AQW structures B563 and B578 relative to the corresponding features for the AlGaAs AQW structures, we just have to compare the calculated magnitudes of (e1lh1-e1hh1) for the GaAs AQW structures with the C acceptor binding energies for the AlGaAs AQW structures: in the GaAs AQW structures B563 and B578, (e1hh1-e1lh1) ≈ 11 nm ≈ 21 meV, while for the AlGaAs AQW structures typically we might have E_C ≈ 30 - 40 meV [16,17]. Hence, at 300 K (kT ≈ 26 meV) we would expect lh1 for the GaAs structures to be thermally populated to a greater extent than hh1 would be for the AlGaAs AQW structures. This results in correspondingly larger e1lh1 features on the shorter wavelength side of the room temperature PL spectra for the GaAs structures compared with the e1hh1 features on the shorter wavelength side of the room temperature PL spectra for the AlGaAs structures.

Finally, we must make some comments on the FWHM values of the various PL peaks observed at 77 K in Figs. 5.15 - 5.21. Firstly, the PL spectra observed for the AlGaAs AQW structures were broader than PL spectra for the B563 and B578 GaAs AQW structures due to Al inhomogeneities. Furthermore, the B635 ASQW exhibited the largest PL FWHM at 77 K by far, for reasons which become immediately obvious when we examine the ASQW structure in Appendix A : due to the deep (GaAs layer sandwiched between $Al_{0.6}Ga_{0.4}As$ and $Al_{0.4}Ga_{0.6}As$ layers) narrow (6 monolayers ≈ 17Å) well regions, variations as small as ±1 monolayer in the GaAs layer thickness throughout the multiple AQW result in large variations in the first bound electron and heavy hole levels. It is no coincidence either, that the AQW structure exhibiting the next largest FWHM is the QT613 AQW structure which has relatively deep ($Al_{0.15}Ga_{0.85}As$ layer sandwiched between $Al_{0.44}Ga_{0.56}As$ and $Al_{0.37}Ga_{0.63}As$ layers) narrow (30Å) well regions. Any variations in the $Al_{0.15}Ga_{0.85}As$ layer thickness over the multiple AQW will therefore result in substantial variations in the e1 energy and the C acceptor binding energy E_C.

5.4 Conclusions

Asymmetric quantum well structures have several different tensor elements associated with them by virtue of the asymmetry of the two first bound electron envelope functions and a first bound hole function. The AQW layer thicknesses and compositions must be carefully chosen to maximise these tensor elements. In addition, the AQWs should be designed to ensure that the fundamental photon energy is below the half-bandgap (and the second harmonic photon energy is below the bandgap) to avoid two-photon absorption of the fundamental beam (and linear absorption of the second harmonic beam). The MQW layer should also be designed to ensure negligible coupling between neighbouring wells. The growth of asymmetric stepped QW structures with three different Al fractions using only two Al cells can pose a further practical constraint on the layer compositions. Characterisation measurements have shown that the growth of AQW structures within all of these constraints is relatively demanding. Therefore, with the exception of the QT613 ASQW structure, all of the AQW structures were designed to satisfy the design constraints in the presence of growth inaccuracies.

There are several important considerations for the design of waveguide epitaxial structures for SHG, including single-moded operation at the fundamental wavelength, minimum leakage to the substrate, and a maximum overlap factor for SHG. The waveguide structures were therefore designed in accordance with these principles.

From absorption measurements, it was apparent that all of the AQW structures studied (especially the structures with higher Al fractions in the AQW layers) provided more quantum confinement than the nominal structures. This was attributed to the actual QW layers being thinner than the nominal QW layers. In particular, there was no evidence of any features in the absorption spectrum of the QT613 ASQW structure corresponding to interband transitions from a second bound electron to a second bound hole level. Calculations were therefore performed which showed that the e2 level was a relatively strong function of the QW layer thicknesses and it was concluded that the QT613 QW layers were so thin that no e2 level was supported in the wells. This conclusion is also consistent with the failure to observe any unphase-matched SHG associated with the AQW tensor component $\chi^{(2)}_{zzz}$ in waveguides fabricated from the QT613 material (see Chapter 7).

For the higher Al fraction AQW structures, (both MOCVD- and MBE-grown) the observed PL peak wavelength was ≈ 10 nm longer than the observed wavelength of the e1hh1 exciton absorption peak. This was attributed to the incorporation of more carbon in the higher Al fraction layers during growth and PL via the extrinsic e1 -> C transition. The PL peak wavelength for the MBE-grown AQW structures with GaAs layers was, however, consistent with intrinsic PL via the e1hh1 transition. Higher C concentrations in the higher

Al fraction AQW structures should not have any particularly detrimental consequences for SHG in these structures.

The PL FWHM spectral widths for the different AQW structures studied were all approximately less than 20 meV at 77 K indicating good growth uniformity across the MQW layers in every case except the narrow ASQW B635 structure. The PL FWHM in the case of the B635 structure was greater than 100 meV and this was attributed to monolayer fluctuations in the thickness of the deep narrow well layers across the MQW. Consequently, no further experiments were attempted with the B635 structure.

X-ray diffraction measurements indicated that the actual MQW periods and the average Al fractions in the different waveguide epitaxial layers of the AQW structures studied were approximately equal to those of the nominal structures with the exception of the B672 structure. Consequently no further experiments were performed with the B672 structure.

No additional information about the B563 or B578 AQW structures was gained from PLE measurements at 77 K over the information obtained from room temperature absorption measurements. The non-destructive nature of PLE was also outweighed by the considerable complexity of the measurement and PLE experiments were accordingly abandoned.

TEM measurements for the determination of the AQW layer thicknesses were also abandoned due to the time-consuming destructive nature of the sample preparation process.

From all of the characterisation results, it would appear that the B563, B578, B690 and QT849A AQW structures were the only AQW structures grown approximately to specification. Quantum well intermixing and SHG experiments were therefore performed with these structures and these experiments are described in the following chapters.

---

[1] S. Adachi, "GaAs, AlAs, and $Al_xGa_{1-x}As$: Material Parameters for Use in Research and Device Applications", J. Appl. Phys. **58**, R1 (1985)

[2] E. S. Koteles and J. Y. Chi, "Experimental Exciton Binding Energies in $GaAs/Al_xGa_{1-x}As$ Quantum Wells as a Function of Well Width", Phys. Rev. B **37**, 6332 (1988)

[3] D. A. B. Miller, J. S. Weiner, and D. S. Chemla, "Electric-Field Dependence of Linear Optical Properties in Quantum Well Structures: Waveguide Electroabsorption and Sum Rules", J. Quantum Electron. **22**, 1816 (1986)

[4] C. Kelaidis, D. C. Hutchings, and J. M. Arnold, "Asymmetric Two-Step GaAlAs Quantum Well for Cascaded Second-Order Processes", Transactions on Quantum Electron. **30**, 2998 (1994)

[5] S. I. Hansen, "The Refractive Index Change in GaAs/AlGaAs Quantum Wells Produced by Neutral Impurity Induced Disordering Using Boron and Fluorine", PhD Thesis, University of Glasgow (1993), and M. A. Afromowitz, "Refractive Index of $Ga_{1-x}Al_xAs$", Solid State Commun. **15**, 59 (1974)

[6] R. L. Greene and K. K. Bajaj, "Binding Energies of Wannier Excitons in $GaAs/Ga_{1-x}Al_xAs$ Quantum Well Structures", Solid State Commun. **45**, 831 (1983)

[7] J. Singh, "Semiconductor Optoelectronics", McGraw-Hill, New York, 1995

[8] D. S. Chemla and D. A. B. Miller, "Room-temperature Excitonic Nonlinear-optical Effects in Semiconductor Quantum-well Structures", J. Opt. Soc. Am. B **2**, 1155 (1985)

[9] R. C. Miller, D. A. Kleinman, W. A. Nordland Jr., and A. C. Gossard, "Luminescence Studies of Optically Pumped Quantum Wells in $GaAs/Al_xGa_{1-x}As$ Multilayer Structures", Phys. Rev. B **22**, 863 (1980)

[10] W. T. Masselink, P. J. Pearah, J. Klem, C. K. Peng, H. Morkoc, G. D. Sanders and Y. Chang, "Absorption Coefficients and Exciton Oscillator Strengths in AlGaAs/GaAs Superlattices", Phys. Rev. B **32**, 8027 (1985)

[11] G. Wicks, W. I. Wang, C. E. C. Wood, L. F. Eastman, and L. Rathbun, "Photoluminescence of $Al_xGa_{1-x}As$ Grown by Molecular Beam Epitaxy", J. Appl. Phys. **52**, 5792 (1981)

[12] G. B. Stringfellow and R. Linnebach, "Photoluminescence of Shallow Acceptors in Epitaxial $Al_xGa_{1-x}As$", J. Appl. Phys. **51**, 2212 (1980)

[13] M. Heiblum, E. E. Mendez, and L. Osterling, "Growth by Molecular Beam Epitaxy and Characterisation of High Purity GaAs and AlGaAs", J. Appl. Phys. **54**, 6982 (1983)

[14] A. Mircea-Roussel, A. Brière, J. Hallais, A. T. Vink, and H. Veenvliet, "Photoluminescence Investigation of Residual Shallow Acceptors in $Al_xGa_{1-x}As$ Grown by Metalorganic Vapor Phase Epitaxy", J. Appl. Phys. **53**, 4351 (1982)

[15] W. T. Masselink, Y. Chang, and H. Morkoç, "Binding Energies of Acceptors in $GaAs/Al_xGa_{1-x}As$ Quantum Wells", Phys. Rev. B **28**, 7373 (1983)

[16] R. C. Miller, A. C. Gossard, W. T. Tsang, and O. Munteanu, "Extrinsic Photoluminescence from GaAs Quantum Wells", Phys. Rev. B **25**, 3871 (1982)

[17] D. S. Chemla, D. A. B. Miller, P. W. Smith, A. C. Gossard, and W. Wiegmann, "Room Temperature Excitonic Nonlinear Absorption and Refraction in GaAs/AlGaAs Multiple Quantum Well Structures", J. Quantum. Electron. **20**, 265 (1984)

[18] H. Kawai, K. Kaneko, and N. Watanabe, "Photoluminescence of AlGaAs/GaAs Quantum Wells Grown by Metalorganic Chemical Vapor Deposition", J. Appl. Phys. **56**, 463 (1984)

6

Impurity-free Vacancy Disordering for the Control of GaAs/AlGaAs AQW Second Order Non-linearities

From Chapter 2, it may be recalled that the control of second order non-linear effects using quasi-phase-matching requires that the second order non-linearity is periodically modulated. As mentioned briefly in Section 3.3, the tensor elements $\chi^{(2)}_{xzx}$, $\chi^{(2)}_{zxx}$, and $\chi^{(2)}_{zzz}$ associated with AQW structures only exist due to the well asymmetry. GaAs/AlGaAs MQW structures also have associated tensor elements $\chi^{(2)}_{xyz} \approx \chi^{(2)}_{yxz} \approx \chi^{(2)}_{zxy}$ due to the non-centro-symmetric crystal structure of the bulk GaAs/AlGaAs material itself. All of the above tensor elements ($\chi^{(2)}_{xzx}$, $\chi^{(2)}_{zxx}$, $\chi^{(2)}_{zzz}$, $\chi^{(2)}_{xyz}$, $\chi^{(2)}_{yxz}$, and $\chi^{(2)}_{zxy}$) are resonant at the half-bandgap. Intermixing AQW structures causes *both* bandgap widening *and* a reduction in the asymmetry. Therefore, for sub-half-bandgap operation, $\chi^{(2)}_{xzx}$, $\chi^{(2)}_{zxx}$, and $\chi^{(2)}_{zzz}$ are potentially reduced due to a combination of bandgap widening *and* a reduction in the QW asymmetry, while $\chi^{(2)}_{xyz} \approx \chi^{(2)}_{yxz} \approx \chi^{(2)}_{zxy}$ are potentially reduced due to bandgap widening *alone*. Quasi-phase-matching may therefore be feasible by periodically intermixing a multiple AQW waveguide structure along its length.

Several techniques exist for quantum well intermixing in the GaAs/AlGaAs material system including impurity induced disordering (IID) and impurity-free vacancy disordering (IFVD). IID involves implantation or diffusion of either an electrically-active impurity or a neutral impurity into the epitaxial structure incorporating the MQW layer, followed by a high temperature annealing stage. The presence of the dopant species leads to the formation of group III vacancies or interstitials during annealing which subsequently migrate through the crystal lattice to the MQW layer where they facilitate intermixing. However, to enhance the intermixing process significantly (over and above the intermixing which occurs due to native defects in the crystal lattice), the dopant concentrations must be in excess of $\approx 10^{18}$ cm^{-3}. For the case of electrically-active dopants, this results in high free carrier absorption losses in waveguide devices, while for neutral impurity induced disordering, high waveguide losses are observed due to residual implantation damage [1]. IFVD, on the other hand, requires only the deposition of a dielectric cap layer onto the surface of the epitaxial GaAs/AlGaAs structure prior to annealing, and therefore circumvents the problems associated with IID. During annealing, the dielectric cap is relatively impermeable to As, while Ga, in contrast, diffuses readily through the cap material. This generates group III vacancies at the GaAs/dielectric interface which subsequently diffuse through the MQW layer where they promote the intermixing process.

Silica is the most widely used IFVD dielectric cap material in practice [2,3,4,5]. This is because Ga diffuses particularly well through SiO_2 resulting in enhanced Al-Ga interdiffusion coefficients in the AlGaAs epitaxial structure which are over an order of magnitude greater than the interdiffusion coefficients due to native-defect-induced disordering for similar epitaxial structures at the same temperature [6,7]. The use of a SiO_2 cap for IFVD then imposes certain constraints on the design of a waveguide epitaxial structure which is comprised of an MQW guiding layer sandwiched between two cladding layers and capped with a thin GaAs protective layer. Firstly, Guido *et al.* [2] have shown that, if the GaAs protective cap layer is too thin, a reaction occurs at the GaAs/SiO_2 interface which effectively results in Si impurity-induced disordering of the epitaxial layers with its inherent problems. To avoid these problems, Guido *et al.* advocate the growth of a GaAs surface layer of a thickness approximately ≥ 1000 Å, so that the later GaAs/AlGaAs multiple AQW structures grown for this project all had 1000 Å GaAs cap layers.

Another constraint on the waveguide epitaxial structure arises because choosing the upper cladding layer to be too thick means that the spatial resolution of the selective area IFVD process is likely to be reduced (see Section 6.3). The upper cladding layer should not, however, be so thin that surface roughness results in significantly increased waveguide losses or that ridge waveguide etch depth inaccuracies lead to undesirable waveguiding behaviour such as mulitmoded operation. An upper cladding layer thickness of 0.8 μm was therefore chosen for all the AQW waveguide structures used in this work as it was believed to represent the best compromise between the above effects.

6.1 Modelling the IFVD Process for Suppression of the Multiple AQW Second Order Non-linearities

6.1.1 Modelling the Interdiffusion of Ga and Al in GaAs/AlGaAs MQW Structures

To model the QW intermixing behaviour which occurs as a result of IFVD (which is essentially a 1D phenomenon for thin epitaxial layers), it may be assumed that the Al-Ga interdiffusion coefficient D is constant everywhere. Furthermore, it will be assumed that D is independent of the initial Al fraction profile in the MQW layer. The Al fraction x as a function of depth z and time t then obeys Fick's law:

$$\frac{\partial x(z,t)}{\partial t} = D\frac{\partial^2 x(z,t)}{\partial z^2} \qquad (6.1)$$

For a given initial MQW Al fraction profile, $x(z,0)$, (6.1) may be solved to yield the intermixed Al fraction profile at any subsequent time t, $x(z,t)$ subject to appropriate boundary conditions. When modelling the intermixing of an *entire* MQW layer comprised of several QW periods incorporated in a waveguide structure for example, a sensible approximation would be to assume infinitely thick waveguide cladding layers. For the MQW waveguide epitaxial structures of interest for this work however, with 50 wells or more in each, this was not very appropriate. Intuitively however, the interdiffusion of Al and Ga within a QW near the middle of such an MQW layer, will not be influenced to any great extent by interdiffusion occurring at the outermost QW's. To a first approximation therefore, when modelling the intermixing of a QW at the centre of such an MQW layer, the diffusion equation of (6.1) may be solved for a 3-well system sandwiched between infinitely thick barrier layers as illustrated in Fig. 6.1a. The intermixed central QW potential profile of the 3-well system should then approximately resemble the intermixed profile of a QW at the centre of an MQW layer with a much larger number of periods. To this end, the diffusion length L_d is defined by:

$$L_d = \sqrt{Dt} \qquad (6.2)$$

D is an increasing function of temperature, so that L_d reflects the extent of interdiffusion i.e. the more severe the anneal to which a GaAs/AlGaAs structure is subjected (the higher the temperature and the longer the duration), the greater the diffusion length. The solution of Fick's law for a *single* ASQW structure such as that depicted in Fig. 3.1 in terms of error functions involving z and L_d is then given by (6.3) where the z co-ordinate origin is defined in Fig. 6.1a [8,9]:

$$\begin{aligned} x(z,L_d) = x_b - \tfrac{1}{2}(x_b - x_1)\cdot \mathrm{erf}\left\{\frac{z-(W_b/2)}{2L_d}\right\} \\ +\tfrac{1}{2}(x_2 - x_1)\cdot \mathrm{erf}\left\{\frac{z-\left[(W_b/2)+W_1\right]}{2L_d}\right\} \\ +\tfrac{1}{2}(x_b - x_2)\cdot \mathrm{erf}\left\{\frac{z-\left[(W_b/2)+W_1+W_2\right]}{2L_d}\right\} \end{aligned} \qquad (6.3)$$

Here x_b, x_1, and x_2 are the Al fractions in the barriers, the deeper well layer and the shallower well layer of the starting material ASQW structure respectively, and W_b, W_1, and W_2 are the thicknesses of the barriers, the deeper well layer and the shallower well layer of the starting material structure respectively. Similarly, for a *single* ACQW such as that depicted in Fig. 3.2 we have:

$$
\begin{aligned}
x(z,L_d) = x_b &- \tfrac{1}{2}(x_b - x_w)\cdot \operatorname{erf}\left\{\frac{z-(W_b/2)}{2L_d}\right\} \\
&+ \tfrac{1}{2}(x_b - x_w)\cdot \operatorname{erf}\left\{\frac{z-[(W_b/2)+W_1]}{2L_d}\right\} \\
&- \tfrac{1}{2}(x_b - x_w)\cdot \operatorname{erf}\left\{\frac{z-[(W_b/2)+W_1+W_2]}{2L_d}\right\} \\
&+ \tfrac{1}{2}(x_b - x_w)\cdot \operatorname{erf}\left\{\frac{z-[(W_b/2)+W_1+W_2+W_3]}{2L_d}\right\}
\end{aligned}
\tag{6.4}
$$

where x_b, and x_w are the Al fractions in the barrier and well layers of the ACQW as-grown structure and W_b, W_1, W_2, and W_3 are the thicknesses of the thicker barrier layers, the thicker well layer, the thinner barrier layer, and the thinner well layer respectively. For the case of a *single* symmetric well of width W, barrier layer thickness W_b, and Al fractions of x_w and x_b in the well and barrier layers respectively, we obtain a rather simpler expression for $x(z,L_d)$:

$$
\begin{aligned}
x(z,L_d) = x_b &- \tfrac{1}{2}(x_b - x_w)\cdot \operatorname{erf}\left\{\frac{z-(W_b/2)}{2L_d}\right\} \\
&+ \tfrac{1}{2}(x_b - x_w)\cdot \operatorname{erf}\left\{\frac{z-[(W_b/2)+W]}{2L_d}\right\}
\end{aligned}
\tag{6.5}
$$

Expressions (6.3) to (6.5) are then easily extended to yield the Al fraction profiles across an MQW layer with an arbitrary number of periods. Figs. 6.2, 6.3 and 6.4 show the Al fraction profiles thus obtained for 3 periods of the B563, B578 and B690 multiple AQW structures respectively for several values of the diffusion length. The Al fraction profiles for 3 periods of the partially intermixed symmetric QW structures A776 and B579 are also shown in Figs. 6.5 and 6.6 respectively to allow a comparison of experimental intermixing results obtained for these structures with intermixing results for the B563, B578 and B690 structures. Finally, it should be mentioned that the diffusion equation was also solved for different 5-well systems. In each case, it was found that the central well Al fraction profile was not significantly different from the central well profile in the corresponding 3-well system provided $L_d \leq 50Å$. It was therefore concluded that, in so far as the central well profile was concerned, the 3-well approximation was valid for $L_d \leq 50Å$.

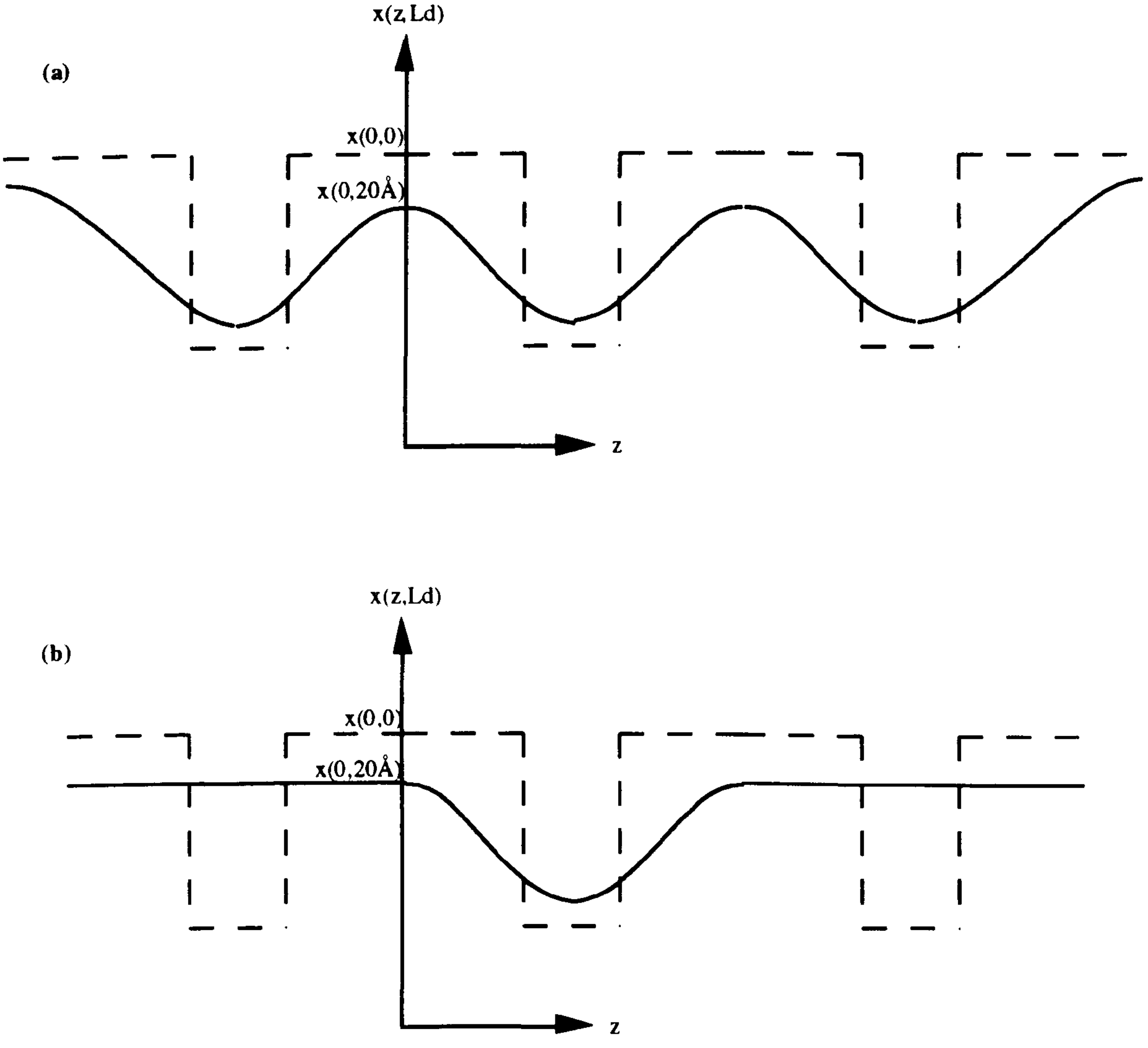

Fig. 6.1 Partially intermixed 3-well system **(a)** partially intermixed Al fraction profile of a 3-well system with infinitely thick barriers **(b)** partially intermixed Al fraction profile assumed for solution of Schrödinger's equation in central well with infinitely thick barriers

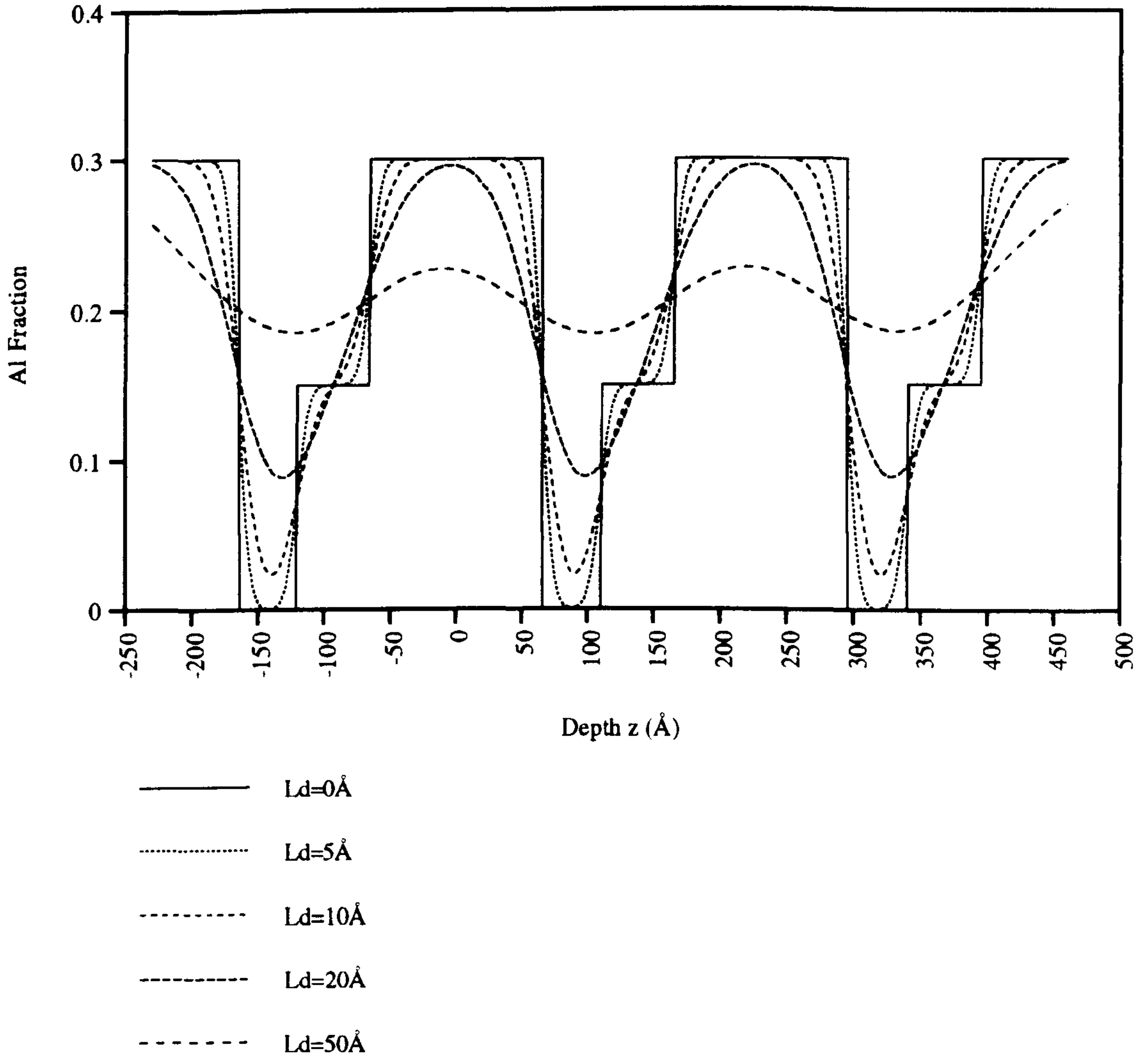

Fig. 6.2 B563 Al fraction profiles in a partially intermixed 3-well system for several different diffusion lengths

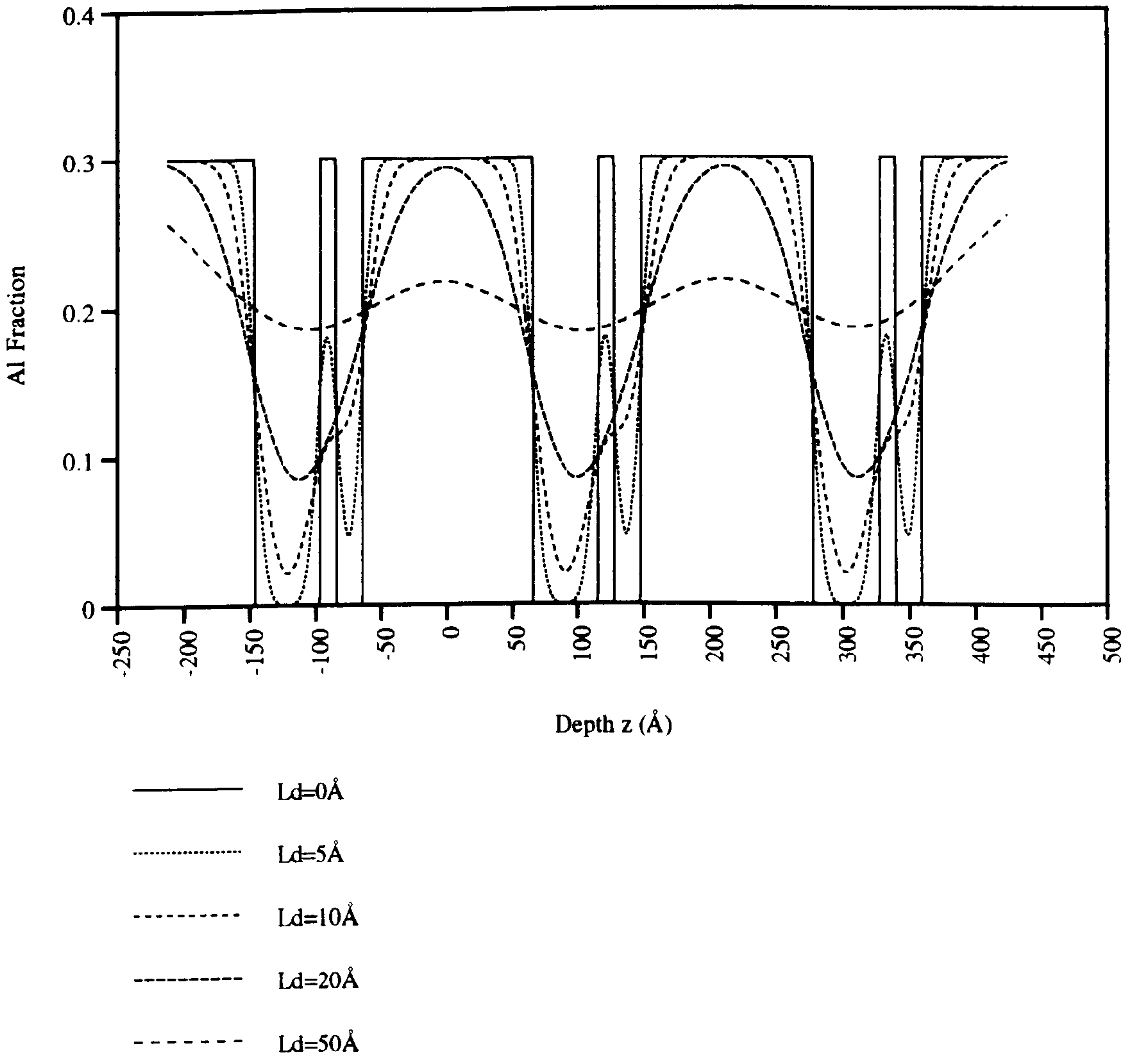

Fig. 6.3 B578 Al fraction profiles in a partially intermixed 3-well system for several different diffusion lengths

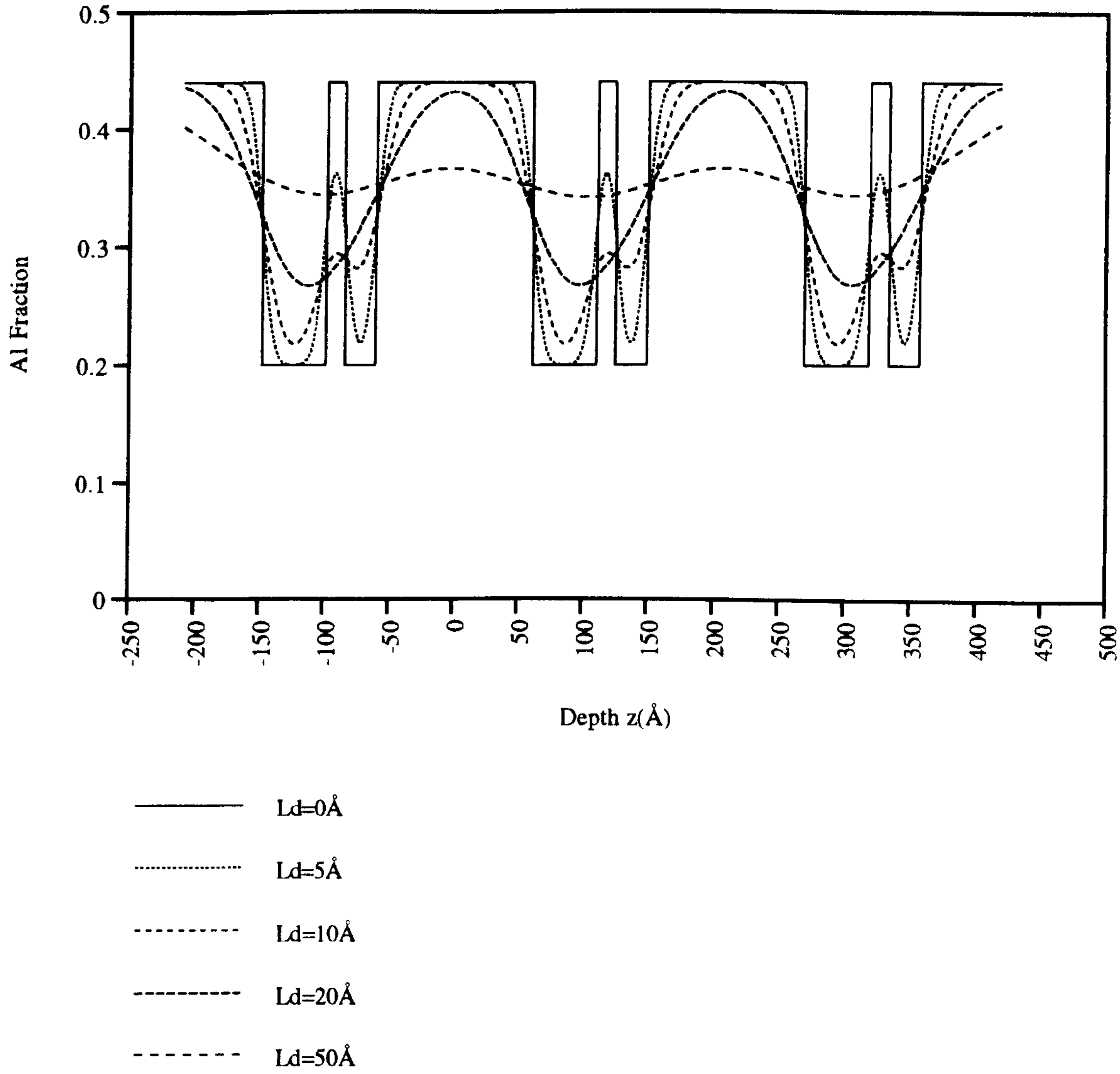

Fig. 6.4 B690 Al fraction profiles in a partially intermixed 3-well system for several different diffusion lengths

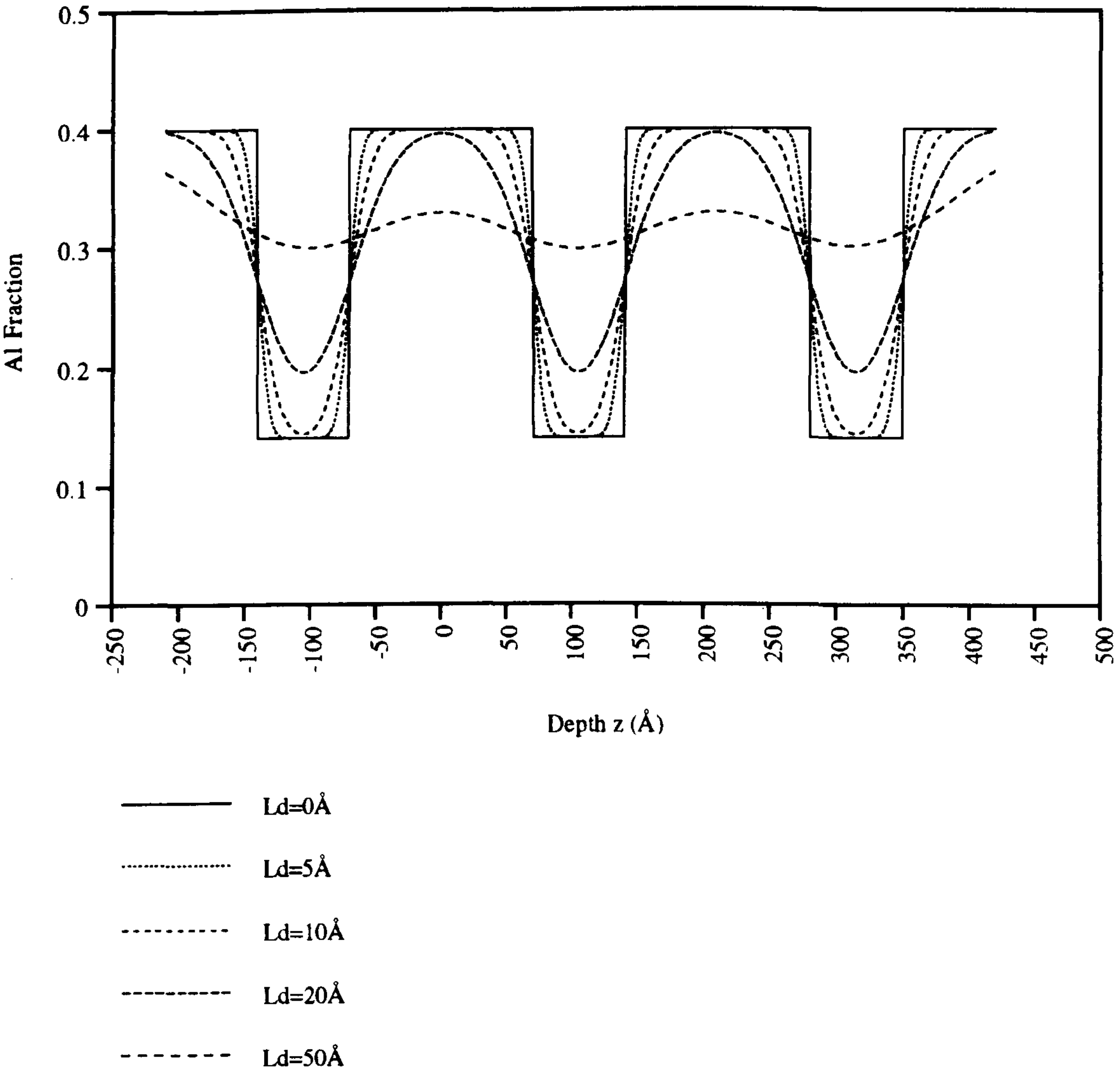

Fig. 6.5 A776 Al fraction profiles in a partially intermixed 3-well system for several different diffusion lengths

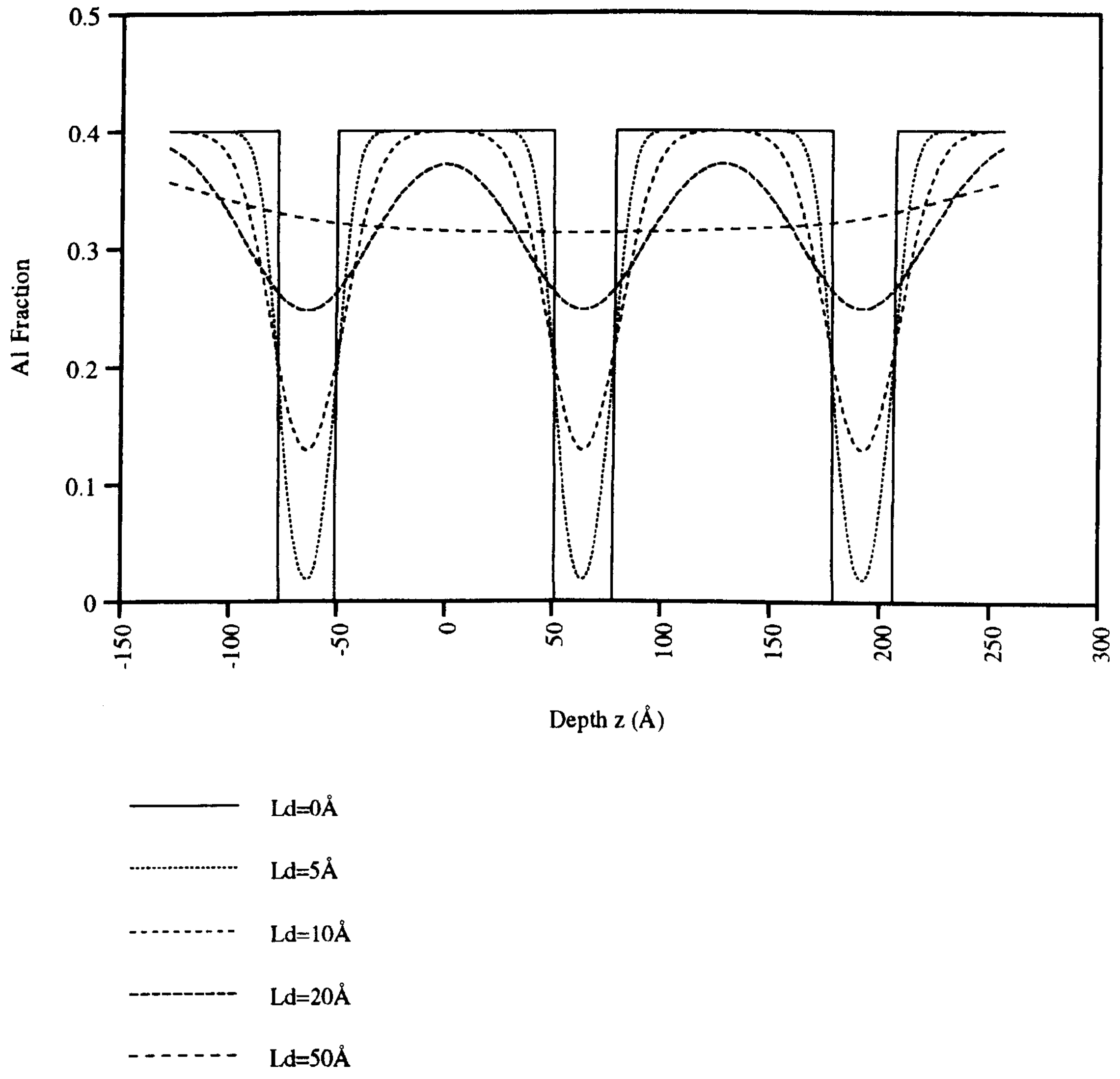

Fig. 6.6 B579 Al fraction profiles in a partially intermixed 3-well system for several different diffusion lengths

6.1.2 The Peak PL Wavelength Blueshift of GaAs/AlGaAs MQW Structures as a Measure of the Degree of Intermixing

From the central well profiles of Figs. 6.2 to 6.6 it is possible to make some general comments about the intermixing process: initially, the bottom half of a QW is "squeezed", while the upper half becomes wider; as intermixing continues, the minimum Al fraction in the deepest well region begins to increase while the maximum Al fraction in the barrier layers begins to fall, and, in the limit as $L_d \rightarrow \infty$, we would expect a bulk alloy to be formed with a composition equal to the average composition of the starting material MQW layers. Since we have assumed infinitely thick barriers for our 3-well model however, in the limit as $L_d \rightarrow \infty$, a bulk alloy is obtained with a composition equal to that of the barrier layers. Provided L_d does not exceed 50 Å, however, we believe the infinitely thick barrier approximation remains valid for the central well profile in the 3-well system. The narrowing at the bottom of the QWs and the increase in the minimum Al fraction both combine to push the lowest bound electron level upwards (and the lowest bound hole levels correspondingly downwards). The result is that the intrinsic PL bandgap widens i.e. the intrinsic PL peak wavelength blueshifts. The intrinsic peak PL wavelength blueshift observed after annealing a sample at high temperature, therefore reflects the extent to which the MQW layer has been intermixed.

For the B690 ACQW structure with $Al_{0.2}Ga_{0.8}As$ in the well layers, it was established in Chapter 6 that the dominant PL mechanism was the extrinsic e1->C transition. Therefore, in order to use the PL peak wavelength blueshift as a measure of the degree of intermixing for this structure, we must estimate in some way the change in the e1->C bandgap which occurs during intermixing. Now, if E_{e1hh1} denotes the energy of the e1hh1 transition and E_{e1C} denotes the energy of the e1->C transition, then:

$$E_{e1C} = E_{e1hh1} - E_C \tag{6.6}$$

where E_C is the carbon acceptor binding energy.

From the experimental data of Miller *et al.* [10], in conjunction with the modelling results of Masselink *et al.* [11], we estimate that, for a symmetric 100 Å-wide GaAs QW with $Al_{0.3}Ga_{0.7}As$ barriers (which we believe to offer a similar degree of 2D confinement to the first bound heavy hole level as our AlGaAs AQW structures), $E_C \approx 31$ meV. Furthermore, E_C for narrower GaAs symmetric wells with identical $Al_{0.3}Ga_{0.7}As$ barriers, is no greater than 43 meV, while E_C in bulk $Al_{0.3}Ga_{0.7}As$ (i.e. in a symmetric GaAs well of zero width between $Al_{0.3}Ga_{0.7}As$ barriers) is approximately 32 meV. Therefore, if we imagine a 100 Å-wide symmetric GaAs well with $Al_{0.3}Ga_{0.7}As$ barriers reducing in width *without changing shape or depth*, we would not expect E_C to increase by more than approximately 10 meV. Now, during the *intermixing* of the B690 ACQW structure, the depth of the well begins to reduce, until, in the limit, a bulk alloy is formed with the average as-grown MQW composition. The hh1 level therefore experiences progressively less 2D confinement as intermixing proceeds, so that we might expect E_C to increase by significantly less during the *intermixing* of the B690 structure than it would during the *reduction of the width (without changes in the shape or depth)* of our "equivalent" symmetric QW. We conclude that, during intermixing of the B690 ACQW structure, E_C varies by significantly less than +10 meV and is therefore effectively constant. Furthermore, by applying similar arguments, we also believe that E_C is effectively constant for the A776 symmetric QW structure with $Al_{0.14}Ga_{0.86}As$ in the wells. Then, denoting the energy of the e1hh1 transition after intermixing of such structures by E'_{e1hh1}, and the energy of the e1->C transition after intermixing by E'_{e1C}, from (6.6) we have, for E_C constant:

$$E'_{e1C} - E_{e1C} = E'_{e1hh1} - E_{e1hh1} \tag{6.7}$$

i.e. the peak extrinsic PL wavelength blueshift obtained on intermixing the B690 ACQW and the A776 symmetric QW structures is approximately equal to the peak intrinsic PL wavelength blueshift. To calculate the expected PL blueshifts in the AlGaAs AQW structures therefore, we need only estimate the intrinsic PL blueshifts in these structures.

There are many different examples in the literature of the calculation of intrinsic PL blueshifts obtained on QW intermixing [6,2,3,12]. In the present work, Schrödinger's equation was solved across the central well of the partially-intermixed 3-well system of Fig. 6.1a, where infinitely thick QW barriers were assumed on either side of the intermixed central well as illustrated in Fig. 6.1b. The peak PL wavelength blueshifts at both 300 K and 77 K as functions of L_d calculated in this way, for the multiple AQW B563, B578 and B690 nominal structures, appear in Figs. 6.7a, 6.8a and 6.9a respectively. In addition, the peak PL wavelength blueshifts at 300 K and 77 K as functions of L_d calculated for the symmetric QW structures A776 and B579, are also shown in Figs. 6.10 and 6.11 respectively.

From Figs. 6.7 - 6.11 and the corresponding Al fraction profiles of Figs. 6.2 - 6.6, it is possible to make some general observations. Firstly, the deeper the starting material QW's, the greater the saturated PL blueshift that can be obtained (the PL blueshifts of the shallower MQW structures B690 and A776 saturate at approximately 40 - 50 nm and 60 nm respectively while the PL blueshifts of the deeper B563, B578 and B579 structures all saturate at approximately 80 nm). Also, the narrower the well layers (for a constant barrier thickness), the lower the diffusion length at which the PL blueshift becomes saturated (for the B579 structure, the PL blueshift saturates for $L_d \approx 20 - 30$ Å, while for the other structures the PL blueshift saturates for $L_d > 50$ Å). The latter observation essentially just reflects the fact that a saturated PL blueshift is achieved more readily (i.e. using shorter anneals at lower temperatures) for narrow QW structures (for a constant barrier thickness). Clearly, from the foregoing observations, it does not make any sense to compare the degree of intermixing achieved for different MQW structures in terms of the PL blueshift observed; rather, we should compare the degree of QW intermixing achieved in terms of diffusion lengths, which may be inferred from the observed PL blueshifts using Figs. 6.7 to 6.11 for the different MQW structures of interest here.

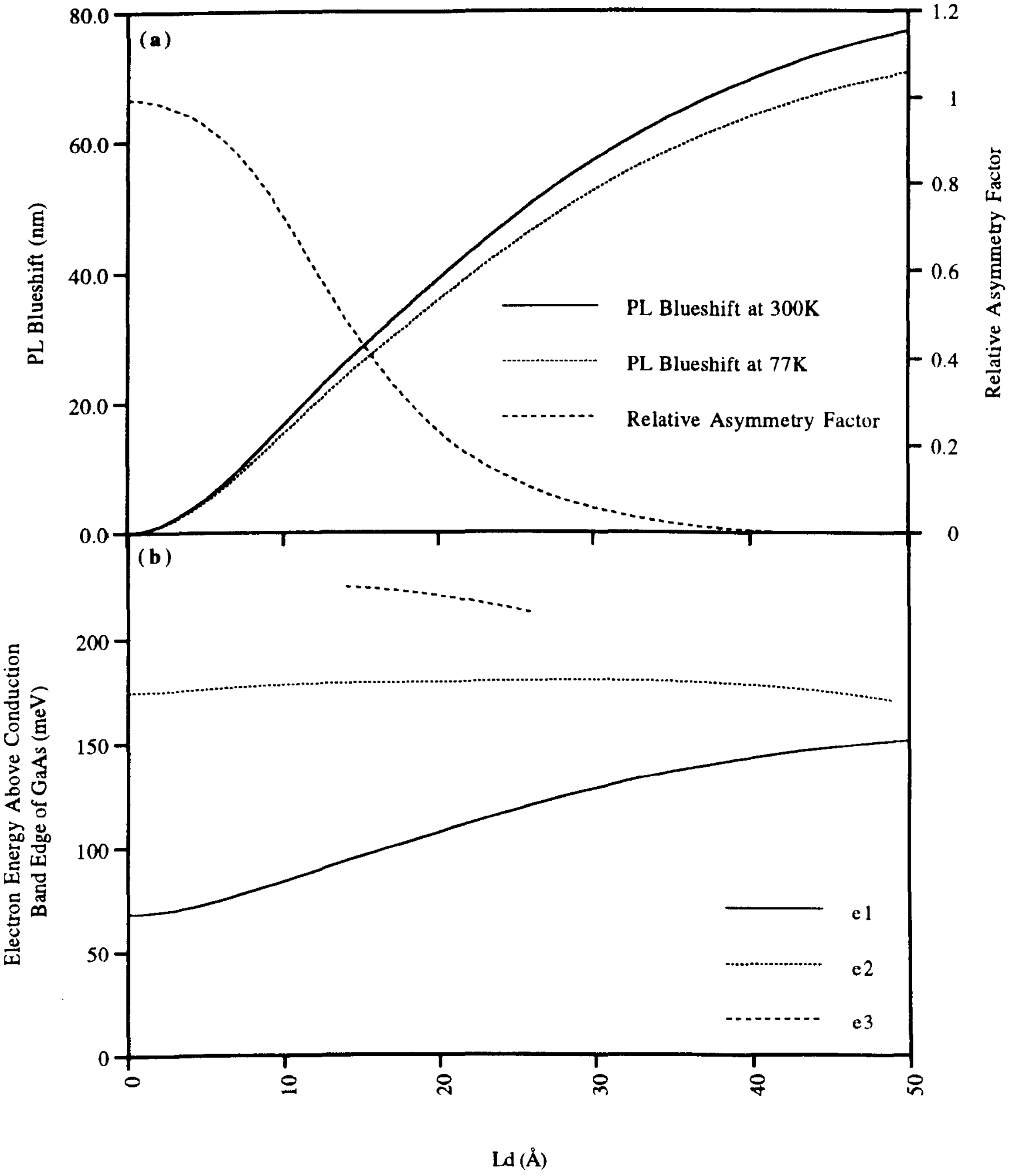

Fig. 6.7 Changes in the B563 multiple AQW structure occurring during intermixing (a) the PL blueshifts at 300 K and 77 K, and the relative $\chi^{(2)}_{zzz}$ asymmetry factor as functions of the diffusion length (b) the bound electron levels at 300 K as functions of the diffusion length

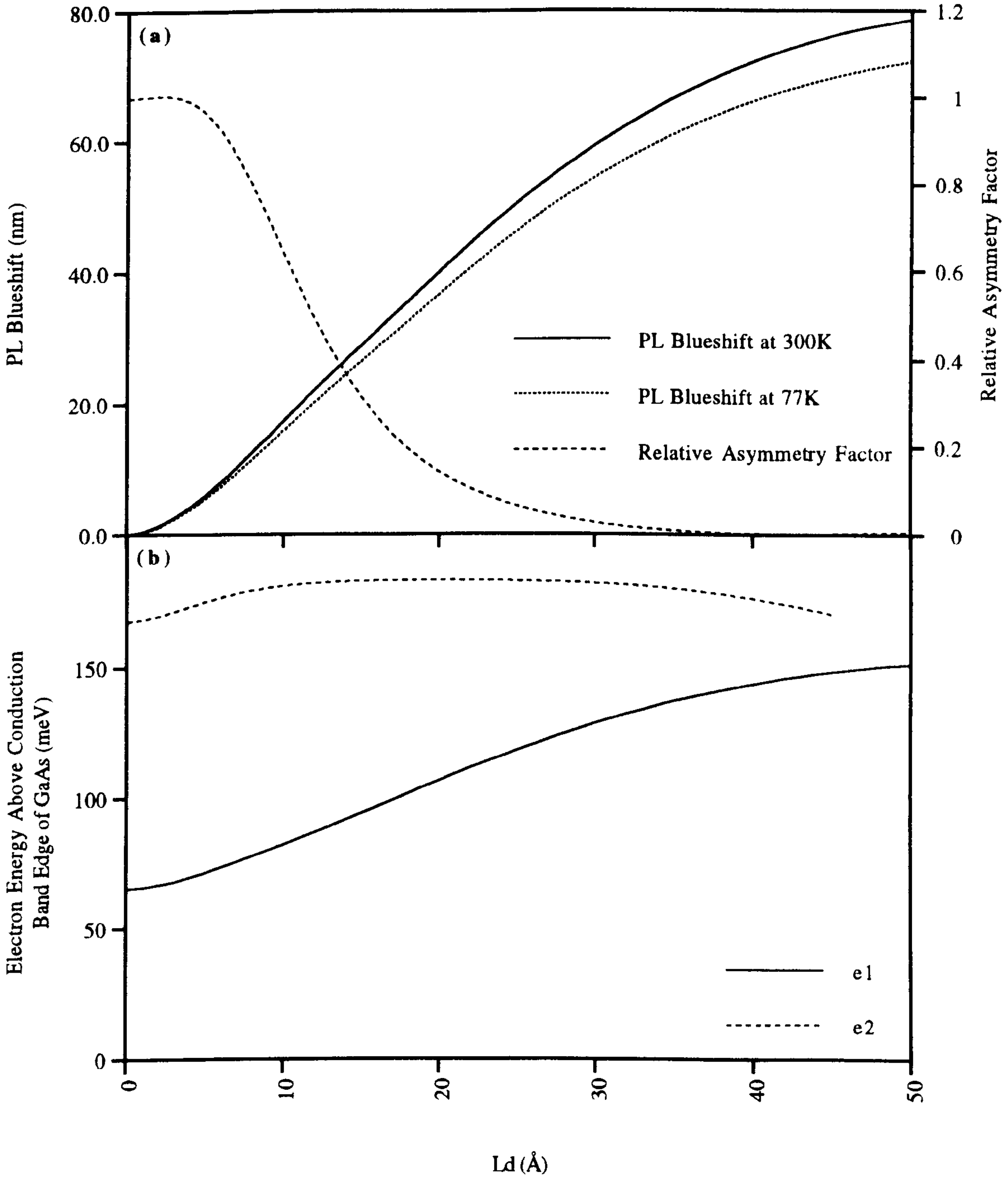

Fig. 6.8 Changes in the B578 multiple AQW structure occurring during intermixing (**a**) the PL blueshifts at 300 K and 77 K, and the relative $\chi^{(2)}_{zzz}$ asymmetry factor as functions of the diffusion length (**b**) the bound electron levels at 300 K as functions of the diffusion length

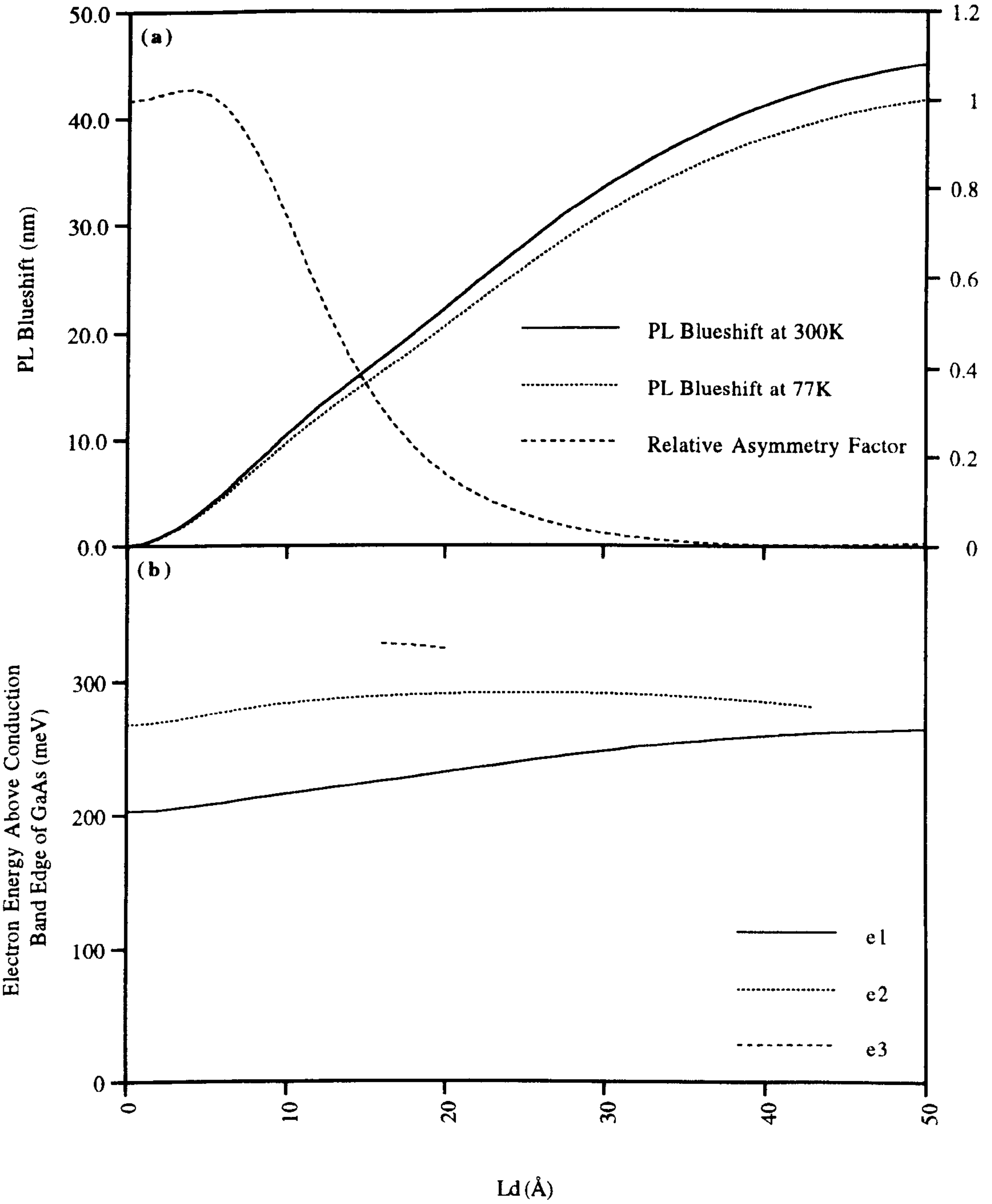

Fig. 6.9 Changes in the B690 multiple AQW structure occurring during intermixing (a) the PL blueshifts at 300 K and 77 K, and the relative $\chi^{(2)}_{zzz}$ asymmetry factor as functions of the diffusion length (b) the bound electron levels at 300 K as functions of the diffusion length

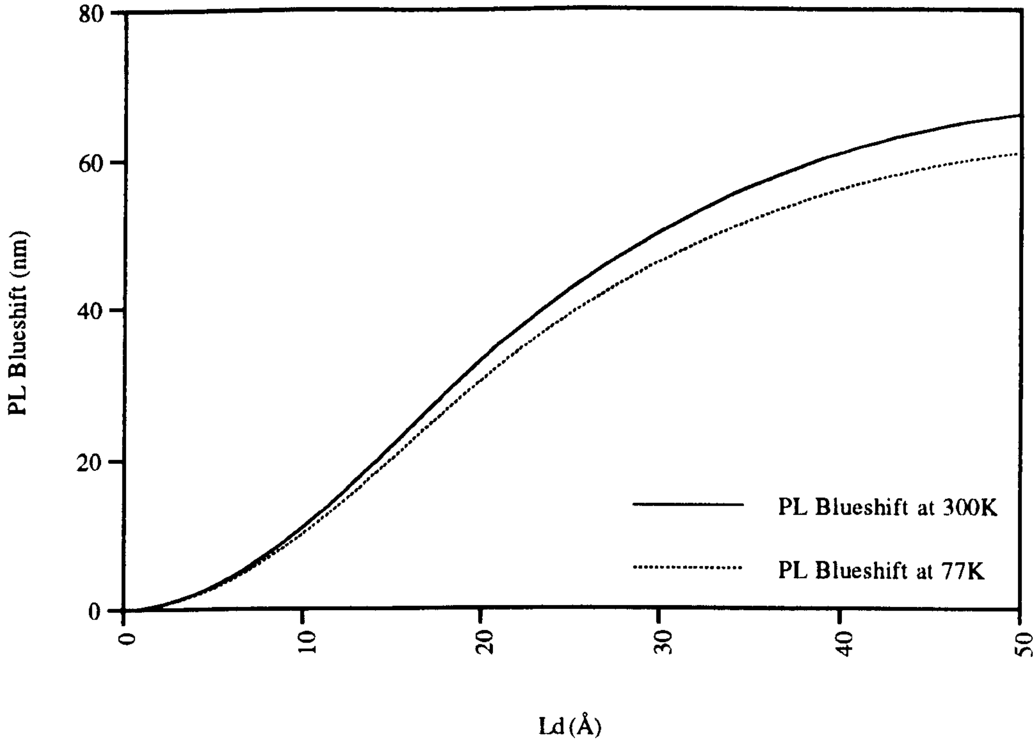

Fig. 6.10 A776 PL blueshifts at 300 K and 77 K as functions of the diffusion length

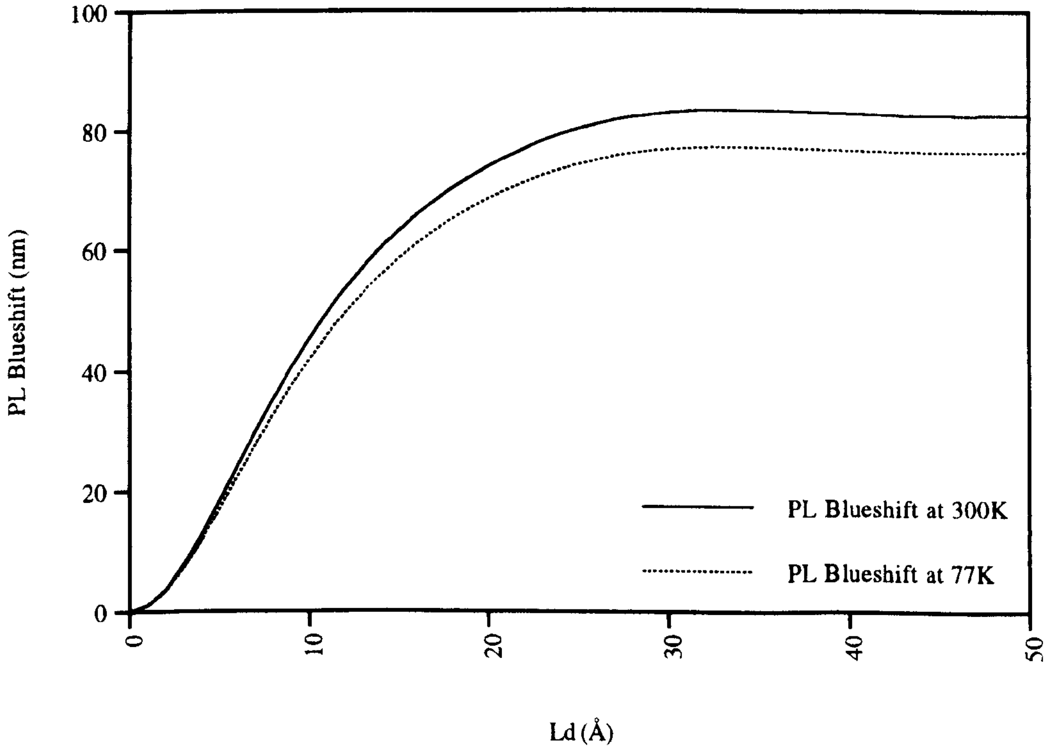

Fig. 6.11 B579 PL blueshifts at 300 K and 77 K as functions of the diffusion length

6.1.3 The Second Order Non-linear Susceptibilities of GaAs/AlGaAs Multiple AQW Structures as a Function of the Degree of Intermixing

It may be recalled from Section 3.1 that, for a constant detuning from the half-band-gap, and when working within the effective mass approximation, the second order non-linear susceptibility tensor component $\chi^{(2)}_{zzz}$ associated with GaAs/AlGaAs multiple AQW structures, is proportional to the product of 3 momentum matrix elements:

$$\chi^{(2)}_{zzz} \propto \langle \phi_{lh1}(z)|\phi_{e1}(z)\rangle\langle \phi_{e1}(z)|-i\hbar\, d/dz|\phi_{e2}(z)\rangle\langle \phi_{e2}(z)|\phi_{lh1}(z)\rangle \tag{6.8}$$

Plotting this asymmetry factor as a function of L_d (i.e. as a function of the degree of QW intermixing) relative to its value for the relevant starting material MQW structure, should then reflect the magnitude of $\chi^{(2)}_{zzz}$ for a constant detuning as intermixing proceeds. This relative asymmetry factor is therefore plotted as a function of L_d for the B563, B578 and B690 multiple AQW structures on the same set of axes as the calculated PL blueshifts in Figs. 6.7a, 6.8a and 6.9a respectively. From these graphs it may be seen that to suppress $\chi^{(2)}_{zzz}$, effectively requires that a diffusion length of approximately 30 Å must be obtained on intermixing. This corresponds to 77 K PL blueshifts of ≈ 50 - 60 nm for the B563 and B578 multiple AQW structures, and a 77 K blueshift of ≈ 30 nm for the B690 ACQW structure. It should be emphasised, however, that when operating at a constant wavelength below the half-band-gap of the as-grown MQW material, QW-intermixing also results in an increased detuning from the half band-gap. This means that $\chi^{(2)}_{zzz}$ may be suppressed for a smaller diffusion length, and therefore smaller PL blueshifts than those quoted above.

For completeness, all the bound electron levels for the multiple AQW structures are also plotted in Figs. 6.7b, 6.8b, and 6.9b, to show that the electron level e2 remains bound in all three cases for $L_d \leq 40$ Å. The somewhat curious behaviour of the e3 level in the B563 and B690 cases can be explained qualitatively as follows: during intermixing the top of the QW's widen while the bottom of the wells are "squeezed", so that the energy of a bound electron level near the top of the QW tends to decrease during intermixing while that of an electron level near the bottom of the well tends to increase. This means that, as intermixing continues, the electron levels tend to converge to an intermediate energy within the well and a third electron level is supported. As the MQW is intermixed still further, however, the peak barrier potentials on either side of each well begin to fall (as is seen from Figs. 6.2 - 6.4). Eventually, the barriers fall so far that they "overtake" the e3 level and only the two original bound electron levels e1 and e2 remain.

6.2 Impurity-free Vacancy Disordering Experiments and the Suppression of Multiple AQW Second Order Non-linear Susceptibilities

In this section we shall be concerned with experimental quantum well intermixing results for the B563, B578, B690 and QT849A multiple AQW structures, and for the B579 symmetric MQW structure, using IFVD under a variety of annealing conditions. In addition, we shall discuss some intermixing results reported by Hamilton [13], for the A776 symmetric MQW structure. All of the samples were rinsed with standard solvents in an ultrasonic bath for a few minutes prior to deposition of a 2000 Å layer of either e-beam evaporated or PECVD SiO_2. The samples were then placed epitaxial side down onto a Si susceptor wafer in a rapid thermal processor, and annealed over a range of temperatures and times. Figs. 6.12 - 6.16 show the resulting PL spectra at 77 K obtained for the B563, B578, B690, QT849A and B579 MQW structures using the set-up described in Section 5.3.5. With the exception of the very anomalous B578 PL spectrum for a 90 s anneal at 925 °C, it may be seen that intermixing the MQW structures does not significantly broaden the PL peaks, suggesting that the MQW is uniformly intermixed, and that the vacancy concentration is relatively constant within the MQW layers. These results therefore validate the modelling assumption of a constant Al-Ga interdiffusion coefficient in the MQW layer.

Even stronger evidence for uniform intermixing using the IFVD process is provided by the room temperature absorption spectra of Figs. 6.17 and 6.18, which were obtained from intermixed B563 and B578 samples respectively after annealing for 60 s at 950 °C. An exciton absorption peak is still clearly visible in these figures which may be attributed to the superposition of the e1hh1 and e1lh1 exciton absorption peaks (which are much closer in energy for the intermixed structure). We further believe that the absorption features corresponding to e2hh2 and e2lh2 are so close in energy to one another, and to the QW barrier absorption edge, that they cannot be resolved at 300 K. Unlike PL, for which the uppermost QW's contribute most to the observed spectrum, an absorption spectrum is essentially an unbiased product of the absorption in *all* the MQW layers. This means that any depth-dependent intermixing effects should be more evident from an absorption spectrum than from a PL spectrum. The fact that a first bound electron to first bound hole exciton peak is visible at all in Figs. 6.17 and 6.18, and is not significantly broader than either of the e1hh1 or e1lh1 exciton peaks for the as-grown material, therefore re-enforces the fact that the intermixing of the MQW layers is highly uniform.

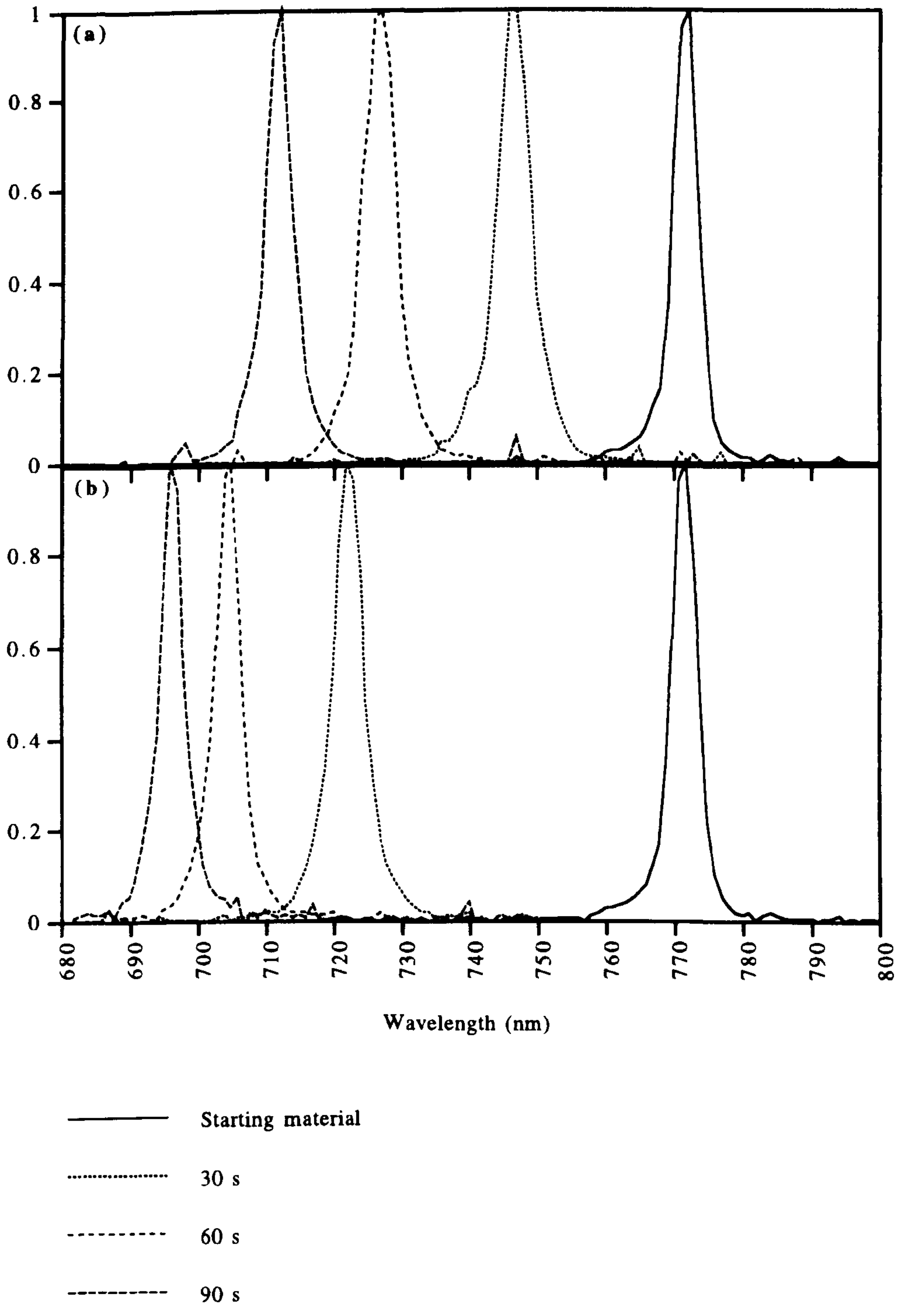

Fig. 6.12 B563 normalised PL spectra at 77K for several different anneal times and for anneal temperatures of **(a)** 900 °C and **(b)** 925 °C

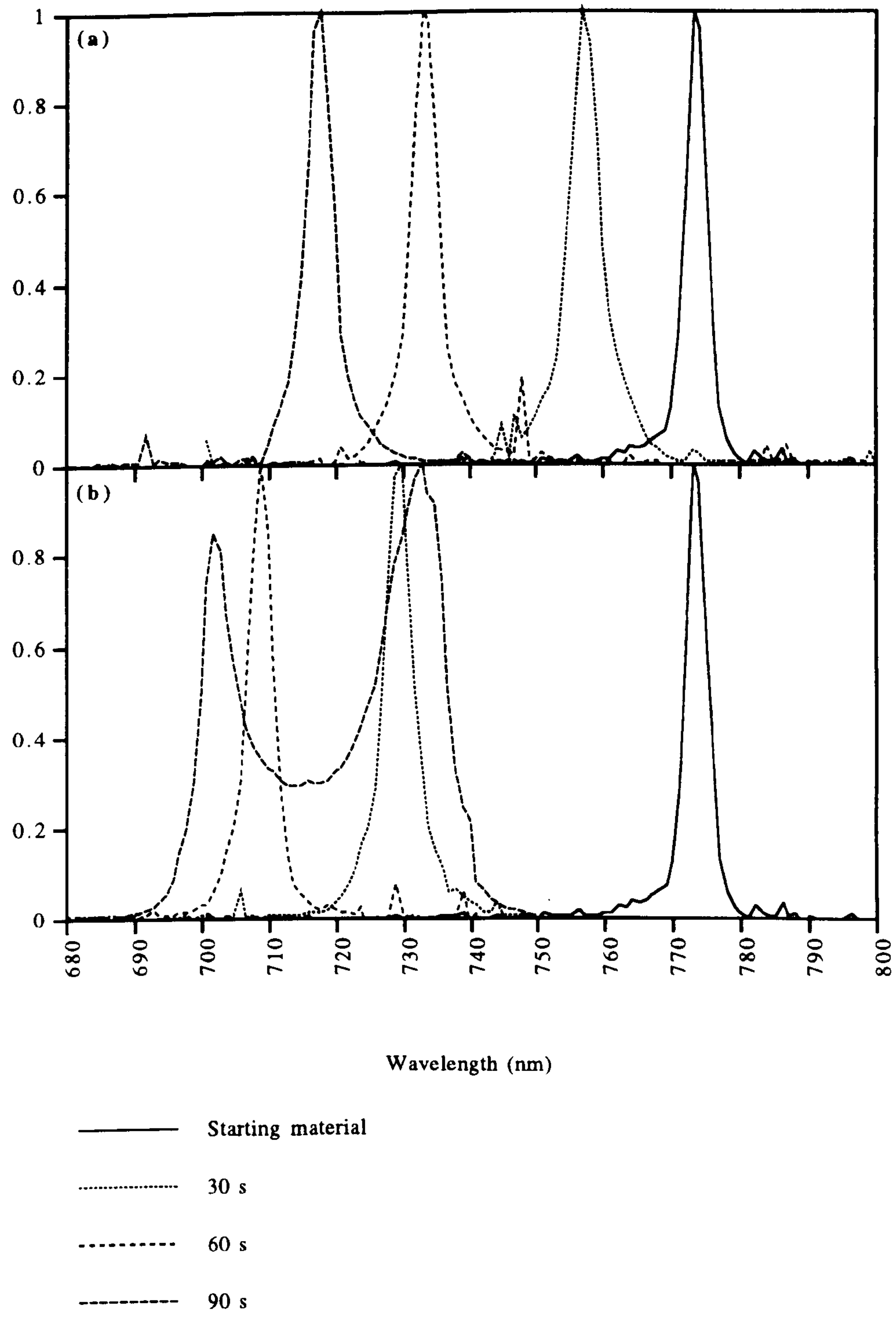

Fig. 6.13 B578 normalised PL spectra at 77K for several different anneal times and for anneal temperatures of (**a**) 900 °C and (**b**) 925 °C

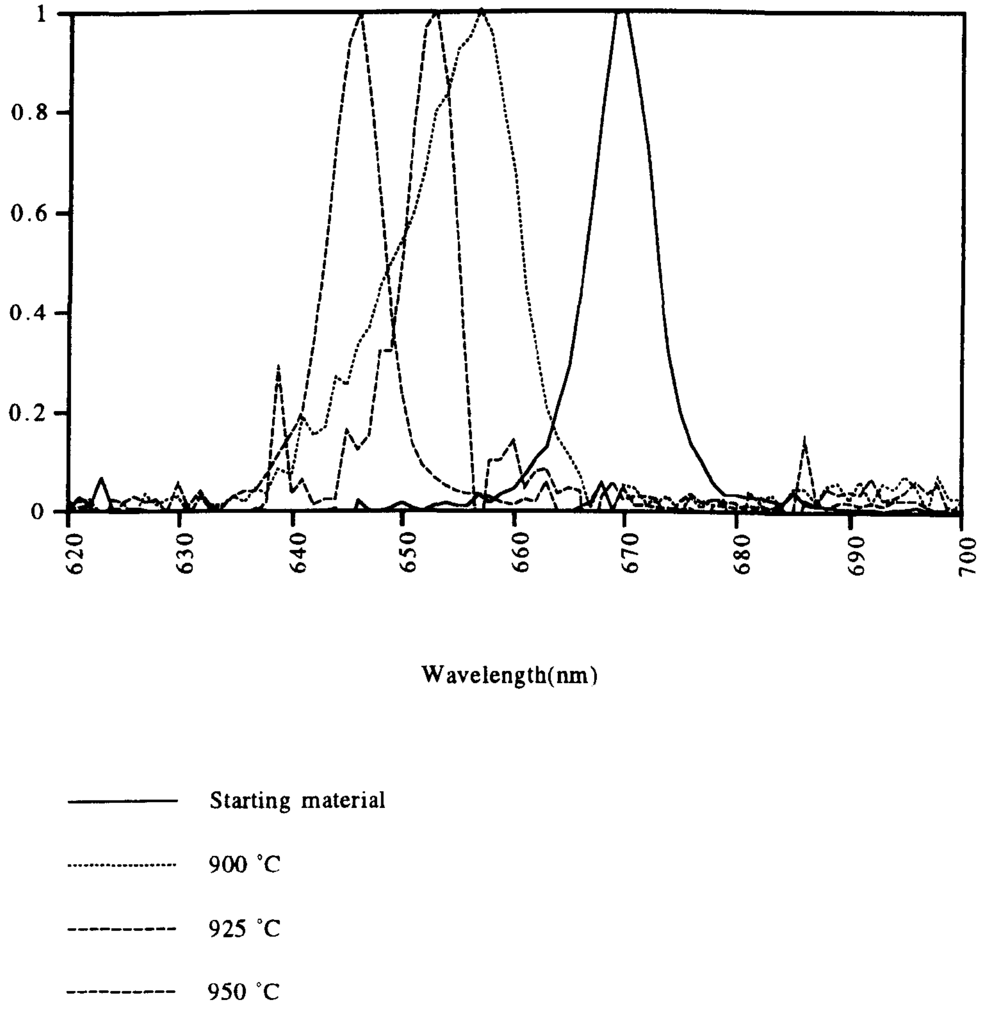

Fig. 6.14 B690 PL spectra at 77 K for 90 s anneals at several different temperatures

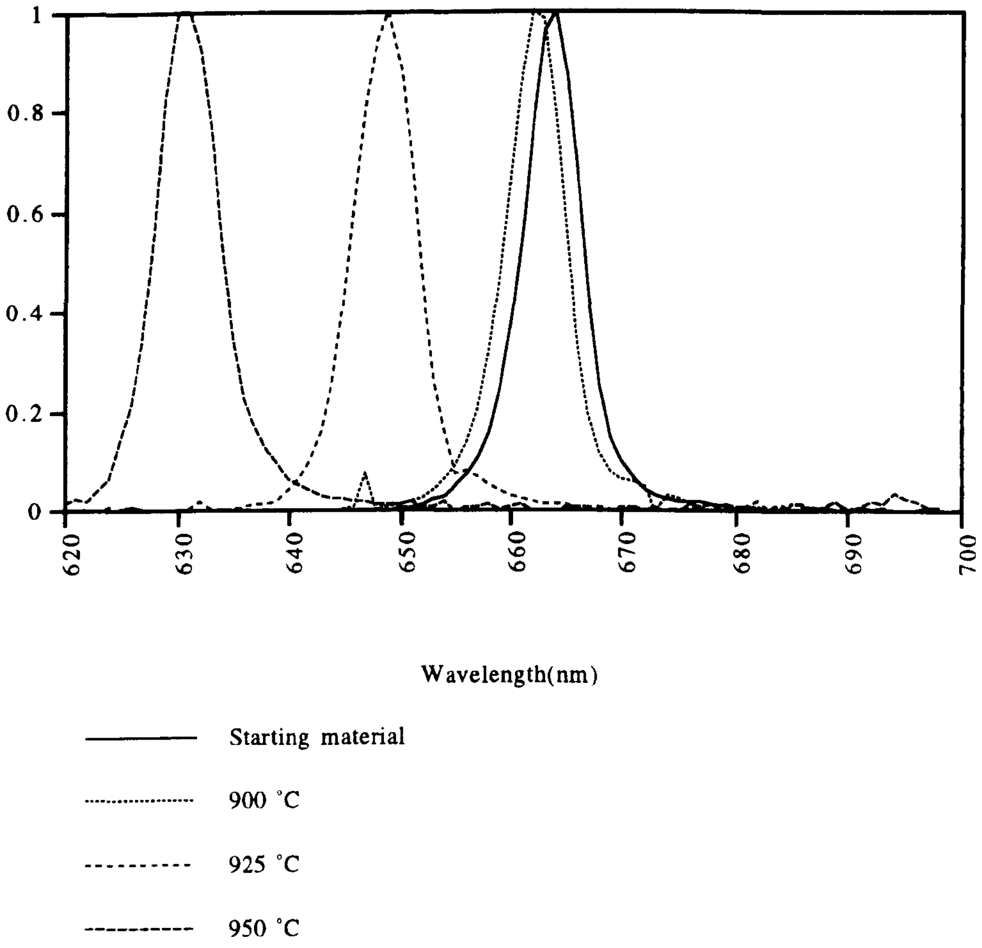

Fig. 6.15 QT849A PL spectra at 77 K for 90 s anneals at several different temperatures

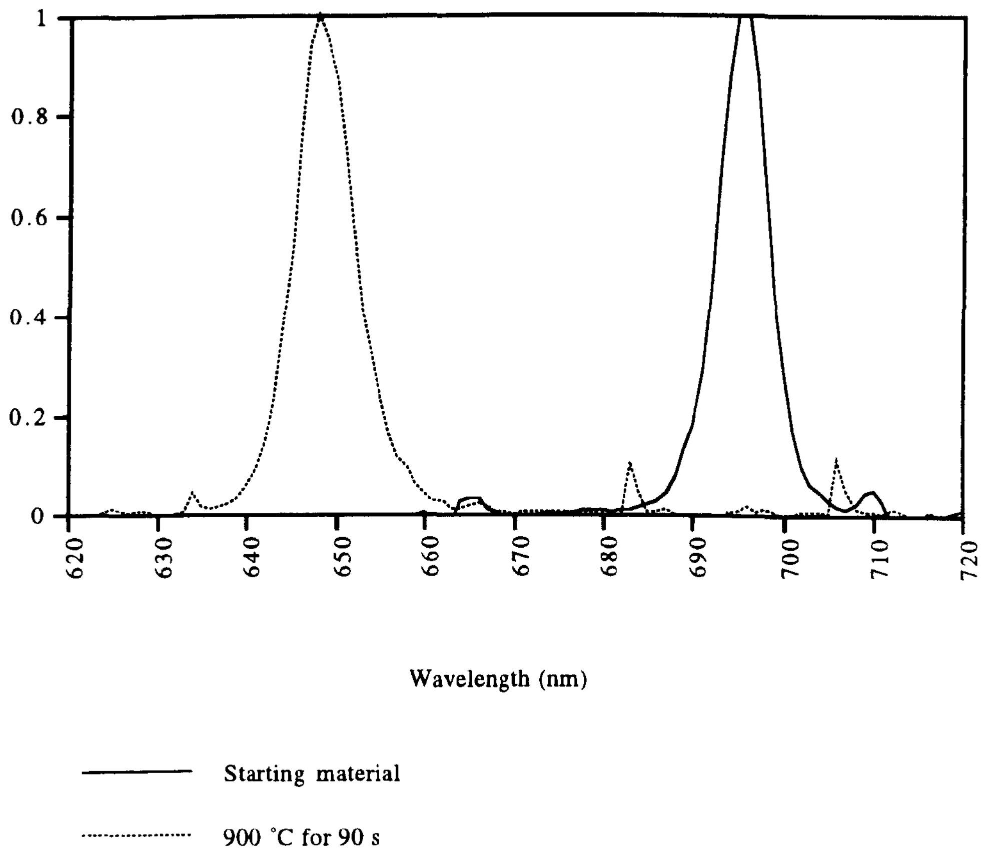

Fig. 6.16 B579 PL spectra at 77 K

Fig. 6.17 B563 room temperature absorption spectrum after IFVD at 950 °C for 60 s

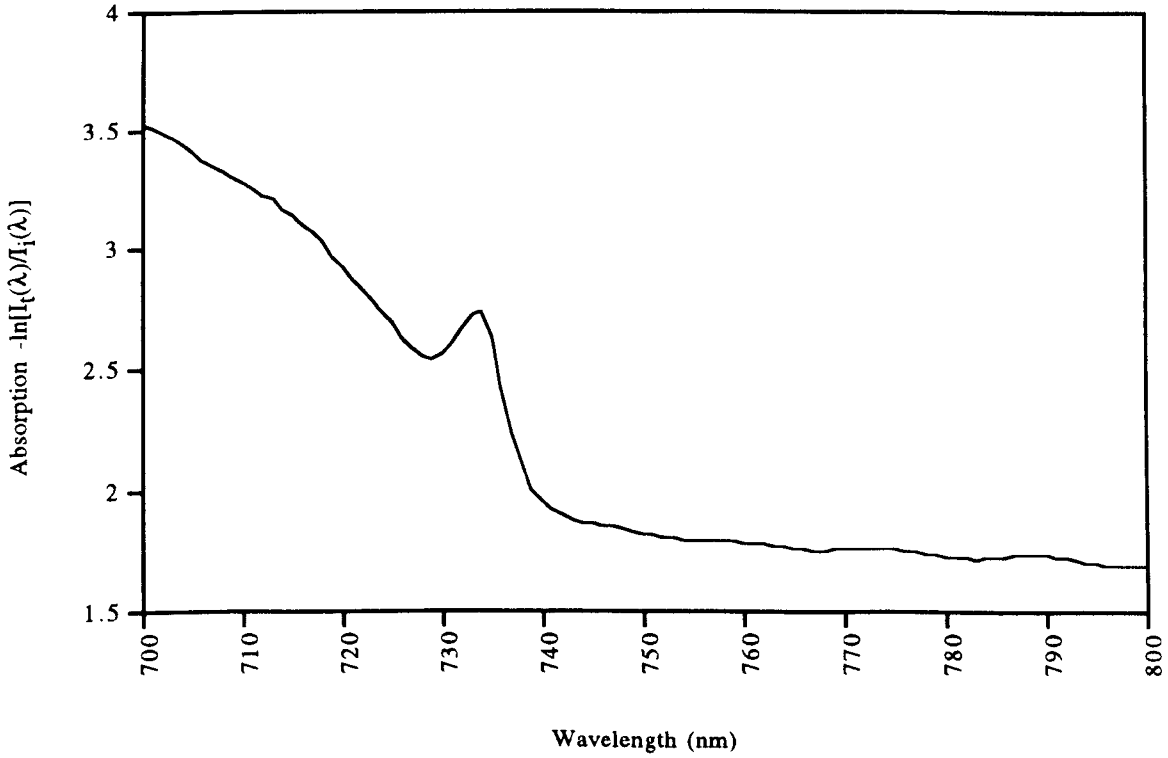

Fig. 6.18 B578 room temperature absorption spectrum after IFVD at 950 °C for 60 s

Next, the diffusion lengths achieved by IFVD for the different MQW structures are compared when annealing at 900 °C for 90 s. The PL blueshifts obtained at 77 K for these annealing conditions, and the corresponding diffusion lengths as inferred from Figs. 6.7 to 6.11, are listed in Table 6.1.

Material	PL Blueshift at 77 K (nm)	L_d (Å)	SiO_2 Deposition Method	GaAs Cap Thickness (Å)	Upper Cladding Al Fraction
B563 (MBE)	60	37	e-beam	100	0.32
B578 (MBE)	57	33	e-beam	100	0.34
B690 (MBE)	14	14	PECVD	1000	0.47
QT849A (MOCVD)	2	4	PECVD	1000	0.47
A776 (MBE)	13*	12	PECVD	100	0.37
B579 (MBE)	48	13	PECVD	1000	0.4

Table 6.1 Experimental IFVD results for several different MQW materials after a 90 s anneal at 900 °C. SiO_2 cap thickness in all cases was 2000 Å.

* Reported by Hamilton [13]

From Table 6.1, it is obvious that the diffusion lengths obtained for the B563 and B578 structures were significantly greater than the diffusion lengths obtained for the other structures under the same conditions. To explain these observations, we need to consider some of the relevant IFVD variables as identified by Ralston *et al* [3]. Firstly, we notice that e-beam evaporated SiO_2 caps were used for the disordering of the B563 and B578 structures, while PECVD caps were used for the other structures. This suggests that the use of e-beam evaporated SiO_2 caps may enhance the degree of disordering achieved. This is in agreement with the results of Ralston *et al.*, who attributed such effects to the more porous nature of the e-beam evaporated SiO_2. From Table 6.1 it may also be seen that there is no clear correlation between the diffusion lengths obtained and the thickness of the GaAs protective cap layer. This suggests that there are effectively no Si IID effects occurring for any of the structures.

Ralston *et al.* have also identified the epitaxial growth method and temperture as important factors for the IFVD process. This is to be expected, since different growth methods result in different native defect densities and different unintentional dopant concentrations which can both contribute to different interdiffusion rates. In particular, it is known, that higher concentrations of p-type impurities such as C which is present in the higher Al fraction layers, can lead to a reduction in the vacancy concentration, and thus a reduction in the degree of intermixing obtained [1]. The relatively low diffusion length of 4 Å attained for the MOCVD-grown QT849A structure annealed at 900 °C for 90 s could, therefore, be explained by a much lower equilibrium vacancy concentration.

It may also be recalled that the interdiffusion coefficient was assumed to be independent of the Al fraction profile so that the diffusion length L_d, should be independent of the material structure. This assumption may not, however, be strictly true. We could, for example, speculate that, due to the greater strength of the Al-As bond relative to the Ga-As bond, intermixing of higher Al fraction layers does not occur as readily as the intermixing of lower Al fraction layers. This hypothesis is then consistent with the observation that lower diffusion lengths were observed for the MQW structures with Al fractions of 0.4 or above in the upper cladding layers or the QW layers as seen from Table 6.1.

It should, of course, be acknowledged that there are several other factors which could affect the extent of quantum well intermixing occurring during the IFVD process, so that many more columns could have been included in Table 6.1. In particular, the chemistry of the SiO_2/GaAs interface could be an important factor (see Section 6.3). On the basis of the results presented here, we may therefore only tentatively ascribe the higher diffusion lengths attained for the B563 and B578 structures to the use of more porous e-beam evaporated SiO_2 caps, and/or the presence of lower Al fractions in the epitaxial layers of these materials.

The IFVD results of Figs. 6.12 to 6.15 have implications for the suppression of the multiple AQW second order non-linear susceptibility tensor components. From the conclusions of Section 6.1.3, it may be recalled that the effective suppression of the AQW non-linearities requires PL blueshifts of approximately 50 - 60 nm for the B563 and B578 structures, and a PL blueshift of approximately 30 nm for the B690 structure (which is nominally identical to the QT849A structure). From consideration of Figs. 6.12 to 6.15, it may therefore be seen that appropriate annealing conditions for the effective suppression of the AQW non-linearities are 90 s at 900 °C for the B563 and B578 structures, and 90 s at 950 °C for the B690 and QT849A structures.

6.3 Selective Area IFVD Using Hydrogen Plasma Processing for the Control of Multiple AQW Second Order Non-linearities

It was shown in the previous section, that it is possible to achieve quantum well intermixing using the IFVD process for the suppression of the AQW non-linearities over an entire MQW epitaxial layer, and that the extent of QW intermixing is dependent on the anneal conditions and several other factors. For efficient quasi-phase-matching and the control of AQW second order effects, however, it is necessary to periodically suppress the AQW non-linearities. In this section we will therefore be concerned with the suppression of quantum well intermixing in selected areas using hydrogen plasma processing to modify the native oxide layer at the GaAs epitaxial surface.

It is well known that the native oxide layer which forms on a GaAs surface exposed to the atmosphere over a period of weeks, is a mixture of As_2O_3 and Ga_2O_3. Hamilton *et al.* [14] have further demonstrated that the As_2O_3 in the native oxide layer may be reduced using a hydrogen plasma to form Ga_2O_3 and the volatile product AsH_3. For a sufficiently long exposure to a hydrogen plasma at a high enough plasma power, a complete covering of Ga_2O_3 may result. Since Ga_2O_3 is thought to be relatively impermeable to Ga atoms during the annealing stage of the IFVD process, such an oxide layer should inhibit Ga vacancy formation and suppress QW intermixing [14].

6.3.1 Selective Area IFVD Experiments with GaAs/AlGaAs Multiple AQW Structures

To evaluate the effectiveness of hydrogen plasma processing for the suppression of QW intermixing in selected areas, two IFVD experiments were performed with both the B690 and the QT849A multiple AQW structures. For both experiments the samples were cleaned using standard solvents in an ultrasonic bath and coated with 2000 Å of PECVD SiO_2. Half of the SiO_2 was then stripped using buffered HF solution to expose the GaAs cap surface underneath. In the first experiment, the samples were subjected to a hydrogen plasma in a reactive ion-etching machine for 30 minutes under the conditions listed in Table 6.2 (which are approximately optimum [13]). In the second experiment (which was a control experiment), the samples were not subjected to a hydrogen plasma.

Temperature	40 °C
Gas Flow Rate	20 sccm
Pressure	900 mT
RF Power	70 W
DC Bias	-80 V
Time	30 mins.

Table 6.2 Optimum H plasma conditions used for the modification of the GaAs surface oxide layer

All of the samples were subsequently annealed in a rapid thermal processor at 950 °C for 90 s, and the PL results of Figs. 6.19 and Fig. 6.20 were obtained at 77 K. From the PL blueshifts observed for the B690 material, it would appear that the hydrogen plasma processing has indeed partially suppressed QW intermixing, resulting in a PL blueshift in the SiO_2-free region exposed to the plasma of only 8 nm (see Fig. 6.19b). This compares with a PL blueshift of approximately 15 nm in the SiO_2-free region of the corresponding control sample due to native-defect-induced disordering (see Fig. 6.19a). Also, since the PL blueshift of 22 nm obtained in the SiO_2-covered region of the sample exposed to the H plasma is almost identical to that observed in the SiO_2-covered region of the control sample, we conclude that the H plasma process does not inhibit the disordering process occurring in the SiO_2-capped areas.

For the QT849A structure however (Fig. 6.20), the hydrogen plasma processing does not appear to have suppressed the native-defect-induced disordering occurring in the SiO_2-free region of the control sample to any significant degree. In light of these observations, and due to time restrictions, no further experiments were performed with the QT849A material.

To determine the consequences of the selective area QW intermixing results for quasi-phase-matching with the B690 structure, we may refer to Fig. 6.9 once again. It may be seen that the 77 K PL blueshifts of 8 nm and 22 nm obtained in the SiO_2-free and SiO_2-covered areas of the sample exposed to the H plasma, correspond to relative asymmetry factors of approximately 0.82 and 0.14 respectively. For ideal domain disordering, $\chi^{(2)}_{zzz}$ should be modulated between its starting material value and zero, so that these relative asymmetry factors compare with 1 and 0 for the ideal domain disordering case respectively.

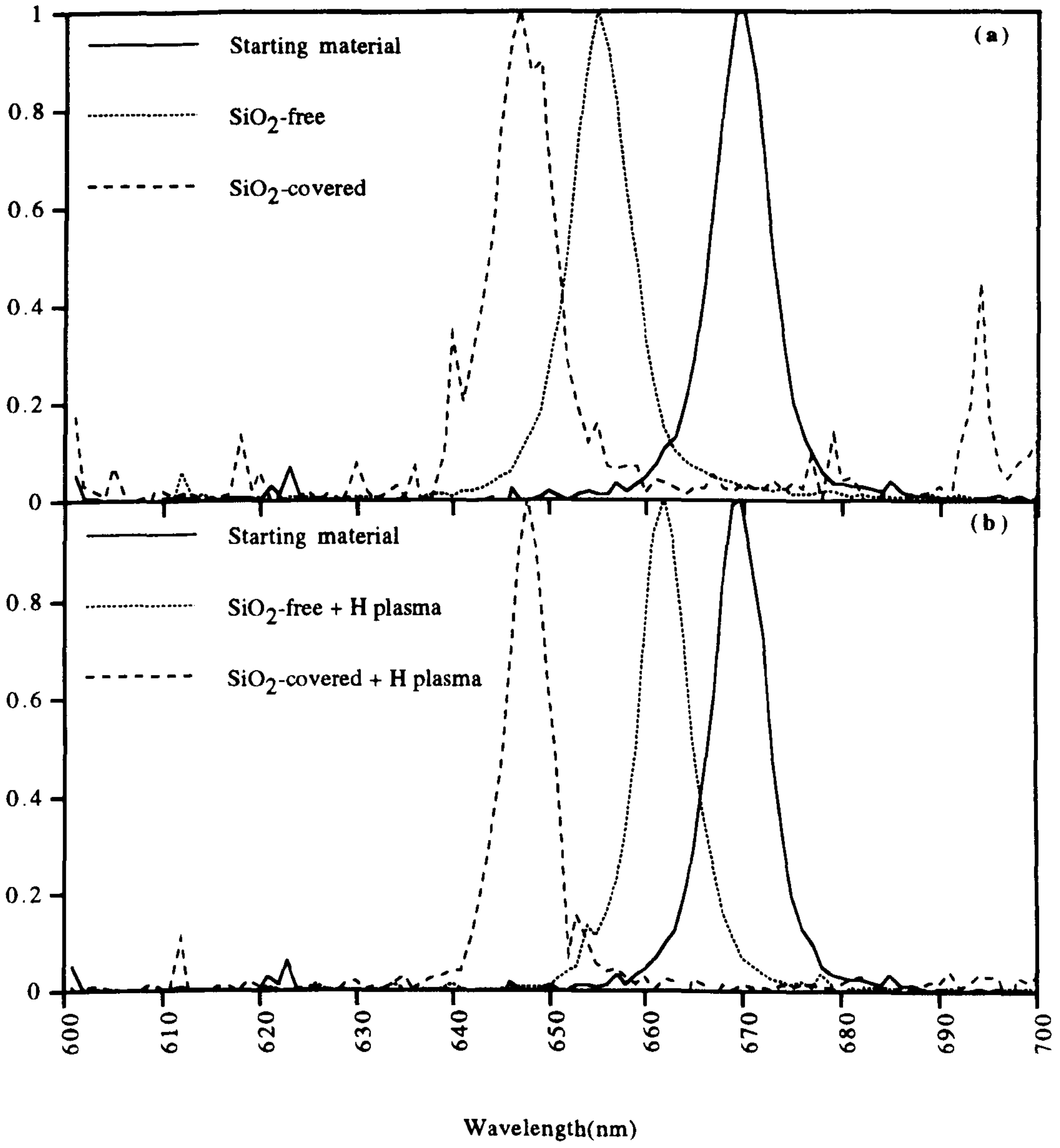

Fig. 6.19 B690 77 K PL spectra for the selective area IFVD process (**a**) without H plasma processing and (**b**) with H plasma processing, prior to annealing at 950 °C for 90 s.

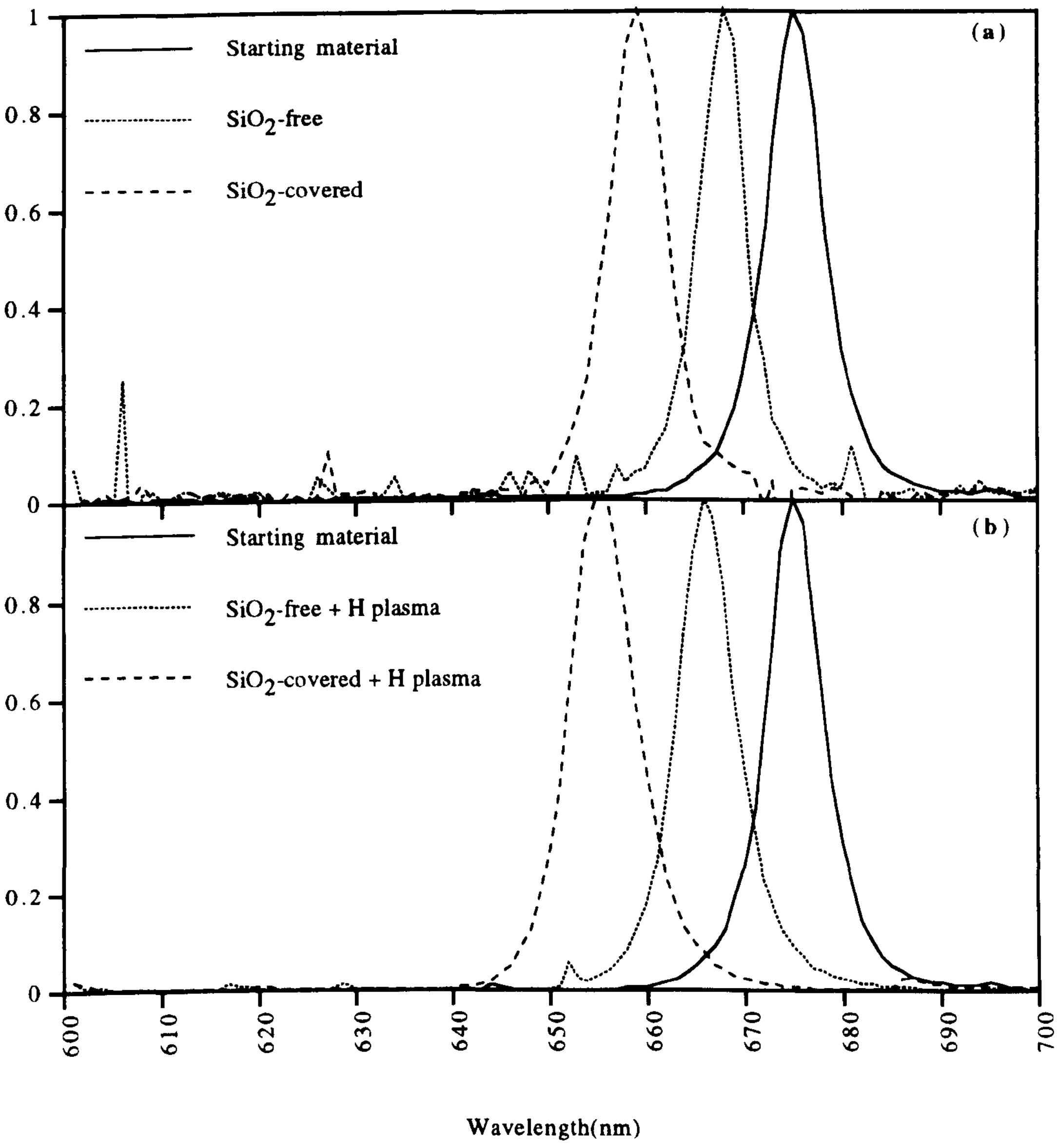

Fig. 6.20 QT849A 77 K PL spectra for selective area IFVD process (**a**) without H plasma processing and (**b**) with H plasma processing, prior to annealing at 950 °C for 90 s.

6.3.2 The Spatial Resolution of Selective Area IFVD for the Control of Multiple AQW Second Order Susceptibilities

During selective area intermixing using hydrogen plasma processing, Ga vacancies created at the GaAs/SiO_2 interface, may diffuse in different directions. This will result in lateral spreading of the Ga vacancy concentration and therefore of the Al-Ga interdiffusion coefficient as illustrated in Fig. 6.21. If the extent of such lateral vacancy diffusion is too great, and/or the lateral dimension of the surface area in which we wish to suppress QW intermixing is too small, then clearly QW intermixing will occur everywhere and no as-grown MQW regions will remain. In other words, the IFVD process has a limited spatial resolution which may be defined as the lateral dimension of the smallest surface area under which the as-grown MQW structure is preserved after annealing.

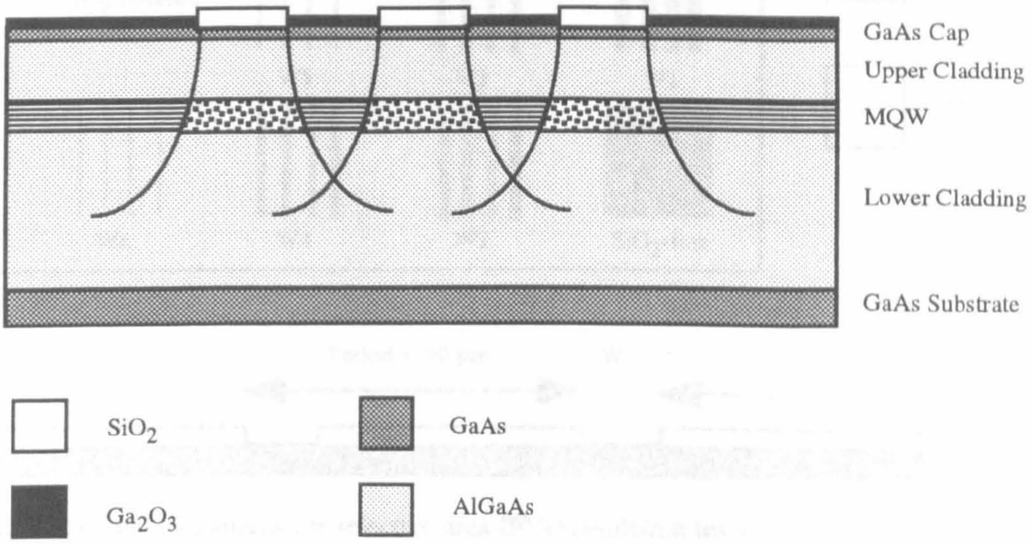

Fig. 6.21 Schematic diagram illustrating the lateral diffusion of Ga vacancies during the selective area IFVD process

Obviously the spatial resolution is an important issue when periodically intermixing multiple AQW structures for the control of second order non-linear effects using quasi-phase-matching. For the B690 structure, for example, we estimate (see Chapter 8) that a modulation period of 2.6 μm is required for first-order quasi-phase-matched SHG at a fundamental wavelength of 1.55 μm. This means that the resolution of the selective area IFVD process should correspondingly be better than 1.3 μm.

Selective area IFVD resolution experiments were performed with both the B579 and B690 structures. The test sample in each case was first cleaned and then coated with 200 nm of PECVD SiO_2. Subsequently, 2 mm by 2 mm areas were defined in the SiO_2 as shown in Fig. 6.22. In every area, windows were opened in the SiO_2 to expose the GaAs surface underneath. The period of the window pattern in each area was 30 μm, while the nominal window width W was varied from W1 in the first area down to W6 in the last area. (W1 = 16.3 μm, W2 = 11.1 μm, W3 = 6.3 μm, W4 = 4.0 μm, W5 = 2.5 μm, and W6 = 1.5 μm for the B579 sample. W1 = 17.3 μm, W2 = 11.5 μm, W3 = 6.7 μm, W4 = 4.9 μm, W5 = 2.6 μm, and W6 = 2.2 μm for the B690 sample.) Finally, there were also 2 control regions: one in which the SiO_2 cap was completely removed, and the other in which the SiO_2 cap was left intact. The samples were exposed to a hydrogen plasma under the conditions summarised in Table 6.3 prior to annealing.

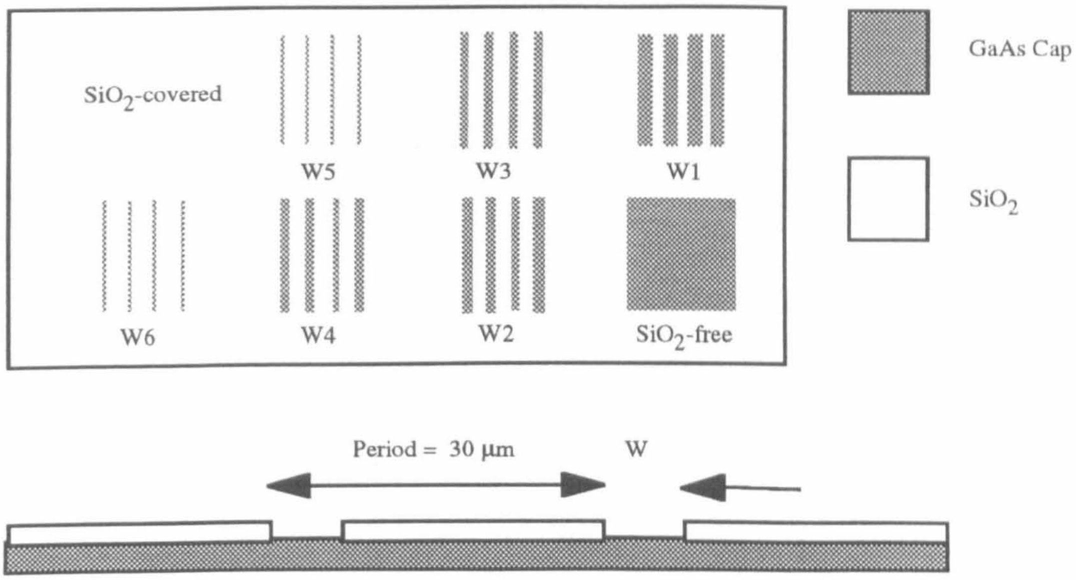

Fig. 6.22 SiO_2 window patterns for selective area IFVD resolution tests

Temperature	40 °C
Gas Flow Rate	20 sccm
Pressure	900 mT
RF Power	80 W
Time	40 mins.

Table 6.3 Hydrogen plasma conditions for selective area IFVD resolution measurements

Figs. 6.23 and 6.24 are the resulting 77 K PL spectra observed from the different areas of the B579 and B690 resolution samples after annealing at 900 °C for 90 s, and 950 °C for 90 s respectively. Also marked on these figures, are the actual measured window widths in the different areas. We see that for both samples, a peak in the PL spectra is observed in every region which corresponds to the peak PL wavelength in the SiO_2-free intermixing-suppressed region. More specifically, we see that an intermixing-suppressed PL peak is observed for the B579 structure even for window widths as small as 1.5 μm, while for the B690 structure, an intermixing-suppressed PL peak persists for window widths down to 2.2 μm. This indicates that the spatial resolution of the selective area IFVD process using hydrogen plasma processing is better than 1.5 μm for the B579 structure (annealed at 900 °C for 90 s), and better than 2.2 μm for the B690 structure (annealed at 950 °C for 90 s).

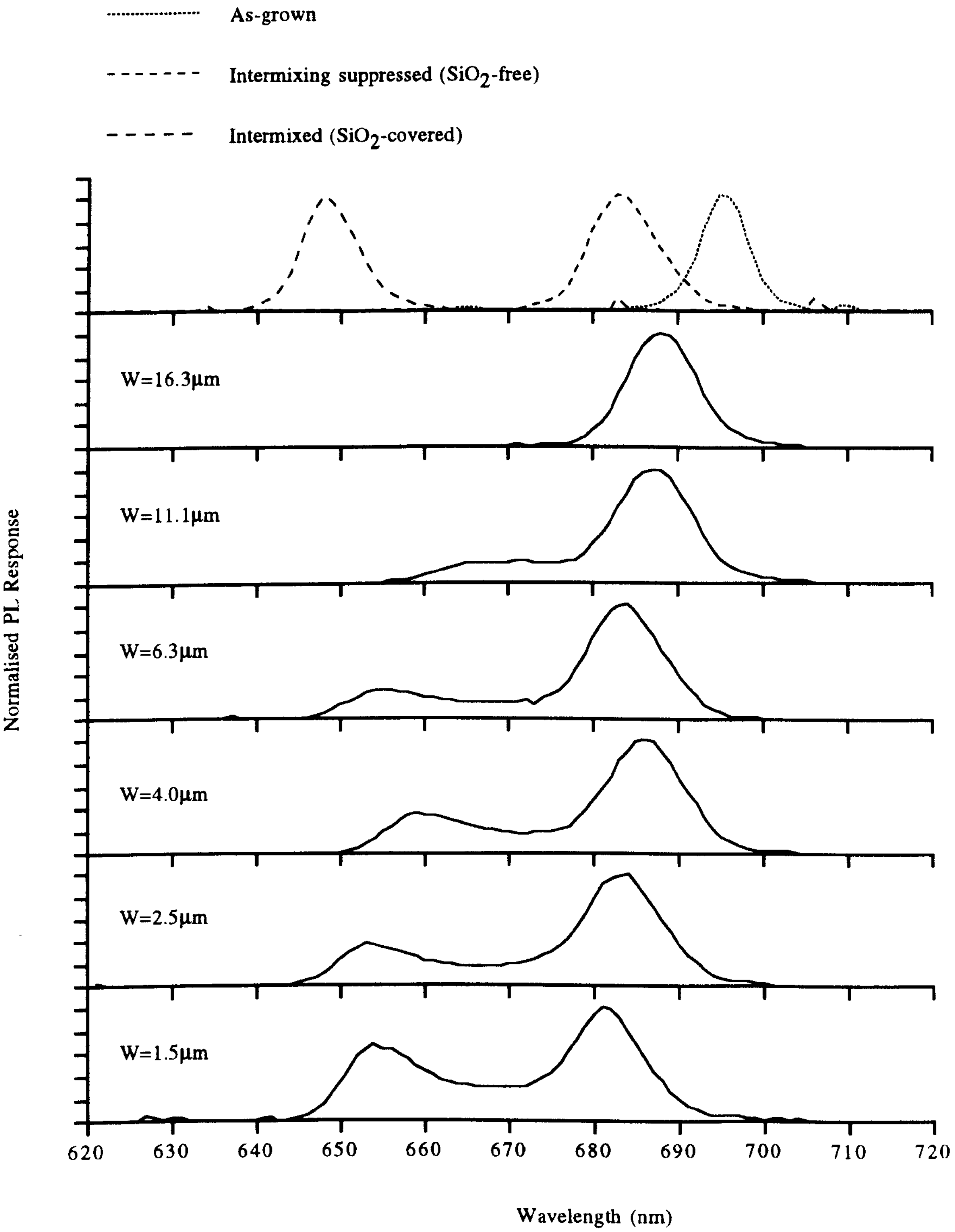

Fig. 6.23 B579 IFVD resolution experiment PL spectra at 77 K

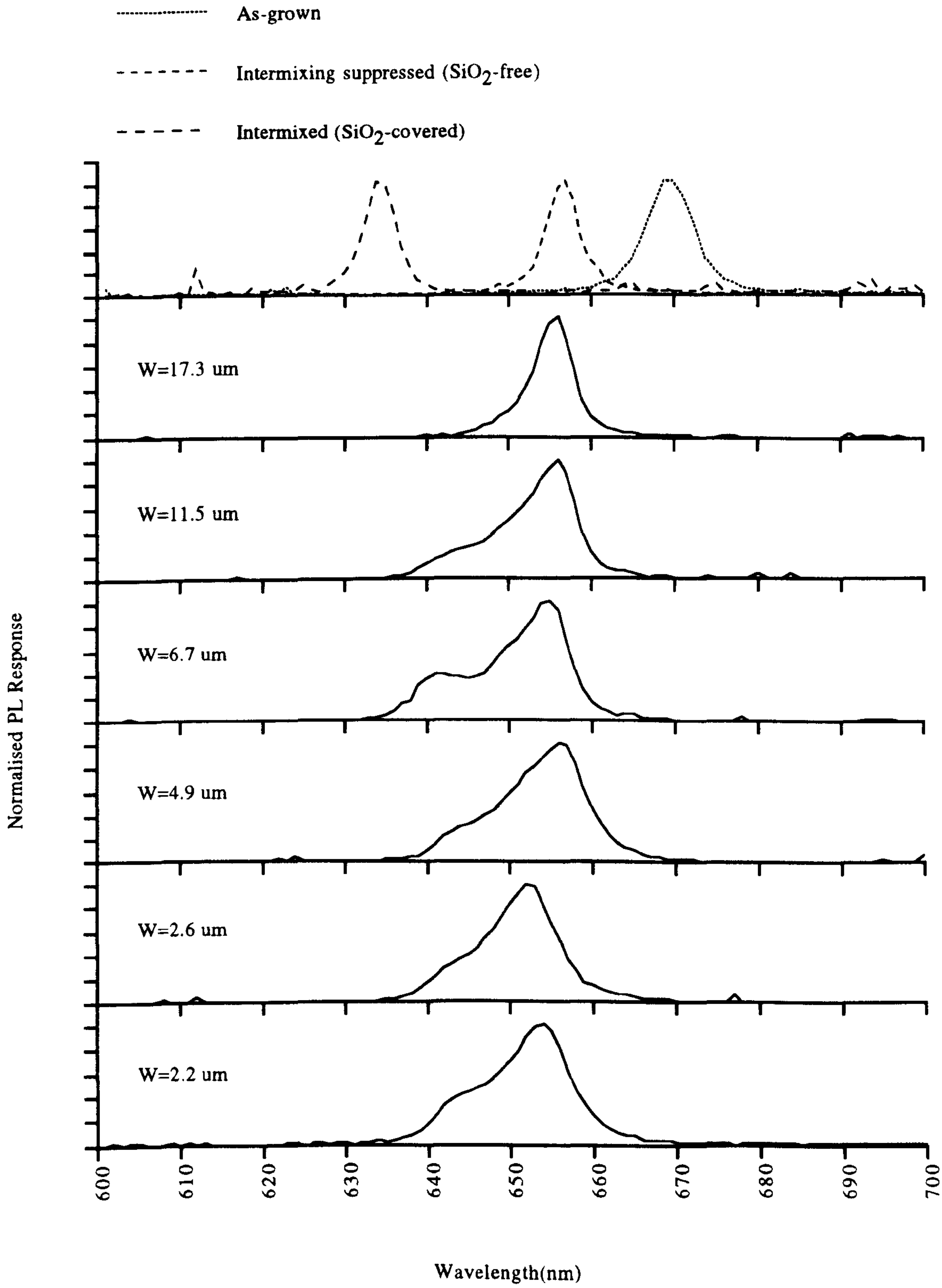

Fig. 6.24 B690 IFVD resolution experiment PL spectra at 77 K

For the case of the B579 structure, a pronounced PL peak corresponding to the intermixed PL peak wavelength also appears gradually as the window width decreases. This is to be expected because, as the window width is reduced, the fractional coverage of SiO_2 increases (for a constant window patter period), and the fractional area of the MQW which is intermixed increases. To explain the absence of any similarly conspicuous "QW-intermixed" PL peaks for the B690 sample in the regions with smaller window widths, we must consider the consequences of subjecting this sample to the more severe annealing schedule of 90 s at 950 °C. The PL blueshifts obtained in the intermixed (SiO_2 intact) and intermixing-suppressed (SiO_2-free) control regions for the B690 sample were 36 and 13 nm respectively, and from Fig. 6.9 it may be seen that these PL blueshifts correspond to diffusion lengths of approximately 37 and 13 Å respectively. For the B579 sample, on the other hand, which was subjected to a less severe anneal of 90 s at 900 °C, PL blueshifts of 48 and 14 nm were obtained in the intermixed (SiO_2 intact) and intermixing-suppressed (SiO_2-free) control regions respectively. From Fig. 6.11 it may be seen that these PL blueshifts correspond to diffusion lengths of approximately 13 and 4 Å respectively.

The intermixed Al fraction profiles for the B690 material corresponding to L_d = 37 Å and L_d = 13 Å have been plotted in Fig. 6.25, while the Al fraction profiles for the B579 material corresponding to L_d = 13 Å and L_d = 4 Å are plotted in Fig. 6.26. Now, from the L_d = 37 Å Al fraction profile for the B690 material of Fig. 6.25, it may be seen that the maximum Al fraction, occurring on either side of the central well, is ≈ 0.38. This corresponds to a bandgap energy of ≈ 1996 meV at 77 K. The PL wavelength detected from the SiO_2-covered (i.e. intermixed everywhere) control regions at 77 K was approximately 634 nm, which translates into an energy of 1956 meV. Recalling then, that the 77 K PL transition for the B690 ACQW material with $Al_{0.2}Ga_{0.8}As$ in the well layers is the e1->C transition, and, assuming a C acceptor binding energy of 30 meV in the shallow well, we estimate the e1hh1 energy gap for this structure to be approximately 1986 meV. This means that the e1 level is within ≈ 6 meV of the conduction band QW barrier energy in the intermixed control region of the B690 sample. Since kT ≈ 6.6 meV at 77 K, we would therefore expect any electrons residing in the e1 level (and holes residing in the hh1 level) to have sufficient thermal energy to "jump" out of the shallow intermixed QWs for the B690 sample. During the measurement of the PL at 77 K from a region with narrow window widths therefore, we can imagine the electrons beginning to thermalise after excitation into the conduction band continuum. Any electrons relaxing into the deeper wells underneath the windows in the SiO_2, will rapidly thermalise to the e1 level where they remain for ≈ 1 ns on average before undergoing radiative recombination into the C acceptor level. Electrons that relax into the e1 level in the shallower intermixed wells underneath the SiO_2 strips on the other hand, will still have sufficient thermal energy to "jump" out of these wells and to relax into another well at some later time. We can therefore imagine electrons "hopping" in and out of such shallow wells, until they eventually fall into one of the deeper wells underneath a window in the SiO_2 where they relax to e1 and eventually undergo radiative recombination. We would not therefore expect to see a strong "QW-intermixed" PL peak feature from the areas of the B690 sample with narrow windows in the SiO_2 (and a correspondingly higher fractional SiO_2 coverage).

For the B579 material, in contrast, with GaAs in the QW layers, the dominant PL transition is the e1hh1 transition at 77 K, and we estimate that in the intermixed control region, the difference in energy between the QW barrier bandgap and the e1hh1 bandgap is approximately 94 meV. During a PL measurement at 77 K from a region of the B579 sample with narrow window widths in the SiO_2 therefore, any electrons thermalising into the shallower wells underneath a SiO_2 strip will thermalise to e1 and remain trapped. Eventually, they may recombine with holes in the hh1 level resulting in an intermixed PL peak. For the B579 sample, we would therefore expect to see a "QW-intermixed" PL peak feature from a region with narrow windows in the SiO_2.

In summary, it has been established, that the spatial resolution of the selective area IFVD process using hydrogen plasma is better than 2.2 μm for the B690 structure. However, first order quasi-phase-matched SHG in this structure requires the spatial resolution of the selective area IFVD process to be approximately 1.3 μm or better. Therefore, although the actual resolution may have been significantly less than 2.2 μm, we have no way of confirming this without performing a more exhaustive set of resolution experiments. We therefore conclude that the spatial resolution of the selective area IFVD process for the B690 structure is only really good enough for third order quasi-phase-matched SHG. Finally, for the B690 resolution sample (which was the best B690 resolution sample measured), we estimate from Fig. 6.9, that the relative $\chi^{(2)}_{zzz}$ AQW non-linearity, is approximately 0.48 and 0 in the intermixing-suppressed and QW-intermixed regions respectively.

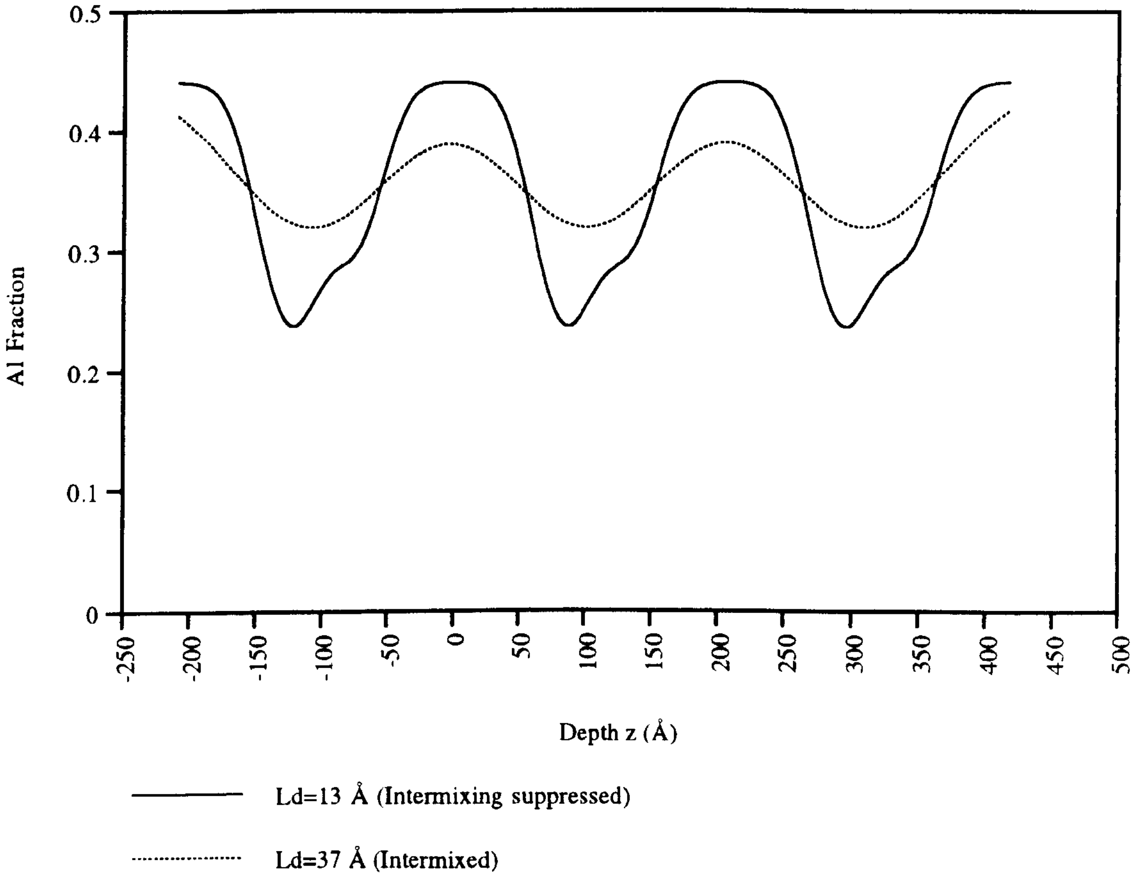

Fig. 6.25 B690 intermixed Al fraction profiles corresponding to intermixing-suppressed and intermixed regions of resolution sample

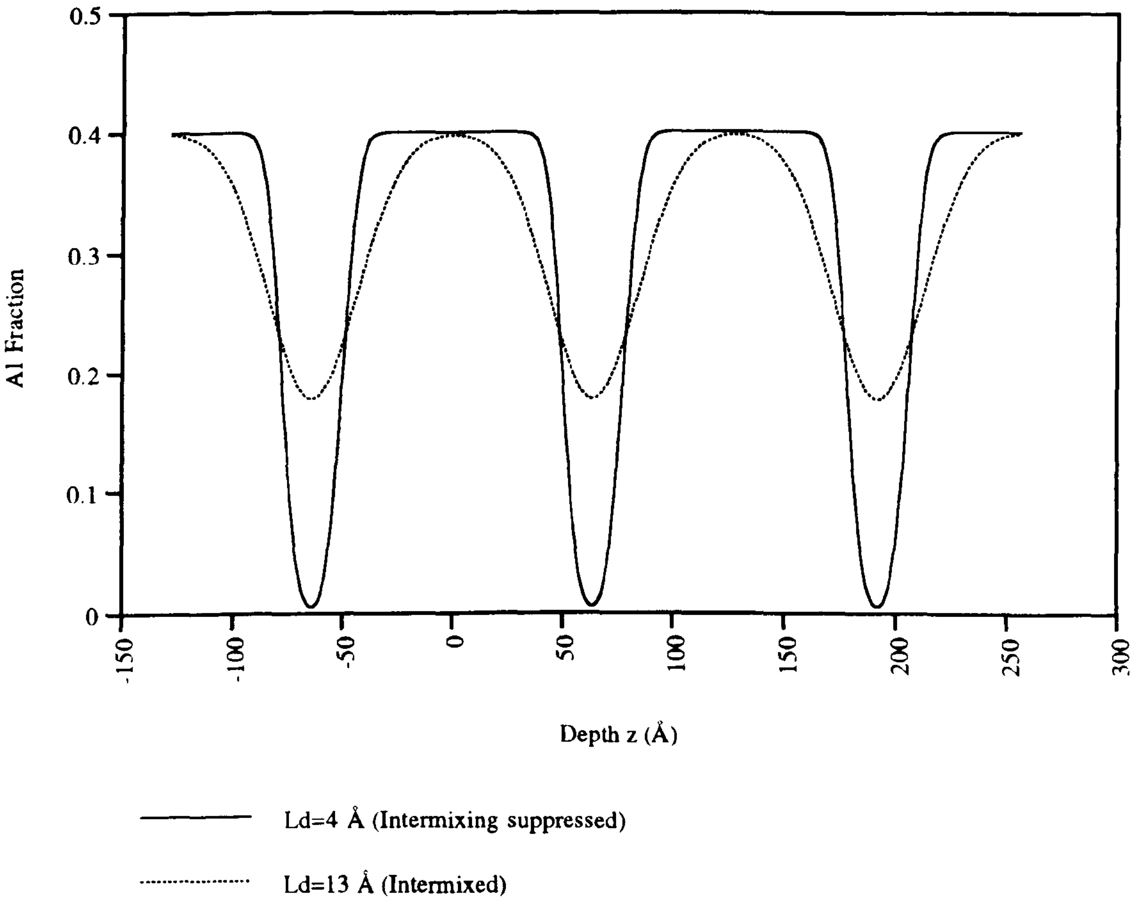

Fig. 6.26 B579 intermixed Al fraction profiles corresponding to intermixing-suppressed and intermixed regions of resolution sample

6.4 Conclusions

Photoluminescence peak blueshifts have been observed on intermixing of multiple AQW structures using the IFVD process. In each case the PL peak FWHM was not significantly broadened by intermixing. This suggested that uniform intermixing of the MQW layers had occurred. Furthermore, a first bound electron to first bound hole exciton peak was observed in the absorption spectrum of intermixed AQW material, providing even stronger evidence of uniform MQW intermixing. Such observations indicate that the vacancy concentration is highly uniform across the MQW layer and that the Al-Ga interdiffusion coefficient D may be assumed to be constant during annealing.

The 1D diffusion equation was solved for 3-well systems assuming D constant and the Al fraction profiles of the AQW structures of interest were evaluated as a function of the degree of intermixing, as represented by the diffusion length L_d. Schrödinger's equation was subsequently solved in the intermixed AQW potential profiles to yield the PL transition wavelengths as a function of L_d. It was therefore possible to infer the degree of intermixing L_d from the observed PL blueshift occurring on intermixing. In addition, the reductions in the "asymmetry factors" of the AQWs were evaluated as a function of L_d. It was therefore also possible to infer the reduction in the asymmetry (and hence estimate the reduction in the non-linear tensor elements associated with the asymmetric wells) from the observed PL blueshift occurring on intermixing. Different diffusion lengths were inferred from the PL blueshifts observed from the different AQW structures annealed under the same nominal conditions. Most notably, larger values of L_d were obtained for MBE-grown AQW layers with lower Al fractions, when e-beam evaporated SiO_2 caps were used. This may be tentatively attributed to several factors including lower vacancy concentrations in the higher Al fraction AQW structures due to higher C concentrations, the more porous nature of the e-beam evaporated SiO_2 compared with PECVD SiO_2, and different semiconductor surface conditions. A more systematic study of these factors is therefore required to determine their relative effect on the degree of intermixing.

The second harmonic conversion efficiency increases with the depth of the periodic modulation in $\chi^{(2)}$. It was therefore desirable to completely suppress quantum well intermixing in selected areas while maximising the degree of intermixing in other areas. Selective area intermixing using H plasma processing for intermixing suppression was not, however, very successful. In fact no suppression of the IFVD process was observed using the H plasma treatment for the MOCVD-grown QT849A material. Consequently, no waveguide devices were fabricated from the QT849A material for SHG experiments. Partial suppression of the IFVD process was however achieved with the B690 AQW material and a suppressed PL blueshift of 8 nm was obtained after H plasma processing. This compared with a PL blueshift of 16 nm in a SiO_2-free region of a B690 control sample which was not exposed to a H plasma but was annealed in parallel with the sample exposed to the H plasma. The suppression of the IFVD process after exposure of the B690 sample to the H plasma is believed to be the result of the formation of a Ga_2O_3 layer in the exposed regions which is impervious to Ga atoms during annealing.

The spatial resolution of the selective area H plasma IFVD process for the B690 material was measured to be better than 2.2 μm for a 90 s anneal at 950 °C. This resolution is certainly sufficient for third order quasi-phase-matching by domain disordering and is possibly also sufficient for first order quasi-phase-matching.

---

[1] J. H. Marsh, "Quantum Well Intermixing", Semicond. Sci. Technol. **8**, 1136 (1993)

[2] L. J. Guido, N. Holonyak Jr., K. C. Hsieh, R. W. Kaliski, W. E. Plano, R. D. Burnham, R. L. Thornton, J. E. Epler, and T. L. Paoli, "Effects of Dielectric Encapsulation and As Overpressure on Al-Ga Interdiffusion in $Al_xGa_{1-x}As$-GaAs Quantum-well Heterostructures", J. Appl. Phys. **61**, 1372 (1987)

[3] J. D. Ralston, S. O'Brien, G. W. Wicks, and L F. Eastman, "Room-Temperature Exciton Transitions in Partially Intermixed GaAs/AlGaAs Superlattices", Appl. Phys. Lett. **52**, 1511 (1988)

[4] K. B. Kahen, D. L. Peterson, G. Rajeswaran, and D. J. Lawrence, "Properties of Ga Vacancies in AlGaAs Materials", Appl. Phys. Lett. **55**, 651 (1989)

[5] L. J. Guido, J. S. Major Jr., J. E. Baker, W. E. Plano, N. Holonyak Jr., K. C. Hsieh, and R. D. Burnham, "Column III Vacancy- and Impurity-induced Layer Disordering of $Al_xGa_{1-x}As$-GaAs Heterostructures with SiO_2 or Si_3N_4 Diffusion Sources", J. Appl. Phys. **67**, 6813 (1990)

[6] T. E. Schlesinger and T. Kuech, "Determination of the Interdiffusion of Al and Ga in Undoped (Al,Ga)As/GaAs Quantum Wells", Appl. Phys. Lett. **49**, 519 (1986)

[7] L. J. Guido, N. Holonyak Jr., K. C. Hsieh, and J. E. Baker, "Depth-dependent Native-defect-induced Layer Disordering in $Al_xGa_{1-x}As$-GaAs Quantum Well Structures", Appl. Phys. Lett. **54**, 262 (1989)

[8] B. Tuck, "Introduction to Diffusion in Semiconductors", Peter Peregrinus Ltd., Stevenage, (1974)

[9] J. Crank, "The Mathematics of Diffusion", Clarendon, Oxford, (1975)

[10] R. C. Miller, A. C. Gossard, W. T. Tsang, and O. Munteanu, "Extrinsic Photoluminescence from GaAs Quantum Wells", Phys. Rev. B **25**, 3871 (1982)

[11] W. T. Masselink, Yia-Chung Chang, and H. Morkoç, "Binding Energies of Acceptors in GaAs-$Al_xGa_{1-x}As$ Quantum Wells", Phys. Rev. B **28**, 7373 (1983)

[12] I. Gontijo, T. Krauss, J. H. Marsh, and R. M. De La Rue, "Postgrowth Control of GaAs/AlGaAs Quantum-Well Shapes by Impurity-free Vacancy Diffusion", J. Quantum Electron. **30**, 1189 (1994)

[13] C. J. Hamilton, "Novel Structures and Fabrication Techniques for the Observation of Solitons in AlGaAs", PhD Thesis, University of Glasgow, 1995

[14] C. J. Hamilton, S. E. Hicks, B. Vögele, J. H. Marsh and J. S. Aitchison, "Suppression of Bandgap Shifts in GaAs/AlGaAs MQWs Using Hydrogen Plasma Processing", Electron. Lett. **31**, 1393 (1995)

7

Experiments with GaAs/AlGaAs Multiple AQW Starting Material and QW-intermixed Ridge Waveguides

As discussed in previous chapters, to utilise a second order effect in GaAs/AlGaAs requires quasi-phase-matching. In a multiple AQW waveguide this can be achieved by periodic suppression of the non-linearity using QW-intermixing. Thus, if we can achieve efficient quasi-phase-matched SHG in this way, it is also possible that, by tuning the input wavelength away from phase-matching wavelength, a small quasi-phase-mismatch will be produced, as required for the cascaded second order effect. In this respect, the achievement of efficient SHG may be regarded as a precursor to the efficient production of non-linear phase shifts via the $\chi^{(2)}:\chi^{(2)}$ effect. To achieve efficient quasi-phase-matched SHG, an important initial objective is the demonstration of unphase-matched SHG in the starting material, and the suppression of this unphase-matched SHG. Ridge waveguides were therefore fabricated from QT613, B563, B578 and B690 starting materials, and from QT613, B563, B578 and B690 QW-intermixed materials. Identical experiments were performed with these devices in an attempt to observe unphase-matched SHG which was attributable to the AQW non-linearities alone.

In this chapter, results will be presented which also show that the bulk GaAs/AlGaAs component $\chi^{(2)}_{xyz}$ is modified significantly on QW-intermixing, suggesting exciting new possibilities for efficient quasi-phase-matching in the GaAs/AlGaAs material system.

7.1 The Design and Fabrication of Ridge Waveguides for Unphase-matched SHG

In this section, the design and fabrication of ridge waveguides from B690 starting material and B690 intermixed material will be described. The fabrication of samples based on wafer structures QT613, B563 and B578 followed the same process.

Ridge waveguides were fabricated from both the B690 starting material, and from the B690 intermixed material. On annealing, a 77 K PL blueshift of 23 nm was observed as a result of the intermixing process. From Fig. 6.9 it may be seen that a 77 K PL blueshift of 23 nm corresponds to a diffusion length of 22 Å and we would therefore expect $\chi^{(2)}_{zzz}$ for the QW-intermixed sample to be reduced to at least 10% of its starting material value. Rib waveguides with a range of widths from 1 μm - 10 μm were formed by dry etching with $SiCl_4$. The nominal etch depth was 0.9 μm to guarantee reasonable confinement of the lowest order modes at both the fundamental wavelength of 1.55 μm and the second harmonic wavelength of 775 nm. From a surface profile measurement, etch depths of 1.0 μm and 0.8 μm were observed for the starting material and the intermixed samples respectively. The waveguide samples were subsequently thinned and cleaved into 2 mm long devices.

7.2 Waveguide Loss Measurements

Light from a narrow linewidth DFB laser diode source at 1.556 μm was end-fire coupled into the 2 mm-long B690 starting material and intermixed waveguides in turn. Waveguides with 3 μm rib widths were selected in each case, as calculations suggested that such waveguides would be essentially single-moded at 1.556 μm. The light transmitted by the waveguides was focused onto the end of an optical fibre which was connected to an optical spectrum analyser operating in "zero span" mode. In this mode, the analyser displayed the optical power collected by the fibre as a function of time. The fibre end was then carefully translated across the beam at the output of the waveguide until maximum power was detected by the analyser. A cotton bud was soaked in liquid nitrogen and held in close proximity to the waveguide sample to achieve cooling. During cooling of the waveguide sample, Fabry-Perot oscillations were observed in the transmitted power T, due to incremental changes in the waveguide length. The waveguide loss coefficient α was then estimated from the visibility $V = T_{max}/T_{min}$ of the transmission oscillations [1]:

$$\alpha(\mathrm{dB/cm}) = \frac{4.34}{L}\ln\left[\frac{R\left(\sqrt{V}+1\right)}{\left(\sqrt{V}-1\right)}\right] \qquad (7.1a)$$

where

$$R = \frac{(n_{eff} - 1)^2}{(n_{eff} + 1)^2} \tag{7.1b}$$

and L is the waveguide length in cm.

The loss coefficients α for the B690 starting material and intermixed material waveguides measured in this way were 20.9 dB/cm and 7.9 dB/cm respectively, and it may be seen that the starting material waveguide losses were actually higher than the intermixed waveguide losses. This was attributed to the fact that the starting material waveguides were over-etched slightly as mentioned in Section 7.1. Nevertheless, the losses measured for the QW-intermixed waveguide sample of 7.9 dB/cm are encouragingly low, especially when compared with losses of 30 dB/cm measured at 1.06 μm in waveguides which were disordered by As^+-implantation for the suppression of the bulk GaAs/AlGaAs non-linear coefficient d_{14} and subsequently annealed [2].

7.3 Unphase-matched SHG Experiments

A schematic of the experimental set-up used for unphase-matched SHG measurements is shown in Fig. 7.1. The KCl colour-centre laser was coupled-cavity mode-locked and produced 660 fs pulses at a repetition rate of 82 MHz and a wavelength of 1.524 μm. The laser beam was chopped, linearly polarised and end-fire coupled into the waveguide samples. The transmitted fundamental beam was end-fire coupled out of the waveguides along with any generated second harmonic. The output polariser was adjusted to transmit linearly-polarised TM field components at ω and 2ω, and a portable monochromator was used to separate the two frequency components. The second harmonic intensity was monitored using lock-in detection with a photomultiplier tube (PMT). The PMT was only sensitive over the spectral range 400 - 1100 nm.

The average fundamental output power and the second harmonic PMT signal were measured as a function of the input fundamental power. Experiments were performed using both the starting material and intermixed material waveguides, and for both TE and TM configurations of the input polariser. The average fundamental output power was measured before the output polariser with an aperture inserted in the optical path between the output microscope objective of the end-fire rig and the power meter. Inserting the aperture in this way, means that any light which had propagated in the slab regions either side of the waveguide rib was blocked, and thus did not contribute to the measured output power.

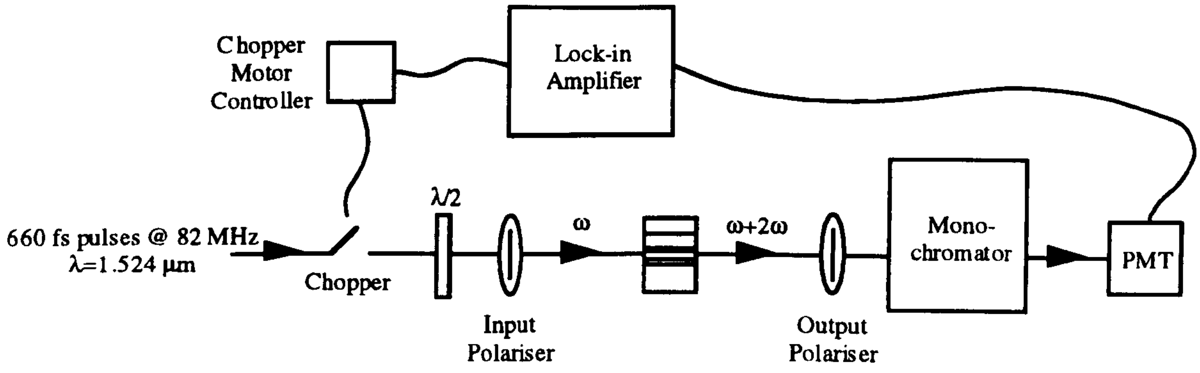

Fig. 7.1 Schematic diagram of the experimental set-up used for unphase-matched SHG experiments

7.4 Unphase-matched SHG Results and Discussion

Before presenting the unphase-matched SHG results, we should consider the consequences of using pulsed laser radiation for the measurements. The FWHM spectral range of the 660 fs mode-locked pulses from the colour-centre laser was 1521.2 nm - 1526.0 nm. Such a spread of wavelengths means that the unphase-matched SHG intensity as a function of length will be different from the monochromatic case plotted in Fig. 2.1. From Section 2.3.2 we know that for monochromatic uniform plane waves:

$$\frac{I_{2\omega}(L)}{I_\omega(0)} = \frac{32\pi^2}{\varepsilon_0 c\lambda^2}\frac{d_{eff}^2}{n_\omega^2 n_{2\omega}}\frac{I_\omega(0)}{(\Delta k)^2}\sin^2\left(\frac{\pi L}{2L_c}\right) \tag{7.2}$$

For the case of unphase-matched SHG in a ridge waveguide this expression is modified to:

$$\frac{P_{2\omega}(L)}{P_\omega(0)} = \frac{32\pi^2}{\varepsilon_0 c\lambda^2}\frac{d_{eff}^2}{n_{\omega eff}^2 n_{2\omega eff}}\frac{P_\omega(0)}{(\Delta k)^2}\sin^2\left(\frac{\pi L}{2L_c}\right)\times F^{(2)} \tag{7.3}$$

where $P_\omega(0)$ and $P_{2\omega}(L)$ are the fundamental and second harmonic powers at the waveguide input and output respectively, and $F^{(2)}$ is the waveguide overlap factor introduced in Section 2.6. Also $\Delta k = (n_{\omega eff} - n_{2\omega eff})\cdot 4\pi/\lambda$ and $L_c = \pi/\Delta k$. From (7.3) it can be seen that for a change in L/L_c of 2, there will be an oscillation of $P_{2\omega}(L)/P_\omega(0)$ through one period. Bearing this in mind, L/L_c is plotted as a function of wavelength in

Fig. 7.2 for a 2 mm-long B690 ridge waveguide with a rib width of 3 μm and an etch depth of 0.9 μm. For this graph, the fundamental and the second harmonic fields were both assumed to be propagating in the TM_{00} mode, and the refractive indices of the various waveguide layers were calculated using the modified Afromowitz model [3]. From Fig. 7.2 it can be seen that L/L_c is a strongly decreasing function of wavelength between 1520 and 1530 nm, and, in fact, L/L_c varies by as much as 20 over the FWHM bandwidth of the pulsed laser. For monochromatic light, $P_{2\omega}(L)/P_{\omega}(0)$ will therefore undergo as many as 10 oscillations when the wavelength is varied over the observed bandwidth of the laser pulses. Therefore any oscillations in the unphase-matched SHG as a function of length, will be "washed-out" due to the wavelength spread of the laser pulses. This results in a constant second harmonic power level along the waveguide (assuming negligible losses). Any small change in the waveguide length during pulsed laser operation will not, therefore, result in a significant change in the SHG at the output of the waveguide. This means that, for pulsed laser operation, we would expect the same unphase-matched second harmonic power to be produced at the output of 2 waveguides which are identical in every respect except that one waveguide is a few μm longer than the other.

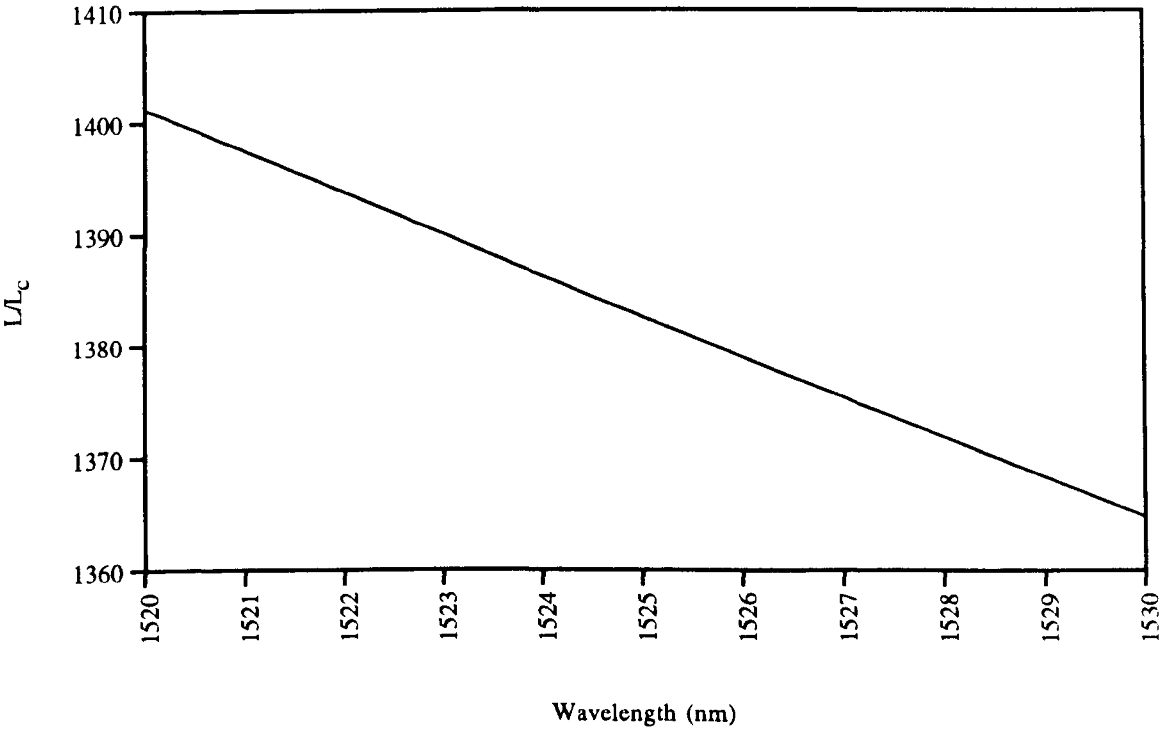

Fig. 7.2 Waveguide length normalised to the SHG coherence length as a function of wavelength over the pulsed laser spectral region

For a refractive index variation, (such as that which may occur on MQW-intermixing), non-oscillatory behaviour of the SHG as a function of length would also be expected for pulsed laser operation. However, from (7.3) it can be seen that $P_{2\omega}(L)/P_{\omega}(0) \propto F^{(2)}/(\Delta k)^2$. On intermixing, the band-gap widens and the detuning of the second harmonic photon energy below the half-band-gap energy increases. This means that, when operating below half the band-gap, the refractive index in the MQW layer $n_{2\omega}$ may decrease on intermixing, while n_{ω} in the MQW is likely to remain approximately constant. In fact, it has previously been reported that, even for a detuning of the photon energy from the band-edge as small as 60 meV, the refractive index change occurring on intermixing GaAs/AlGaAs MQW layers by impurity induced disordering is ~ 1%.[4,5,6] Furthermore, waveguide measurements show that the MQW layer index reduction occurring on intermixing the same structures using IFVD is at least an order of magnitude less than the index reduction obtained using IID.[5] This means that for the non-phase-matched SHG experiments with a detuning of the two-photon energy of ~ 100 meV below the e_1hh_1 band-edge, the reduction in the second harmonic effective index occurring on intermixing by IFVD can be assumed to be less than 0.1%. The reduction in the fundamental effective index can correspondingly be assumed to be considerably less than 0.1%. Such index changes do not significantly affect the SHG overlap factor $F^{(2)}$ in ridge waveguides of the type studied here. Also, for $n_{\omega eff}$ constant and $n_{2\omega eff}$ reduced by 0.1%, $(\Delta k)^2$ is reduced by a few percent, and $P_{2\omega}(L)/P_{\omega}(0)$ is correspondingly larger by a few percent. Hence, for pulsed laser operation, marginally more SHG might be expected from an intermixed waveguide because of the reduction in $n_{2\omega eff}$ *alone* (i.e. assuming the MQW waveguide non-linearities are unchanged on intermixing).

In performing pulsed laser unphase-matched SHG experiments, Fabry-Perot effects within the waveguide cavities should also be considered. A 1 ps pulse is ~100 μm-long in GaAs/AlGaAs. Therefore, for a 2 mm - long waveguide sample we would not expect any interference effects to occur. This means that any small difference in length of the starting material and intermixed material waveguides will not effect the transmission of the fundamental or second harmonic beams. Similarly, any differences between the waveguide indices will not change the waveguide transmission significantly.

Before discussing the unphase-matched SHG results for the B690 waveguide samples, the unphase-matched SHG results obtained for the other multiple AQW waveguide structures QT613, B563 and B578 will be discussed. No unphase-matched TM-polarised SHG was detected for QT613 starting material waveguides for a TM input polarisation when operating at sub-half-band-gap wavelengths. From the conclusions at the end of Section 3.2.3, it may be recalled that, for a TM input polarisation, only TM-polarised second harmonic is generated through the $\chi^{(2)}_{zzz}$ tensor component alone. Due to the absence of any SHG in the "TM_{ω}:$TM_{2\omega}$ polarisation configuration", we therefore conclude that no $\chi^{(2)}_{zzz}$

tensor component exists for the QT613 material. Furthermore, from the characterisation results for the QT613 material of Section 5.3, we assert that no $\chi^{(2)}_{zzz}$ tensor component exists for the QT613 material because no second bound electron level was supported in the conduction band of the QT613 asymmetric stepped QW's.

Unphase-matched SHG experiments were performed at 1.55 μm with both B563 and B578 waveguides. The B563 and B578 materials both had band-gaps around 815 nm (see Table 5.3), so that a fundamental wavelength of 1.55 μm corresponds to a photon energy above half the band-gap. As a consequence, two-photon absorption occurred and the $TE_\omega:TE_\omega$ and $TM_\omega:TM_\omega$ fundamental transmission characteristics for the two materials (i.e. the output fundamental power as a function of the input fundamental power) were sub-linear. From the degree of curvature in the transmission characteristics, it was possible to deduce that the level of two-photon absorption was larger for a TE_ω input than for a TM_ω input. This is to be expected, since a proportion of the second harmonic generated in either case is linearly absorbed, resulting in an *effective* increase in the two-photon absorption observed. For the $TE_\omega:TM_{2\omega}$ configuration, the second harmonic is generated via the large bulk GaAs/AlGaAs coefficient $\chi^{(2)}_{zxy} \approx \chi^{(2)}_{xyz} \approx 380$ pm/V, while for the $TM_\omega:TM_{2\omega}$ configuration, the second harmonic is generated via the much smaller AQW component $\chi^{(2)}_{zzz} \approx 0.1$ pm/V. We would therefore expect more SHG to occur for the $TE_\omega:TM_{2\omega}$ case than for the $TM_\omega:TM_{2\omega}$ case, and the two-photon absorption to be correspondingly higher for the $TE_\omega:TM_{2\omega}$ case. The $TE_\omega:TE_\omega$ and $TM_\omega:TM_\omega$ transmission characteristics were reduced for both the B563 and B578 intermixed waveguide samples due to increased waveguide losses. In addition, the curvature of the transmission characteristics was reduced on intermixing, indicating a reduction in both the two-photon absorption of the fundamental and a reduction in the linear absorption of the second harmonic due to bandgap widening.

The $TE_\omega:TM_{2\omega}$ second harmonic characteristics for the B563 and B578 waveguides appear in Figs. 7.3 and 7.4 respectively. From these figures it can be seen that more SHG was observed from the intermixed waveguides. To explain these observations it should be emphasised that, when operating at photon energies above half the bandgap, the magnitude of the SHG signal is determined not only by the size of the non-linear component, but also by the linear absorption at the second harmonic frequency and the two-photon absorption at the fundamental frequency. The results of Figs. 7.3 and 7.4 may therefore be explained in terms of these competing effects: on intermixing, the relative reduction in the absorption of the second harmonic beam is greater than the relative reduction in $\chi^{(2)}_{xyz}$ and a net increase in the SHG signal results (see Section 7.4.1(iv) for a full discussion).

The $TM_\omega:TM_{2\omega}$ second harmonic signals for the B563 and B578 waveguides were both reduced on intermixing, suggesting a larger relative reduction of the $\chi^{(2)}_{zzz}$ AQW component than in the second harmonic absorption in both instances. However, from theory, $\chi^{(2)}_{xyz}$ is over three orders of magnitude greater than $\chi^{(2)}_{zzz}$, and it may be shown (see Section 7.4.2) that, for a $TM_\omega:TM_{2\omega}$ configuration, a small field component in the direction of propagation or any small misalignment of the polariser axes with respect to the crystal axes can lead to the production of a significant second harmonic signal via the large $\chi^{(2)}_{xyz}$ component. This means that the reduction in the $TM_\omega:TM_{2\omega}$ SHG on intermixing could simply reflect a reduction in $\chi^{(2)}_{xyz}$, and it is therefore impossible to make any conclusions relating to the change in $\chi^{(2)}_{zzz}$ on intermixing.

For the B690 material, a fundamental wavelength of 1.524 μm corresponds to a detuning of the photon energy below the half-band-gap of approximately 60 meV. We would not therefore expect any linear absorption at the second harmonic frequency or any two-photon absorption at the fundamental frequency to occur. The fundamental transmission characteristics of the B690 waveguide samples for TE and TM input polarisations appear in Figs. 7.5 and 7.6 respectively. Since these characteristics are both linear we conclude that no two-photon absorption occurred in either the B690 starting material or intermixed waveguides. It may also be seen that the coupling efficiencies for the QW-intermixed waveguides are actually higher. This was attributed to higher losses in the starting material waveguides (see Section 7.2) due to a slight "over-etch" of the starting material waveguide ribs.

The B690 waveguide unphase-matched SHG plots of Figs. 7.7 and 7.8 were the most significant results obtained during this work. Clearly, the TM-polarised SHG was reduced on MQW-intermixing for *both* TE and TM input polarisations. For the TE input polarisation, the TM-polarised SHG was scaled by a factor of 0.518 on intermixing, while for the TM input polarisation, the TM-polarised SHG was scaled by a factor of 0.207 on intermixing. A detailed discussion of these results is presented in the following sections.

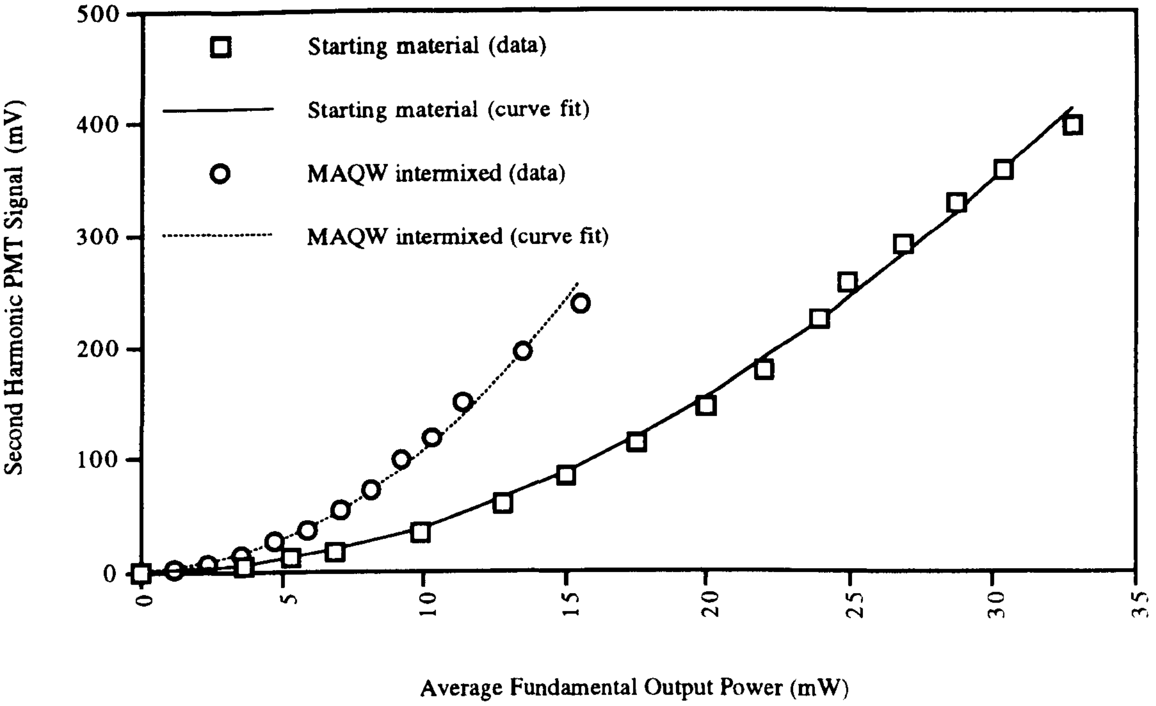

Fig. 7.3 $TE_{\omega}:TM_{2\omega}$ unphase-matched SHG for B563 multiple ASQW waveguides

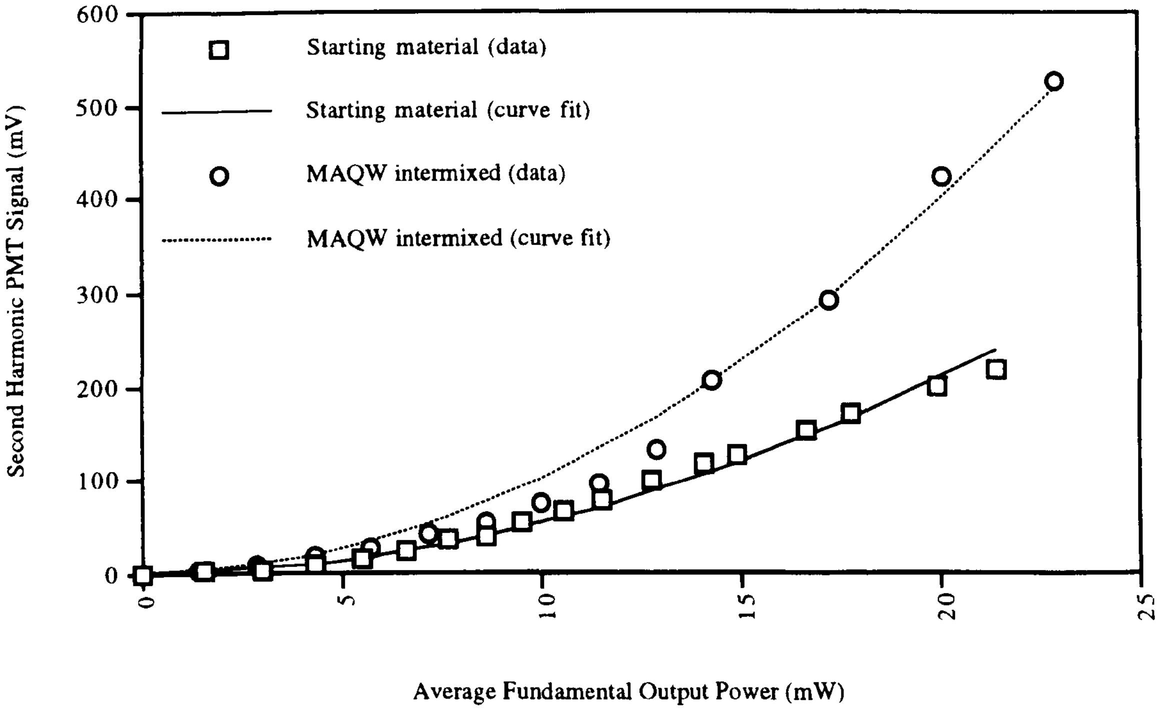

Fig. 7.4 $TE_{\omega}:TM_{2\omega}$ unphase-matched SHG for B578 multiple ACQW waveguides

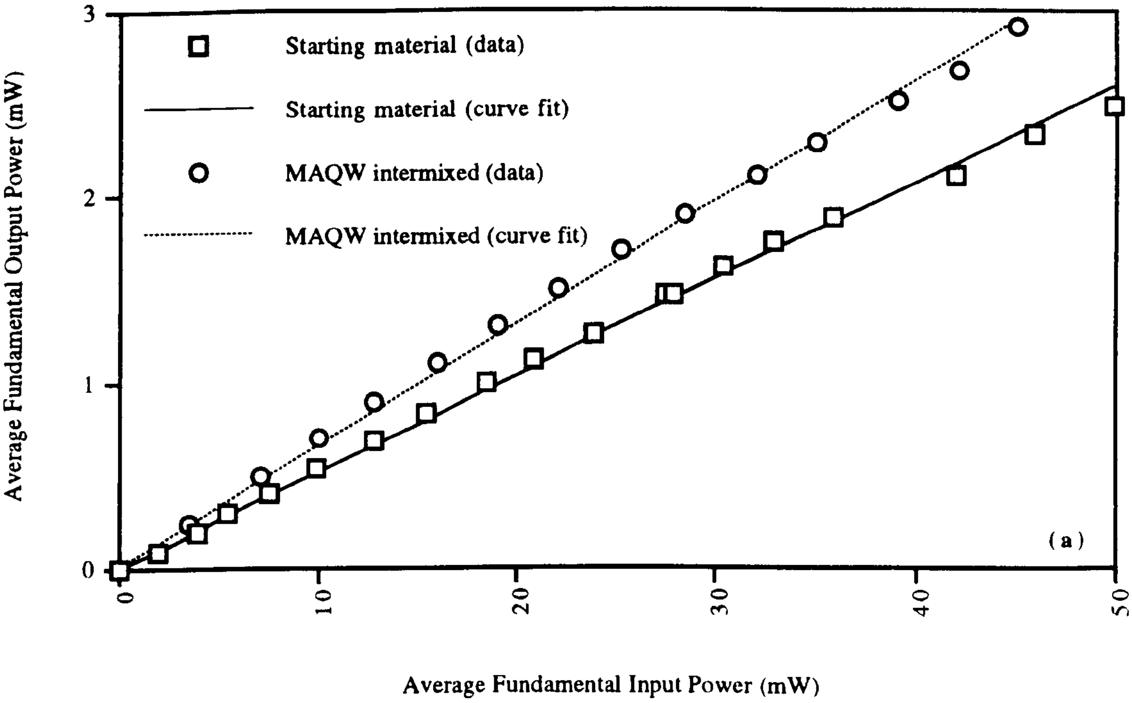

Fig. 7.5 TE_{ω}:TE_{ω} fundamental transmission characteristics at 1.524 μm for B690 multiple ACQW waveguides

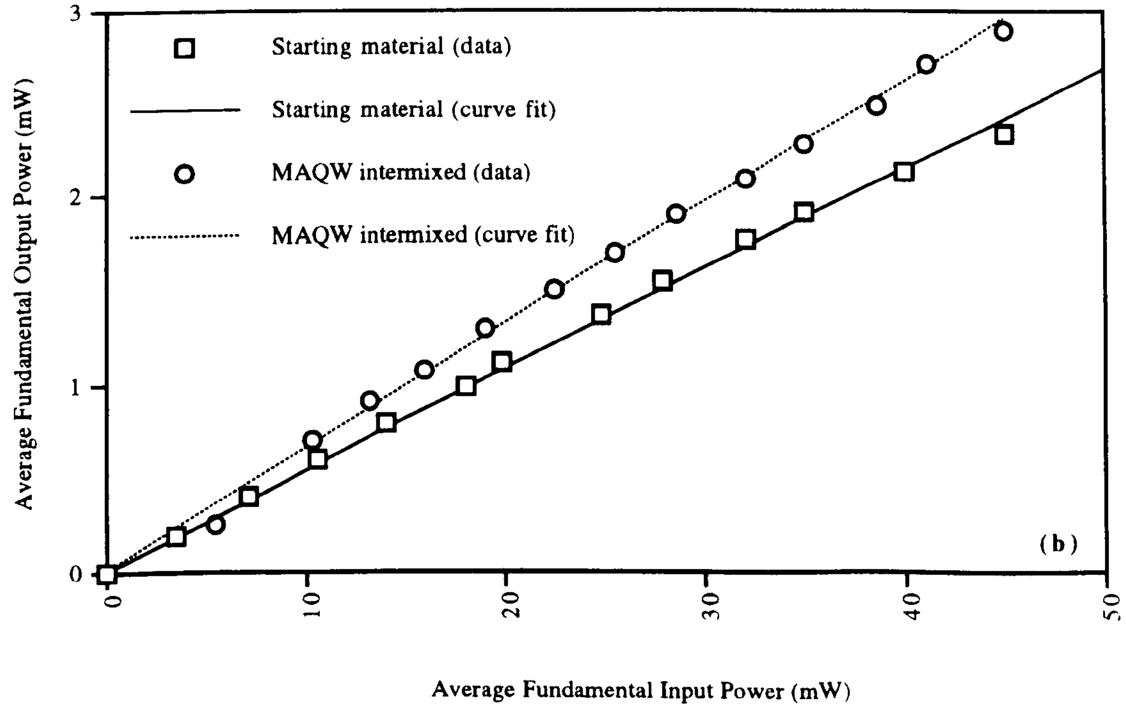

Fig. 7.6 TM_{ω}:TM_{ω} fundamental transmission characteristics at 1.524 μm for B690 multiple ACQW waveguides

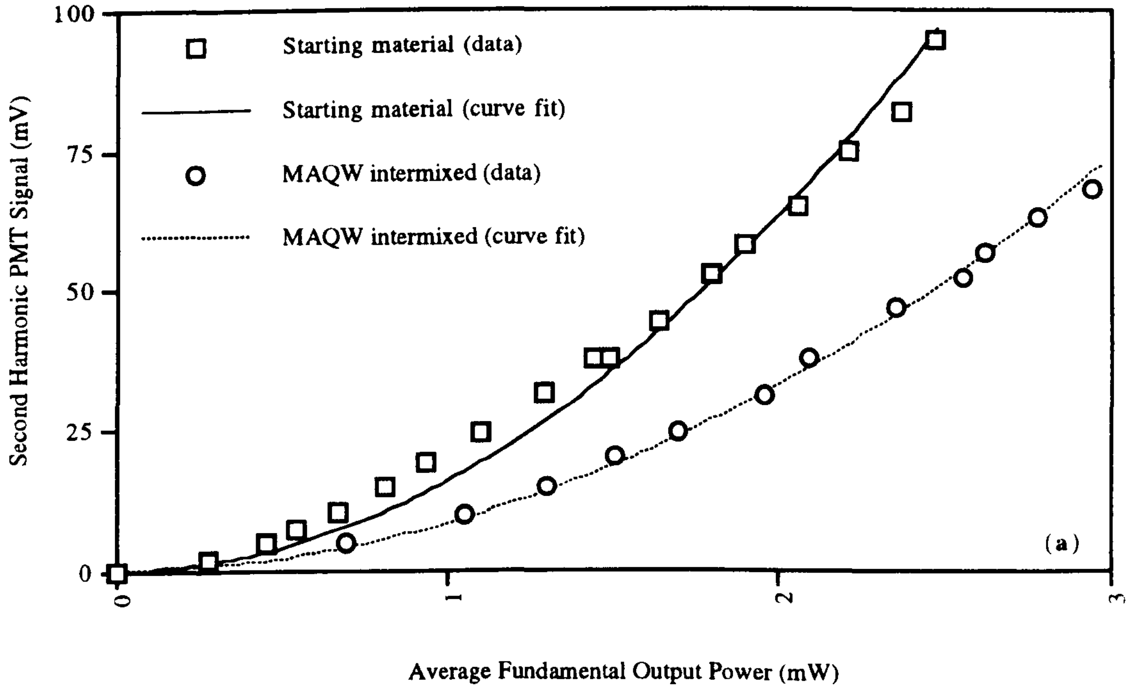

Fig. 7.7 TE$_{\omega}$:TM$_{2\omega}$ unphase-matched SHG for B690 multiple ACQW waveguides for a fundamental wavelength of 1.524 μm

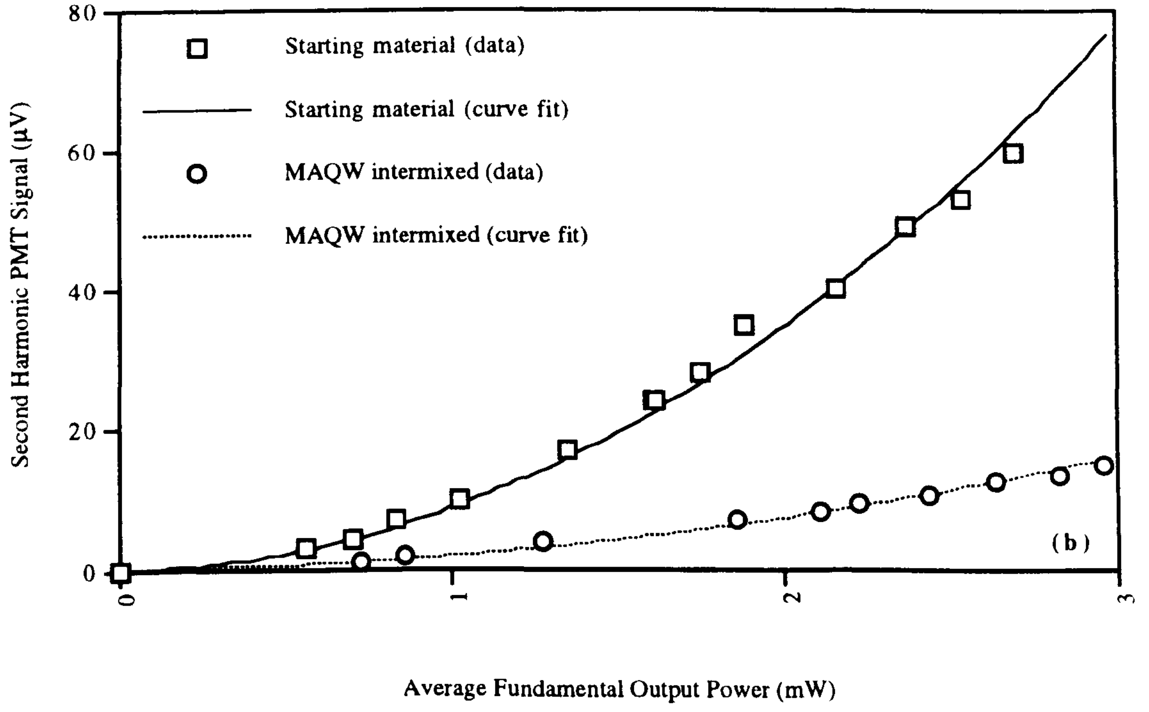

Fig. 7.8 TM$_{\omega}$:TM$_{2\omega}$ unphase-matched SHG for B690 multiple ACQW waveguides for a fundamental wavelength of 1.524 μm

7.4.1 Unphase-matched SHG in B690 Waveguides for a TE_ω:$TM_{2\omega}$ Polarisation Configuration

For a TE_ω:$TM_{2\omega}$ polarisation configuration, the only contributing tensor components for SHG are the bulk component $\chi^{(2)}_{xyz}$, and the AQW component $\chi^{(2)}_{zxx}$ (see Section 3.2). The reduction in the unphase-matched TE_ω:$TM_{2\omega}$ SHG observed in Fig. 7.7 for the intermixed waveguide relative to that for the starting material waveguide sample, may be caused by a combination of several factors. These factors will now be discussed in turn.

(i) Reduction in the Overlap Factor $F^{(2)}_{xyz}$

Due to the shallower etch depth for the intermixed waveguide sample we would expect a reduced SHG efficiency overlap factor $F^{(2)}_{xyz}$ as defined by (3.8b). For the B690 waveguides with 3 μm-wide ribs, overlap factors $F^{(2)}_{xyz}$ of 1.844×10^{11} /m^2 and 1.387×10^{11} /m^2 were calculated at 1.524 μm for the starting material waveguide with an etch depth of 1.0 μm and the intermixed waveguide with an etch depth of 0.8 μm respectively. As a consequence of the different etch depths alone, we would therefore expect the unphase-matched SHG power observed from the intermixed waveguide to be approximately 75.2% of that from the starting material waveguide (all other parameters being equal) i.e.

$$\frac{F^{(2)'}_{xyz}}{F^{(2)}_{xyz}} = 0.752 \qquad (7.4)$$

where $F^{(2)'}_{xyz}$ denotes the overlap factor for the intermixed material waveguide.

(ii) Angular Deviation of the Fundamental Polarisation from the TE Axis (and the Second Harmonic Polarisation from the TM Axis)

During the unphase-matched SHG experiments in the TE_ω:$TM_{2\omega}$ configuration, the transmission axis of the output polariser was vertical with respect to the optical bench, and the input polariser was adjusted for minimum transmission of the fundamental TE field after the output polariser. For a small angular deviation θ of the waveguide sample normal from the vertical as indicated in Fig. 7.9, the fundamental and second harmonic field polarisations would have been deviated by θ from the TE and TM axes respectively. From uniform plane wave considerations we may then deduce (see Appendix D):

$$\frac{I_{2\omega}(\theta)}{I_{2\omega}(\theta=0)} = \left|\cos^3\theta - 2\sin^2\theta\cos\theta\right|^2 \tag{7.5}$$

where $I_{2\omega}$ denotes the output second harmonic intensity. In addition, the AQW tensor components are assumed to be negligible with respect to the bulk tensor component $\chi^{(2)}_{xyz}$ in line with the predictions of Hutchings and Arnold as discussed in Section 3.1. Fig. 7.10, is a plot of $I_{2\omega}(\theta)/I_{2\omega}(\theta=0)$ as defined by (7.5). From this figure it may be seen that $I_{2\omega}(\theta)/I_{2\omega}(\theta=0)$ is only a weakly decreasing function of θ for $0<\theta<5°$. Thus, any small deviation in either the starting material or intermixed waveguide sample normals from the vertical, will have a negligible effect on the TM-polarised SHG.

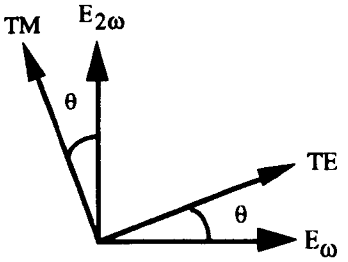

Fig 7.9 Angular deviation of the horizontal and vertical field components with respect to the waveguide axes for an angular deviation of the waveguide surface normal to the vertical

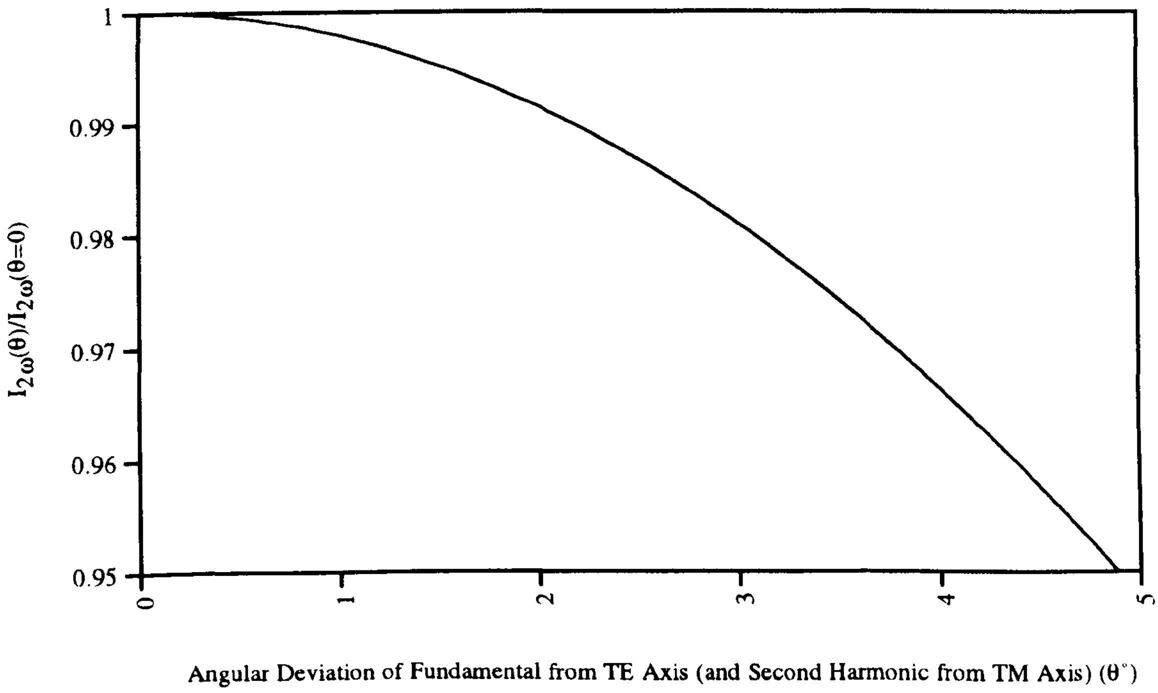

Fig. 7.10 Normalised SHG intensity $I_{2\omega}(\theta)/I_{2\omega}(\theta=0)$ as a function of the angular deviaion of the fundamental field polarisation from the TE axis (and the second harmonic field polarisation from the TM axis)

(iii) Reduction in $\chi^{(2)}_{zxx}$

Given that the AQW tensor component for the B690 structure as predicted by Hutchings and Arnold (see Section 3.1) was only 0.2 pm/V at 1.55 μm, as compared to $\chi^{(2)}_{xyz}$ = 380 pm/V, it seems reasonable to assume that any reduction of $\chi^{(2)}_{zxx}$ due to intermixing, will have a negligible effect on the TM-polarised SHG observed.

(iv) Reduction in $\chi^{(2)}_{xyz}$

From (i) to (iii) above, we conclude that the observed reduction in the TM-polarised SHG for a TE-polarised fundamental from the intermixed waveguide sample is, in part, due to a reduction in the overlap factor $F^{(2)}_{xyz}$, but mostly due to a reduction in $\chi^{(2)}_{xyz}$. To extract the reduction in $\chi^{(2)}_{xyz}$ from the observed reduction in the second harmonic signal for the intermixed waveguide of Fig. 7.7, the following relation can be applied:

$$P_{2\omega} \propto \left|\chi^{(2)}_{xyz}\right|^2 \cdot F^{(2)}_{xyz} \tag{7.6}$$

where $P_{2\omega}$ denotes the output second harmonic power. This gives:

$$\left|\chi^{(2)}_{xyz}\right|' \approx 0.83\left|\chi^{(2)}_{xyz}\right| \tag{7.7}$$

where $\left|\chi^{(2)}_{xyz}\right|'$ denotes the bulk GaAs/AlGaAs non-linearity for the MQW-intermixed sample. The implications of (7.7) are potentially very important: by intermixing the MQW layer a significant reduction in the large (380 pm/V) $\chi^{(2)}_{xyz}$ tensor component is obtained, as required for quasi-phase-matching. From the arguments regarding the pulsed operation of the laser and the consequences for unphase-matched SHG, it may be recalled that, any reduction in the effective index at the second harmonic wavelength that occurs on QW-intermixing will lead to an increase in the unphase-matched SHG. Therefore, we may conclude that the reduction in $\chi^{(2)}_{xyz}$ observed on intermixing is *at least* 17%.

To understand how this reduction in $\chi^{(2)}_{xyz}$ comes about, and to gain some insight into how an even larger reduction in $\chi^{(2)}_{xyz}$ may be obtained, qualitative arguments can be used. At photon energies close to the half-band-gap, both SHG and second harmonic absorption occur. These two competing processes are represented by the real and imaginary parts of $\chi^{(2)}_{xyz}$ respectively. For GaAs, the real part of $\chi^{(2)}_{xyz}$, $\mathrm{Re}\left\{\chi^{(2)}_{xyz}\right\}$ rolls off towards its low frequency value of 380 pm/V more slowly than the imaginary part $\mathrm{Im}\left\{\chi^{(2)}_{xyz}\right\}$ rolls off towards zero for decreasing photon energies below the half-band-gap energy $E_g/2$ [7]. This situation is depicted qualitatively in Fig. 7.11a. For low photon energies, SHG will dominate over second harmonic absorption. As the photon energy increases, the second harmonic power $P_{2\omega}(\hbar\omega)$ should increase initially as shown in Fig. 7.11b. For photon energies $\hbar\omega$ closer to $E_g/2$ (such that $\hbar\omega - E_g/2$ is approximately a few tens of meV), some second harmonic absorption will occur, causing $P_{2\omega}$ to increase more slowly. As $\hbar\omega$ increases still further, second harmonic absorption becomes the dominant effect, and $P_{2\omega}(\hbar\omega)$ begins to fall with $\hbar\omega$. $P_{2\omega}(\hbar\omega)$ must, therefore, have a maximum for some photon energy $\hbar\omega_p$.

Now, the $P_{2\omega}(\hbar\omega)$ curve for AlGaAs MQW layers should be qualitatively similar to the bulk GaAs $P_{2\omega}(\hbar\omega)$ curve plotted in Fig. 7.11b, except that now the band-gap is determined by the bound QW energy levels. Furthermore, by intermixing a MQW sample, the band-gap shifts, so that $E_g/2$ and the curve of Fig. 7.11b are effectively translated to higher photon energies. A second curve labelled $P_{2\omega}'(\hbar\omega)$ may therefore be drawn for the intermixed waveguides, which is qualitatively similar to that for the starting material waveguides, but shifted to higher energies as depicted in Fig. 7.11c.

It may be recalled that no two-photon absorption was observed in the B690 starting material or intermixed waveguides. This implies that the photon energy of operation at 1.55 μm $\hbar\omega_{B690} \approx 0.8$ eV, is some way below $\hbar\omega_p$ as indicated in Fig. 7.11c. Also, it may be recalled that the unphase-matched second harmonic power $P_{2\omega}(\hbar\omega)$ observed for the MQW-intermixed B563 and B578 waveguides in a TE_ω:$TM_{2\omega}$ configuration was *greater* than $P_{2\omega}(\hbar\omega)$ for the corresponding starting material waveguides (see Figs. 7.3 and 7.4). This may then also be explained qualitatively with reference to Fig. 7.11c: the photon energy of operation $\hbar\omega_{B563,B578}$ for the B563 and B578 starting material devices was above $E_g/2$ as indicated in Fig. 7.11c, so that on QW-intermixing, an increase in $P_{2\omega}(\hbar\omega)$ is obtained.

When modulating $\chi^{(2)}_{xyz}$ in this way for quasi-phase-matching, it would appear that the ideal operating photon energy $\hbar\omega$ for any material should be somewhere around $\hbar\omega_p$ for the starting material. For such a detuning, limited second harmonic absorption will occur resulting in a reduction in the effective mode index at the second harmonic frequency $n_{2\omega eff}$ on intermixing. To compensate for any such index changes when quasi-phase-matching, it would then be necessary to periodically intermix the waveguide material along the direction of propagation with a non-unity mark to space ratio.

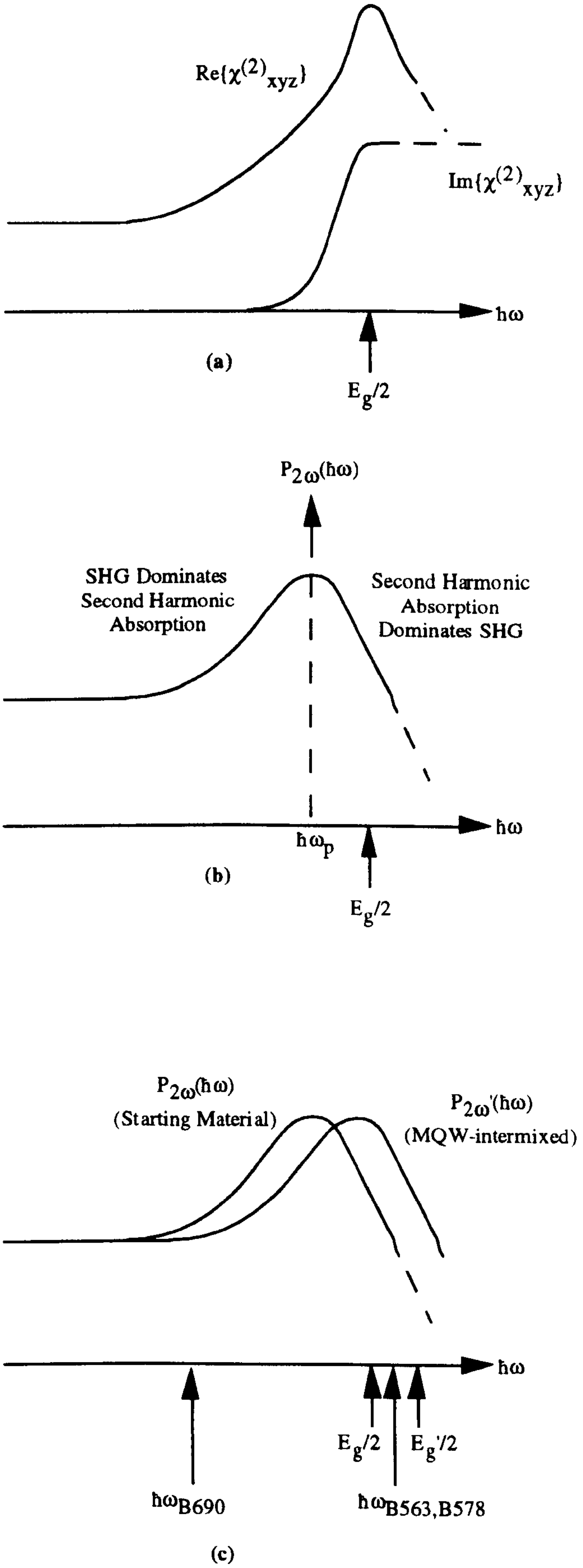

Fig. 7.11 Schematic diagrams illustrating the modulation of the bulk tensor component $\chi^{(2)}_{xyz}$ by QW-intermixing

7.4.2 Unphase-matched SHG in B690 Waveguides for a TM_ω:$TM_{2\omega}$ Polarisation Configuration

The reduction in the unphase-matched SHG observed in Fig. 7.8 for a TM_ω:$TM_{2\omega}$ configuration may be attributed to several different factors:

(i) Reduction in the AQW Tensor Component $\chi^{(2)}_{zzz}$

As mentioned in Section 7.1, due to the reduction in the QW asymmetry alone, it might be expected that $\chi^{(2)}_{zzz}$ would be reduced by 90% for the B690 intermixed sample relative to the starting material sample.

(ii) Reduction in the Overlap Factor $F^{(2)}_{zzz}$

Overlap factors $F^{(2)}_{zzz}$ of 1.636×10^{11} /m^2 and 1.255×10^{11} /m^2 were estimated from (3.9b) at 1.524 μm, for the starting material waveguide with an etch depth of 1.0 μm, and the intermixed waveguide with an etch depth of 0.8 μm respectively. As a consequence of the different etch depths therefore, we would expect the unphase-matched SHG power observed from the QW-intermixed waveguide to be approximately 76.7% of that from the starting material waveguide (all other parameters being equal) i.e.

$$\frac{F^{(2)'}_{zzz}}{F^{(2)}_{zzz}} = 0.767 \tag{7.8}$$

where $F^{(2)'}_{zzz}$ denotes the overlap factor for the intermixed material waveguide.

(iii) Field Component in the Direction of Propagation

The observed reduction in the bulk $\chi^{(2)}_{xyz}$ coefficient can contribute to a reduction in the unphase-matched SHG observed in the TM_ω:$TM_{2\omega}$ configuration because, TM waveguide modes have small but non-zero field components in the direction of propagation. Since, in theory, $\left|\chi^{(2)}_{xyz}\right| >> \left|\chi^{(2)}_{zzz}\right|$, a small field component in the direction of propagation can make a significant contribution to the total TM-polarised second harmonic field. Adopting the co-ordinate definitions of Fig. 3.3 it can be shown (see Appendix E), that for a 1D slab multiple AQW waveguide, the TM-polarised second harmonic power $P_{2\omega z}$ for the TM_ω:$TM_{2\omega}$ configuration obeys the relation:

$$P_{2\omega z} \propto \left| \chi^{(2)}_{zzz} \int\limits_{MAQW} E^2_{\omega z}(z) E_{2\omega TM}(z) dz - \chi^{(2)}_{xyz} \int_{-\infty}^{\infty} E^2_{\omega Y}(z) E_{2\omega TM}(z) dz \right|^2 \tag{7.9}$$

Here, $E_{\omega z}(z)$ is the lowest order TM-polarised fundamental mode, $E_{2\omega z}(z)$ is the lowest order TM-polarised second harmonic mode, and $E_{\omega Y}(z)$ is the lowest order fundamental mode profile of the field component in the direction of propagation. The first integration in (7.9) is only performed over the multiple AQW (MAQW) layer since $\chi^{(2)}_{zzz}$ is zero outside this layer. Writing

$$\int\limits_{MAQW} = \int\limits_{MAQW} E^2_{\omega z}(z) E_{2\omega TM}(z) dz \tag{7.10a}$$

and

$$\int\limits_{BULK} = \int_{-\infty}^{\infty} E^2_{\omega Y}(z) E_{2\omega TM}(z) dz \tag{7.10b}$$

we have:

$$\frac{P'_{2\omega z}}{P_{2\omega z}} = \left| \frac{\chi^{(2)'}_{zzz} \int\limits_{MAQW}' - \chi^{(2)'}_{xyz} \int\limits_{BULK}'}{\chi^{(2)}_{zzz} \int\limits_{MAQW} - \chi^{(2)}_{xyz} \int\limits_{BULK}} \right|^2 \tag{7.11}$$

where the prime notation denotes quantities corresponding to the QW-intermixed waveguide sample. Then

$$\frac{P'_{2\omega z}}{P_{2\omega z}} = \left| \frac{\chi^{(2)'}_{zzz} \int\limits_{MAQW} \Big/ \int\limits_{BULK} - \chi^{(2)'}_{xyz}}{\chi^{(2)}_{zzz} \int\limits_{MAQW} \Big/ \int\limits_{BULK} - \chi^{(2)}_{xyz}} \right|^2 \tag{7.12}$$

For the B690 multiple AQW material at a fundamental wavelength of 1.55 μm the effective index method can be used to calculate (see Appendix E):

$$\int_{\text{MAQW}} \Big/ \int_{\text{BULK}} \approx 247 \qquad (7.13)$$

From Section 7.4.2(i) it may be recalled that, due to the reduction in QW asymmetry alone, $\chi^{(2)}_{zzz}$ for the intermixed sample should be approximately 10% of $\chi^{(2)}_{zzz}$ for the starting material sample i.e. $\chi^{(2)\prime}_{zzz} = 0.1\chi^{(2)}_{zzz}$. Further, assuming $\chi^{(2)\prime}_{xyz} = 0.83\chi^{(2)}_{xyz}$ (see Section 7.3.1) and choosing $\chi^{(2)\prime}_{xyz} = 380$ pm/V and $\chi^{(2)}_{zzz} = 0.1$ pm/V, gives:

$$\frac{P_{2\omega z}'}{P_{2\omega z}} = 0.760 \qquad (7.14)$$

Finally, to account for the reduction in $F^{(2)}_{zzz}$ on intermixing we can apply a further scaling factor:

$$\frac{P_{2\omega z}'}{P_{2\omega z}} = 0.760 \times \frac{F^{(2)\prime}_{zzz}}{F^{(2)}_{zzz}} = 0.583 \qquad (7.15)$$

This compares with the observed ratio $P_{2\omega z}'/P_{2\omega z}$ of 0.207 for the TM_{ω}:$TM_{2\omega}$ configuration (see Fig. 7.8). Hence, it would appear that, within the accuracy of the modelling assumptions used, and for the tensor coefficients assumed, the large reduction in the TM_{ω}:$TM_{2\omega}$ unphase-matched SHG observed in Fig. 7.8, cannot be fully explained. The effects of polarisation errors will therefore be considered in the next section.

(iv) Angular Deviation of the Fundamental and Second Harmonic Polarisations from the TM Axis

During the unphase-matched SHG experiments using the TM_{ω}:$TM_{2\omega}$ configuration, the transmission axis of the output polariser was set to be vertical with respect to the optical bench, and the input polariser was adjusted for maximum transmission of the TM fundamental field after the output polariser. For an angular deviation of the waveguide sample normal from the vertical of θ as indicated in Fig. 7.12, an angular deviation of θ for both the fundamental and second harmonic fields from the TM axis would be expected.

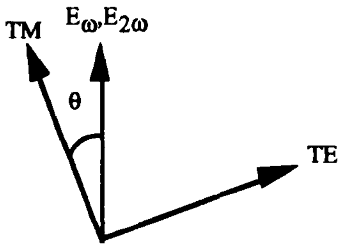

Fig 7.12 Angular deviation of the vertical field components with respect to the waveguide TM axis for an angular deviation of the waveguide surface normal to the vertical

From uniform plane wave considerations (see Appendix F) it may be shown that:

$$E_{2\omega}(\theta) \propto 3\chi^{(2)}_{xyz}\sin^2\theta\cos\theta + \chi^{(2)}_{zzz}\cos^3\theta \qquad (7.16)$$

where $E_{2\omega}$ is the second harmonic field polarised in the direction with an angular deviation of θ from the TM axis as indicated in Fig. 7.12 and where the AQW tensor components $\chi^{(2)}_{xzx}$ and $\chi^{(2)}_{zxx}$ are both assumed to be negligible with respect to $\chi^{(2)}_{xyz}$. From (7.16) it may be seen, that if $\chi^{(2)}_{xyz} >> \chi^{(2)}_{zzz}$, then the term $3\chi^{(2)}_{xyz}\sin^2\theta\cos\theta$ is likely to be significant relative to the $\chi^{(2)}_{zzz}\cos^3\theta$ term for small θ. Hence, if, during the unphase-matched SHG experiments, the starting material and intermixed waveguide samples were *both* mounted so that the angular deviation of their surface normals from the vertical was θ, then:

$$\frac{I_{2\omega}(\theta)'}{I_{2\omega}(\theta)} = \left| \frac{3\chi^{(2)'}_{xyz}\sin^2\theta\cos\theta + \chi^{(2)'}_{zzz}\cos^3\theta}{3\chi^{(2)}_{xyz}\sin^2\theta\cos\theta + \chi^{(2)}_{zzz}\cos^3\theta} \right|^2 \qquad (7.17)$$

where $I_{2\omega}$ denotes the output second harmonic intensity and all primed quantities correspond to the intermixed sample. Assuming, as for Section 7.4.2(iii), that $\chi^{(2)'}_{zzz} = 0.1\chi^{(2)}_{zzz}$ and $\chi^{(2)'}_{xyz} = 0.83\chi^{(2)}_{xyz}$, and, further, that $\chi^{(2)'}_{xyz} = 380$ pm/V and $\chi^{(2)}_{zzz} = 0.1$ pm/V, $I_{2\omega}(\theta)'/I_{2\omega}(\theta)$ as defined by (7.17) is plotted in Fig. 7.13. From this graph, it can be seen that a small equal angular deviation of θ for both starting material and intermixed waveguides, leads to an *increase* in $I_{2\omega}(\theta)'/I_{2\omega}(\theta)$. This is due to the contribution to $I_{2\omega}(\theta)$ and $I_{2\omega}(\theta)'$ from $\chi^{(2)}_{xyz}$ and $\chi^{(2)'}_{xyz}$ respectively for $\theta \neq 0$. Clearly, the discrepancy between the observed value of $P_{2\omega z}'/P_{2\omega z} = 0.207$ and the value of $P_{2\omega z}'/P_{2\omega z} = 0.760$ calculated in Section 7.4.2(iii) cannot then be attributed to a small equal angular deviation of θ for both the starting material and intermixed waveguides.

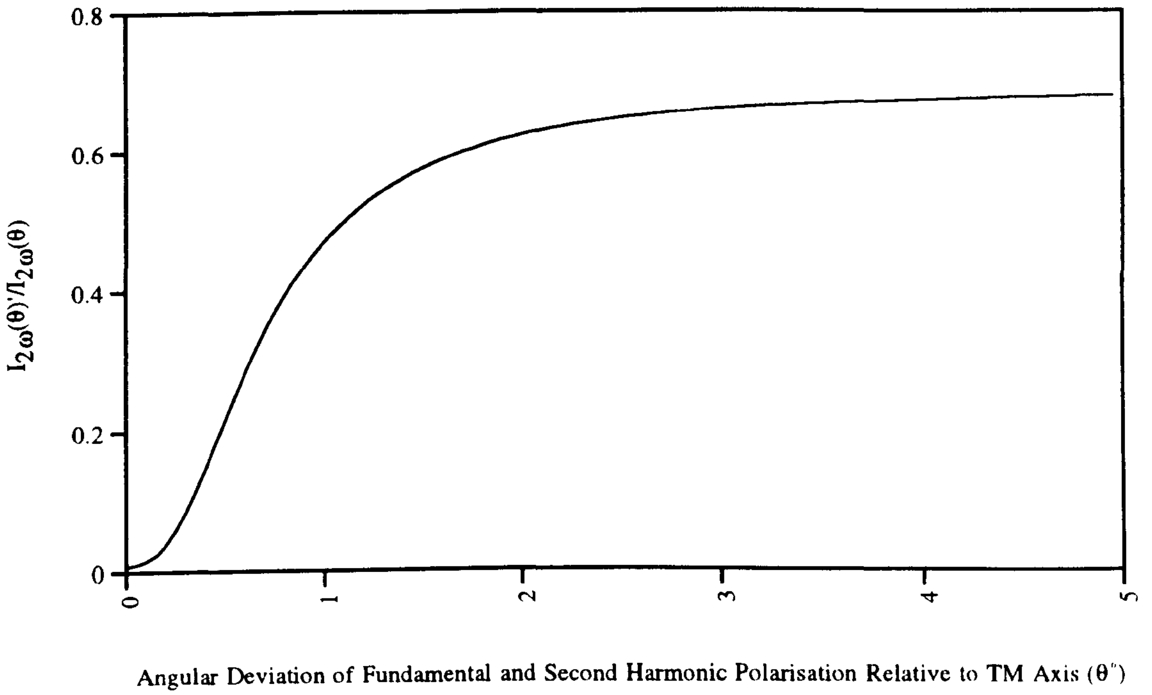

Fig. 7.13 Calculated reduction in SHG intensity $I_{2\omega}(\theta)'/I_{2\omega}(\theta)$ on QW-intermixing as a function of the angular deviation of both the starting material and QW-intermixed waveguide normals from the vertical

If, however, only one of the waveguide samples has a surface normal angular deviation from the vertical of θ then:

$$\frac{I_{2\omega}(\theta)}{I_{2\omega}(\theta = 0)} = \left| \frac{3\chi_{xyz}^{(2)} \sin^2\theta\cos\theta + \chi_{zzz}^{(2)}\cos^3\theta}{\chi_{zzz}^{(2)}} \right|^2 \tag{7.18}$$

where the relation of (7.16) has been used. Fig. 7.14 is a plot of $I_{2\omega}(\theta)/I_{2\omega}(\theta = 0)$ as defined by (7.18). From this figure it may be seen that $I_{2\omega}(\theta)/I_{2\omega}(\theta = 0)$ is a strongly increasing function of θ. This is to be expected since $\chi_{zzz}^{(2)} << \chi_{xyz}^{(2)}$ for the B690 structure. If the angular deviation for the starting material waveguide sample is denoted by θ, and the angular deviation for the intermixed waveguide sample is denoted by θ', then, for $\theta' < \theta$, $I_{2\omega}(\theta') < I_{2\omega}(\theta)$. More specifically, for θ' only marginally smaller than θ, we would expect significantly less unphase-matched SHG from the intermixed waveguide sample.

In conclusion, we tentatively assert that, within the accuracy and assumptions of the models, the reason why the reduction in the $TM_{\omega}:TM_{2\omega}$ unphase-matched SHG observed in practice was larger than that predicted from (7.15), was that the waveguide deviations θ and θ' were such that $\theta' < \theta$ and/or the AQW non-linearity $\chi^{(2)}_{zzz}$ was larger than its predicted value of 0.1 pm/V.

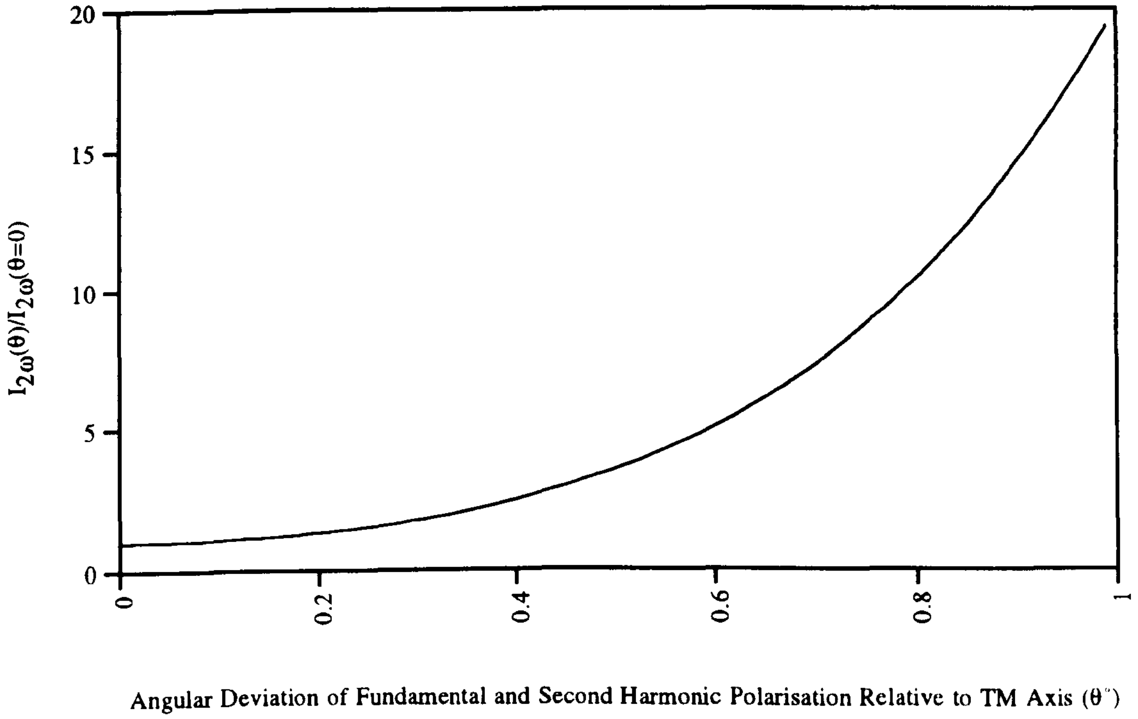

Fig. 7.14 Normalised SHG intensity $I_{2\omega}(\theta)/I_{2\omega}(\theta=0)$ as a function of the angular deviation of the fundamental and second harmonic field polarisations from the TM axis

7.5 Conclusions

In this chapter unphase-matched SHG conversion efficiencies and waveguide losses were compared in waveguides fabricated from asymmetric QW materials, before and after intermixing. It should be emphasised that the $\chi^{(2)}_{zxy}$ tensor component ($\approx \chi^{(2)}_{xyz}$) exists by virtue of the non-centro-symmetric crystal structure of bulk GaAs/AlGaAs, while the $\chi^{(2)}_{zzz}$ tensor element exists only by virtue of quantum well asymmetry. Any second harmonic generated in AQW waveguides via $\chi^{(2)}_{zxy}$ in the $TE_{\omega}:TM_{2\omega}$ polarisation configuration does not therefore depend on the QW asymmetry, and qualitatively similar $TE_{\omega}:TM_{2\omega}$ SHG results would be expected with symmetric QWs with the same bandgap.

For photon energies above the half-bandgap energy, the second harmonic signal observed at the output of the waveguides for a $TE_{\omega}:TM_{2\omega}$ polarisation configuration is the net result of the linear absorption at the second harmonic frequency and SHG via the $\chi^{(2)}_{zxy}$ component. On intermixing, bandgap widening occurs resulting in a reduction of both the second harmonic absorption and $\chi^{(2)}_{zxy}$. Hence, an increase or a decrease in the second harmonic power at the output of the waveguides may be observed on intermixing, depending on whether the relative reduction in the second harmonic absorption is greater or less than the relative reduction in $\chi^{(2)}_{zxy}$ respectively. For the B563 asymmetric stepped QW (ASQW) and B578 asymmetric coupled QW (ACQW) starting material waveguides, unphase-matched SHG experiments were performed at 1.55 μm, corresponding to a photon energy ≈ 40 meV *above* half the bandgap. Accordingly, sub-linear $TE_{\omega}:TE_{\omega}$ fundamental transmission characteristics were observed due to two-photon absorption. The curvature of these characteristics decreased on intermixing, indicating a reduction in the two-photon absorption. Since an increase in the TM-polarised second harmonic output power was also observed on intermixing, it was concluded that the relative reduction in the second harmonic absorption occurring on intermixing was larger than the relative reduction in $\chi^{(2)}_{zxy}$.

In contrast, the unphase-matched $TE_{\omega}:TM_{2\omega}$ SHG experiments with the B690 waveguides were performed at a wavelength of 1.524 μm, corresponding to a detuning of the photon energy of ≈ 60 meV *below* half the bandgap. The $TE_{\omega}:TE_{\omega}$ fundamental transmission characteristics were correspondingly linear, indicating that there was no two-photon absorption of the fundamental and therefore no linear absorption of the second harmonic. Having accounted for a small reduction in the waveguide SHG overlap factor $F^{(2)}$ due to a slight over-etch of the starting material waveguide, the observed reduction in the second harmonic signal was therefore attributed to a reduction in $\chi^{(2)}_{zxy}$ of at least 17%. Such a reduction in $\chi^{(2)}_{zxy}$ may be explained in terms of bandgap widening: $\chi^{(2)}_{zxy}$ is resonant at the half-bandgap so that, when operating at a photon energy below the half-bandgap, the blueshift in the band-edge occurring on intermixing results in a larger detuning of the half-bandgap resonance energy from the fundamental photon energy. Thus the fact that the QWs were asymmetric is immaterial to the reduction of $\chi^{(2)}_{zxy}$ on intermixing, and qualitatively similar results would be expected with symmetric QW structures.

For the $TM_{\omega}:TM_{2\omega}$ unphase-matched SHG experiments with B563, B578 and B690 waveguides it was not possible to make any conclusions regarding a possible reduction in $\chi^{(2)}_{zzz}$ on intermixing. This is because calculations have predicted that $\chi^{(2)}_{zxy}$ is more than three orders of magnitude greater than $\chi^{(2)}_{zzz}$ so that a small field component in the direction of propagation (such as that associated with a TM waveguide mode) or a slight misalignment of the polariser axes with respect to the crystal axes could lead to a significant

TM_ω:$TM_{2\omega}$ second harmonic output signal via $\chi^{(2)}_{zxy}$. The reduction in the TM_ω:$TM_{2\omega}$ second harmonic output signals observed on intermixing could therefore simply reflect the reduction in the large $\chi^{(2)}_{zxy}$ component.

Waveguide losses as low as 7.9 dB/cm were measured at 1.556 μm (corresponding to a sub-half-bandgap photon energy) in intermixed B690 ACQW waveguides using the Fabry-Perot technique. Such losses are not prohibitively high. Therefore, given the observed reduction in $\chi^{(2)}_{zxy}$ of 17% on intermixing, quasi-phase-matching by periodic quantum well intermixing could lead to useful frequency conversion efficiencies. More specifically, a periodic reduction in $\chi^{(2)}_{zxy}$ of 17% (i.e. $\gamma = 0.17$) translates into a first-order QPM efficiency factor of $d^2_{QPM}/n^2_\omega n_{2\omega} \approx 66\ pm^2/V^2$. This compares with an efficiency factor of $d^2_{QPM}/n^2_\omega n_{2\omega} \approx 39\ pm^2/V^2$ for ideal lossless first-order domain inversion (i.e. $\gamma = -1$) in $LiNbO_3$. Furthermore, if optimised AQW structures can be designed with associated significant $\chi^{(2)}_{zxx}$ non-linearities, an even larger TE_ω:$TM_{2\omega}$ effective non-linearity $\chi^{(2)}_{xyz} + \chi^{(2)}_{zxx}$ will result, with correspondingly higher QPM efficiency parameters.

---

[1] E. Kapon and R. Bhat, "Low-loss Single-mode GaAs/AlGaAs Optical Waveguides Grown by Organometallic Vapor Phase Epitaxy", Appl. Phys. Lett. **50**, 1628 (1987)

[2] S. Janz, M. Buchanan, F. Chatenoud, J. P. McCaffrey, R. Normandin, U. G. Akano, and I. V. Mitchell, "Modification of the Second-order Optical Susceptibility in $Al_xGa_{1-x}As$ by Ion-beam Induced Amorphization", Appl. Phys. Lett. **65**, 216 (1994)

[3] S. I. Hansen, "The Refractive Index Change in GaAs/AlGaAs Quantum Wells Produced by Neutral Impurity Induced Disordering Using Boron and Fluorine", PhD Thesis, University of Glasgow (1993), and M. A. Afromowitz, "Refractive Index of $Ga_{1-x}Al_xAs$", Solid State Commun. **15**, 59 (1974)

[4] E. Kapon, N. G. Stoffel, E. A. Dobisz, and R. Bhat, "Birefringent Channel Waveguides Defined by Impurity-induced Superlattice Disordering", Appl. Phys. Lett. **52**, 351 (1988)

[5] T. Wolf, C. L. Shieh, R. Engelmann, K. Alavi, and J. Mantz, "Lateral Refractive Index Step in GaAs/AlGaAs Multiple Quantum Well Waveguides Fabricated by Impurity-induced Disordering", Appl. Phys. Lett. **55**, 1412 (1989)

[6] S. I. Hansen, J. H. Marsh, J. S. Roberts, and R. Gwilliam, "Refractive Index Changes in a GaAs Multiple Quantum Well Structure Produced by Impurity-induced Disordering Using Boron and Fluorine", Appl. Phys. Lett. **58**, 1398 (1991)

[7] D. J. Moss, J. E. Sipe, and H. M. van Driel, "Empirical Tight-binding Calculation of Dispersion in the Second-order Nonlinear Optical Constant for Zinc-blende Cystals", Phys. Rev. B **36**, 9708 (1987)

8

Periodically Intermixed GaAs/AlGaAs Multiple AQW Waveguides for Quasi-phase-matched SHG Around 1.5 μm

As mentioned at the beginning of the last chapter, efficient quasi-phase-matching is an important precursor for the production of non-linear phase shifts via the cascaded second order effect. Also, efficient frequency conversion is important in its own right for wavelength division multiplexing and optical parametric oscillator applications.

The results of the previous chapter have shown that QW-intermixing techniques can be used to control the magnitude of the bulk GaAs/AlGaAs second order non-linear coefficient d_{14}, and, in addition, that they can potentially be used to control the magnitude of AQW coefficients. In light of these promising results, waveguides were fabricated from periodically-intermixed GaAs/AlGaAs AQW material for quasi-phase-matching. Experiments with these devices will be described in the following sections. It should be acknowledged that N. D. Whitbread designed the mask used in the fabrication of the periodically intermixed waveguide devices, and that he further performed most of the fabrication himself.

8.1 The QW-intermixing Period for Quasi-phase-matched SHG Around 1.5 μm

From Section 2.5 it may be recalled that, the required modulation period of the non-linearity for quasi-phase-matched SHG is given by:

$$\Lambda = 2mL_c \tag{8.1}$$

where m is the order of the quasi-phase-matching scheme. Now , in a waveguide,

$$L_c = \frac{\lambda}{4\Delta n_{eff}} \tag{8.2a}$$

where

$$\Delta n_{eff} = n_{2\omega eff} - n_{\omega eff} \tag{8.2b}$$

Hence

$$\Lambda = \frac{m\lambda}{2\Delta n_{eff}} \tag{8.3}$$

Equation (8.3) represents the condition for quasi-phase-matched SHG in a waveguide device. For the particular case of periodically-intermixed MQW devices, Λ represents the intermixing period required for quasi-phase-matched SHG. For a B690 ridge waveguide with 3 µm-wide ribs and a 0.9 µm etch depth, the nominal Δn_{eff} for the TM_{00} modes was found to be ≈ 0.282193 for a fundamental wavelength of λ = 1.5 µm, where all the layer refractive indices were calculated using the modified Afromowitz model [1], and the MQW layer refractive index was calculated from (3.5b). From (8.3) the period was then given by $\Lambda = 2.657756 \times m$ µm.

There are, however, large uncertainties associated with the calculation of the refractive index n_{MQW} of an AlGaAs MQW layer which is, in general, given by [2,3,4]:

$$n_{MQW} = n_{RMS} + n_X \tag{8.4}$$

In equation (8.4), n_{RMS} is a weighted average term given by (3.5) and depends on the well and barrier layer indices and thicknesses, and on the polarisation of the optical field. The term n_X arises through the Kramer's Kronig relation as a consequence of excitonic absorption. However, for 100 Å-wide GaAs wells sandwiched between 100 Å $Al_{0.3}Ga_{0.7}As$ barriers, n_X was estimated to be ~ 0.03 for a detuning of 30 meV below the e1hh1 energy [5]. For the B690 ACQW structure at a fundamental wavelength of 1.5 µm, the second harmonic wavelength of 750 nm corresponds to a detuning of approximately 120 meV below the e1hh1 energy, and the n_X contribution is likely to be significantly less than 0.03. Hence, the major source of uncertainty when estimating the B690 MQW layer refractive index, is likely to be the uncertainty in the individual QW layer indices used to calculate n_{RMS}. For example, the refractive index of $Al_{0.2}Ga_{0.8}As$ as a function of wavelength in the range 0.8 - 1.5 μm calculated from three different models is plotted in Fig. 8.1. The three models used are, the Adachi model [6], the Sellmeier model [7], and the modified Afromowitz model [1]. From Fig. 8.1, it can be seen that the refractive index varies by up to 0.05 between the different models, and there is, therefore, a large uncertainty associated with the calculation of Δn_{eff}. Any quasi-phase-matching period calculated from (8.3) will then also have large associated uncertainties.

Assuming a variation in Δn_{eff} of Δn_{eff}(nominal)±0.1, a photolithographic mask was therefore designed with 30 grating periods ranging from approximately 5.8 - 12.4 μm for third order quasi-phase-matching. The individual grating periods were chosen so that by tuning the laser over a range of 1.48 - 1.52 μm, the quasi-phase-matching condition of (8.3) was satisfied for one of the 30 grating periods. More specifically, if, for Δn_{eff} (nominal)-0.1 < Δn_{eff} < Δn_{eff} (nominal)+0.1, the quasi-phase-matching condition was satisfied for one of the grating periods at a wavelength of 1.52 μm, then it would also be satisfied for the next closest grating period at 1.48 μm.

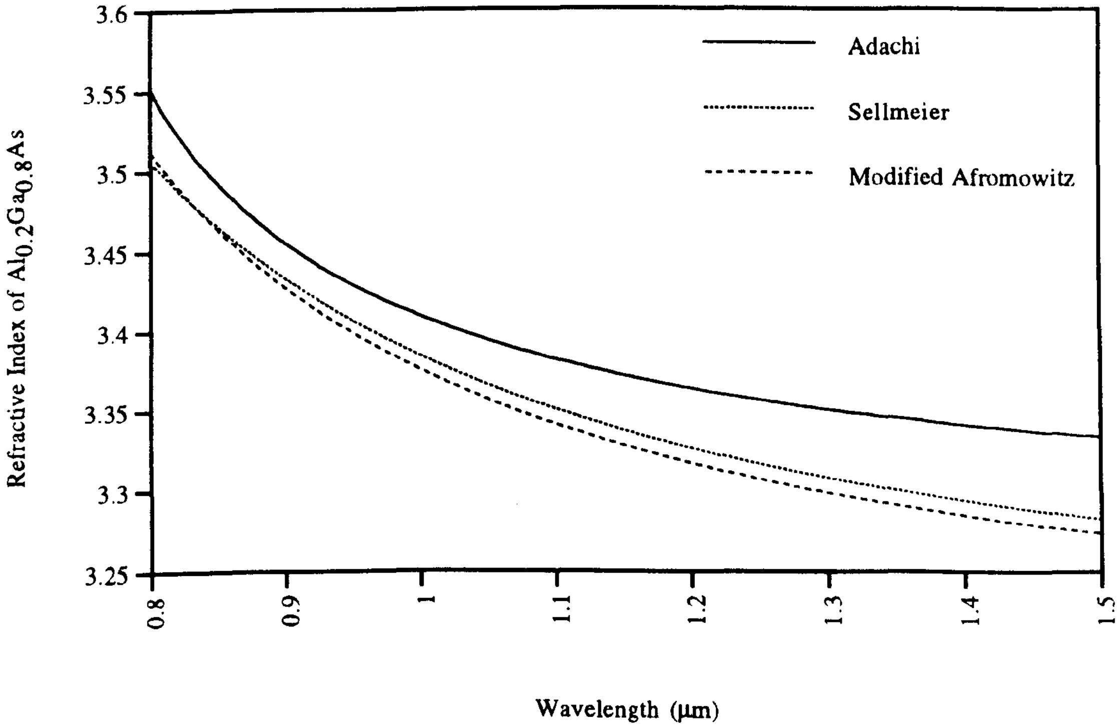

Fig. 8.1 The refractive index of $Al_{0.2}Ga_{0.8}As$ as a function of wavelength calculated from three different models

8.2 Fabrication of Periodically Intermixed GaAs/AlGaAs Multiple AQW Ridge Waveguides for Quasi-phase-matched SHG Around 1.5 μm

Due to the large number of factors influencing the IFVD process for MQW-intermixing (see Chapter 6), different PL blueshifts were often observed for the same nominal IFVD process parameters. To circumvent these reproducibility problems, periodically intermixed B690 waveguide samples were fabricated in parallel with periodically intermixed B690 IFVD resolution samples using the selective area IFVD process described in Chapter 6. The periodically intermixed waveguide sample corresponding to the IFVD resolution sample which showed the greatest differential PL blueshift was then selected. The PL blueshift results from the best IFVD resolution sample are those of Fig. 6.25. Recalling the discussion at the end of Section 6.3.2, we would then expect the $\chi^{(2)}_{zzz}$ non-linearity relative to the starting material $\chi^{(2)}_{zzz}$ non-linearity to be approximately 0.48 and 0 in the intermixing-suppressed and intermixed regions respectively. Furthermore, it was concluded that the IFVD spatial resolution measured for this sample was better than 2.2 μm. This indicates that periodic QW-intermixing is only guaranteed for periods of 4.4 μm or greater.

Using $SiCl_4$ for dry-etching, 3 μm wide and 0.9 μm deep waveguide ridges were fabricated from periodically intermixed material with a *third-order* grating period. Fig. 8.2a shows a scanning electron microscope (SEM) image of one of the rib waveguides. A corrugated pattern can be seen on the surface to either side of the rib waveguide. This results because the intermixed and non-intermixed regions etch at slightly different rates. From Fig. 8.2b, which shows the surface at the edge of the periodically intermixed region, it is possible to establish that the "trenches" correspond to the intermixed regions. From a surface profile measurement, the trench depth was found to be 0.1 μm. Such an effective index grating should not, have an appreciable effect on quasi-phase-matching.

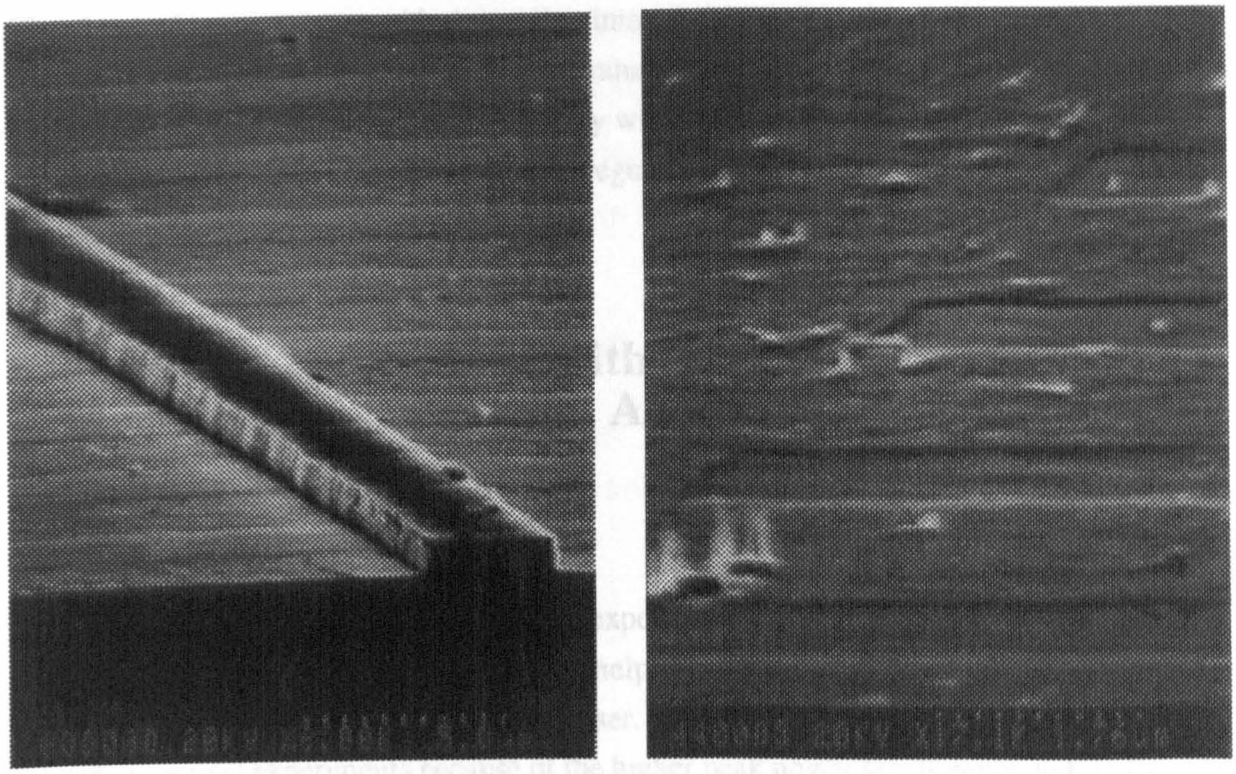

(a) (b)

Fig. 8.2 SEM images of a B690 periodically-intermixed waveguide sample **(a)** in the vicinity of a waveguide rib and **(b)** at the edge of the periodically-intermixed region

8.3 Periodically Intermixed Waveguide Losses

Using an identical experimental method to that outlined in Section 7.2, the waveguide losses listed in Table 8.1 were measured for a 4 mm-long periodically-intermixed B690 waveguide sample at 1.556 μm.

Intermixing Period (μm)	α (dB/cm)
5.80	18.0
7.35	14.4
9.55	13.6
12.40	3.7

Table 8.1 B690 periodically-intermixed waveguide losses at 1.556 μm

Clearly, the losses increase with decreasing intermixing period, as might be expected due to any small index variations and/or the introduction of more vacancies in the intermixed regions. The losses compare very favourably with waveguide losses of 45 dB/cm measured in periodically domain inverted AlGaAs waveguides at 771 nm [8].

8.4 SHG Experiments with Periodically Intermixed GaAs/AlGaAs Multiple AQW Ridge Waveguides Around 1.5 μm

Before making any reference to the experimental set-up used to test the periodically intermixed waveguide devices, it will be helpful to address some issues relating to the general operation of a KCl colour-centre laser. Pulsed laser radiation is generally used for non-linear optical experiments because of the higher peak power levels generated. In fact, for pulsed operation, and for a weakly wavelength-dependent non-linearity, we would expect an enhancement of $\sim 1/f\tau$ in the second harmonic average power detected, when compared with cw operation for the same average fundamental power, where f is the pulse repetition rate and τ is the pulsewidth.

For a strongly wavelength dependent non-linear interaction such as quasi-phase-matched SHG, the situation is slightly different. To appreciate this, the tuning curves of Figs. 8.3 and 8.4 were plotted for 2 mm-long periodically intermixed B690 waveguide devices with 3 μm rib widths and 0.9 μm etch depths in the TM_{ω}:$TM_{2\omega}$ and TE_{ω}:$TM_{2\omega}$ configurations respectively. These curves were generated using a computer program written by N. D. Whitbread which used the fourth order Runge-Kutta algorithm to integrate the scalar coupled wave equations of Section 3.2. Average input powers of 5 mW and an effective cross-sectional area of 10 μm^2 were assumed in each case. For both Figs. 8.3 and 8.4, a third-order grating period was selected which satisfied the quasi-phase-matching condition at 1.5 μm for the TM_{ω}:$TM_{2\omega}$ case. The translation of the quasi-phase-matching peak to shorter wavelengths for the TE_{ω}:$TM_{2\omega}$ case, simply reflects the fact that the lowest order TE waveguide mode effective index at the fundamental wavelength $TE_{\omega 00}$, is different from the $TM_{\omega 00}$ mode effective index, and the quasi-phase-matching condition is therefore satisfied at a different wavelength. In accordance with the resolution sample results, $\chi^{(2)}_{zzz}$ was assumed to be modulated by factors of 0.48 and 0 relative to its starting material value, in the intermixing-suppressed and intermixed regions respectively for the TM_{ω}:$TM_{2\omega}$ case of Fig. 8.3. In other words, for a starting material value of $\chi^{(2)}_{zzz} = 0.1$ pm/V, $\chi^{(2)}_{zzz}$ was assumed to be modulated between 0.048 pm/V and 0. For the TE_{ω}:$TM_{2\omega}$ case of Fig. 8.4, it was assumed that $\chi^{(2)}_{xyz}$ is the only significant contributing tensor component. Then, assuming that $\chi^{(2)}_{xyz}$ in the intermixing-suppressed regions is equal to that in starting material waveguides, and that $\chi^{(2)}_{xyz}$ in the intermixed regions is equal to that in waveguides fabricated from material intermixed everywhere, we have from Chapter 7:

$$\chi^{(2)}_{xyz}(\text{intermixed}) = 0.83\,\chi^{(2)}_{xyz}(\text{intermixing-suppressed}) \tag{8.5}$$

Further, assuming that $\chi^{(2)}_{xyz}$ in the intermixed regions is equal to the low frequency value of 380 pm/V, we estimate:

$$\chi^{(2)}_{xyz}(\text{intermixed}) = 380\ \text{pm/V} \tag{8.6a}$$

$$\chi^{(2)}_{xyz}(\text{intermixing-suppressed}) = 458\ \text{pm/V} \tag{8.6b}$$

The tuning curve of Fig. 8.4 was generated using these $\chi^{(2)}_{xyz}$ tensor component values.

From the bandwidths of the tuning curves of Figs. 8.3 and 8.4, it is apparent that, for cw laser operation, any mode-hopping by more than a few nm's would mean that the phase-matching condition would be missed. When using pulsed laser radiation, however, with a bandwidth of several nm's, it is more likely that an enhancement in the SHG signal due to quasi-phase-matching will be observed in the presence of mode-hopping. Problems with pulsed laser operation can arise, due to changes in the pulse shape which can occur during tuning. Such pulse shape variations translate into peak power variations which, in turn, can give rise to fluctuations in the second harmonic power. Such fluctuations will tend to obscure any variations in the second harmonic power occurring due to quasi-phase-matching alone. The laser should therefore ideally be operated pulsed with a constant pulseshape independent of wavelength. Alternatively, if the pulseshape cannot be maintained constant, it may be monitored during tuning instead, to allow the deconvolution of the peak power level as a function of wavelength.

For the quasi-phase-matched SHG experiments performed, no pulsed colour-centre laser source was readily available, so that it was necessary to resort to cw operation. Continuous, or near continuous, tuning and minimal mode-hopping were then very important in order that any sharp quasi-phase-matched SHG enhancements should be detected. The experimental set-up used for cw testing of the periodically intermixed

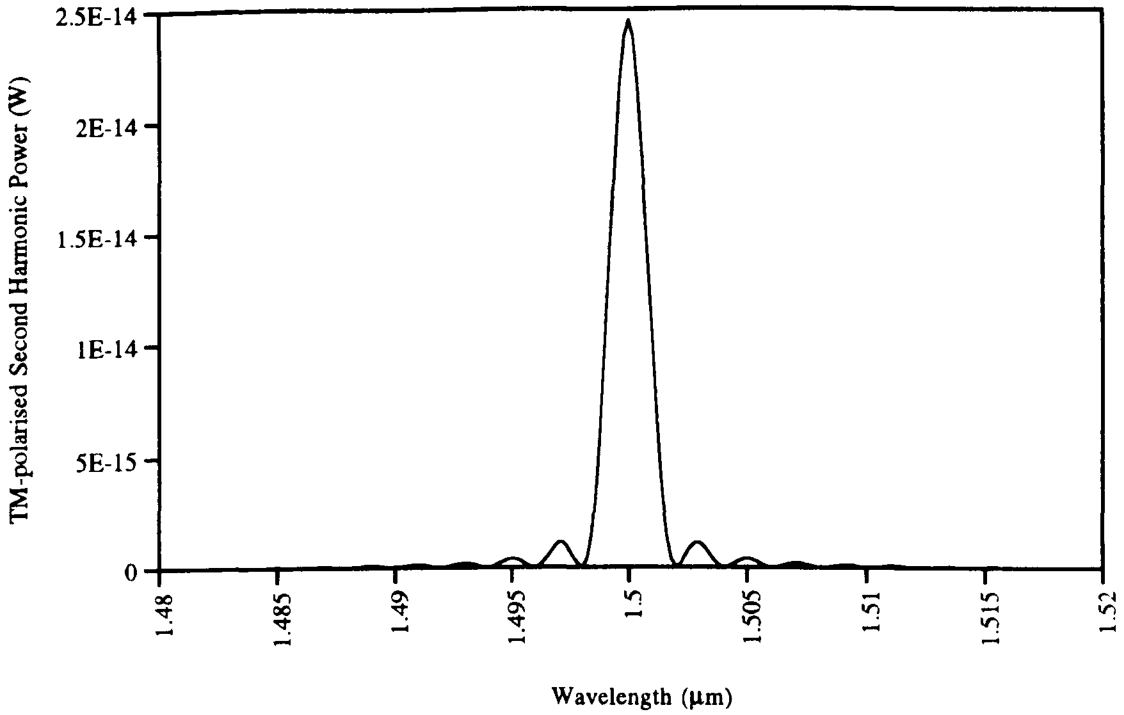

Fig. 8.3 Calculated quasi-phase-matched SHG tuning curve for a 2 mm-long periodically-intermixed B690 waveguide in the $TM_{\omega}:TM_{2\omega}$ polarisation configuration

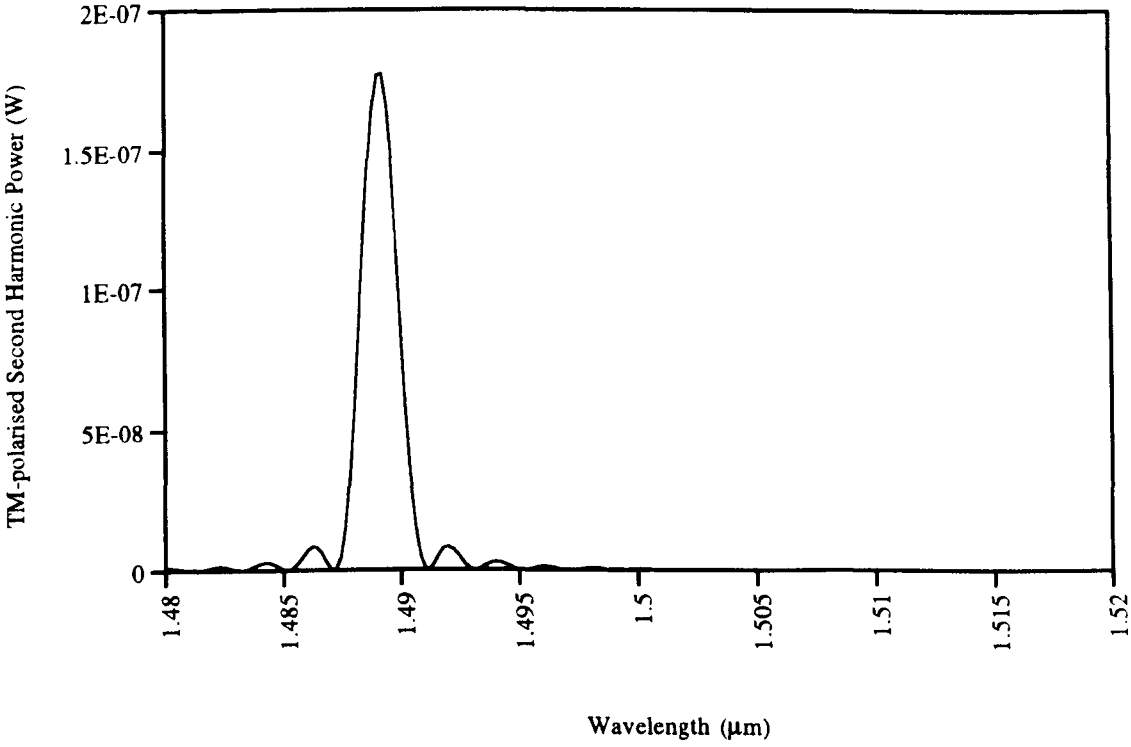

Fig. 8.4 Calculated quasi-phase-matched SHG tuning curve for a 2 mm-long periodically-intermixed B690 waveguide for a $TE_{\omega}:TM_{2\omega}$ polarisation configuration

waveguides is sketched in Fig. 8.5. The KCl colour-centre laser depicted in Fig. 8.5a was pumped with a cw YLF laser with up to 2 W of power at 1.047 μm. The YLF beam was chopped to allow lock-in detection of fundamental and second harmonic signals during the experiment. The colour-centre laser cavity had a "five-mirror configuration", with tuning provided by an equilateral glass prism as shown in Fig. 8.5a. Tuning was achieved by finely adjusting the rotation of the output coupler mirror about its vertical axis. A scanning Fabry-Perot interferometer was then used to monitor the cw laser wavelength by inserting a gold mirror into the optical path as indicated.

Light from the colour-centre laser was TE-polarised and end-fire coupled into the waveguide as shown in Fig. 8.5b. The output polariser was crossed with the input polariser so that it transmitted only TM-polarised light. A dielectric mirror which was highly reflective at both the YLF wavelength, and across the fundamental wavelength tuning range of 1480 - 1520 nm, but *not* across the second harmonic wavelength range of 740 - 760 nm, was inserted in the optical path in front of the photomultiplier tube (PMT). This mirror blocked all power at the YLF wavelength (both in the beam and scattered), and all power in the fundamental beam around 1.5 μm. The PMT was also insensitive to wavelengths outside the range 400 - 1100 nm, so that the PMT signal was a measure of the TM second harmonic power generated. Lock-in detection with a time constant of 3 s was then used to monitor the PMT signal as a function of wavelength for each of the 30 waveguides with different intermixing periods in turn. Due to the condition of the KCl crystal, the maximum unchopped cw power measured after the output coupler was 50 - 60 mW. The corresponding unphase-matched second harmonic PMT signal was typically a few hundred μV at the centre of the laser tuning range near 1.5 μm.

As mentioned earlier, due to time restrictions, and because a superior dispersive element was not readily available, tuning was accomplished with a glass prism in the colour-centre laser cavity, by rotating the output coupler mirror about its vertical axis. Tuning in this way, was however, far from continuous, with lasing modes typically occurring 2 - 3 nm apart in the range 1480 - 1520 nm. Furthermore, the lasing wavelength did not change with translation of the output coupler along the optical path. This suggested the presence of a second dispersive element (possibly the cryostat windows) in the laser cavity which was giving rise to a "ripple" in the laser gain spectrum. Furthermore, mode-hopping between two, or more, of the modes was observed on a sub-second timescale. The tuning technique was even less satisfactory still, when one considers that on adjusting the output coupler, the laser beam "wandered" i.e. the angular deviation of the beam varied during tuning. This had quite serious consequences for the alignment of the various different optical components in the optical path during tuning. Firstly, it was prohibitively time-consuming to use an isolator with a small aperture during tuning. As a consequence, the power measured as a function of wavelength with a Ge photodiode immediately before the input objective, was not

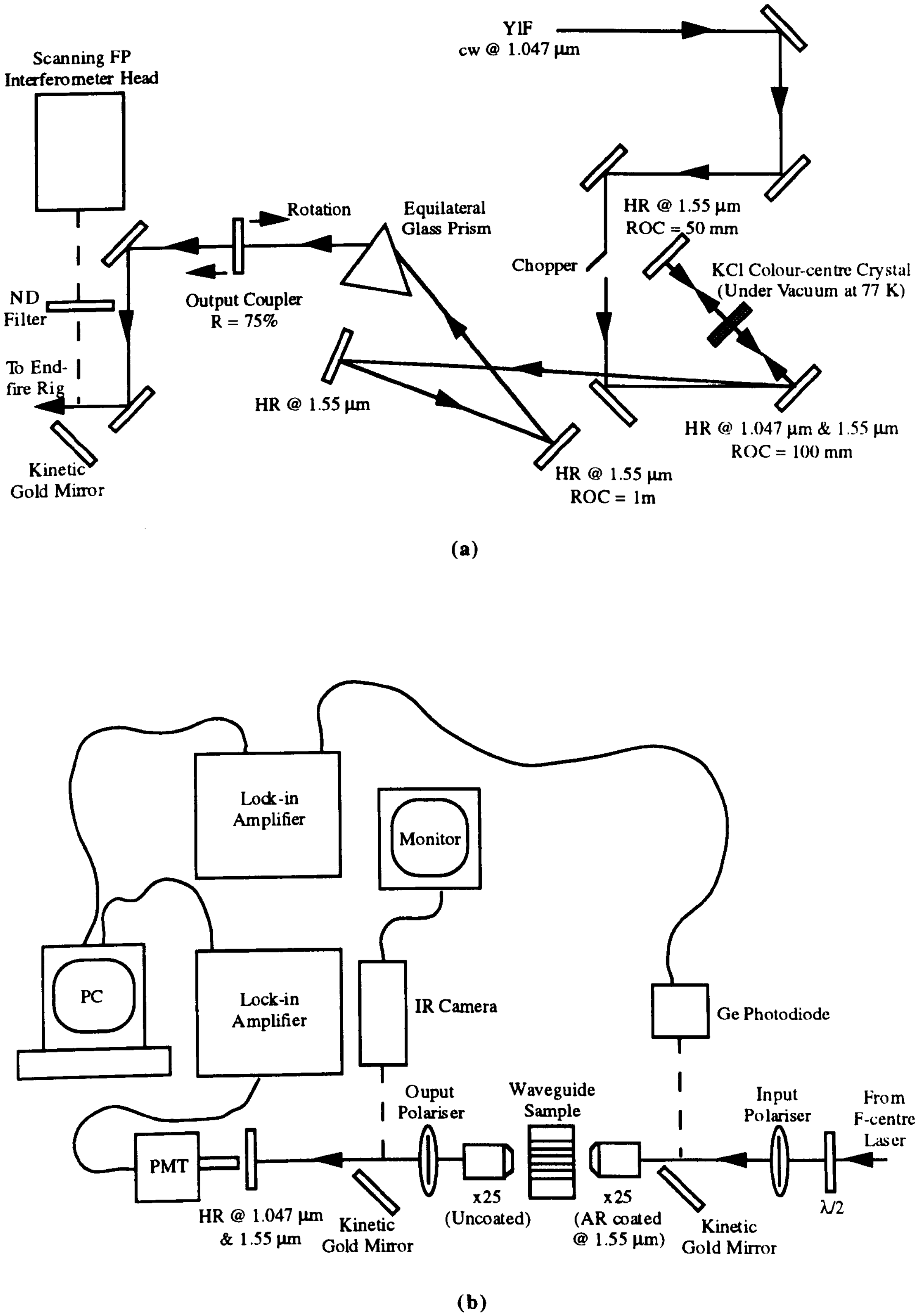

Fig. 8.5 Schematic diagram of experimental set-up used to look for quasi-phase-matched SHG in periodically-intermixed waveguide samples (a) KCl colour-centre laser set-up (b) waveguide test set-up

proportional to the power measured as a function of wavelength with a power meter immediately after the laser output coupler. This was attributed to the reflection of power from the different elements in the optical path back into the laser cavity i.e. the laser output was not independent of the elements in the optical path. This meant that monitoring the laser power by changing the optical path in any way was pointless. Due to serious power restrictions, "tapping-off" some on the input power and maximising the photodiode signal at each wavelength, was also out of the question since the PMT signal was only a few hundred μV at the centre of the laser tuning range. It was therefore resolved to proceed with the measurements by monitoring only the second harmonic PMT signal as a function of wavelength in the hope that any quasi-phase-matched enhancement in the SHG would be very obvious.

For each wavelength, the second harmonic PMT signal was maximised through optimisation of the waveguide coupling with an adjustment of the beam-steering mirror of Fig. 8.5a just before the half-wave plate of Fig. 8.5b. The normalised TM-polarised second harmonic PMT signals thus obtained as a function of wavelength for all 30 waveguides with different intermixing periods in the range 5.8 - 12.4 μm, were not very meaningful, and have therefore been plotted in Appendix G. From these results, it may be seen that no obvious quasi-phase-matched SHG peak was observed for any of the periodically intermixed waveguides in the TE_{ω}:$TM_{2\omega}$ polarisation configuration. Furthermore, none of the observed tuning curves appeared to be real, in that, repeating the tuning measurement for a given device, did not result in the same tuning curve features. This suggests that the tuning curves of Appendix G are simply the product of random effects such as noise, laser power fluctuations, mode-hopping, unphase-matched SHG oscillations, and Fabry-Perot effects. In light of these observations, no experiments were performed in the TM_{ω}:$TM_{2\omega}$ configuration.

There are several possible explanations for failing to observe a large quasi-phase-matched enhancement in the second harmonic signal. Firstly, from Fig. 8.4, it may be recalled that the estimated bandwidth for third-order quasi-phase-matching in a 2 mm-long device is 2 - 3 nm. Due to discontinuous tuning of the colour-centre laser, it might have been the case that the quasi-phase-matched peak was located at a wavelength between two lasing modes separated by 3 nm or more. Lasing in one of the modes either side of the quasi-phase-matched peak, would not then have given rise to a spectacular enhancement in the second harmonic signal. Another possibility is that, due to the mode-hopping observed, any quasi-phase-matching enhancement in the SHG would only have occurred momentarily. Using lock-in detection with a 3 s time constant, would then have meant that such instantaneous "spikes" in the second harmonic PMT signal would not have been observable. Fluctuations in the laser power too, would tend to have masked any SHG enhancement, especially when we consider that the second harmonic signal is proportional to the square of the fundamental power.

The laser tuning range was also not very satisfactory in that tuning between 1480 and 1520 nm was not always possible. This was probably symptomatic of the reduced colour-centre gain available due to the poor condition of the KCl crystal. Any quasi-phase-matched SHG at one of the tuning range extremes may not, therefore, have given rise to a large second harmonic PMT signal. It is also possible that the uncertainties in the effective waveguide mode indices at the fundamental and second harmonic wavelengths, were larger than assumed for the design of the mask for periodic intermixing. The quasi-phase-matching condition would not then have been satisfied for any of the intermixing periods or laser wavelengths used.

Finally, it should be recalled that for the IFVD resolution sample processed in parallel with the periodically-intermixed waveguide sample, MQW-intermixed and intermixing-suppressed PL blueshifts of 36 and 13 nm were observed. This indicates that some band-gap widening is likely to have occurred in both the MQW-intermixed *and* the intermixing-suppressed regions of the waveguide sample. This would mean that only a small modulation of the $\chi^{(2)}_{xyz}$ non-linearity may exist and that the corresponding quasi-phase-matched SHG enhancement may not be very significant.

8.5 Conclusions

Periodically intermixed waveguides were fabricated from B690 ACQW material using H plasma processing for the periodic suppression of the IFVD intermixing process. Due to the uncertainty in the effective index difference at the fundamental and second harmonic frequencies, $\Delta n_{eff} = n_{eff2\omega} - n_{eff\omega}$, thirty different intermixing periods were chosen to ensure that, for a variation of Δn_{eff} by ±0.1 from its nominal value, the phase-matching condition would be satisfied for one of the intermixed waveguides during tuning of the fundamental wavelength between 1480 and 1520 nm.

Waveguide losses measured at 1.556 μm ranged from 3.7 dB/cm for an intermixing period of 12.4 μm up to 18 dB/cm for an intermixing period of 5.8 μm. The losses were thought to increase with decreasing intermixing period as a result of scattering losses associated with the additional interfaces between the intermixed and intermixing-suppressed regions in the samples with shorter intermixing periods.

A serious experimental attempt was made to achieve quasi-phase-matched SHG in the periodically intermixed waveguides using cw excitation from a KCl colour centre laser. With an equilateral glass prism in the laser cavity, tuning was achieved between approximately 1480 and 1520 nm by rotating the output coupler mirror. However, due to the resulting angular deviation in the laser output beam during tuning, it was impractical to use an isolator. This fact, in conjunction with a lack of power due to the poor condition of the KCl crystal, meant that it was impossible to monitor the laser power during tuning. The experimental SHG tuning curves were therefore obtained without deconvolving fluctuations in the laser power during tuning, in the hope that any quasi-phase-matched SHG peak features would be very obvious. However, the SHG signals measured as a function of wavelength were not reproducible and were therefore probably the result of laser power fluctuations, mode-hopping and Fabry-Perot effects which occurred during tuning. Any minor QPM peak would then, of course, have been obscured by such effects.

The most likely explanation for the absence of a major QPM peak is that the intermixing periods chosen were incorrect due to a larger than anticipated uncertainty in Δn_{eff}. This could have been, at least in part, caused by a change in Δn_{eff} on intermixing. Measured index data should therefore strictly be used to ensure the correct choice of QPM period. Another possible explanation for failing to observe phase-matched SHG would be that there was a negligible modulation in $\chi^{(2)}_{zxy}$ due to poor suppression of the IFVD process. A superior selective-area intermixing process should therefore be developed. Discontinuous laser tuning could also have meant that the QPM condition with its narrow bandwidth was never satisfied at any of the limited number of different mode wavelengths. This problem could have been circumvented if a pulsed colour centre laser system had been available for the tuning experiments.

---

[1] S. I. Hansen, "The Refractive Index Change in GaAs/AlGaAs Quantum Wells Produced by Neutral Impurity Induced Disordering Using Boron and Fluorine", PhD Thesis, University of Glasgow (1993), and M. A. Afromowitz, "Refractive Index of Ga$_{1-x}$Al$_x$As", Solid State Commun. **15**, 59 (1974)

[2] G. J. Sonek, J. M. Ballantyne, Y. J. Chen, G. M. Carter, S. W. Brown, E. S. Koteles, and J. P. Salemo, "Dielectric Properties of GaAs/AlGaAs Multiple Quantum Well Waveguides", J. Quantum Electron. **22**, 1015 (1986)

[3] K. B. Kahen and J. P. Leburton, "Exciton Effects in the Index of Refraction of Multiple Quantum Wells and Superlattices", Appl. Phys. Lett. **49**, 734 (1986)

[4] R. A. Sammut and I. M. Skinner, "Effective Index Models for MQW Waveguides", Opt. Comms. **76**, 213 (1990)

[5] B. S. Bhumbra, "Nonlinear Optical Waveguide Devices in GaAs/AlGaAs", PhD Thesis, University of Glasgow (1990)

[6] S. Adachi, "GaAs, AlAs and Al$_x$Ga$_{1-x}$As: Material Parameters for Use in Research and Device Applications", J. Appl. Phys. **58**, R1 (1985)

[7] J. T. Boyd, "Theory of Parametric Oscillation Phase Matched in GaAs Thin-Film Waveguides", J. Quantum. Electron. **8**, 788 (1972)

[8] S. J. B. Yoo, C. Caneau, R. Bhat, M. A. Koza, A. Rajhel, and N. Antoniades, "Wavelength Conversion by Difference Frequency Generation in AlGaAs Waveguides with Periodic Domain Inversion Achieved by Wafer Bonding", Appl. Phys. Lett. **68**, 2609, 1996

Further Work and Conclusions

This work is concerned with the control of second order non-linearities in GaAs/AlGaAs multiple asymmetric QW (AQW) waveguides using QW-intermixing for domain-disordering.

From characterisation measurements, it is clear that the growth of GaAs/AlGaAs multiple AQW epitaxial structures is relatively demanding. AQW structures were therefore designed to be "tolerant" to growth inaccuracies.

QW-intermixing was accomplished using the impurity free vacancy disordering (IFVD) process. Intermixing was observed to occur more readily (i.e. shorter anneal times and lower anneal temperatures were required to achieve the same degree of intermixing) in AQW samples which were encapsulated with e-beam evaporated SiO_2 and which incorporated lower Al fractions in the epitaxial layers. This may have been due to the more porous nature of e-beam evaporated SiO_2 compared with PECVD SiO_2, and/or lower C impurity concentrations in the lower Al fraction AQW layers. Further experiments should therefore be designed to quantify the influence of these two factors.

Unphase-matched second harmonic generation (SHG) experiments were performed with both as-grown and intermixed GaAs/AlGaAs multiple AQW waveguides at the sub-half-band-gap wavelength of 1.524 μm. No conclusive evidence was found for the existence of any AQW tensor components. These observations are consistent with recent calculations which predict that the second order susceptibility tensor components $\chi^{(2)}_{xzx}$, $\chi^{(2)}_{zxx}$, and $\chi^{(2)}_{zzz}$, associated with the *particular* AQW structures tested, are negligible. Unphase-matched SHG was, however, observed due to the large bulk GaAs/AlGaAs $\chi^{(2)}_{xyz}$ component. Furthermore, QW-intermixing resulted in an estimated reduction of $\chi^{(2)}_{xyz}$ by 17%. $\chi^{(2)}_{xyz}$ is resonant at the half-band-gap, so that the observed reduction may be attributed to the increased detuning of the band-edge from the two-photon energy which occurs on QW-intermixing. Since the quasi-phase-matching conversion efficiency is proportional to both the square of the magnitude of the non-linearity and the square of the modulation depth, a small but significant reduction in the large $\chi^{(2)}_{xyz}$ non-linearity such as this, could lead to useful conversion efficiencies. Larger reductions in $\chi^{(2)}_{xyz}$, and therefore potentially higher conversion efficiencies, may also be possible by re-designing the MQW structure and/or operating at a wavelength closer to the half-band-gap.

Quasi-phase-matching requires the periodic modulation of the MQW waveguide non-linearities. Selective-area IFVD was therefore demonstrated using hydrogen plasma processing to inhibit QW-intermixing in selected-areas. However, only partial suppression of the intermixing process was achieved in this way. Superior techniques for the suppression of the IFVD process should therefore be developed for efficient domain disordering. For example, it may be possible to grow a substantial Ga_2O_3 layer in selected areas. Such an oxide layer may be almost completely impermeable to Ga atoms during annealing and would therefore suppress the IFVD process. Alternatively, the properties of the SiO_2 cap could be modified in selected areas to make it impermeable to Ga atoms during annealing.

Experiments were performed to determine the spatial resolution of the selective-area IFVD process. For an epitaxial waveguide structure with a MQW layer extending from between approximately 1 and 2 μm below the sample surface, the measured resolution of the IFVD process was better than 2.2 μm. This result is quite remarkable since it implies that, during annealing, Ga vacancies diffuse downwards through the epitaxial layers faster than they diffuse in a lateral direction. Furthermore, this result means that the resolution of the IFVD process is sufficiently good for quasi-phase-matching in GaAs/AlGaAs MQW waveguides.

Waveguides were fabricated in periodically-intermixed GaAs/AlGaAs MQW material with measured losses which increased from 3.7 dB/cm up to 18.0 dB/cm as the intermixing period was reduced from 12.4 to 5.8 μm. These losses are not prohibitively high. Furthermore, lower losses would be expected for an optimised waveguide design. However, no TE_{ω}:$TM_{2\omega}$ quasi-phase-matched SHG was observed in the periodically-intermixed waveguides. This could have been the result of several factors. For example, laser mode-hopping and discontinuous tuning could have meant that the narrow bandwidth phase-matching condition was not satisfied. Alternatively, because of the uncertainty in the waveguide mode effective indices, the range of intermixing periods and wavelengths used may not have been sufficiently extensive i.e. the phase-matching condition may not have been satisfied for any of the intermixing periods and wavelengths used. Another possibility is that, because the suppression of the QW-intermixing process in selected areas was not very successful, the resulting periodic modulation in the bulk $\chi^{(2)}_{xyz}$ non-linearity may have been negligible.

In summary, if a superior selective-area IFVD process can be developed, efficient quasi-phase-matching may be possible through modulation of the large $\chi^{(2)}_{xyz}$ non-linearity. If, in addition, an optimised AQW structure can be designed with an associated $\chi^{(2)}_{zxx}$ component which is comparable to $\chi^{(2)}_{xyz}$, then periodic modulation of the total non-linearity $\chi^{(2)}_{xyz}+\chi^{(2)}_{zxx}$ by QW-intermixing could result in conversion efficiencies of several hundred %/Wcm^2.

Appendices

A

Material Data

All the interband transition wavelengths and oscillator strengths appearing in this appendix were calculated using the algorithm of Chapter 4 for the solution of the 1D Schrödinger equation, where all band-gap and effective mass data was taken from Adachi's review paper [1]. Also, all waveguide mode effective indices were calculated using a multilayer slab solver routine where all refractive index data was generated using the modified Afromowitz model [2].

---

[1] S. Adachi, "GaAs, AlAs and $Al_xGa_{1-x}As$: Material Parameters for Use in Research and Device Applications", J. Appl. Phys. **58**, R1 (1985)

[2] S. I. Hansen, "The Refractive Index Change in GaAs/AlGaAs Quantum Wells Produced by Neutral Impurity Induced Disordering Using Boron and Fluorine", PhD Thesis, University of Glasgow (1993), and M. A. Afromowitz, "Refractive Index of $Ga_{1-x}Al_xAs$", Solid State Commun. **15**, 59 (1974)

QT613
(MOCVD)

500 Å		GaAs Cap
0.8 μm	Upper Cladding	49% AlGaAs
1.52 μm 50 wells 51 barriers	MQW	See below
4 μm	Lower Cladding	49% AlGaAs
	Substrate	n+ GaAs

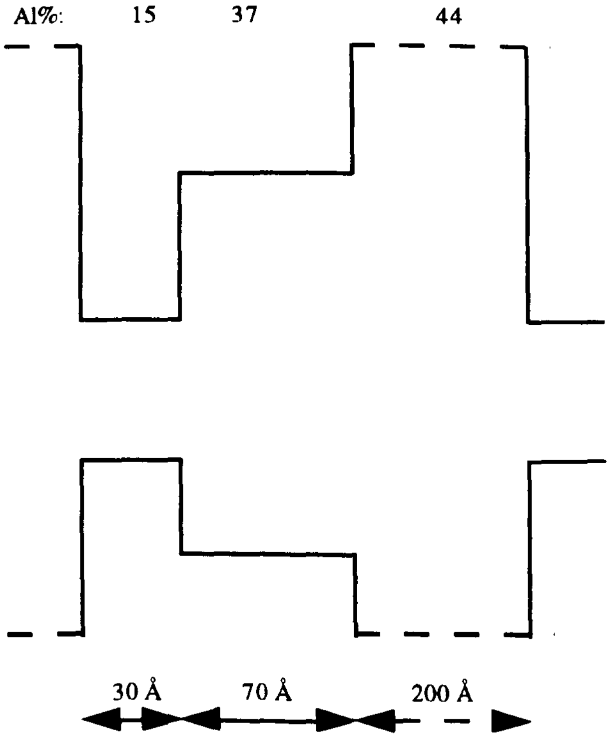

N.B. All epitaxial layers nominally undoped

QT613
(Interband Transition Wavelengths in nm Calculated for Nominal Structure)

300K

	e1	e2
lh1	694.06	657.53
lh2	670.15	636.03
hh1	712.02	673.62
hh2	683.20	647.77
hh3	676.97	642.17
hh4	669.22	635.19

77K

	e1	e2
lh1	659.31	625.52
lh2	637.20	605.59
hh1	675.77	640.32
hh2	649.43	616.62
hh3	643.47	611.25
hh4	636.40	604.86

QT613
(Interband Transition Oscillator Strengths in a.u. Calculated for Nominal Structure)

300K

Polarisation ‖ to Layers	e1	e2
lh1	0.1653707	0.0005397
lh2	0.0004135	0.1615342
hh1	0.4264055	0.0118124
hh2	0.0072404	0.0882657
hh3	0.0193096	0.3089924
hh4	0.0167674	0.0492597

Polarisation ⊥ to Layers	e1	e2
lh1	0.6614830	0.0021587
lh2	0.0016539	0.6461369

77K

Polarisation ‖ to Layers	e1	e2
lh1	0.1653831	0.0005350
lh2	0.0004127	0.1616902
hh1	0.4272135	0.0116156
hh2	0.0066001	0.0826719
hh3	0.0192914	0.3172912
hh4	0.0168341	0.0459772

Polarisation ⊥ to Layers	e1	e2
lh1	0.6615325	0.0021401
lh2	0.0016508	0.6467608

QT613
Individual Layer Refractive Indices and 1D Mode Effective Indices at 1.55 μm

	Refractive Index at 1.55 μm
49% AlGaAs	3.146528
MQW(TE)	3.186440
MQW(TM)	3.185579
TE_0	3.171787
TM_0	3.170719

B563
(MBE)

100 Å		GaAs Cap
0.8 μm	Upper Cladding	32% AlGaAs
1.163 μm 50 wells 51 barriers	MQW	See below
3 μm	Lower Cladding	42% AlGaAs
	Substrate	GaAs

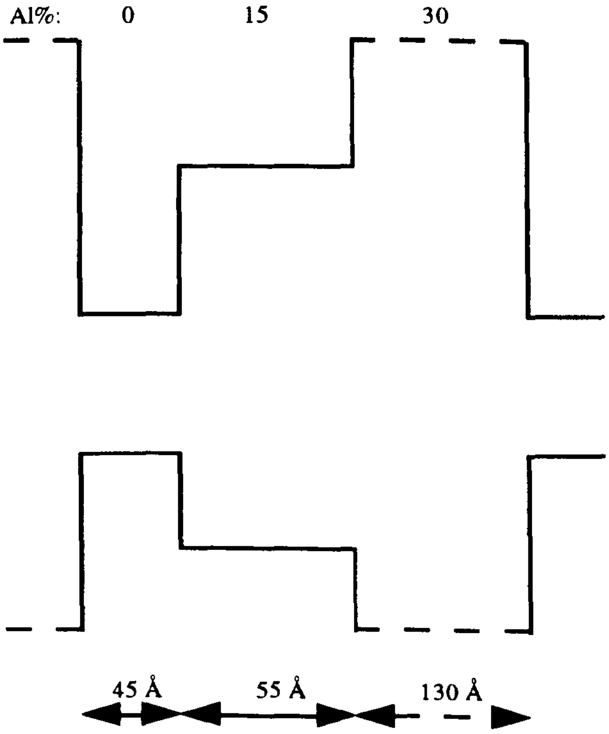

N.B. Substrate and all epitaxial layers nominally undoped

B563
(Interband Transition Wavelengths in nm Calculated for Nominal Structure)

300K

	el	e2
lh1	804.05	752.22
lh2	767.52	720.16
hh1	822.02	767.93
hh2	798.62	747.47
hh3	784.19	734.82
hh4	770.40	722.70
hh5	757.59	711.41

77K

	el	e2
lh1	759.99	712.81
lh2	726.77	683.50
hh1	776.26	727.10
hh2	755.18	708.58
hh3	741.84	696.82
hh4	729.54	685.95
hh5	717.89	675.65

B563
(Interband Transition Oscillator Strengths in a.u. Calculated for Nominal Structure)

300K

Polarisation ∥ to Layers	e1	e2
lh1	0.1662076	0.0002481
lh2	0.0002254	0.1648640
hh1	0.4327726	0.0251030
hh2	0.0071087	0.1322106
hh3	0.0390489	0.2584565
hh4	0.0110560	0.0356384
hh5	0.0043107	0.0002163

Polarisation ⊥ to Layers	e1	e2
lh1	0.6648302	0.0009923
lh2	0.0009014	0.6594560

77K

Polarisation ∥ to Layers	e1	e2
lh1	0.1662101	0.0002487
lh2	0.0002266	0.1649224
hh1	0.4334495	0.0248636
hh2	0.0067697	0.1300553
hh3	0.0388747	0.2622342
hh4	0.0110614	0.0352286
hh5	0.0039086	0.0001641

Polarisation ⊥ to Layers	e1	e2
lh1	0.6648404	0.0009948
lh2	0.0009064	0.6596895

B563

Individual Layer Refractive Indices and 1D Mode Effective Indices at 1.7 μm

	Refractive Index at 1.7 μm
32% AlGaAs	3.205496
42% AlGaAs	3.164963
MQW(TE)	3.259602
MQW(TM)	3.257551
TE_0	3.231903
TE_1	3.169682
TM_0	3.229178
TM_1	3.166841

B578
(MBE)

100 Å		GaAs Cap
0.8 μm	Upper Cladding	34% AlGaAs
1.073 μm 50 wells 51 barriers	MQW	See below
3 μm	Lower Cladding	44% AlGaAs
	Substrate	GaAs

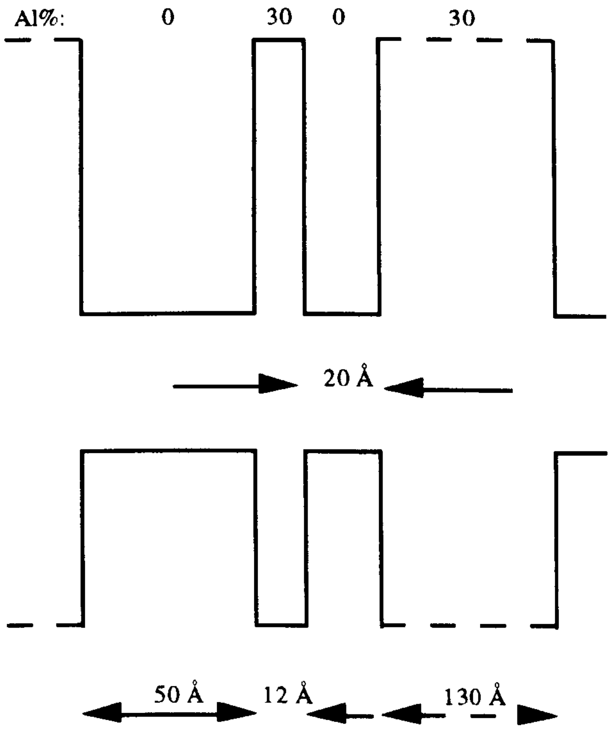

N.B. Substrate and all epitaxial layers nominally undoped

B578
(Interband Transition Wavelengths in nm Calculated for Nominal Structure)

300K

	e1	e2
lh1	806.33	756.42
lh2	769.74	724.13
hh1	824.09	772.03
hh2	805.44	755.64
hh3	799.22	750.17
hh4	767.77	722.39

77K

	e1	e2
lh1	762.06	716.84
lh2	728.90	687.42
hh1	778.13	731.04
hh2	761.29	716.15
hh3	755.84	711.33
hh4	727.38	686.07

B578
(Interband Transition Oscillator Strengths in a.u. Calculated for Nominal Structure)

300K

Polarisation ‖ to Layers	e1	e2
lh1	0.1662958	0.0001718
lh2	0.0001536	0.1644309
hh1	0.4319626	0.0292050
hh2	0.0338570	0.3808363
hh3	0.0059949	0.0011598
hh4	0.0167335	0.0076157

Polarisation ⊥ to Layers	e1	e2
lh1	0.6651833	0.0006870
lh2	0.0006144	0.6577236

77K

Polarisation ‖ to Layers	e1	e2
lh1	0.1662963	0.0001746
lh2	0.0001567	0.1645017
hh1	0.4325471	0.0291300
hh2	0.0333452	0.3826183
hh3	0.0059144	0.0013043
hh4	0.0166939	0.0066877

Polarisation ⊥ to Layers	e1	e2
lh1	0.6651851	0.0006986
lh2	0.0006270	0.6580068

B578

Individual Layer Refractive Indices and 1D Mode Effective Indices at 1.7 μm

	Refractive Index at 1.7 μm
34% AlGaAs	3.197279
44% AlGaAs	3.156941
MQW(TE)	3.263890
MQW(TM)	3.260911
TE_0	3.231522
TE_1	3.160220
TM_0	3.227795
TM_1	3.157899

B635
(MBE)

1000 Å		GaAs Cap
0.8 µm	Upper Cladding	55% AlGaAs
1.132 µm 60 wells 61 barriers	MQW	See below
3 µm	Lower Cladding	56% AlGaAs
	Substrate	GaAs

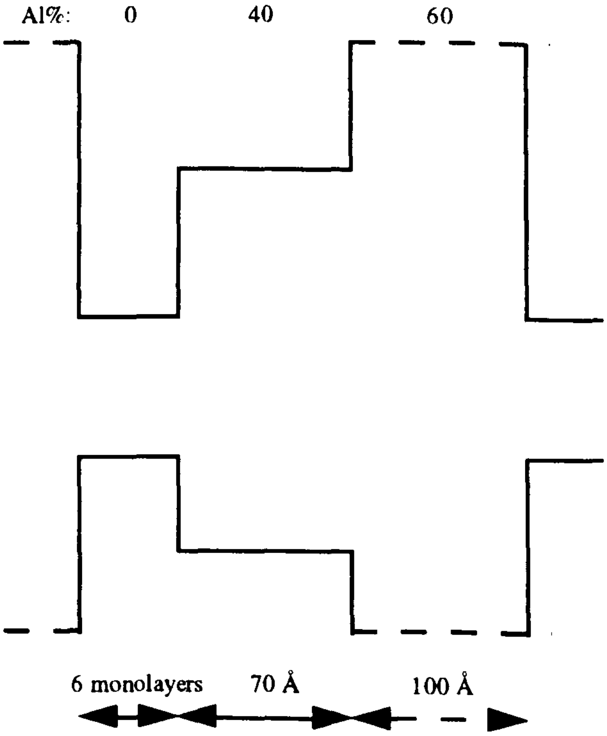

N.B. Substrate and all epitaxial layers nominally undoped

B635

(Interband Transition Wavelengths in nm Calculated for Nominal Structure)

300K

	e1	e2
lh1	682.86	638.23
lh2	652.84	611.93
hh1	717.46	668.35
hh2	667.06	624.40
hh3	659.70	617.95
hh4	649.70	609.17
hh5	637.81	598.70

77K

	e1	e2
lh1	649.30	607.94
lh2	621.57	583.56
hh1	681.19	635.81
hh2	634.49	594.94
hh3	627.89	589.13
hh4	618.87	581.18
hh5	607.88	571.48

B635

(Interband Transition Oscillator Strengths in a.u. Calculated for Nominal Structure)

300K

Polarisation ‖ to Layers	e1	e2
lh1	0.1645859	0.0013553
lh2	0.0012222	0.1636423
hh1	0.3995159	0.0228456
hh2	0.0453088	0.3966302
hh3	0.0099038	0.0541338
hh4	0.0009876	0.0042700
hh5	0.0130802	0.0023593

Polarisation ⊥ to Layers	e1	e2
lh1	0.6583437	0.0054214
lh2	0.0048890	0.6545690

77K

Polarisation ‖ to Layers	e1	e2
lh1	0.1646004	0.0013380
lh2	0.0012078	0.1637170
hh1	0.4005378	0.0221214
hh2	0.0442095	0.3969386
hh3	0.0097172	0.0552689
hh4	0.0010998	0.0040314
hh5	0.0128861	0.0023288

Polarisation ⊥ to Layers	e1	e2
lh1	0.6584017	0.0053519
lh2	0.0048313	0.6548681

B635

Individual Layer Refractive Indices and 1D Mode Effective Indices at 1.55 μm

	Refractive Index at 1.55 μm
55% AlGaAs	3.121650
56% AlGaAs	3.117440
MQW(TE)	3.157492
MQW(TM)	3.153627
TE_0	3.138070
TM_0	3.134654

B690
(MBE)

1000 Å		GaAs Cap
0.8 µm	Upper Cladding	47% AlGaAs
1.018 µm 48 wells 49 barriers	MQW	See below
4 µm	Lower Cladding	47% AlGaAs
	Substrate	GaAs

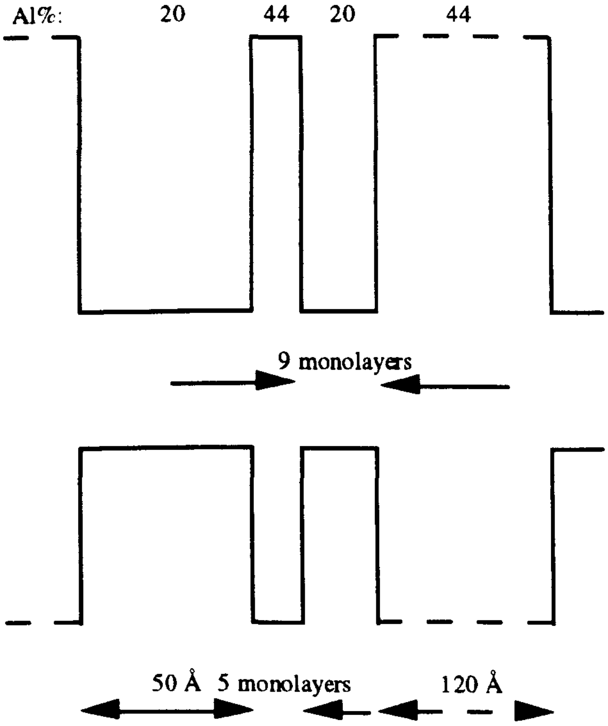

N.B. Substrate and all epitaxial layers nominally undoped

B690, B672 and QT849A (Interband Transition Wavelengths in nm Calculated for Nominal Structure)

300K

	e1	e2
lh1	701.44	676.17
lh2	681.91	658.01
hh1	712.10	686.07
hh2	703.62	678.19
hh3	695.69	670.82
hh4	675.42	651.96

77K

	e1	e2
lh1	665.92	642.89
lh2	648.12	626.29
hh1	675.67	651.98
hh2	667.94	644.78
hh3	660.80	638.12
hh4	642.23	620.78

B690, B672 and QT849A (Interband Transition Oscillator Strengths in a.u. Calculated for Nominal Structure)

300K

Polarisation ‖ to Layers	e1	e2
lh1	0.1659271	0.0004045
lh2	0.0003667	0.1636148
hh1	0.4271049	0.0394425
hh2	0.0443522	0.3839885
hh3	0.0001348	0.0107173
hh4	0.0147934	0.0108493

Polarisation ⊥ to Layers	e1	e2
lh1	0.6637086	0.0016181
lh2	0.0014666	0.6544592

77K

Polarisation ‖ to Layers	e1	e2
lh1	0.1659222	0.0004135
lh2	0.0003761	0.1637002
hh1	0.4276852	0.0392827
hh2	0.0437943	0.3852518
hh3	0.0001123	0.0108980
hh4	0.0150624	0.0094153

Polarisation ⊥ to Layers	e1	e2
lh1	0.6636890	0.0016540
lh2	0.0015042	0.6548009

B690, B672 and QT849A
Individual Layer Refractive Indices and 1D Mode Effective Indices at 1.55 μm

	Refractive Index at 1.55 μm
47% AlGaAs	3.154717
MQW(TE)	3.204053
MQW(TM)	3.202569
TE_0	3.179883
TM_0	3.178131

B690, B672 and QT849A
2D Overlap Factors for Second Harmonic Generation at 1.55 μm in Waveguides with a Rib Width of 3 μm and an Etch Depth of 0.9 μm

$TM_{\omega}:TM_{2\omega}$

Overlap Factor $F^{(2)}_{zzz}$ /m^2	$TM_{\omega 00}$ (3.173982)	$TM_{\omega 01}$ (3.164927)
$TM_{2\omega 00}$ (3.425296)	1.455673×10^{11}	2.342599×10^{10}
$TM_{2\omega 01}$ (3.422996)	2.820805×10^{-7}	6.660567×10^{-9}
$TM_{2\omega 10}$ (3.392157)	6.406366×10^{7}	5.713705×10^{6}
$TM_{2\omega 11}$ (3.387801)	7.387521×10^{-10}	9.587967×10^{-11}

$TE_{\omega}:TM_{2\omega}$

Overlap Factor $F^{(2)}_{xyz}$ /m^2	$TE_{\omega 00}$ (3.176010)	$TE_{\omega 01}$ (3.168460)
$TM_{2\omega 00}$ (3.425296)	1.632129×10^{11}	4.570926×10^{9}
$TM_{2\omega 01}$ (3.422996)	3.024854×10^{4}	7.779384×10^{3}
$TM_{2\omega 10}$ (3.392157)	7.880680×10^{7}	1.038151×10^{6}
$TM_{2\omega 11}$ (3.387801)	1.431481×10^{1}	3.681508

N.B. Quantities in brackets are the 2D mode effective indices for a fundamental wavelength of 1.55 μm

A776
(MBE)

100 Å		GaAs Cap
0.8 μm	Upper Cladding	37% AlGaAs
1.484 μm 70 wells 71 barriers	MQW	See below
4 μm	Lower Cladding	37% AlGaAs
	Substrate	GaAs

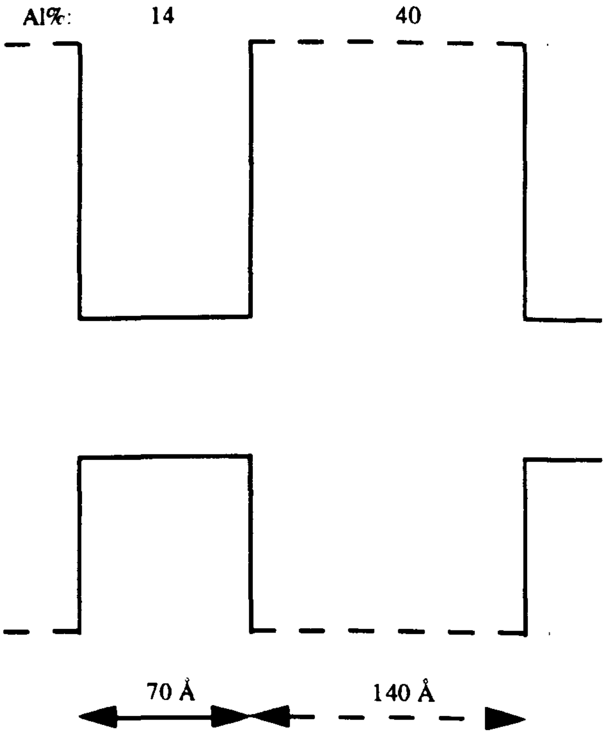

N.B. Substrate and all epitaxial layers nominally undoped

A776
(Interband Transition Wavelengths in nm Calculated for Nominal Structure)

300K

	e1	e2
lh1	740.73	693.62
lh2	705.96	663.04
hh1	751.79	703.31
hh2	740.75	693.64
hh3	723.72	678.68
hh4	703.95	661.27

77K

	e1	e2
lh1	702.05	659.16
lh2	670.33	631.12
hh1	712.07	667.98
hh2	702.11	659.22
hh3	686.72	645.63
hh4	668.65	629.63

A776
(Interband Transition Oscillator Strengths in a.u. Calculated for Nominal Structure)

300K

Polarisation ∥ to Layers	e1	e2
lh1	0.1663642	0.0000000
lh2	0.0000000	0.1619641
hh1	0.4756019	0.0000000
hh2	0.0000000	0.3677510
hh3	0.0126422	0.0000000
hh4	0.0000000	0.0816312

Polarisation ⊥ to Layers	e1	e2
lh1	0.6654566	0.0000000
lh2	0.0000000	0.6478564

77K

Polarisation ∥ to Layers	e1	e2
lh1	0.1663698	0.0000000
lh2	0.0000000	0.1621306
hh1	0.4759488	0.0000000
hh2	0.0000000	0.3712381
hh3	0.0123918	0.0000000
hh4	0.0000000	0.0765285

Polarisation ⊥ to Layers	e1	e2
lh1	0.6654792	0.0000000
lh2	0.0000000	0.6485222

B579
(MBE)

1000 Å		GaAs Cap
0 8 μm	Upper Cladding	40% AlGaAs
1 0084 μm 78 wells 79 barriers	MQW	See below
4 μm	Lower Cladding	40% AlGaAs
	Substrate	GaAs

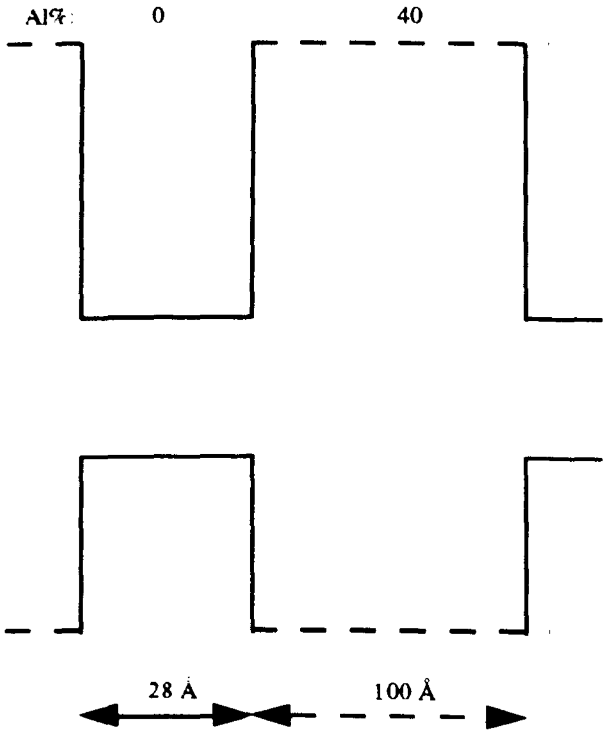

N.B. Substrate and all epitaxial layers nominally undoped

B579

(Interband Transition Wavelengths in nm Calculated for Nominal Structure)

300K

	e1
lh1	740.57
hh1	772.03
hh2	725.42

77K

	e1
lh1	702.36
hh1	731.05
hh2	688.76

B579
(Interband Transition Oscillator Strengths in a.u. Calculated for Nominal Structure)

300K

Polarisation ‖ to Layers	e1
lh1	0.1660915
hh1	0.4384580
hh2	0.0000000

Polarisation ⊥ to Layers	e1
lh1	0.6643658

77K

Polarisation ‖ to Layers	e1
lh1	0.1660928
hh1	0.4389244
hh2	0.0000000

Polarisation ⊥ to Layers	e1
lh1	0.6643711

B

Quasi-phase-matching Conversion Efficiency as a Function of the Non-linearity Modulation Depth

In the limit of low pump depletion when $\hat{E}_\omega(z) \approx \hat{E}_\omega(0)$ and $\Delta\Phi^{NL}(z) \approx 0$, we have from (2.49):

$$\frac{d\hat{E}_{2\omega}(z)}{dz} = iK\exp(i\Delta kz) \tag{B.1a}$$

where

$$K = \frac{\omega}{n_{2\omega}c} d_{eff}\left[\hat{E}_\omega(0)\right]^2 \tag{B.1b}$$

and

$$\Delta k = \frac{4\pi}{\lambda}\left(n_\omega - n_{2\omega}\right) \tag{B.1c}$$

Now, for a quasi-phase-matching scheme with a modulation period in the non-linearity of $\Lambda = 2mL_c$, the domain length L_d may be defined according to:

$$L_d = \frac{\Lambda}{2} = mL_c \tag{B.2}$$

For the Mth quasi-phase-matching period along the medium, we may define effective non-linear coefficients of d_{eff} and d_{eff}' over the first and second domains respectively as illustrated in Fig. B.1:

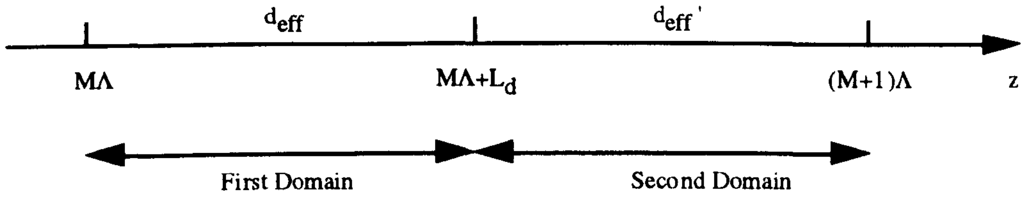

Fig. B.1 The d coefficients in the Mth quasi-phase-matching period along a second order non-linear medium

Then, integrating (B.1a) over the first and second domains in the Mth QPM period gives (B.3a) and (B.3b) respectively:

$$\int_{M\Lambda}^{M\Lambda+L_d} d\hat{E}_{2\omega} = iK \int_{M\Lambda}^{M\Lambda+L_d} \exp(i\Delta kz)dz \tag{B.3a}$$

$$\int_{M\Lambda}^{M\Lambda+L_d} d\hat{E}_{2\omega} = iK' \int_{M\Lambda}^{M\Lambda+L_d} \exp(i\Delta kz)dz \tag{B.3b}$$

where

$$K' = \frac{\omega}{n_{2\omega}c} d_{eff}' \left[\hat{E}_{\omega}(0)\right]^2 \tag{B.3c}$$

Evaluating (B.3a) and (B.3b) gives (B.4a) and (B.4b) respectively:

$$\hat{E}_{2\omega}(M\Lambda + L_d) = \hat{E}_{2\omega}(M\Lambda) + \frac{K}{\Delta k}\exp(i\Delta kM\Lambda)\cdot\left[\exp(i\Delta kL_d) - 1\right] \tag{B.4a}$$

$$\hat{E}_{2\omega}[(M+1)\Lambda] = \hat{E}_{2\omega}(M\Lambda + L_d) + \frac{K'}{\Delta k}\exp(i\Delta kM\Lambda)\cdot\left[\exp(i\Delta k\Lambda) - \exp(i\Delta kL_d)\right] \tag{B.4b}$$

Then, combining (B.4a) and (B.4b) we may relate $\hat{E}_{2\omega}[(M+1)\Lambda]$ to $\hat{E}_{2\omega}(M\Lambda)$:

$$\begin{aligned}\hat{E}_{2\omega}[(M+1)\Lambda] &= \hat{E}_{2\omega}(M\Lambda) + \\ &\frac{\exp(i\Delta kM\Lambda)}{\Delta k}\left\{K\left[\exp(i\Delta kL_d) - 1\right] + K'\left[\exp(i\Delta k\Lambda) - \exp(i\Delta kL_d)\right]\right\}\end{aligned} \tag{B.5}$$

Now, $\Lambda = 2mL_c$ where m is the (odd) order of the QPM scheme. Hence,

$$\exp(i\Delta kM\Lambda) = \exp(i\Delta k\Lambda) = 1 \tag{B.6}$$

Furthermore, since m is odd:

$$\exp(i\Delta kL_d) = -1 \tag{B.7}$$

Using (B.6) and (B.7), (B.5) then becomes:

$$\hat{E}_{2\omega}[(M+1)\Lambda] = \hat{E}_{2\omega}(M\Lambda) - \frac{2(K-K')}{\Delta k} \tag{B.8}$$

Hence, for $\hat{E}_{2\omega}(0) = 0$, we have:

$$\hat{E}_{2\omega}(M\Lambda) = -\frac{2M(K-K')}{\Delta k} \tag{B.9}$$

Or, in terms of the second harmonic field intensity:

$$I_{2\omega}(M\Lambda) = \frac{2\varepsilon_0 cn_{2\omega} \cdot M^2|K-K'|^2}{(\Delta k)^2} \tag{B.10}$$

Finally, substituting for K and K′ from (B.1b) and (B.3c) respectively, and writing $|\Delta k| = \pi/L_c$ gives:

$$I_{2\omega}(M \cdot 2mL_c) = \frac{8\pi^2}{\varepsilon_0 c\lambda^2}\frac{\left|d_{eff} - d_{eff}'\right|}{n_\omega^2 n_{2\omega}} I_\omega^2(0)\frac{4M^2L_c^2}{\pi^2} \tag{B.11}$$

C

Derivation of the Full Scalar Wave Equation Model for Second Order Non-linear Effects in GaAs/AlGaAs AQW Waveguides

When operating in the "sub-half-band-gap" spectral region, it may be assumed that there is no absorption of the fundamental or second harmonic fields, and that the relations of (2.28) apply. The 4 scalar coupled wave equations which govern the evolution of the TE and TM-polarised fundamental and second harmonic fields will now be derived. The up-conversion process is treated first and expressions are derived for the second harmonic TE and TM components of the polarisation vector. Next, the down-conversion process is considered and the TE and TM components of the fundamental polarisation vector are derived. Finally the polarisation vector components are combined to give the desired set of coupled wave equations. For the general case, the input fundamental beam is polarised with both TE and TM electric field components, and by referring to Fig. 3.3 we may write:

$$(E_\omega)_x = (E_\omega)_y = \frac{(E_\omega)_{TE}}{\sqrt{2}} \qquad \text{(C.1a)}$$

$$(E_\omega)_z = (E_\omega)_{TM} \qquad \text{(C.1b)}$$

Similarly, for the second harmonic fields:

$$(E_{2\omega})_x = (E_{2\omega})_y = \frac{(E_{2\omega})_{TE}}{\sqrt{2}} \qquad \text{(C.2a)}$$

$$(E_{2\omega})_z = (E_{2\omega})_{TM} \qquad \text{(C.2b)}$$

Up-conversion

From (2.11), the second harmonic polarisation vector is given by:

$$\mathbf{P}_{2\omega}^{(2)}(z) = \tfrac{1}{2}\varepsilon_0\chi^{(2)}(-2\omega;\omega,\omega)\vert\mathbf{E}_\omega(z)\mathbf{E}_\omega(z) \tag{2.11}$$

Summing over all non-zero (bulk and AQW) tensor elements we may then deduce the following second harmonic polarisation components:

Summing over all non-zero (bulk and AQW) tensor elements, the following second harmonic polarisation components are obtained:

$$\begin{aligned}\left(P_{2\omega}^{(2)}\right)_x = \tfrac{1}{2}\varepsilon_0\Big[&\chi_{xzx}^{(2)}(-2\omega;\omega,\omega)(E_\omega)_z(E_\omega)_x + \chi_{xxz}^{(2)}(-2\omega;\omega,\omega)(E_\omega)_x(E_\omega)_z \\ &+\chi_{xyz}^{(2)}(-2\omega;\omega,\omega)(E_\omega)_y(E_\omega)_z + \chi_{xzy}^{(2)}(-2\omega;\omega,\omega)(E_\omega)_z(E_\omega)_y\Big]\end{aligned} \tag{C.3a}$$

$$\begin{aligned}\left(P_{2\omega}^{(2)}\right)_y = \tfrac{1}{2}\varepsilon_0\Big[&\chi_{yzy}^{(2)}(-2\omega;\omega,\omega)(E_\omega)_z(E_\omega)_y + \chi_{yyz}^{(2)}(-2\omega;\omega,\omega)(E_\omega)_y(E_\omega)_z \\ &+\chi_{yxz}^{(2)}(-2\omega;\omega,\omega)(E_\omega)_x(E_\omega)_z + \chi_{yzx}^{(2)}(-2\omega;\omega,\omega)(E_\omega)_z(E_\omega)_x\Big]\end{aligned} \tag{C.3b}$$

$$\begin{aligned}\left(P_{2\omega}^{(2)}\right)_z = \tfrac{1}{2}\varepsilon_0\Big[&\chi_{zxx}^{(2)}(-2\omega;\omega,\omega)(E_\omega)_x^2 + \chi_{zyy}^{(2)}(-2\omega;\omega,\omega)(E_\omega)_y^2 \\ &+\chi_{zzz}^{(2)}(-2\omega;\omega,\omega)(E_\omega)_z^2 + \chi_{zxy}^{(2)}(-2\omega;\omega,\omega)(E_\omega)_x(E_\omega)_y \\ &+\chi_{zyx}^{(2)}(-2\omega;\omega,\omega)(E_\omega)_y(E_\omega)_x\Big]\end{aligned} \tag{C.3c}$$

Now

$$\left(P_{2\omega}^{(2)}\right)_{TE} = \frac{\left(P_{2\omega}^{(2)}\right)_x}{\sqrt{2}} + \frac{\left(P_{2\omega}^{(2)}\right)_y}{\sqrt{2}} \tag{C.4a}$$

$$\left(P_{2\omega}^{(2)}\right)_{TM} = \left(P_{2\omega}^{(2)}\right)_z \tag{C.4b}$$

Using intrinsic permutation symmetry, and the symmetry relations of (3.1) and (3.2) we may then deduce:

$$\left(P_{2\omega}^{(2)}\right)_{TE} = \varepsilon_0\left[\chi_{xzx}^{(2)}(-2\omega;\omega,\omega) + \chi_{xyz}^{(2)}(-2\omega;\omega,\omega)\right](E_\omega)_{TM}(E_\omega)_{TE} \tag{C.5a}$$

$$\begin{aligned}\left(P_{2\omega}^{(2)}\right)_{TM} = \tfrac{1}{2}\varepsilon_0\Big\{&\left[\chi_{zxx}^{(2)}(-2\omega;\omega,\omega) + \chi_{xyz}^{(2)}(-2\omega;\omega,\omega)\right](E_\omega)_{TE}^2 \\ &+\chi_{zzz}^{(2)}(-2\omega;\omega,\omega)(E_\omega)_{TM}^2\Big\}\end{aligned} \tag{C.5b}$$

Down-conversion

For the case of down-conversion the fundamental polarisation vector is given by (2.8a) with $\omega_\sigma = \omega$, $\omega_1 = 2\omega$, and $\omega_2 = -\omega$:

$$\mathbf{P}_\omega^{(2)}(z) = \varepsilon_0\chi^{(2)}(-\omega;2\omega,-\omega)|\mathbf{E}_{2\omega}(z)\mathbf{E}_{-\omega}(z) \tag{2.8a}$$

Summing over all non-zero tensor elements as for the up-conversion case, we may deduce the fundamental polarisation components:

$$\begin{aligned}\left(P_\omega^{(2)}\right)_x = \varepsilon_0\Big[&\chi_{xzx}^{(2)}(-\omega;2\omega,-\omega)(E_{2\omega})_z(E_{-\omega})_x + \chi_{xxz}^{(2)}(-\omega;2\omega,-\omega)(E_{2\omega})_x(E_{-\omega})_z \\ &+\chi_{xyz}^{(2)}(-\omega;2\omega,-\omega)(E_{2\omega})_y(E_{-\omega})_z + \chi_{xzy}^{(2)}(-\omega;2\omega,-\omega)(E_{2\omega})_z(E_{-\omega})_y\Big]\end{aligned} \tag{C.6a}$$

$$\begin{aligned}\left(P_\omega^{(2)}\right)_y = \varepsilon_0\Big[&\chi_{yzy}^{(2)}(-\omega;2\omega,-\omega)(E_{2\omega})_z(E_{-\omega})_y + \chi_{yyz}^{(2)}(-\omega;2\omega,-\omega)(E_{2\omega})_y(E_{-\omega})_z \\ &+\chi_{yxz}^{(2)}(-\omega;2\omega,-\omega)(E_{2\omega})_x(E_{-\omega})_z + \chi_{yzx}^{(2)}(-\omega;2\omega,-\omega)(E_{2\omega})_z(E_{-\omega})_x\Big]\end{aligned} \tag{C.6b}$$

$$\begin{aligned}\left(P_\omega^{(2)}\right)_z = \varepsilon_0\Big[&\chi_{zxx}^{(2)}(-\omega;2\omega,-\omega)(E_{2\omega})_x(E_{-\omega})_x + \chi_{zyy}^{(2)}(-\omega;2\omega,-\omega)(E_{2\omega})_y(E_{-\omega})_y \\ &+\chi_{zzz}^{(2)}(-\omega;2\omega,-\omega)(E_{2\omega})_z(E_{-\omega})_z + \chi_{zxy}^{(2)}(-\omega;2\omega,-\omega)(E_{2\omega})_x(E_{-\omega})_y \\ &+\chi_{zyx}^{(2)}(-\omega;2\omega,-\omega)(E_{2\omega})_y(E_{-\omega})_x\Big]\end{aligned} \tag{C.6c}$$

To convert these expressions containing elements of the down-conversion tensor $\chi^{(2)}(-\omega;2\omega,-\omega)$, to an equivalent set of expressions containing elements of the up-conversion tensor $\chi^{(2)}(-2\omega;\omega,\omega)$ only, we may apply the relations of (2.28) to obtain:

$$\begin{aligned}\left(P_\omega^{(2)}\right)_x = \varepsilon_0\Big[&\chi_{zxx}^{(2)}(-2\omega;\omega,\omega)(E_{2\omega})_z(E_{-\omega})_x + \chi_{xxz}^{(2)}(-2\omega;\omega,\omega)(E_{2\omega})_x(E_{-\omega})_z \\ &+\chi_{yxz}^{(2)}(-2\omega;\omega,\omega)(E_{2\omega})_y(E_{-\omega})_z + \chi_{zxy}^{(2)}(-2\omega;\omega,\omega)(E_{2\omega})_z(E_{-\omega})_y\Big]\end{aligned} \tag{C.7a}$$

$$\begin{aligned}\left(P_\omega^{(2)}\right)_y = \varepsilon_0\Big[&\chi_{zyy}^{(2)}(-2\omega;\omega,\omega)(E_{2\omega})_z(E_{-\omega})_y + \chi_{yyz}^{(2)}(-2\omega;\omega,\omega)(E_{2\omega})_y(E_{-\omega})_z \\ &+\chi_{xyz}^{(2)}(-2\omega;\omega,\omega)(E_{2\omega})_x(E_{-\omega})_z + \chi_{zyx}^{(2)}(-2\omega;\omega,\omega)(E_{2\omega})_z(E_{-\omega})_x\Big]\end{aligned} \tag{C.7b}$$

$$\begin{aligned}\left(P_\omega^{(2)}\right)_z = \varepsilon_0\Big[&\chi_{xzx}^{(2)}(-2\omega;\omega,\omega)(E_{2\omega})_x(E_{-\omega})_x + \chi_{yzy}^{(2)}(-2\omega;\omega,\omega)(E_{2\omega})_y(E_{-\omega})_y \\ &+\chi_{zzz}^{(2)}(-2\omega;\omega,\omega)(E_{2\omega})_z(E_{-\omega})_z + \chi_{xzy}^{(2)}(-2\omega;\omega,\omega)(E_{2\omega})_x(E_{-\omega})_y \\ &+\chi_{yzx}^{(2)}(-2\omega;\omega,\omega)(E_{2\omega})_y(E_{-\omega})_x\Big]\end{aligned} \tag{C.7c}$$

Proceeding as for the up-conversion case, we have:

$$\left(P_\omega^{(2)}\right)_{TE} = \frac{\left(P_\omega^{(2)}\right)_x}{\sqrt{2}} + \frac{\left(P_\omega^{(2)}\right)_y}{\sqrt{2}} \tag{C.8a}$$

$$\left(P_\omega^{(2)}\right)_{TM} = \left(P_\omega^{(2)}\right)_z \tag{C.8b}$$

Then, using intrinsic permutation symmetry and the symmetry relations of (3.1) and (3.2), we may deduce:

$$\left(P_{\omega}^{(2)}\right)_{TE} = \varepsilon_0\Big\{\Big[\chi_{zxx}^{(2)}(-2\omega;\omega,\omega) + \chi_{xyz}^{(2)}(-2\omega;\omega,\omega)\Big](E_{2\omega})_{TM}(E_{-\omega})_{TE} + \Big[\chi_{xzx}^{(2)}(-2\omega;\omega,\omega) + \chi_{xyz}^{(2)}(-2\omega;\omega,\omega)\Big](E_{2\omega})_{TE}(E_{-\omega})_{TM}\Big\} \tag{C.9a}$$

$$\left(P_{\omega}^{(2)}\right)_{TM} = \varepsilon_0\Big\{\Big[\chi_{xzx}^{(2)}(-2\omega;\omega,\omega) + \chi_{xyz}^{(2)}(-2\omega;\omega,\omega)\Big](E_{2\omega})_{TE}(E_{-\omega})_{TE} + \chi_{zzz}^{(2)}(-2\omega;\omega,\omega)(E_{2\omega})_{TM}(E_{-\omega})_{TM}\Big\} \tag{C.9b}$$

Now, applying the relation of (2.7) at both ω and 2ω gives:

$$\frac{\partial \hat{\mathbf{E}}_{2\omega}(Y)}{\partial Y} = \frac{i\omega}{n_{2\omega}c}\frac{\mathbf{P}_{2\omega}^{(2)}(Y)}{\varepsilon_0}\exp(-ik_{2\omega}Y) \tag{C.10a}$$

and

$$\frac{\partial \hat{\mathbf{E}}_{\omega}(Y)}{\partial Y} = \frac{i\omega}{2n_{\omega}c}\frac{\mathbf{P}_{\omega}^{(2)}(Y)}{\varepsilon_0}\exp(-ik_{\omega}Y) \tag{C.10b}$$

where Y denotes the distance travelled in the direction of propagation as indicated in Fig. 3.3. In terms of TE and TM vector components these equations become:

$$\frac{\partial\left(\hat{E}_{2\omega}\right)_{TE}}{\partial Y} = \frac{i\omega}{(n_{2\omega})_{TE}c}\frac{\left(P_{2\omega}^{(2)}\right)_{TE}}{\varepsilon_0}\exp\left[-i(k_{2\omega})_{TE}Y\right] \tag{C.11a}$$

$$\frac{\partial\left(\hat{E}_{2\omega}\right)_{TM}}{\partial Y} = \frac{i\omega}{(n_{2\omega})_{TM}c}\frac{\left(P_{2\omega}^{(2)}\right)_{TM}}{\varepsilon_0}\exp\left[-i(k_{2\omega})_{TM}Y\right] \tag{C.11b}$$

$$\frac{\partial\left(\hat{E}_{\omega}\right)_{TE}}{\partial Y} = \frac{i\omega}{2(n_{\omega})_{TE}c}\frac{\left(P_{\omega}^{(2)}\right)_{TE}}{\varepsilon_0}\exp\left[-i(k_{\omega})_{TE}Y\right] \tag{C.11c}$$

$$\frac{\partial\left(\hat{E}_{\omega}\right)_{TM}}{\partial Y} = \frac{i\omega}{2\left(n_{\omega}\right)_{TM}c}\frac{\left(P_{\omega}^{(2)}\right)_{TM}}{\varepsilon_0}\exp\left[-i\left(k_{\omega}\right)_{TM}Y\right] \tag{C.11d}$$

where $\left(n_{\omega}\right)_{TE}$ and $\left(n_{\omega}\right)_{TM}$ are the TE and TM mode indices at the fundamental frequency and $\left(n_{2\omega}\right)_{TE}$ and $\left(n_{2\omega}\right)_{TM}$ are the effective mode indices at the second harmonic frequency. The different propagation constants are also defined by:

$$\left(k_{\omega}\right)_{TE} = \left(n_{\omega}\right)_{TE}\cdot\frac{2\pi}{\lambda_{\omega}} \tag{C.12a}$$

$$\left(k_{\omega}\right)_{TM} = \left(n_{\omega}\right)_{TM}\cdot\frac{2\pi}{\lambda_{\omega}} \tag{C.12b}$$

$$\left(k_{2\omega}\right)_{TE} = \left(n_{2\omega}\right)_{TE}\cdot\frac{2\pi}{\lambda_{2\omega}} \tag{C.12c}$$

$$\left(k_{2\omega}\right)_{TM} = \left(n_{2\omega}\right)_{TM}\cdot\frac{2\pi}{\lambda_{2\omega}} \tag{C.12d}$$

Finally, invoking the relations of (2.9) and substituting the relations of (C.5) and (C.9) into equations (C.11) yields the 4 scalar coupled wave equations of (C.13) which constitute the full model for second order non-linear interactions in GaAs/AlGaAs AQW waveguides:

$$\frac{\partial\left(\hat{E}_{2\omega}\right)_{TE}}{\partial Y}=\frac{i\omega}{\left(n_{2\omega}\right)_{TE}c}\times$$

$$\left[\chi^{(2)}_{xzx}(-2\omega;\omega,\omega)+\chi^{(2)}_{xyz}(-2\omega;\omega,\omega)\right]\left(\hat{E}_{\omega}\right)_{TM}\left(\hat{E}_{\omega}\right)_{TE}\exp\left[i\left(\left(k_{\omega}\right)_{TM}+\left(k_{\omega}\right)_{TE}-\left(k_{2\omega}\right)_{TE}\right)Y\right]$$

(C.13a)

$$\frac{\partial\left(\hat{E}_{2\omega}\right)_{TM}}{\partial Y}=\frac{i\omega}{2\left(n_{2\omega}\right)_{TM}c}\times$$

$$\left\{\left[\chi^{(2)}_{zxx}(-2\omega;\omega,\omega)+\chi^{(2)}_{xyz}(-2\omega;\omega,\omega)\right]\left(\hat{E}_{\omega}\right)^{2}_{TE}\exp\left[i\left(2\left(k_{\omega}\right)_{TE}-\left(k_{2\omega}\right)_{TM}\right)Y\right]\right.$$

$$\left.+\chi^{(2)}_{zzz}(-2\omega;\omega,\omega)\left(\hat{E}_{\omega}\right)^{2}_{TM}\exp\left[i\left(2\left(k_{\omega}\right)_{TM}-\left(k_{2\omega}\right)_{TM}\right)Y\right]\right\}$$

(C.13b)

$$\frac{\partial\left(\hat{E}_{\omega}\right)_{TE}}{\partial Y}=\frac{i\omega}{2\left(n_{\omega}\right)_{TE}c}\times$$

$$\left\{\left[\chi^{(2)}_{zxx}(-2\omega;\omega,\omega)+\chi^{(2)}_{xyz}(-2\omega;\omega,\omega)\right]\left(\hat{E}_{2\omega}\right)_{TM}\left(\hat{E}_{\omega}\right)^{*}_{TE}\exp\left[i\left(\left(k_{2\omega}\right)_{TM}-2\left(k_{\omega}\right)_{TE}\right)Y\right]+\right.$$

$$\left.\left[\chi^{(2)}_{xzx}(-2\omega;\omega,\omega)+\chi^{(2)}_{xyz}(-2\omega;\omega,\omega)\right]\left(\hat{E}_{2\omega}\right)_{TE}\left(\hat{E}_{\omega}\right)^{*}_{TM}\exp\left[i\left(\left(k_{2\omega}\right)_{TE}-\left(k_{\omega}\right)_{TM}-\left(k_{\omega}\right)_{TE}\right)Y\right]\right\}$$

(C.13c)

$$\frac{\partial\left(\hat{E}_{\omega}\right)_{TM}}{\partial Y}=\frac{i\omega}{2\left(n_{\omega}\right)_{TM}c}\times$$

$$\left\{\left[\chi^{(2)}_{xzx}(-2\omega;\omega,\omega)+\chi^{(2)}_{xyz}(-2\omega;\omega,\omega)\right]\left(\hat{E}_{2\omega}\right)_{TE}\left(\hat{E}_{\omega}\right)^{*}_{TE}\exp\left[i\left(\left(k_{2\omega}\right)_{TE}-\left(k_{\omega}\right)_{TE}-\left(k_{\omega}\right)_{TM}\right)Y\right]\right.$$

$$\left.+\chi^{(2)}_{zzz}(-2\omega;\omega,\omega)\left(\hat{E}_{2\omega}\right)_{TM}\left(\hat{E}_{\omega}\right)^{*}_{TM}\exp\left[i\left(\left(k_{2\omega}\right)_{TM}-2\left(k_{\omega}\right)_{TM}\right)Y\right]\right\}$$

(C.13d)

D

SHG with an Angular Deviation of the Fundamental and Second Harmonic Polarisations from the TE and TM Axes Respectively

Assuming an angular deviation of the waveguide sample surface normal to the vertical as defined in Fig. D.1, and, further assuming an orientation of the crystallographic axes as defined in Fig. D.2, we have:

$$(E_\omega)_x = (E_\omega)_y = \frac{E_\omega \cos\theta}{\sqrt{2}} \tag{D.1}$$

$$(E_\omega)_z = -E_\omega \sin\theta \tag{D.2}$$

Neglecting all AQW tensor components, and assuming uniform plane waves, from Appendix C we have:

$$(E_{2\omega})_x \propto 2\chi^{(2)}_{xyz}(E_\omega)_y(E_\omega)_z = -\sqrt{2}\chi^{(2)}_{xyz}E_\omega^2 \sin\theta\cos\theta \tag{D.3}$$

$$(E_{2\omega})_y \propto 2\chi^{(2)}_{yxz}(E_\omega)_x(E_\omega)_z = -\sqrt{2}\chi^{(2)}_{xyz}E_\omega^2 \sin\theta\cos\theta \tag{D.4}$$

$$(E_{2\omega})_z \propto 2\chi^{(2)}_{zxy}(E_\omega)_x(E_\omega)_y = \chi^{(2)}_{xyz}E_\omega^2 \cos^2\theta \tag{D.5}$$

where we have used the relations of (D.1) and (D.2). Furthermore

$$\begin{aligned} E_{2\omega} &\propto \tfrac{1}{\sqrt{2}}(E_{2\omega})_x \sin\theta + \tfrac{1}{\sqrt{2}}(E_{2\omega})_y \sin\theta + (E_{2\omega})_z \cos\theta \\ &= \chi^{(2)}_{xyz} E^2_\omega \left(\cos^3\theta - 2\sin^2\theta\cos\theta\right) \end{aligned} \tag{D.6}$$

where we have used relations (D.3) - (D.5). Hence

$$\frac{I_{2\omega}(\theta)}{I_{2\omega}(\theta=0)} = \left|\cos^3\theta - 2\sin^2\theta\cos\theta\right|^2 \tag{D.7}$$

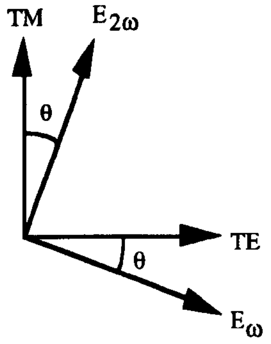

Fig. D.1 Angular deviation of the horizontal and vertical field components with respect to the waveguide axes for an angular deviation of the waveguide surface normal to the vertical

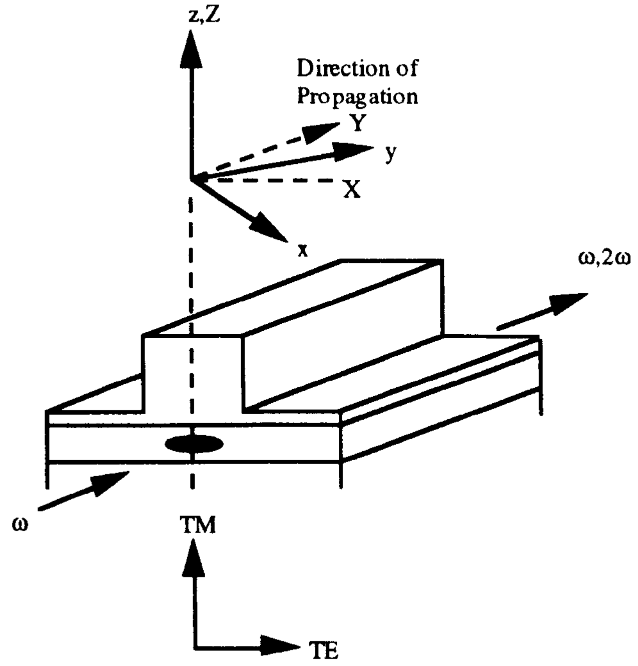

Fig. D.2 The orientation of a GaAs/AlGaAs waveguide device with respect to the crystallographic axes

E

SHG with a Field Component in the Direction of Propagation for a TM Waveguide Mode

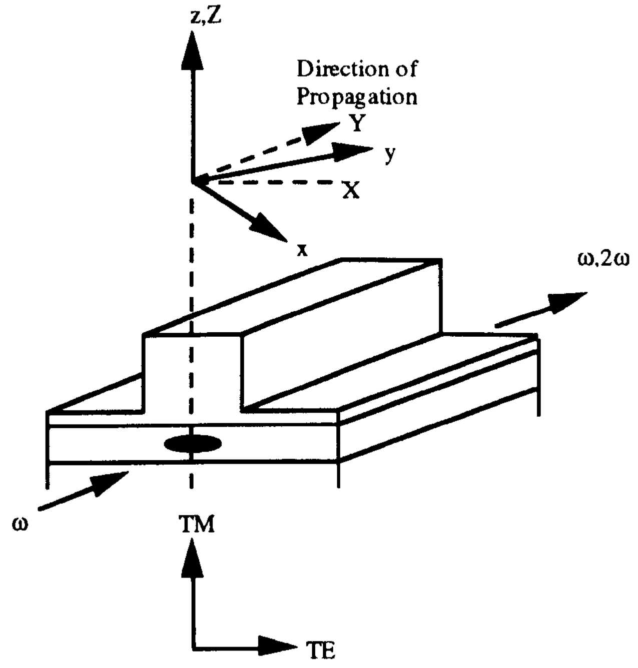

Fig. E.1 The orientation of a GaAs/AlGaAs waveguide device with respect to the crystallographic axes

For the co-ordinate definitions of Fig. E.1 we have:

$$E_{\omega_x} = \frac{1}{\sqrt{2}} E_{\omega X} - \frac{1}{\sqrt{2}} E_{\omega Y} \tag{E.1}$$

$$E_{\omega_y} = \frac{1}{\sqrt{2}} E_{\omega Y} + \frac{1}{\sqrt{2}} E_{\omega X} \tag{E.2}$$

From uniform plane wave considerations we also have (see Appendix C):

$$\begin{aligned} E_{2\omega_z} &\propto \chi^{(2)}_{zxx}E^2_{\omega x} + \chi^{(2)}_{zyy}E^2_{\omega y} + \chi^{(2)}_{zzz}E^2_{\omega z} \\ &+\chi^{(2)}_{zxy}E_{\omega x}E_{\omega y} + \chi^{(2)}_{zyx}E_{\omega y}E_{\omega x} \\ &= \chi^{(2)}_{zxx}\left(E^2_{\omega x} + E^2_{\omega y}\right) + \chi^{(2)}_{zzz}E^2_{\omega z} + 2\chi^{(2)}_{xyz}E_{\omega x}E_{\omega y} \end{aligned} \tag{E.3}$$

Now, for a TM mode, $E_{\omega X} = 0$. Therefore substituting for $E_{\omega x}$ and $E_{\omega y}$ from (E.1) and (E.2) respectively into (E.3) with $E_{\omega X} = 0$ gives:

$$E_{2\omega z} \propto \chi^{(2)}_{zzz}E^2_{\omega z} + \left(\chi^{(2)}_{zxx} - \chi^{(2)}_{xyz}\right)E^2_{\omega Y} \tag{E.4}$$

Now, for $\chi^{(2)}_{xyz} >> \chi^{(2)}_{zxx}$ we have the approximate relationship:

$$E_{2\omega z} \propto \chi^{(2)}_{zzz}E^2_{\omega z} - \chi^{(2)}_{xyz}E^2_{\omega Y} \tag{E.5}$$

For a slab waveguide, all the quantities in (E.5) are depth dependent i.e. they are functions of z:

$$E_{2\omega z}(z) \propto \chi^{(2)}_{zzz}(z)E^2_{\omega z}(z) - \chi^{(2)}_{xyz}(z)E^2_{\omega Y}(z) \tag{E.6}$$

In a slab waveguide, we must also remember that any second harmonic generated through non-linear interactions in regions where it is not supported by the waveguide, will not contribute to the second harmonic beam at the waveguide output. Performing an overlap integration to account for this we may derive a relationship for the TM-polarised second harmonic power $P_{2\omega z}$:

$$P_{2\omega z} \propto \left| \int_{-\infty}^{\infty} dz \left[\chi^{(2)}_{zzz}(z)E^2_{\omega z}(z) - \chi^{(2)}_{xyz}(z)E^2_{\omega Y}(z)\right] \times E_{2\omega TM}(z) \right|^2 \tag{E.7}$$

where $E_{2\omega TM}(z)$ has been used to denote the second harmonic TM mode profile in the slab waveguide to distinguish it from the TM-polarised SHG distribution $E_{2\omega z}(z)$ as defined by (E.6).

Now, from consideration of the time-independent Maxwell equations for the TM mode of a slab waveguide it may be shown that within any waveguide layer [3]:

$$E_{\omega Y} = \frac{-j}{\beta}\frac{\partial E_{\omega z}}{\partial z} \qquad \text{(E.8)}$$

where β is the modal propagation constant i.e. $E_{\omega Y}$ and $\partial E_{\omega z}/\partial z$ are 90° out of phase. Hence, $E_{\omega Y}$ and $E_{\omega z}$ are either in phase or in antiphase, and $E^2_{\omega Y}$ and $E^2_{\omega z}$ are in phase, and E.7 does not need to be ammended to take account of the phase relationship between the different fields.

Then, assuming:

$$\chi^{(2)}_{zzz}(z) = \begin{cases} 0, & \text{z outside MAQW} \\ \chi^{(2)}_{zzz}, & \text{z within MAQW} \end{cases} \qquad \text{(E.9)}$$

and using (E.9) in (E.8) we have:

$$P_{2\omega z} \propto \left| \chi^{(2)}_{zzz} \int_{MAQW} E^2_{\omega z}(z) E_{2\omega TM}(z) dz - \chi^{(2)}_{xyz} \int_{-\infty}^{\infty} E^2_{\omega Y}(z) E_{2\omega TM}(z) dz \right|^2 \qquad \text{(E.10)}$$

Using a multilayer effective index slab solver routine, the integral terms in (E.10) may be evaluated for any given slab waveguide structure. For example, for the particular case of the B690 material at 1.55 μm, the calculated mode profiles $E_{\omega z}(z)$ and $E_{\omega Y}(z)$ for the $TM_{\omega 00}$ mode are plotted in Fig. E.2, where both plots have been normalised to the maximum calculated $E_{\omega z}(z)$ value. $E^2_{\omega z}(z)$, $E^2_{\omega Y}(z)$ and $E_{2\omega TM}(z)$ are also plotted for the B690 material at 1.55 μm in Fig. E.3 from which we have calculated:

$$\int_{MAQW} E^2_{\omega z}(z) E_{2\omega TM}(z) dz = 2.917 \times 10^8 \text{ (a.u.)} \qquad \text{(E.11)}$$

and

$$\int_{-\infty}^{\infty} E_{\omega Y}^{2}(z)E_{2\omega TM}(z)dz = 1.181\times 10^{6} \text{ (a.u.)} \tag{E.12}$$

---

[3] T. Tamir (ed.) with contributions from H. Kogelnik, "Guided-wave Optoelectronics" 2nd ed., Springer, Berlin and London, (1990)

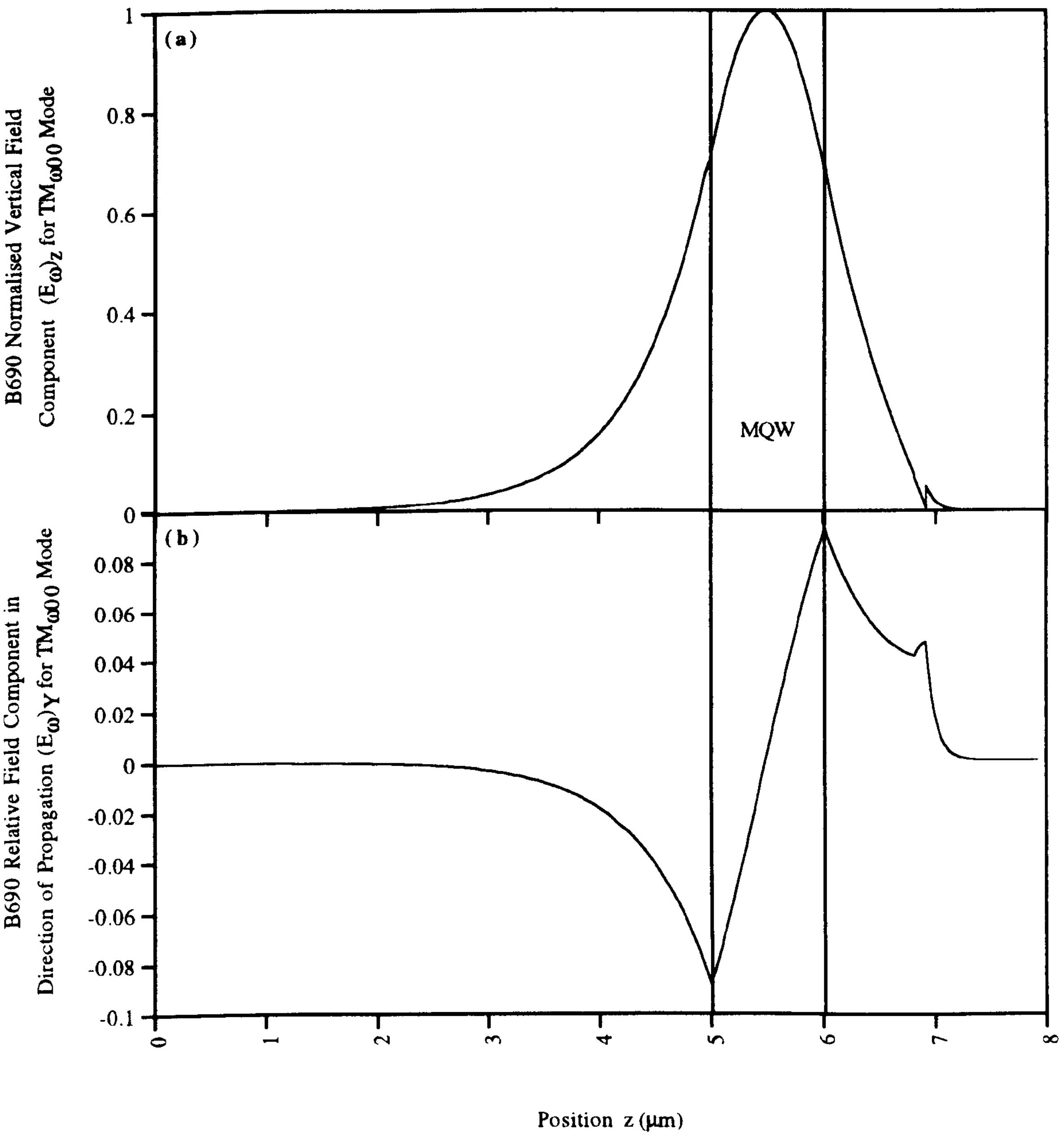

Fig. E.2 Field component depth profiles for the $TM_{\omega 00}$ mode of a B690 slab waveguide at 1.55 μm

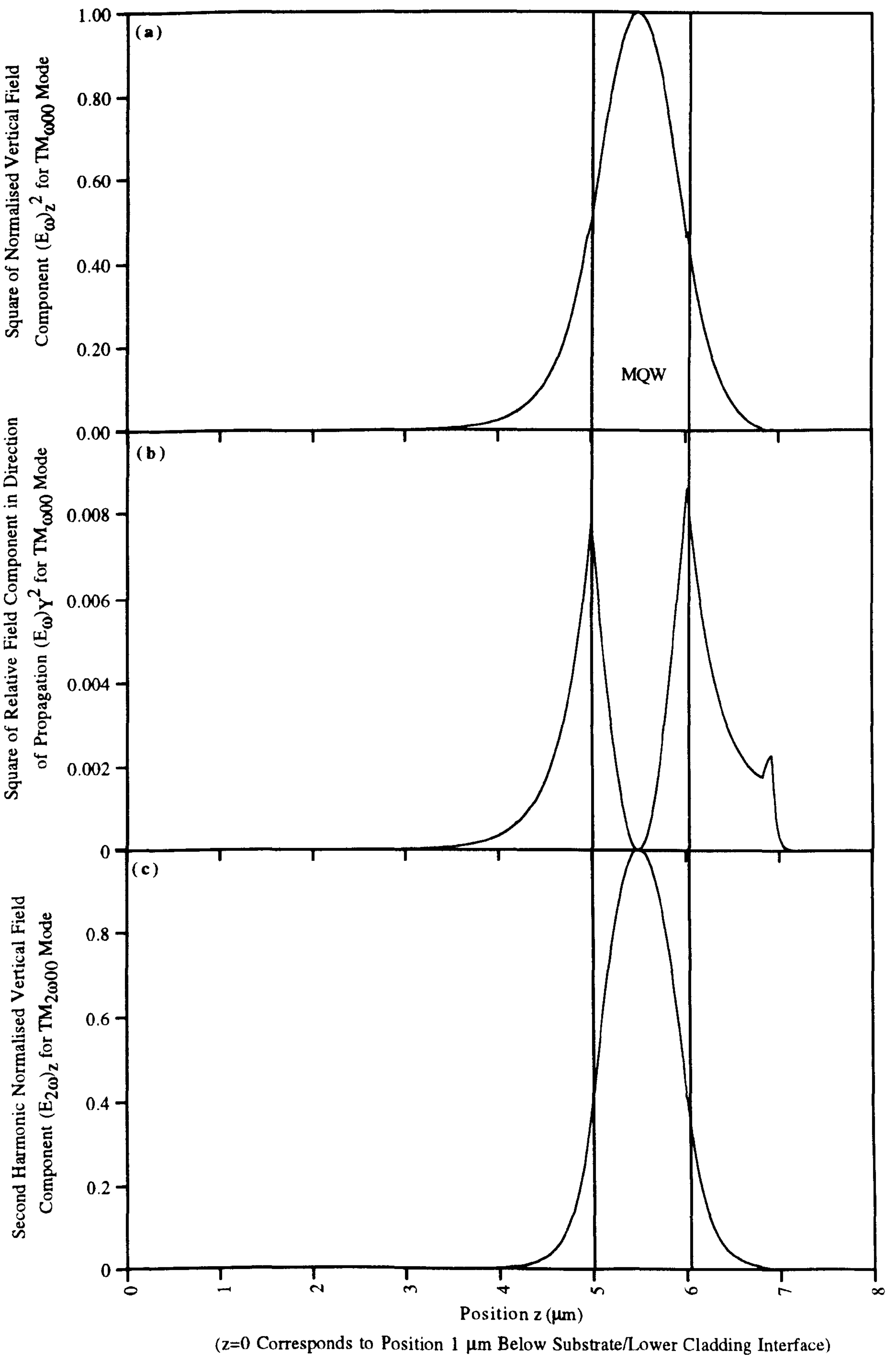

Fig. E.3 Field component depth profiles for the evaluation of the overlap integrals of (E.11) and (E.12)

F

SHG with an Angular Deviation of the Fundamental and Second Harmonic Polarisations from the TM Axis

Assuming an angular deviation of the waveguide sample surface normal to the vertical as defined in Fig. F.1, and, further assuming an orientation of the crystallographic axes as defined in Fig. F.2, we have:

$$(E_\omega)_x = (E_\omega)_y = \frac{E_\omega \sin\theta}{\sqrt{2}} \qquad \text{(F.1)}$$

$$(E_\omega)_z = E_\omega \cos\theta \qquad \text{(F.2)}$$

Neglecting the AQW tensor components $\chi^{(2)}_{xzx}$ and $\chi^{(2)}_{zxx}$, and assuming uniform plane waves, from Appendix C we have:

$$(E_{2\omega})_x \propto 2\chi^{(2)}_{xyz}(E_\omega)_y(E_\omega)_z = \sqrt{2}\chi^{(2)}_{xyz}E^2_\omega \sin\theta\cos\theta \qquad \text{(F.3)}$$

$$(E_{2\omega})_y \propto 2\chi^{(2)}_{yxz}(E_\omega)_x(E_\omega)_z = \sqrt{2}\chi^{(2)}_{xyz}E^2_\omega \sin\theta\cos\theta \qquad \text{(F.4)}$$

$$(E_{2\omega})_z \propto \chi^{(2)}_{zzz}(E_\omega)^2_z + 2\chi^{(2)}_{zxy}(E_\omega)_x(E_\omega)_y = \chi^{(2)}_{zzz}E^2_\omega \cos^2\theta + \chi^{(2)}_{xyz}E^2_\omega \sin^2\theta \qquad \text{(F.5)}$$

where we have used the relations of (F.1) and (F.2). Furthermore

$$E_{2\omega} \propto \frac{1}{\sqrt{2}}\left(E_{2\omega}\right)_x \sin\theta + \frac{1}{\sqrt{2}}\left(E_{2\omega}\right)_y \sin\theta + \left(E_{2\omega}\right)_z \cos\theta$$
$$= \left[3\chi^{(2)}_{xyz}\sin^2\theta\cos\theta + \chi^{(2)}_{zzz}\cos^3\theta\right]E^2_\omega \qquad \text{(F.6)}$$

where we have used relations (F.3) - (F.5).

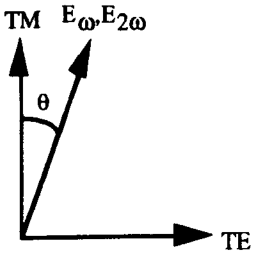

Fig. F.1 Angular deviation of the vertical field components with respect to the waveguide axes for an angular deviation of the waveguide surface normal to the vertical

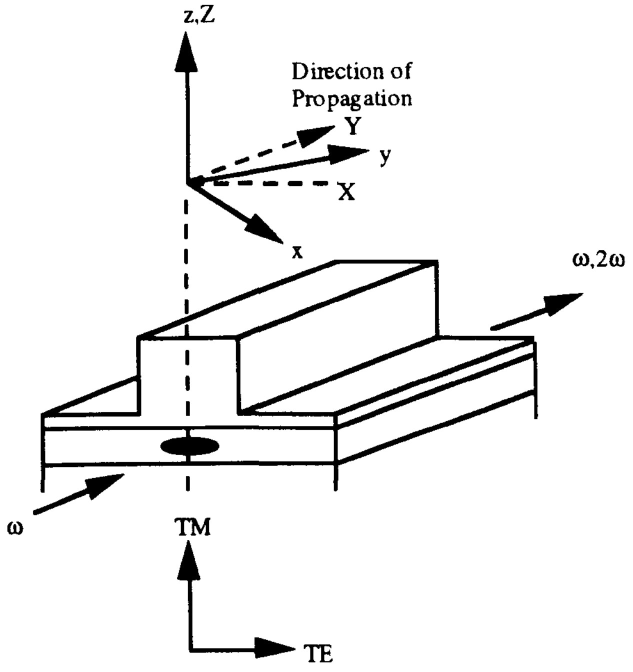

Fig. F.2 The orientation of a GaAs/AlGaAs waveguide device with respect to the crystallographic axes

G

SHG Tuning Curves for Periodically-intermixed B690 AlGaAs ACQW Waveguides

The SHG tuning curves obtained for 2 mm-long periodically-intermixed B690 waveguide samples in the $TE_{\omega}:TM_{2\omega}$ polarisation configuration are shown in Figs. G.1 to G.6. The data plotted in these figures was obtained under cw conditions as described in Section 8.4.

Absolute PMT signal scales are not shown in Figs. G.1 to G.6, but rather absolute maximum PMT signal values are listed alongside each tuning curve to give an indication of the signal magnitude during tuning. This was done deliberately to de-emphasise the absolute magnitude of the PMT signals, since the fundamental input power was not monitored during the tuning experiments i.e. different absolute PMT signal magnitudes could simply reflect different fundamental input powers and are not, therefore, very meaningful.

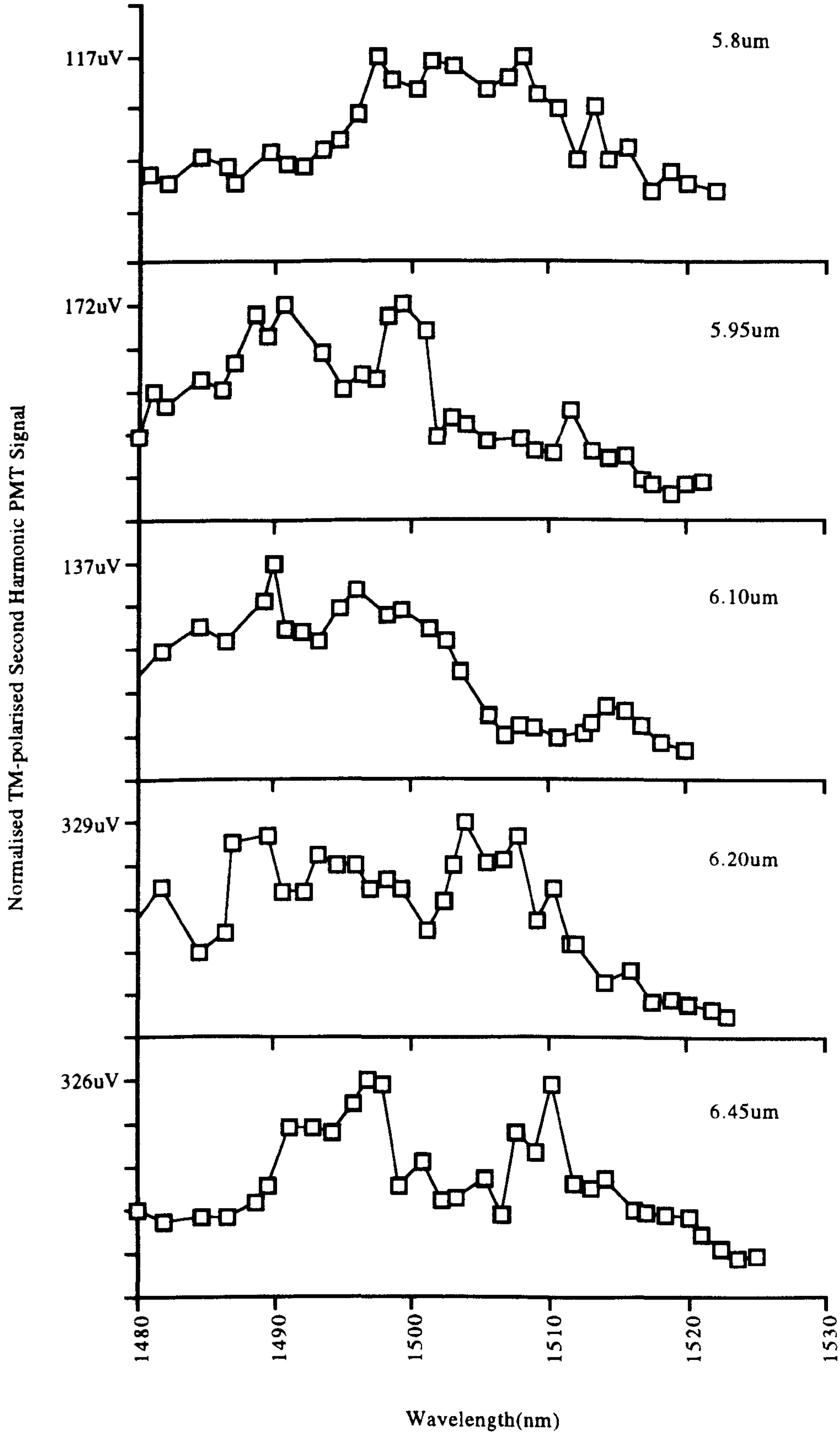

Fig. G.1 TE$_{\omega}$:TM$_{2\omega}$ SHG tuning curves obtained for 2 mm-long B690 waveguide samples with intermixing periods of 5.80 - 6.45 μm

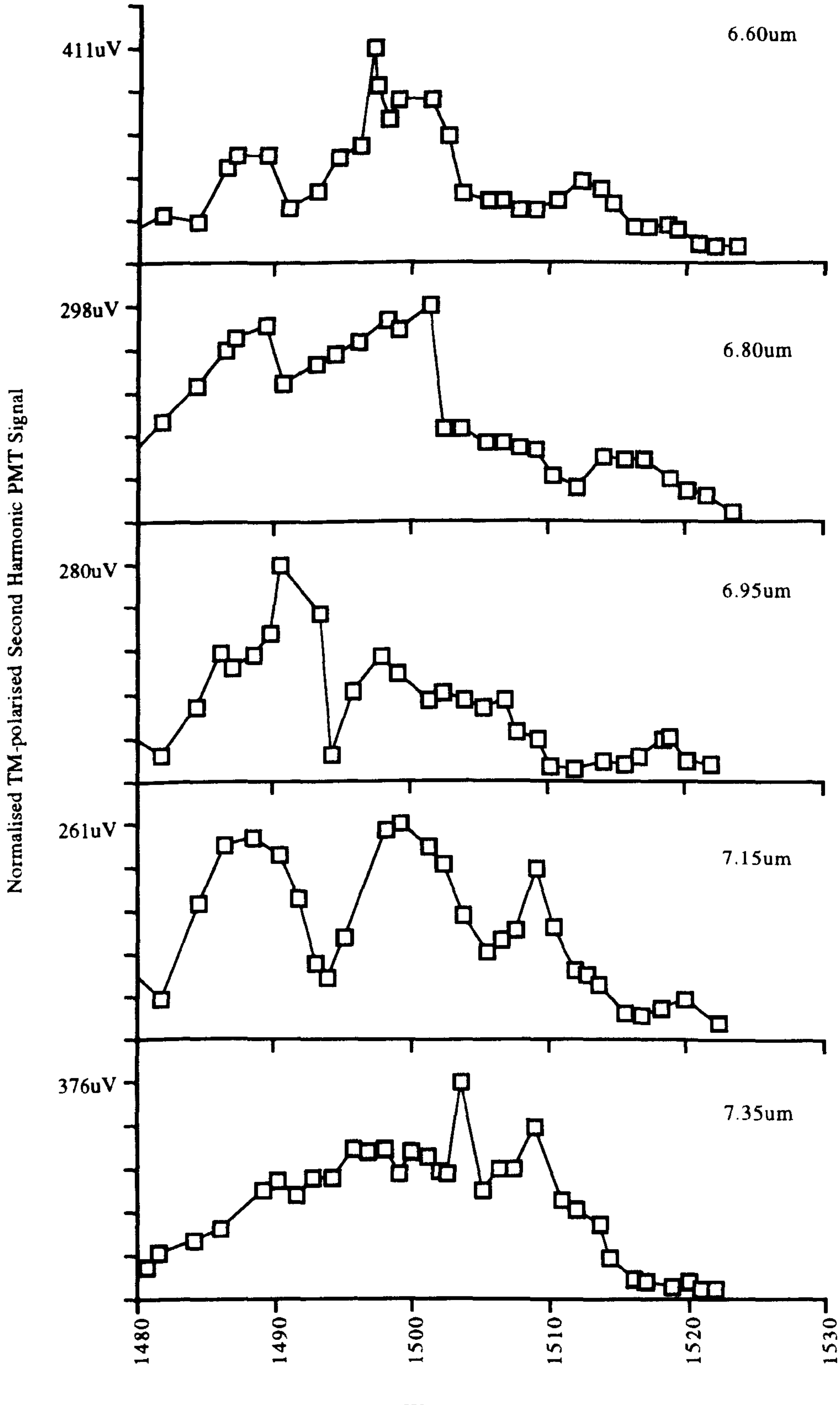

Fig. G.2 TE_{ω}:$TM_{2\omega}$ SHG tuning curves obtained for 2 mm-long B690 waveguide samples with intermixing periods of 6.60 - 7.35 μm

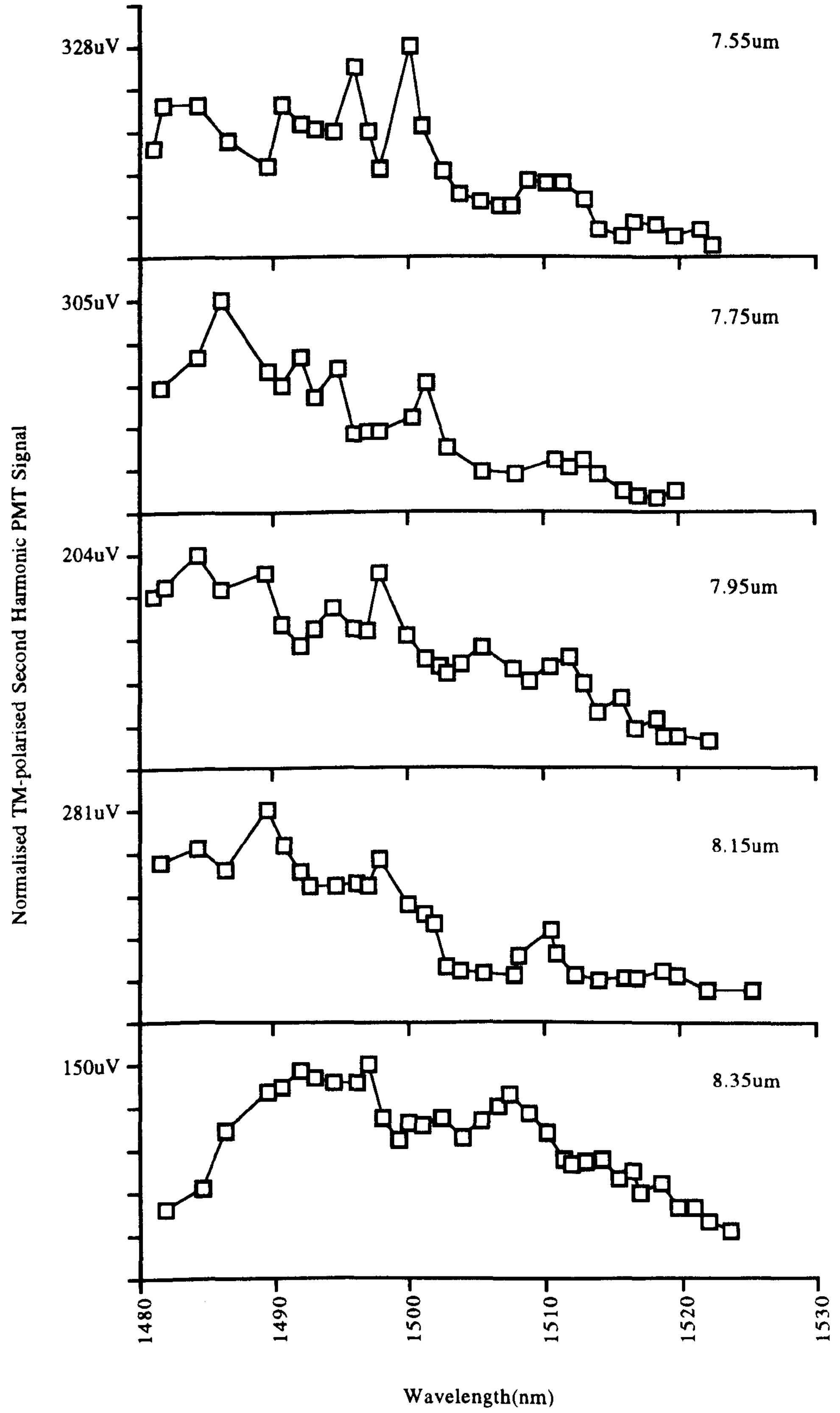

Fig. G.3 $TE_{\omega}:TM_{2\omega}$ SHG tuning curves obtained for 2 mm-long B690 waveguide samples with intermixing periods of 7.55 - 8.35 μm

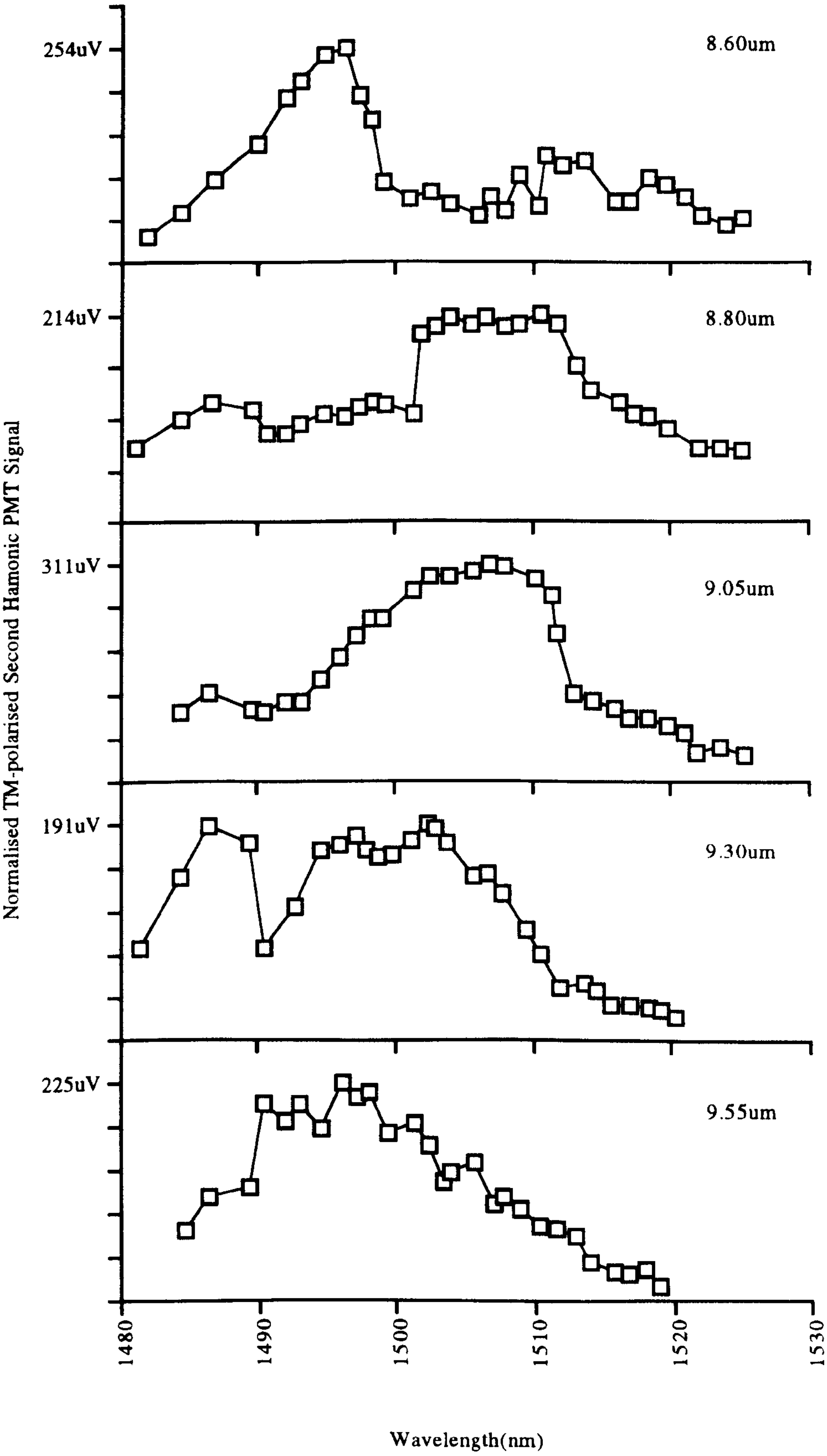

Fig. G.4 TE$_{\omega}$:TM$_{2\omega}$ SHG tuning curves obtained for 2 mm-long B690 waveguide samples with intermixing periods of 8.60 - 9.55 μm

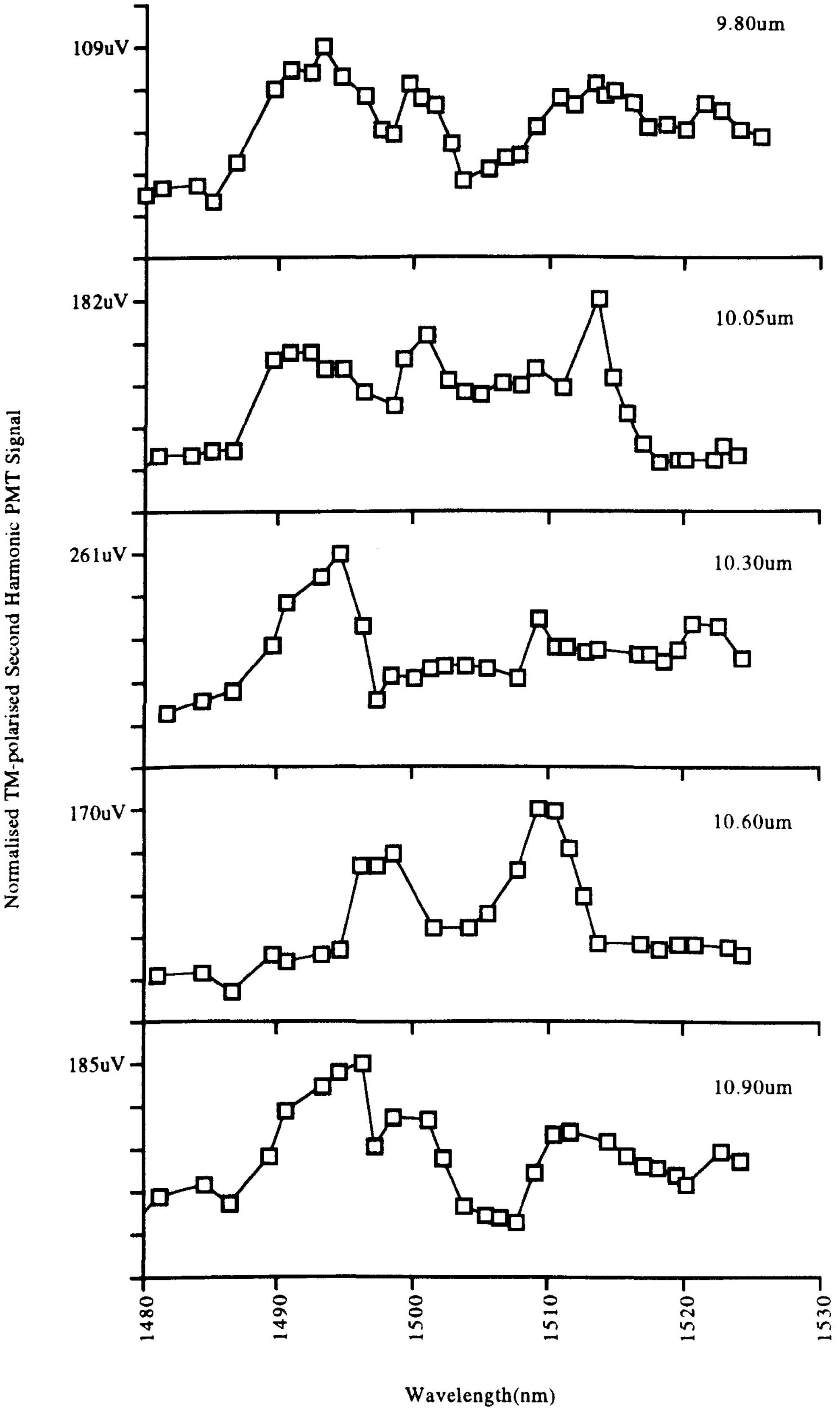

Fig. G.5 TE_{ω}:$TM_{2\omega}$ SHG tuning curves obtained for 2 mm-long B690 waveguide samples with intermixing periods of 9.80 - 10.90 μm

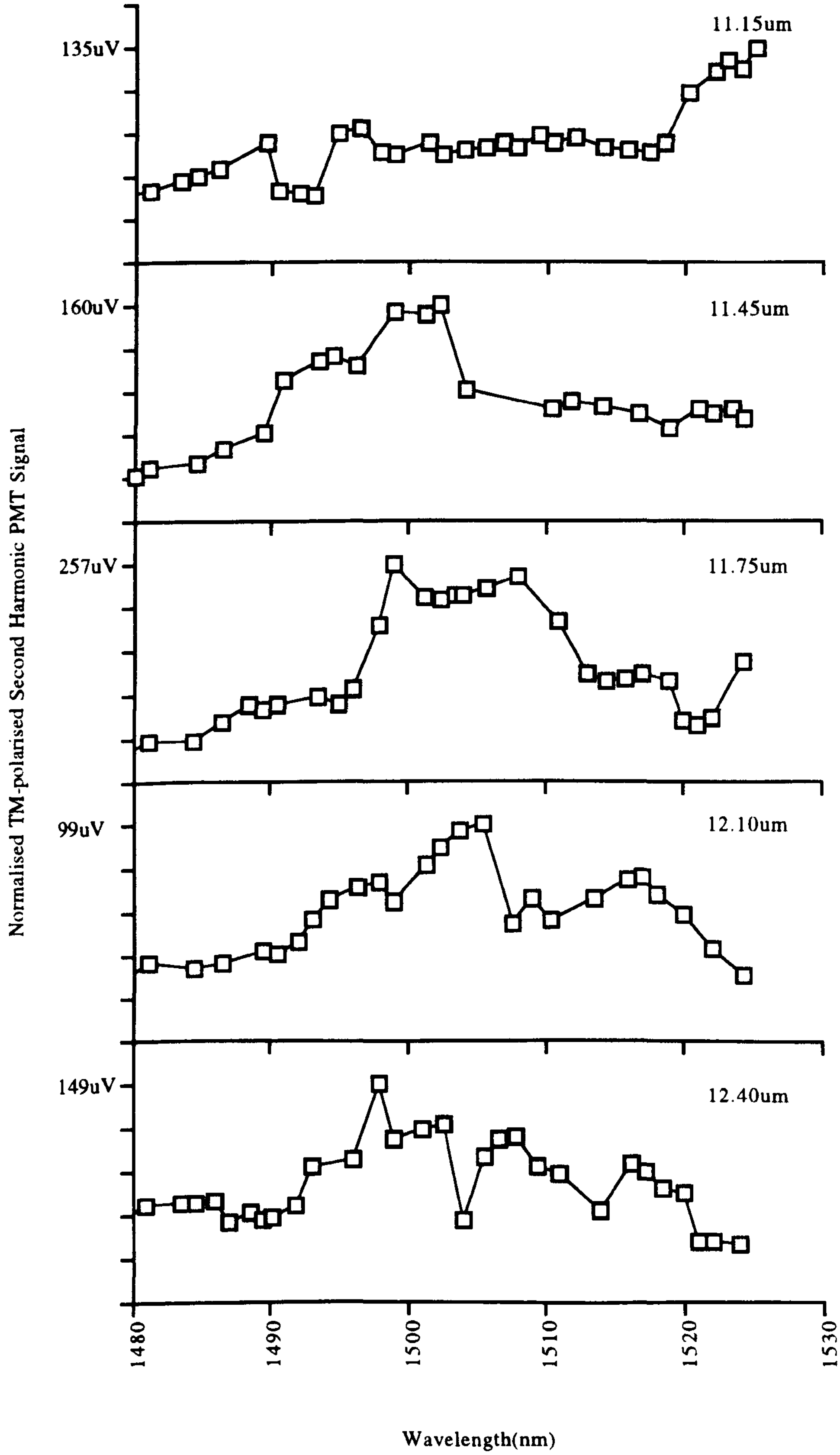

Fig. G.6 TE_{ω}:$TM_{2\omega}$ SHG tuning curves obtained for 2 mm-long B690 waveguide samples with intermixing periods of 11.15 - 12.40 μm